CONSTRUCTION AND MODIFICATION OF DEBRIS-FLOW ALLUVIAL FANS AS CAPTURED IN THE GEOMORPHIC AND SEDIMENTARY RECORD: EXAMPLES FROM THE WESTERN SANGRE DE CRISTO MOUNTAINS, SOUTH-CENTRAL COLORADO

by

Sylvia Rose Nicovich

A dissertation submitted in partial fulfillment
of the requirements for the degree

of

Doctor of Philosophy

in

Earth Sciences

MONTANA STATE UNIVERSITY
Bozeman, Montana

April 2020

ACKNOWLEDGEMENTS

Foremost, I would like to thank my advisor, Dr. Jim Schmitt, whose guidance through the last five years has been formative to not only my understanding of geology, but also to my personal and professional growth. Thank you to my committee members Dr. Mary Hubbard, Dr. Jeannie Dixon, and Cal Ruleman for their thoughtful feedback and useful knowledge.

Endless gratitude belongs to my number-one field companion, Ashley Ferguson for a month of scarce showers and abundant mosquito bites. I would like to recognize all who helped me in the field; Dr. Jim Schmitt, Cal Ruleman, Mike Frothingham, Dr. Andy Cyr, Dr. Sam Johnstone, Jesse Gremore, Dr. Ralph Klinger, Bob Kirkham, Dr. Adam Hudson, and Dr. Jim Paces. Thank you to the park geologist of Great Sand Dunes National Park, Andrew Valdez, and Zapata Falls campground hosts, Jim and Jaqueline.

The collaboration and friendship of Shannon Mahan and Dr. Harrison Gray of the USGS Optically Stimulated Luminescence Lab is greatly acknowledged. Thank you to Dr. Christine Gobrogge of Montana State University's Environmental Analytical Lab for helping me operate the Malvern and process grain-size data.

Thanks to my coworkers at Reclamation for their ceaseless encouragement, especially to my group manager, Jeanne Godaire, and my mentors of everything Quaternary and soil, Dr. Ralph Klinger and Dr. Joanna Redwine.

Finally, thanks to my friends and family, especially the Beighley-Willoughby's who fed me dinner nearly every night for the weeks leading to my comprehensive exams, The Stern-Lange Circus of Livingston, and Mike and Flysch Frothingham—much love.

FUNDING ACKNOWLEDGEMENT

Funding for this research provided by the Montana Space Grant Consortium, the United States Geological Survey EDMAP Program, and Montana State University Graduate School and Earth Sciences Department are gratefully acknowledged.

TABLE OF CONTENTS

TABLE OF CONTENTS CONTINUED

LIST OF TABLES

LIST OF FIGURES

Figure Page

LIST OF FIGURES CONTINUED

Figure Page

LIST OF FIGURES CONTINUED

Figure Page

LIST OF FIGURES CONTINUED

Figure Page

LIST OF FIGURES CONTINUED

Figure Page

LIST OF FIGURES CONTINUED

Figure Page

LIST OF FIGURES CONTINUED

Figure Page

LIST OF FIGURES CONTINUED

Figure Page

LIST OF FIGURES CONTINUED

Figure Page

LIST OF FIGURES CONTINUED

Figure Page

ABSTRACT

Alluvial fans and their deposits in the stratigraphic record are key in unraveling intricacies of landscape, tectonic, and climatic dynamics, though integrative geomorphologic and sedimentologic studies that comprehensively evaluate processes which build and modify fans are lacking. Therefore, a gap within the current body of literature exists concerning the sedimentological signature of depositional and surface-modifying processes on alluvial fans. This dissertation presents the sedimentological characteristics, both surficial and in the sedimentary record, of processes that build and modify alluvial fans while revisiting the contemporary concept of what defines an active surface. Detailed analysis of a suite of Quaternary active debris-flow alluvial fans on the western range front of the Sangre de Cristo Mountains in south-central Colorado was made using integrative sedimentological and geomorphic analysis, facies and soils mapping, along with infrared stimulated luminescence (IRSL) geochronology to document timing of fan construction and modification processes recorded in the alluvial fan deposits. Analysis of surface geomorphology, facies assemblages, and particle-size distributions of matrix from various facies of exposed alluvial fan deposits were also applied. These data show a clear distinction between sedimentary facies that represent processes of the primary depositional lobe surfaces versus those operating during periods of non-primary deposition, dominant on abandoned lobes. Primary processes on depositional lobes are debris flow and hyperconcentrated flow with minimal secondary modifying processes. Overland flow, input of eolian material, pedogenesis, and rock and mineral weathering are the main secondary modifying processes that govern abandoned lobes. Addition of wind-blown material, a secondary modifying process, plays a significant part in the sedimentary processes that operate on alluvial fan surfaces, ultimately influencing fan smoothing by mobilizing material derived from primary processes.

CHAPTER ONE

INTRODUCTION

Alluvial Fans and their Deposits

Alluvial fans are semi-conical landforms built by radial sediment dispersal and accumulation at the junctions of mountainous drainages and adjoining piedmont flats (Figure 1.1). They are a pervasive feature of areas with high relief and tectonic activity, and therefore their sedimentation patterns are often leveraged by earth scientists for use as proxy to climatic and tectonic landscape dynamism (Bull, 1972; Ritter et. al., 1995; Blair and McPherson, 1994: Quigley et al., 2007; Densmore et al., 2007; Dunforth et al., 2007, Blair and McPherson, 2009; Harvey, 2011) and their deposits within the ancient record for insight to basin-fill dynamics (Ventra-Nichols, 2013). Nevertheless, the complex development of alluvial fans is difficult to conceptualize due to the impact of both broader allogenic and autogenic drivers and the contemporaneous nature of processes that build, modify, and erode fan surfaces.

The characteristic fan shape of debris-flow alluvial fans is formed due to the downslope transition from a confined source catchment to an open piedmont, providing lateral space for sediment to spread radially. Progressive autogenic switching of depositional foci driven by topographic compensation sustains the fan form (Beaty, 1963; Denny, 1967; Hooke, 1967; Bull, 1972; Blair and McPherson, 1994; Blair and McPherson, 2009; Scheinert et al., 2012; de Haas et al., 2018). Processes on alluvial fans can be reduced to two main categories; primary, depositional processes that build the fan,

and secondary, modifying processes, which rework the fan surface during times of non-primary deposition.

Alluvial fans are constructed by primary processes that occur as episodic sedimentation events, which deliver material from the drainage basin to the fan (Beaty, 1963; Denny, 1967; Bull, 1977; Blair and McPherson, 1994; Blair and McPherson, 2009). Primary depositional processes are the dominant sediment transport process on the depositional lobe of the alluvial fan, yet secondary modifying processes also act on the surface of these lobes. On the abandoned lobes, however, secondary modifying processes are the most prevalent sedimentary transport processes, though primary processes (i.e. debris-flow) may occur on occasion. The most common primary processes on alluvial fans include both sediment-gravity flow (debris flow) and fluid-gravity flow (sheetflood) (Blair and McPherson, 1994; Blair and McPherson, 2009; Harvey, 2011). The focus herein will be on debris-flow formed alluvial fans.

Debris flows are gravity-driven masses of poorly-sorted sediment, with saturation content of 20% to 60% by volume (Beaty, 1961; Costa, 1988; Iverson, 1997). Initiation of debris flow is largely consequent to the addition of fluid from intense precipitation events (Costa, 1988; Iverson, 1997). In non-cohesive debris flows, grains interact with one another and with water, behaving as a single-phased non-Newtonian fluid (Costa, 1988). Conversely, in cohesive debris flow, grain to grain interaction is limited by the aggregation of grains and matrix, which often results in a solid plug flowing between laminar boundaries (Scott et al., 1995). Sheetfloods are Newtonian flash floods of unconfined water, where sediment and fluid remain in two separate phases (Bull, 1972;

Costa, 1988). Determination of sediment-gravity versus fluid-gravity flow is largely driven by drainage basin characteristics and results in distinctly different depositional facies and alluvial fan morphology (Whipple and Dunne, 1992; Blair and McPherson, 1994; Blair, 1999; Moscariello, 2002; Blair and McPherson, 2009).

Though the deposits of primary processes may be distinct when unaltered, secondary (or modifying) processes may subsequently change initial depositional characteristics, masking the original features on alluvial fan surfaces (Blair and McPherson, 1994; Blair and McPherson, 2009; de Haas et al., 2014). Unlike primary processes that occur in punctuated bursts on segregated areas, secondary processes indiscriminately act across all fan surfaces at different stages to varying degrees (Wells et al., 1987; McFadden, 1989; Ritter, 1993). Secondary processes include bioturbation, pedogenesis, modification of initial deposits from sheet wash and overland flow, weathering of rock and minerals, which leads to degradation of original depositional features, gullying, and input of eolian material (Blair and McPherson, 1994; Blair and McPherson, 2009). Generally, time since active deposition has ceased can be discerned through the degree of surface smoothing of the fan (Frankel and Dolan, 2007; Matmon et al., 2008; Mushkin et al, 2014; Johnstone et al., 2018).

Significance of the Problem

A major problem within alluvial fan research is the dearth of integrative geomorphologic and sedimentologic studies working towards comprehensive understanding of processes that build and modify fans. While a unifying objective of alluvial fan research has been to link fan-surface features with formative processes, the

importance of debris-flow processes to alluvial fan formation has been largely overlooked, due to not only their long recurrence interval, but also the reworking of their genetic deposits by more frequent water flows (Lecce, 1990; Costa, 1988; Whipple and Dunne, 1992; Blair and McPherson, 1998). Accordingly, sedimentologic examination of alluvial fans is imperative to understanding the fundamentals of their development; especially given that misinterpretation of formative processes has emerged from inferences lacking consideration of the impact that modifying processes have on fan surface expression. To illustrate, fluvial forms (e.g. braided stream networks) and facies have been interpreted to exist on alluvial fans, later recognized to be extensively modified debris flow deposits (Hooke, 1967; Blair and McPherson, 1992; de Haas et al., 2014). An instrumental aspect in correctly identifying fan-forming processes is the recognition and distinction of processes that modify primary deposits. Additionally, there are multiple secondary processes that modify fan surfaces in a variety of ways. So, distinguishing these processes and the impact of each as sediment contributors and surface modifiers is helpful to the understanding of fan evolution. In particular, few studies have been conducted on the influence of wind-blown material on fan dynamics (McFadden, 1987; Anderson and Anderson, 1990; Shroba et al., 2007). Bounding surface and facies transitions are integral to reconstructing alluvial fan architecture, though interpretation of these features within debris-flow alluvial fan stratigraphy holds considerable uncertainty (Ventra and Nichols, 2013, and references within). Eolian material may be instrumental in surface development on all areas of alluvial fans and thereby necessitates further

consideration, especially in application to fan evolution dynamics through facies interpretations.

Active alluvial fans and fan deposits in the rock record are frequently used as indicators of landscape dynamics, yet the distinction between sedimentological signatures of depositional and surface-modifying processes is often disregarded. Alluvial fan stratigraphy in both the rock record and in modern systems should represent the dichotomy of episodic primary deposition being frequently modified by secondary processes. Therefore, stratigraphic criteria useful for delineating fan processes, both formative and especially modifying, require more attention (Ventra and Clarke, 2018). An advantage to the investigation of modern alluvial fan systems is the possibility for making stratigraphic to surficial sedimentologic association by observing correlations between active surficial processes and their features preserved in exposed deposits of the same fan.

Objectives and Research Questions

The overarching goal of this dissertation is to improve the understanding of debris-flow alluvial fan formation and surface evolution and to bridge the gap between their surface geomorphology and stratigraphic succession. The objectives are separated into two parts with accompanying research questions, each of which are addressed in subsequent chapters comprising a series of three publications.

Objective 1: To investigate formative and modifying processes of debris-flow alluvial fans through sedimentological examination, both on the surface and in vertical exposure.

1. What are the sedimentary facies and surficial characteristics of primary deposition on debris-flow alluvial fans?
2. What are the sedimentary facies and surficial characteristics of surface modification on debris-flow alluvial fans?

Objective 2: To revisit the concept of active versus inactive alluvial fan surfaces.

3. What processes operate on debris-flow alluvial fan surfaces of non-primary deposition?
4. What is the role of eolian input on debris-flow alluvial fan surfaces?

Chapter 2 addresses objective 1 by exploring research questions 1 and 2 through a detailed sedimentological analysis of a suite of Quaternary active debris-flow alluvial fans.

Chapter 3 addresses research question 3 by using integrative sedimentological and geomorphic analysis to applied facies and soils mapping along with infrared stimulated luminescence (IRSL) geochronology to document timing of fan construction and modification processes recorded in alluvial fan deposits. The inventory of modifying processes provided through Chapter 3 inherently addresses Objective 2, being that these processes occur on what are conventionally considered inactive surfaces.

Chapter 4 addresses research question 4, reporting the role of wind-blown sediment on alluvial fan surfaces while revisiting the concept of activity on fan surfaces (Objective 2). Analysis of surface geomorphology, facies assemblages, and particle size distributions of matrix from various facies of exposed alluvial fan deposits suggest that wind-blown material plays a significant part in the sedimentary processes that operate on alluvial fan surfaces.

Chapter 5 is a synthesis of the results and conclusions in each previous chapter, which discusses the findings and applications of this research.

Theoretical Basis

Alluvial fan deposition, depositional lobe avulsion, and surface evolution is complicated, stochastic, and multidimensional. The radial plan-form pattern of alluvial fans is representative of autogenic processes in which sediment distribution from the catchment to the fan surface (depositional lobe) makes successional shifts depending on the existing architecture of the fan. Beyond flow composition and rheology, transposition of depositional activity is principally a result of backfilling and avulsion to an adjacent surface and/or guided by topographically lower pathways between older, abandoned surfaces (Denny, 1967; Whipple and Dunne, 1992; de Haas et al., 2018). These switching patterns exist on two distinct scales and are referred to as lateral and vertical autogenic dynamics, respectively (Ventra and Nichols, 2013). Lateral autogenic dynamics concern the backfilling of discrete depositional pathways within a single flow and avulsions to adjacent areas of the current depositional lobe within a fan. Vertical autogenic dynamics refer to topographic compensation of long-term flow-path selection over the entire fan,

involving generations of flows stacking atop one another until a threshold is passed and a new, topographically lower depositional lobe is occupied (Ventra and Nichols, 2013, de Haas et al., 2018).

Autogenic dynamics of debris-flow alluvial fans are difficult to observe in real time given their episodic incidence, sometimes with a recurrence interval upwards of thousands of years (Costa, 1984). This introduces challenges in elucidating the interplay between primary and secondary process integral to fan evolution. However, because of the radial switching nature of alluvial fans, the genesis of secondary processes modifying primary depositional features can be recognized across surfaces of varying age, providing an optimal space-for-time substitution within a single fan. Through observation of which processes are occurring where on the fan surfaces and how these processes are represented in stratigraphic sequences within the same modern alluvial fan system, more realistic inferences about alluvial fan evolution can be made regarding ancient deposits.

Study Area

The alluvial fans along the western range front of the Sangre de Cristo Mountains within the San Luis Valley in southcentral Colorado present an ideal area to study the formation and evolution of debris-flow alluvial fans. These fans are located adjacent to a variety of neighboring environments including a paleo lake basin, large dune field, and extensively glaciated valleys. Moreover, this area yields excellent vertical exposures of modern alluvial fan deposits, which are easily accessible via a gravel quarry.

Geologic Setting

The Sangre de Cristo Mountains are a roughly north-northwest trending mountain range bound by the Holocene active Sangre de Cristo normal fault system. The range constitutes the extensional footwall of the Sangre de Cristo normal fault system, defining the eastern margin of its extensional hanging wall, the San Luis Valley. Just north of an embayment on the western range front and south of the Great Sand Dunes, the Blanca Peak massif encompasses a series of peaks exceeding elevations of 4,300 meters (Figure 1.2). Pleistocene glaciation is evident in the high-elevation drainages along the Blanca Peak massif where five large alluvial fans (~5-6 km radii) emerge onto the San Luis Valley, each named from its respective source drainage. From north to south they are, South Zapata, Pioneer, Holbrook, Tobin, and Blanca alluvial fans. The South Zapata, Pioneer, and Holbrook fans are capped by moraine complexes that extend downfan beyond the fan apex. Approximately fifteen, much smaller (0.5 to 3 km radii), coalesced fans to the north are sourced from shorter, lower-elevation drainage basins that have no evidence of glaciation (Figure 1.2).

Precambrian Basement Rocks. The crystalline basement of the Sangre de Cristo Mountains includes the Paleoproterozoic mafic volcanic arc rocks of the Yavapai and Mazatzal provinces that were accreted together and sutured to the Wyoming and Mojave provinces, and subsequently intruded by Mesoproterozoic granitic plutons (Shaw and Karlstrom, 1999; Yonkee and Weil, 2015). These basement rocks have been involved in two formative mountain-building events that contributed to formation of the present Sangre de Cristo Mountains. The Paleoproterozoic basement was exposed during the

Pennsylvanian and Permian Ancestral Rockies orogeny as a series of basement-cored arches, creating intraforeland flexural basins (Barbeau et al., 2003). Current basement exposure in the Sangre de Cristo Mountains is a product of Laramide contraction, thrusting a basement wedge over deformed Paleozoic intraforeland basin sedimentary deposits, and ultimately subsequent Neogene extension, uplift, and exhumation along the Sangre de Cristo normal fault system (Kellogg, 1999).

Ancestral Rocky Mountain Orogeny. The Ancestral Rocky Mountain orogeny of the middle Pennsylvanian to late Pennsylvanian-Permian period was broadly driven by the collision of Gondwanaland with Laurentia when the present North American region existed at equatorial latitudes (Lindsey et al., 1986). Recognition of faults that controlled the Ancestral Rockies uplifts is difficult to impossible, due to overprinting and reactivation of Laramide thrusting and Cenozoic extension (Lindsey et al., 1986; Hoy and Ridgeway, 2002). The Sangre de Cristo Mountains and greater Southern Rocky Mountains, however, host a series of Pennsylvanian and Permian syntectonic sedimentary deposits that elucidate mechanistic details pertaining to the highlands from which they originated. The Uncompahgre and Ancestral Front Range uplifts were basement-involved, roughly north-trending ranges separated by the Central Colorado trough, which collected sediment deposited from middle Pennsylvanian to Permian time. Initiation of this deposition is recorded by the marine Minturn Formation comprising interbedded conglomerate, sandstone, mudstone, and limestone (Lindsey et al., 1986; Hoy and Ridgeway, 2002). The Minturn Formation represents a prograding marine fan delta sequence deposited in the west side of Central Colorado trough (Lindsey et al., 1986).

The Minturn was then covered by the non-marine alluvial fan deposits of the Sangre de Cristo Formation (Lindsey et al., 1986). The Sangre de Cristo formation is made up of conglomerate, sandstone and siltstone. The sandstone-dominated lower member represents distal alluvial fan sequences and has been differentiated from the more proximal, cobble-boulder sized Crestone conglomerate (Lindsey et al., 1986; Hoy and Ridgeway, 2002). Aggradation in the Central Colorado trough persisted into the Mesozoic, by which time the Uncompahgre highlands had eroded to plains extending to the filled trough (Hoy and Ridgeway, 2002). Marine deposition ensued during the Mesozoic with the onset of Farallon plate subduction beneath western North America forming the Sevier foreland basin, which accumulated strata atop the eroded Ancestral Rockies (Hoy and Ridgeway, 2002).

Laramide Orogeny. Beginning in the Cretaceous Period and persisting until the Eocene epoch, Laramide compression, driven by a transition to flat-slab subduction of the Farallon plate, deformed the Sevier foreland basin and thrust basement-cored sheets up and over sedimentary sequences interpreted as a series of west-dipping thrusts and reverse faults (Lindsey, 1998; Hoy and Ridgeway, 2002; Yonkee and Weil, 2015). In the Sangre de Cristo Mountains, this is represented by three separate thrust sheets (Marble Mountain, Spread Eagle, and Huckleberry Mountain faults), all of which carry Pennsylvanian-Permian deposits of the Central Colorado trough in their hanging walls (Lindsey et al., 1983; Hoy and Ridgeway, 2002).

Rio Grande Rifting. Crustal compression of the Laramide transitioned to crustal extension and collapse of the highlands by the middle of the Cenozoic Era. For most of western North America, this phase of extension is considered to be associated with development of the Basin and Range province. However, east of the competent Colorado Plateau, the Rio Grande Rift defines extension in a series of north-trending half grabens extending from Central Colorado to Southern New Mexico (Tweto, 1978; Chapin and Cather, 1994). Extensional geometry of the Rio Grande Rift is thought to be a product of rotation of the Colorado Plateau about an Euler pole located in northeastern Utah, forming extensional basins around the perimeter (Chapin and Cather, 1994). The San Luis Valley is the largest axial basin of the Rio Grande Rift.

The San Luis Valley is bound to the east and west by the Sangre de Cristo Mountains and associated fault system and the Oligocene andesitic San Juan volcanic field, respectively. The sand in the Holocene Great Sand Dunes is mostly sourced from the San Juan volcanics (Brister and Gries, 1994; Madole et al., 2008).

Neotectonic Sangre de Cristo Fault System. The Sangre de Cristo normal fault system is the most active expression of continuous Quaternary tectonics in the San Luis Valley. It bounds the western front of the Sangre de Cristo Mountains down-dropping the deepest area of the San Luis Valley, the Baca Graben (Brister and Gries, 1994; Ruleman and Machette, 2007). Prominent fault scarps on alluvial fans along the mountain-piedmont junction are evidence of continuous Pleistocene to Holocene activity on the fault system (McCalpin, 1982; Ruleman and Machette, 2007). This fault system is separated into three sections: the northern, central, and southern. The Blanca Peak massif

encompasses the southern portion of the northern section (Zapata Section) and the northern-most portion of the central section (Blanca Section), where the range takes an eastward step (Figure 1.2). The most recent event (MRE) along the Zapata section is estimated to have occurred at approximately 5.5-5.3 ka (McCalpin, 2006). The Blanca section, which defines the Blanca Massif salient, is less active than the northern section of the Sangre de Cristo fault system and only has only one documented post-35 ka MRE (McCalpin, 1982).

Pleistocene Climate.

Lake Alamosa

Widespread lacustrine deposits and landforms are evidence of the extensive Plio-Pliestocene Lake Alamosa that once occupied the northern San Luis Basin. This lake expanded and contracted for hundreds of thousands of years while it filled the valley with sediment (Machette et al., 2007, Ruleman et al., 2007). Lake Alamosa began to overtop a low Oligocene volcanic topographic sill to the south at about <440 ka, which cut the Rio Grande Gorge over a period of ~200 ky (Ruleman et al., 2007). The evacuation of Lake Alamosa exposed sediments in the valley floor to eolian processes, which have formed the Great Sand Dunes that continue to transport material throughout the valley (Madole et al., 2008).

Quaternary Glaciation

Evidence for at least the last three Pleistocene glaciations are apparent from the deposits on the flanks of the Blanca Massif—Pre-Bull Lake, Bull Lake, and Pinedale (McCalpin, 1982; Pierce, 2003). Moraines from Pre-Bull Lake to the last glacial

maximum cap the proximal portions of the South Zapata, Pioneer, and Holbrook alluvial fans (McCalpin, 1982) (Appendix A, Plate A.1).

Alluvial Fans. The alluvial fans along the west flank of the Sangre de Cristo Range are pervasively built by sediment-gravity flows, specifically boulder-rich debris-flow processes. Clast lithology of fan deposits reflect their drainage basin geology of Paleoproterozoic tonalite gneiss, gneiss, diorite, and quartz diorite, with minor addition of Pennsylvanian/Permian sedimentary rocks.

Primary debris-flow deposits comprise levees of poorly imbricated, sub-angular to round cobbles to large boulders varying from clast-support to matrix-support by fine sand to pebbles. Lobes are generally sedimentologically similar but can sometimes be devoid of matrix. Fresh debris-flow frontal lobes also contain similar sedimentologic features but with varying matrix composition; from open-matrix to muddy, fine-sand to pebble matrix.

Alluvial fan deposits have been differentiated into three main classes, Qao (old), Qai (intermediate), Qay (young). Each class has been subdivided into three sub-classes; 1 being the oldest (stratigraphically lowest) and 3 the youngest (stratigraphically highest). For complete surface descriptions of alluvial fans and map relations see Appendix A and Plate A.1.

Literature Cited

Anderson, R. S. and Anderson, S. P., 1990, Debris-flow benches; dune-contact deposits record paleo-sand dune positions in North Panamint Valley, Inyo County, California: Geology, v. 18, p. 524-527.

Barbeau, D. L., 2003, A flexural model for the Paradox Basin: implications for the tectonics of the Ancestral Rocky Mountains, Basin Research, v. 15, p. 97-115.

Beaty, C. B., 1963, Origin of alluvial fans, White Mountains, California and Nevada: Annals of the Association of American Geographers, v. 53, p. 516-535.

Beaty, C.B., 1961, Topographic effects of faulting: Death Valley, California: Annals of the Association of American Geographers, v. 51, p. 234-240.

Blair, T. C., 1987, Sedimentary processes, vertical stratification sequences, and geomorphology of the Roaring River Alluvial Fan, Rocky Mountain National Park, Colorado: Journal of Sedimentary Petrology, v. 57, p. 1-18.

Blair, T.C., 1999, Cause of dominance by sheetflood vs. debris-flow processes on two adjoining alluvial fans, Death Valley, California: Sedimentology, v. 46, p. 1015-1028.

Blair, T.C., and McPherson, J. G., 1992, The Trollheim alluvial fan and facies model revisited: Geological Society of America Bulliten, v. 104, p. 726-769.

Blair, T.C., and McPherson, J. G., 1994, Alluvial fan processes and forms, *in* Parsons, A.J., and Abrahams, A.D., eds., Geomorphology of desert environments: London, Chapman & Hall, p. 354-402.

Blair, T. C., and McPherson, J. G., 1998, Recent debris-flow processes and resultant form and facies of the Dolomite alluvial fan, Owens Valley, California: Journal of Sedimentary Research, v. 68, p. 801-818.

Blair, T.C., and McPherson, J. G., 2009, Alluvial fan processes and forms, *in* Parsons, A.J., and Abrahams, A.D., eds., Geomorphology of desert environments, 2nd Edition: Berlin, Springer, p. 413-467.

Brister, B. S., and Gries, R. R., 1994, Tertiary stratigraphy and tectonic development of the Alamosa basin (northern San Luis Basin), Rio Grande rift, south-central Colorado, *in* Keller, G. R., and Cather, S. M., eds., Basins of the Rio Grande Rift: Structure, Stratigraphy, and Tectonic Setting: Boulder, Colorado, Geological Society of America Special Paper 291.

Bull, W.B., 1972, Recognition of alluvial-fan deposits in the stratigraphic record, *in* Rigby, J.K., and Hamblin, W.K., eds., Recognition of ancient sedimentary environments: Society of Economic Paleontologists and Mineralogists Special Publication 16, p. 63–83.

Bull, W. B., 1977, The alluvial fan environment, Bull, W. B: Progress in Physical Geography: Earth and Environment, p. 222–270.

Chapin, C. E. and Cather, S. M., 1994, Tectonic setting of the axial basins of the northern and central Rio Grande rift, *in* Keller, G. R., and Cather, S. M., eds., Basins of the Rio Grande Rift: Structure, Stratigraphy, and Tectonic Setting: Boulder, Colorado, Geological Society of America Special Paper 291.

Costa, J. E., 1984, Physical geomorphology of debris flows, *in* Costa, J. E. and Fleisher, P. J., eds., Developments and applications of geomorphology, p. 268-317.

Costa, J. E., 1988, Rheologic, geomorphic, and sedimentologic differentiation of water floods, hyperconcentrated flows, and debris flows: Flood Geomorphology, 113-122.

de Haas, T., Ventra, D., Carbonneau, P. E., and Kleinhans, M. G., 2014, Debris-flow dominance of alluvial fans masked by runoff reworking and weathering: Geomorphology, v. 217, p. 165-181.

de Haas, T., Densmore, A. L., Stoffel, M., Suwa, H., Imaizumi, F., Ballesteros-Cánovas, J. A., and Wasklewicz, T., 2018, Avulsions and the spatio-temporal evolution of debris-flow fans: Earth-Science Reviews, v. 177, p. 53-75.

Denny, C. S., 1967, Fans and pediments: American Journal of Science, v. 265, p. 81-105.

Densmore, A. L., Philip, A. L., and Simpson, G., 2007, Development and response of a coupled catchment fan system under changing tectonic and climatic forcing: Journal of Geophysical Research, v. 112, F01002.

Dünforth, M., 2007, Sediment flux and deposition on arid-region fans, eastern California, USA [Ph.D. thesis]: Zurich, Swiss Federal Institute of Technology.

Frankel, K. L., and Dolan, J. F., 2007, Characterizing arid region alluvial fan surface roughness with airborne laser swath mapping digital topographic data. Journal of Geophysical Research: Earth Surface, v. 112(F2).

Harvey, A.M., 2011, Dryland alluvial fans, *in* Thomas, D.S.G., ed., Arid zone geomorphology: Process, form and change in drylands, Wiley, Chichester, p. 333-371.

Hooke, R. L., 1967, Processes on arid-region alluvial fans: The Journal of Geology, v. 75, 438-460.

Hoy, R. and Ridgeway, K., 2002, Syndepositional thrust-related deformation and sedimentation in an Ancestral Rocky Mountains basin, Central Colorado trough, Colorado, USA: GSA Bulletin, v. 144, no. 7, p. 804-828.

Iverson, R. M., 1997, The physics of debris flows: Reviews of Geophysics v. 35, p. 245-296.

Kellogg, K., 1999, Neogene basins of the northern Rio Grande Rift-partitioning and asymmetry inherited from Laramide and older uplifts: Tectonphysics, v. 305, p. 141-152.

Lecce, S. A., 1990, The alluvial fan problem, *in* Alluvial fans: A field approach, v. 3, p. 24.

Lindsey, D. A., Johnson, B. R., and Andriessen, P. A. M., 1983, Laramide and Neogene structure of the northern Sangre de Cristo Range, south-central Colorado. Rocky Mountain foreland basins and uplifts: Denver, Colorado, Rocky Mountain Association of Geologists, p. 219-228.

Lindsey, D. A., Clark, R. F., and Soulliere, S. J., 1986, Minturn and Sangre de Cristo Formations of Southern Colorado: A Prograding Fan Delta and Alluvial Fan Sequence Shed from the Ancestral Rocky Mountains in Paleotectonics and sedimentation: AAPG, v. 41, p. 541-561.

Lindsey, D. A., 1998, Laramide structure of the central Sangre de Cristo Mountains and adjacent Raton basin, southern Colorado: The Mountain Geologist, v. 35., p. 55-70.

Machette, M.N., Marchetti, D.W., and Thompson, R.A., 2007, Ancient Lake Alamosa and the Pliocene to middle Pleistocene evolution of the Rio Grande, in Machette, M.N., Coates, M.M., and Johnson, M.L., eds., 2007 Rocky Mountain Section Friends of the Pleistocene Field Trip—Quaternary geology of the San Luis Basin of Colorado and New Mexico, September 7-9, 2007: U.S. Geological Survey Open-File Report 2007-1193, p. 157-167.

Madole, R. F., Romig, J. H., Aleinikoff, J. N., VanSistine, D. P., and Yacob, E. Y., 2008, On the origin and age of the Great Sand Dunes, Colorado: Geomorphology, v. 99, p. 99-119.

Matmon, A., Nichols, K., and Finkel, R., 2006, Isotopic insights into smoothening of abandoned fan surfaces, Southern California: Quaternary Research, v. 66, p. 109-118.

McCalpin, J.P., 1982, Quaternary geology and neotectonics of the west flank of the northern Sangre de Cristo Mountains, south-central Colorado: Colorado School of Mines Quarterly, n. 77, 97 p.

McCalpin, J.P., 2006, Active faults and seismic hazards to infrastructure at Great Sand Dunes National Monument and Preserve: Crestone, Colorado: unpublished report by GEO-HAZ Consulting, Inc., 49 p., 1 oversize plate.

McFadden, L.D., Wells, S.G., and Jercinovich, M.J., 1987, Influences of eolian and pedogenic processes on the origin and evolution of desert pavements: Geology, v. 15, p. 504-508.

McFadden, L. D., Ritter, J. B., and Wells, S. G., 1989, Use of multiparameter relative-age methods for age estimation and correlation of alluvial fan surfaces on a desert piedmont, eastern Mojave Desert, California: Quaternary Research, v. 32, p. 276-290.

Moscariello, A., Marchi, L., Maraga, F., and Mortara, G., 2002, Alluvial fans in the Italian Alps: sedimentary facies and processes in Flood and Megaflood Processes and Deposits: Recent and Ancient Examples, p. 141-66.

Mushkin, A., Sagy, A., Trabelci, E., Amit, R., and Porat, N., 2014, Measuring the time and scaledependency of subaerial rock weathering rates over geologic time scales with ground-based LiDAR: Geology, v. 42, no. 12, p. 1063–1066

Pierce, K.L., 2003, Pleistocene glaciation of the Rocky Mountains, in Gillespie, A.R., Porter, S.C., and Atwater, B.F., eds., The Quaternary Period in the United States: Amsterdam, Elsevier, p. 63–76.Quigley, M.C., Sandiford, M., and Cupper, M.L., 2007, Distinguishing tectonic from climatic controls on range-front sedimentation: Basin Research, v. 19, p. 491-505.

Ritter, J. B., Miller, J. R., Enzel, Y., Howes, S. D., Nadon, G., Grubb, M. D., and Summa, C. L., 1993, Quaternary evolution of Cedar Creek alluvial fan, Montana: Geomorphology, v. 8, p. 287-304.

Ritter, J.B., Miller, J.R., Enzel, Y., and Wells, S.G., 1995, Reconciling the roles of tectonism and climate in Quaternary alluvial fan evolution: Geology, v. 23, p. 245-248.

Ruleman, C.A., and Machette, M.N, 2007, An overview of the Sangre de Cristo fault system and new insights to interactions between Quaternary faults in the Northern Rio Grande Rift, *in* Machette, M.N., Coates, M.M., and Johnson, M.L., eds., 2007 Rocky Mountain Section Friends of the Pleistocene Field Trip—Quaternary geology of the San Luis Basin of Colorado and New Mexico, September 7-9, 2007: U.S. Geological Survey Open-File Report 2007-1193, p. 187-197.

Scheinert, C., Wasklewicz, T., and Staley, D., 2012, Alluvial fan dynamics—revisiting the field: Geography Compass, v. 6, p. 752-775.

Scott, K. M., Vallance, J. W., and Pringle, P. T., 1995, Sedimentology, behavior, and hazards of debris flows at Mount Rainier, Washington: US Geological Survey Open-File Report, n. 1547, 106 p.

Shaw, C., and Karlstrom, K. 1999, The Yavapai-Mazatzal boundary in the Southern Rocky Mountains: Rocky Mountain Geology, v. 34, p. 37-52.

Shroba, R. R., Thompson, R. A., and Ruleman, C., 2007, Possible role of eolian sediment in the genesis of boulder debris-flow deposits on the lower flanks of Ute Mountain, northern Taos Plateau volcanic field, New Mexico, *in* Machette, M.N., Coates, M.M., and Johnson, M.L., eds., 2007 Rocky Mountain Section Friends of the Pleistocene Field Trip—Quaternary geology of the San Luis Basin of Colorado and New Mexico, September 7-9, 2007: U.S. Geological Survey Open-File Report 2007-1193, p. 181-185.

Tweto, O., 1978, Northern rift guide 1, Denver-Alamosa, Colorado, *in* Guidebook to the Rio Grande Rift: New Mexico Bureau of Mines and Mineral Resources Circular, v. 163, p. 13-28.

Ventra, D., and Clarke, L. E., 2018, Geology and geomorphology of alluvial and fluvial fans: current progress and research perspectives: Geological Society, London, Special Publications, v. 440, p. 440-16.

Wells, S.G., McFadden, L.D., and Dohrenwend, J.C., 1987, Influence of late Quaternary climatic changes on geomorphic and pedogenic processes on a desert piedmont, eastern Mojave Desert, California: Quaternary Research, v. 27, p. 130-146.

Yonkee, A. and Weil, A., 2015, Tectonic evolution of the Sevier and Laramide belts within the North American Cordillera orogenic system: Earth Science Reviews, v. 150, p. 531-593.

Figure 1.1. The Pioneer debris flow alluvial fan, an example of a debris-flow alluvial fan on the western range front of the Sangre de Crito Mountains in the San Luis Valley, Southern Colorado.

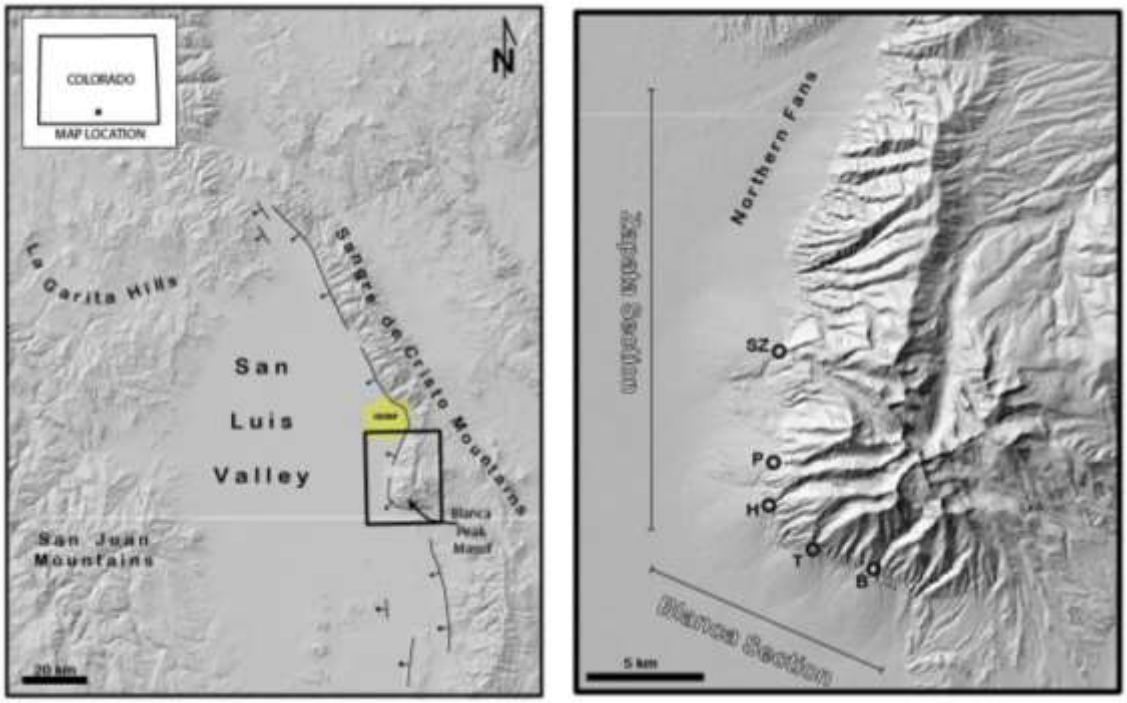

Figure 1.2. (Left) Location of study area within the San Luis Valley of Southern Colorado. The Sangre de Cristo Mountains to the east are bound by the Sangre de Cristo fault system on the western Range front. Black box shows extend of map on right. (Right) The Blanca Massif study area. Approximate Zapata and Blanca sections of the Sangre de Cristo fault system are shown in brackets. Alluvial fan apices are denoted with circle and initials. SZ—South Zapata fan, P—Pioneer fan, H—Holbrook fan, T—Tobin fan, B—Blanca fan.

CHAPTER TWO

DEPOSITION AND MODIFICATION OF DEBRIS-FLOW ALLUVIAL FANS, WESTERN RANGEFRONT OF THE SANGRE DE CRISTO MOUNTAINS, SOUTH-CENTRAL COLORADO

Contribution of Authors and Co-Authors

Manuscript in Chapter 2

Author: Sylvia Nicovich

Contributions: Conceived the study, performed the analyses, interpreted results, and wrote the manuscript.

Co-Author: James Schmitt

Contributions: Conceived the study, assisted the analysis, discussed results and implications, and edited earlier manuscripts.

Manuscript Information

Sylvia Nicovich, Jim Schmitt

Journal of Sedimentary Research

Status of Manuscript:
_X_ Prepared for submission to a peer-reviewed journal
____ Officially submitted to a peer-reviewed journal
____ Accepted by a peer-reviewed journal
____ Published in a peer-reviewed journal

Abstract

A suite of debris-flow alluvial fans emanating from the Holocene-active western range front of the Sangre de Cristo Mountains in south-central Colorado exhibits active depositional lobe surfaces among sequences of abandoned surfaces. Active depositional lobe surfaces display clear debris-flow deposit morphology, while abandoned surfaces display degraded original deposit morphology resulting from modification processes. These alluvial fans are dominantly formed by debris flow, the primary process that dominates the active depositional lobe surface. Secondary processes modify the fan surfaces, both after an active depositional lobe becomes abandoned and on the active depositional surface interrupted by episodic primary depositional events. Unlike primary processes, which only occur on the concomitant active lobe of a given stage, secondary processes dominate the spaciotemporal fan environment. Most alluvial fan studies rely on surficial characteristic and geomorphic interpretations to pinpoint sediment transport processes, leaving the detailed stratigraphic descriptions unreported, typically due to lack of vertical exposures. Debris-flow alluvial fans of the western range front provide ideal access and exposure coupled with available high-resolution topographic data to investigate associations between facies, surface morphology, and process interpretation on both active and abandoned lobes. This study catalogues sedimentary facies that represent both primary and secondary modifying sediment transport processes of two sub-sets of fans on the western range front of the Sangre de Cristo Mountains; a southern set from the extensively glaciated drainages of the Blanca Peak massif and a northern set from the un-glaciated drainages, just south of Great Sand Dunes National Park. Both sets

of fans have: 1) active and successively abandoned surfaces that show evolving degradation of primary features through modification by secondary processes, 2) associated facies that display distinct characteristics representative of primary and secondary processes, 3) evidence of primary debris flow with subsequent modification by secondary processes. The link between morphologies of fan surfaces and the sedimentary facies of their deposits permits a basis for evolutionary process interpretation of debris-flow alluvial fan geomorphology and can elucidate complexities between paleo surfaces, landform morphology, and their deposits in the sedimentary record.

Introduction

Debris-flow alluvial fans are ubiquitous to tectonically active mountain range fronts and span geologic time intervals subject to climatic dynamism. This makes debris-flow alluvial fans a key proxy in understanding landscape evolution controls in both present and ancient settings (Nemec and Steel, 1984; Meyer, 1992; Ritter et al, 1995; Wells, et al., 1995; Horton and Schmitt, 1996; Blair, 2000; Owen et al, 2006; D'Arcy, 2017; Ventra et al., 2017; Palmquist, 2019). Their complex avulsion patterns resulting in numerous stacked surfaces—many topographically high and abandoned among a mobile active depositional lobe surface—pose difficulties to understanding fan formation and surface evolution.

Despite the acknowledgement of this complex architecture, documented examples of detailed sedimentologic and geomorphic characteristics of the major system components (i.e. both active and abandoned surfaces) (Blair, 1987; Blair, 2000; Aschoff and Schmitt, 2008) are relatively uncommon (Ventra and Clarke, 2018). The lack of comprehensive documentation may be related to the inherent difficulties in the distinction between primary depositional deposits and deposits that represent secondary modification.

Integration of the sedimentologic and geomorphic components within alluvial fan studies is necessary for unraveling controls on fan formation and surface evolution, which have broad applications that aid reconstruction of paleoenvironmental conditions. For example, distinctions between formative and modifying processes can elucidate surface processes and fan development. The distinction of active surfaces is important for

hazard mitigation. Recognition of primary and secondary deposits is useful for correlating event horizons within paleoseismic investigations and aids the appropriate application of geochronologic techniques. This work can also be applied to facies associated with subtle-type unconformities in order to notice detailed angular discordance produced during syndepositional structural deformation, evident by modifying processes (Aschoff and Schmitt, 2008). This study fosters these applications and highlights the use of both sedimentologic and geomorphic data on a suite of debris flow alluvial fans within the San Luis Valley of south-central Colorado.

Debris-flow alluvial fans form through episodic avulsing sedimentation events from a mountainous catchment to an adjacent basin (Blair and McPherson, 1994; Blair and McPherson, 2009; Harvey, 2011). Successions of deposits stack vertically and shift laterally, spreading material radially from the opening of the catchment to the piedmont (Denny, 1967; Hooke, 1967; Blair and McPherson, 1994; Blair and McPherson, 2009; de Haas et al., 2014) (Figure 2.1). Switching of primary depositional lobe activity across the fan through time maintains a spatiotemporally variable complex of abandoned and active fan surfaces (Ventra and Nichols, 2014, de Haas et al., 2018). Depositional lobes are generally dominated by primary processes, such as debris flow, whereas abandoned lobes are subject to secondary processes of erosion, weathering, and reworking, which modify evidence of primary deposition (Blair and McPherson, 1994; Blair and McPherson, 2009; de Haas et al., 2014).

Primary processes are processes that move material from the drainage basin to the alluvial fan and occur exclusively on the active depositional lobe of an alluvial fan (Blair

and McPherson, 1994; Blair and McPherson, 2009). As with many alluvial fans, including those in this study, debris flow is the dominant fan-forming sediment transport mechanism (Costa, 1988; Iverson, 1997). Debris flows are sediment-gravity flows; sediment mobilized by gravity with the introduction of water in volumetric concentrations up to 60% (Beaty, 1961; Beaty 1963; Costa, 1984), which have dynamic flow that vary by event or through the duration of an individual flow (Costa, 1984; Costa, 1988; Iverson, 1997; Calhoun and Clauge, 2018). These poorly-sorted slurries of debris, ranging in clast size from mud to large boulders, are responsible for building fans by progressively depositing material on segregated portions of the fan at a time. Characteristically, debris flow deposits express rough topographic textures that include boulder trains, levées, and lobes and a wide variety of sedimentary facies (Nemec and Steel, 1984; Pierson and Scott, 1985; Blair and McPherson, 1994; Blair and McPherson, 1998; Dühnforth, 2007; Blair and McPherson, 2009;).

The locus of deposition, deemed the active depositional lobe, successively switches across the fan surface throughout fan formation resulting in the composite morphologic shape of an alluvial fan (Bull, 1977) (Figure 2.1). Although fan formation is certainly impacted by allogenic changes influencing fan sedimentation (e.g., tectonic, climatic, base-level change) (Bull, 1972; Ritter et al., 1993; Ritter et al., 1995; Harvey, 2011) depositional patterns are driven largely by intrinsic, autogenic processes (Ventra and Nichols, 2014; de Haas et al., 2016; Ventra and Clarke, 2018), namely plugging and backfilling the active fan channel route from preceding flows (de Haas et al., 2019). A chief mechanism of autogenic lobe switching is a consequence of vertical accumulation

of material through stacking of debris flow deposits where, once the accommodation space is full, the depositional loci switches laterally due to topographic compensation (Ventra and Nichols, 2014; de Haas, 2018). Sequentially occupied depositional lobes incise and inset to older, abandoned depositional lobes (Figure 2.2). It is this process that dictates where primary processes turn off and secondary processes become dominant (Blair, 1987).

While active depositional lobes are dominated by primary processes (debris flow), both the depositional and abandoned lobes are subject to secondary processes of erosion, weathering, and reworking, masking primary depositional architecture (Blair and McPherson, 1994; Blair and McPherson, 2009; de Haas et al., 2014). The relative frequency of secondary modifying processes, however, is highest on the abandoned lobes where sedimentation is not overwhelmed by primary processes. So, even on the active depositional lobe, secondary modifying processes affect the fan surfaces most of the time and are merely punctuated by infrequent primary processes. On the other hand, abandoned surfaces are dominated by secondary modifying processes, evident by the eventual smoothing of the surface through time (McFadden, 1989; Mushkin, 2005; Frankel and Dolan, 2007; Johnstone et al., 2018). Secondary modifying processes include reworking by overland flow, eolian activity, weathering, pedogenesis, and bioturbation, occurring on different surfaces to different degrees.

The sedimentological differentiation of processes that dominate active depositional versus abandoned lobes of debris-flow alluvial fans is significant, not only to understanding the geomorphic evolution of a landscape, but also when deciphering past

environmental processes in sedimentary deposits. Consequentially, the objectives of this chapter are to create associations between facies, surface deposit morphologies, and processes interpretation. Specifically, the objectives are to;

1. decipher the sedimentary facies, depositional morphologies, and sediment transport processes represented on the active depositional lobe of debris-flow alluvial fans,
2. distinguish the surficial characteristics of the relict deposits on abandoned surfaces, and
3. catalogue the modifying sediment transport processes on the abandoned surfaces and associated sedimentary facies and depositional morphologies to elucidate how these processes impact initial deposit morphology through time.

This study focuses on the surficial and vertically preserved deposit characteristics of a suite of debris-flow alluvial fans that constitute the western Sangre de Cristo Range piedmont. Rough surface texture accompanied by deposit morphology of levées and lobes present on the active depositional lobe surface with progressive modification on surfaces of greater relative age illustrate debris flow as the dominant primary process on these fans (Figure 2.3). The excellent vertical exposure, land access, and available high-resolution elevation data provides an opportunity to document the sedimentary processes and deposits of a debris-flow alluvial fan system.

Sediment delivered to the western Sangre de Cristo fans is sourced from both glaciated and non-glaciated catchments within the Blanca Peak massif. Fans with

glaciated catchments (southern) are named via their primary watercourse (adopted from McCalpin, 1982) and the unglaciated (northern) fans are numbered. The five large alluvial fans to the south, associated with glaciated catchments are the South Zapata, Pioneer, Holbrook, Tobin, and Blanca fans, from north to south, respectively (Figure 2.4). The Pioneer alluvial fan hosts a gravel quarry at its toe, which exhibits an excellent 16-meter vertical exposure for facies analysis.

Given the different catchment history and morphometric expressions, the western Sangre de Cristo fans are subdivided into two subsets—the smaller northern fans sourced from unglaciated catchments and the larger southern fans sourced from glaciated catchments. Due to property and terrain access in addition to suitable vertical exposures for analysis, the two subsets of fans are described mainly by a few representative fans. The southern fans are mainly represented by the South Zapata, Pioneer, and Holbrook fans and the northern by fans 7, 8, 9, and 15.

Geologic Setting

The physiographic San Luis Valley, structurally the San Luis Basin, of southern Colorado is coincident with an asymmetric extensional half-graben system of the southern Rio Grande rift, extending from the Villa Grove fault zone south to the Embudo accommodation zone near Taos, NM (Wallace, 2004) (Figure 2.5). The San Juan Mountains bound the San Luis Valley to the west with relatively minor faulting, while the eastern margin is defined by high-angle, rift-related extensional faulting along the Sangre de Cristo rangefront. The Blanca Peak horst and Sangre de Cristo horst to the north make up the extensional footwall of this system, the Sangre de Cristo Mountains,

which comprise Laramide thrust sheets of Paleoproterozoic basement rock in fault and depositional contact with Pennsylvanian-Permian terrigenous rocks associated with the Ancestral Rockies orogeny (Lindsey, 1998; Kellogg, 1999; Barbeau, 2003; Ruleman and Machette, 2007) (Figure 2.6).

The Holocene-active Sangre de Cristo normal fault system is responsible for the steep western range front of the Sangre de Cristo Mountains (McCalpin, 1982; McCalpin, 1986; McCalpin, 2006). The fault system has been split into three sections, northern, central, and southern (Ruleman and Machette, 2007). The northern Sangre de Cristo fault system includes the Zapata section, which extends from Medano Pass (approximately the southern edge of the Great Sand Dunes) to Uracca Creek where the southern end of the northern Sangre de Cristo fault system terminates at the Blanca Peak massif (Figure 2.5). From here, the Blanca section of the central Sangre de Cristo fault system defines the southern edge of the Blanca Peak salient (Ruleman and Machette, 2007). The central section continues south on the eastern margin of the Culebra reentrant (Wallace, 2004). Slip rates on individual sections of the Sangre de Cristo normal fault system have varied through the Pliocene to the Quaternary (Ruleman and Machette, 2007).

The San Luis Valley was host to Plio-Pliestocene Lake Alamosa (Machette et al., 2007). Lake Alamosa contracted and expanded for approximately 3 million years before it overtopped a low-elevation sill in the San Luis Hills to the south around 440 ka. As Lake Alamosa drained, it incised the Rio Grande Gorge, integrating the San Luis Valley into the Rio Grande drainage basin.

Evidence for at least three major Pleistocene glaciations is present at the Blanca Peak massif, including glacially carved catchments that source the larger alluvial fans on the western Sangre de Cristo range front. Pre-Bull Lake, Bull Lake, and Pinedale moraines are present within catchments and cap a few of the proximal reaches of alluvial fans. Though only speculation can drive postulations of the allogenic dynamic-affect that glaciations have on fan aggradation, the moraines can be utilized for relative age delineation of some surface packages.

Methods

To integrate the sedimentologic and geomorphic components of the debris-flow alluvial fans on the western rangefront of the Sangre de Cristo, both remote and field mapping and analyses were applied. A geomorphic framework was created to understand specific sedimentological characteristics of specific fan lobes and surfaces. This was done first by mapping using digital elevation models and subsequently testing these results in the field.

Remote Sensing

Surficial mapping was completed from a LiDAR topography dataset with 0.001 m spatial resolution. The data were collected in September 2011 by the United States Geological Survey (USGS) (available for download at www.viewer.nationalmap.gov) (Appendix A, Plate A.1).

Fan surfaces were divided into three domains; old (Qao), intermediate (Qai), and young (Qay) with subcategories for each. Surfaces were initially delineated by relative

topographic position, comparative surface roughness, and level of dissection from LiDAR data. Morphometric analyses including fan area, catchment area, radial slope, radial sub-set slopes, radial decent, and radial and cross profiles, were calculated from the LiDAR. Fan area was determined from geomorphic map unit extents of fans. Catchment area was calculated using the hydrology tools in ArcGIS, which define the catchment area based on upslope cells that flow to a given geographical low point, or "pour point". In this study, the pour points were defined where the drainage contributing to the fan exited the confined catchment (fan apex). Average slope was measured by the inverse tangent of change in elevation from fan apex to toe divided by the radial length of the fan. To calculate proximal, medial, and distal average slopes, segments of each domain for each fan were manually delineated in ArcGIS and average slope (above) per segment was calculated. Radial and cross-fan topographic profiles were generated from the digital elevation model derived from the LiDAR data. Finally, surface roughness was established as standard deviation of slope using focal statistics tools over a 3 m x 3 m (3x3 cells) rectangular neighborhood, measuring standard deviation of the percent-slope in ArcGIS (Brubaker et al., 2013).

Facies Analysis, Field Measurements, and Descriptions

Fan surfaces for each fan mapping unit were described in the field. Surface texture (clast size, shape, sorting), composition, degree of weathering, and deposit morphologies were described at each site. Facies analysis of accessible exposures utilizes variations in grain size, sorting, particle shape and abundance, primary sedimentary structures, grading, deposit thickness and lateral continuity, and matrix content. Limited

natural exposures are present throughout the range front, but a quarry at the toe of the Pioneer fan provides the most extensive exposure of strata.

Results

This section reports the results of this study within two sections: the geomorphology and sedimentology of the debris-flow alluvial fans on the western rangefront of the Sangre de Cristo Mountains. Both sections divide fans into their respective sub-categories of northern versus southern. The geomorphology section discusses morphometrics and surfaces morphologies. The sedimentology section reports facies descriptions and interpretations. The results section culminates in the facies, forms, and depositional histories of each sub-category of debris-flow fans. This includes facies assemblages, deposit morphologies, and depositional processes on specific areas of the fans.

Geomorphology

Morphometrics of all alluvial fans on the western range front of the Blanca Peak massif south of the Great Sand Dunes were measured using the available high-resolution topographic data and are reported in Table 2.1.

Southern fans. The largest, most distinct fans in the area emanate from the extensively glaciated valleys of the Blanca Peak massif. These are the southernmost fans of the study area; the South Zapata, Pioneer, Holbrook, Tobin, and Blanca fans. The west-facing South Zapata, Pioneer, and Holbrook fans all have moraine complexes capping their proximal reaches just past the fan-to-catchment apex point. Tobin and

Blanca fans are south facing and do not have moraines on their proximal fan surfaces (Figures 2.7 and 2.8).

The southern fans have radial lengths between 3.8 and 5.1 km with maximum widths ranging from 2.5 to 4.8 km. The radial decent of the southern fans—elevation lost from apex to edge of fan toe—ranges from 445 to 572 m. All the southern fans have planoconcave-upward radial profile created by the distally decreasing slope until the adjoining sand sheet within the basin (Figure 2.8). Proximal slopes range from 7.9° to 11.4°, medial slopes from 6.9° to 8.9°, and distal slopes from 2.0° to 4.7°. These slopes contrast with the slope of <1° for adjoining, basin-ward sand sheet. Southern fans have areas that range from 7.77 km^2 (Blanca fan) to 19.12 km^2 (Zapata fan) and catchments that range from 3.39 km^2 (Tobin catchment) to 11.95 km^2 (Zapata catchment). Unique to the southern fans, the ratio between individual fan areas and their respective catchment areas are greater than one (Figure 2.7). These ratio values show that the southern alluvial fan plan-view areas are greater than their catchment foot-prints. This 2-dimensional relation is likely due to the U-shaped geometries of the glacially carved catchments (Figure 2.9), allowing for greater volumes of sediment to be produced to form larger fans while maintaining a relatively small catchment area. Alluvial fan-area to catchment-area ratios of unglaciated systems are less than one, for example, in the northern fans as discussed below.

Southern fan surficial mapping units range from Qao, the oldest fan unit, to Qay, the youngest fan units and generally young to the north in each individual fan complex (Appendix A, Plate A.1). As illustrated by the Holbrook fan in Figure 2.10, fan-scale

surfaces roughness reflects deposit-scale features. Older surfaces are smoother than rough, young surfaces.

Northern fans. Northern fans are numbered 1-15 starting at the northern most point of the mapping area, just south of Great Sand Dunes National Park, increasing in value south to the South Zapata fan (Figure 2.5). The northern fans are sourced from non-glaciated drainage basins and have generally more variable morphometric characteristics than the southern fans.

Overall, northern fans are much smaller than the southern fans. Fan 14 sourced from the North Zapata drainage lies on the boundary between the northern and southern fan sets. Although categorized with the northern fans, it has distinct characteristics, outlier values for much of the northern fan morphometrics, and is discussed below. Apart from size, distinctions of all other northern fans from southern fans are the shorter radial descents (values that range from 87 m to 252 m) and fan-area to catchment-area ratios below one, as opposed to values above one for the southern fans (Figure 2.7). Radial lengths of the northern fans range between 0.62 km and 2.4 and maximum widths of 0.19 km to 1.3 km. Except for Fan 14, the northern fans have planoconcave-upward radial profile created by the distally decreasing slope until the adjoining sand sheet within the basin (Figure 2.8). The northern fans have average slopes of 4.7 to 8.4, proximal slopes between 7.5° and 10.4°, medial slopes from 4.7° to 9.3°, and a distal slopes between 2.7° and 7.3 degrees°, which contrast with the slope of <1° for the adjoining sand sheet. Fan 14 is an outlier for all morphometric categories except for fan-area to catchment-area ratio. It has much larger radial length, at 3.5 km and a width of 2.8 km. The average slope

of Fan 14 is much lower than all other fans at 3.2°, a proximal slope of 3.8°, medial of 3.7°, and distal slope of 2.0°. The radial profile of Fan 14 is planar unlike all other fans' planoconcave-upward radial profiles.

Sedimentology

Facies analysis were conducted primarily at the Pioneer Quarry and at a natural incision of northern fan 7. Important physical parameters of the deposits are grain-size distribution, particle shape, particle abundance, deposit thickness, and sedimentary structures. Facies codes, abbreviated descriptions, and interpretations are reported in Table 2.2.

Facies Gms (matrix-supported gravel). This facies consists of ungraded to very crudely coarse-tail inverse (i) or normally (n) graded, poorly- to very poorly-sorted, matrix-supported, pebble to boulder-sized framework grains with silt to granule-sized matrix. Typical clast sizes are 3-35 cm in diameter, though larger (<50 cm) clasts are abundant. Matrix texture varies from very poorly-sorted, angular to subround silt to granules (1), well-sorted silt to very-fine sand (2), and mixtures of both (3). Facies Gms lacks internal stratification (Figures 2.11, 2.12, 2.13) and bed thickness ranges from ~30 to 300 cm. Upper boundaries of Gms with matrix 2 composition typically diffuse up to sandy facies. Matrix composition 2 variation of Gms (Gms2) occurs interbedded with sandy facies or increases in abundance, grading upward from Gms. Lower boundaries that overlie sandy facies are abrupt and range from planar to low and high amplitude wavy. These lower boundaries often incorporate material from sandy horizons below as

oversized rip-up clasts with minimal internal deformation. Upper boundaries typically transition into other facies gradually.

Interpretation. Facies Gms is interpreted to be produced by cohesive debris flow. Internal resistance to flow in cohesive debris flow is derived from both electrostatic forces of small grain size (clay-rich, >3%) and friction (Costa, 1984). The differential movement and settling of coarse particles (gravel), and overall mixing is limited in these flows due to cohesive matrix properties (Scott et al., 1995). This component of flow behavior is responsible for the poorly developed grading structures within this facies. Another aspect of this facies is the variation in matrix content—Matrix composition 1 is interpreted to be drainage basin-sourced material, given its poor sorting and angularity. This material was likely entrained in the flow upon inception. Matrix 2 is interpreted to be sourced from eolian material, given its well-sorted and fine-grained texture, deposited on the fan surface before the time of flow. Finally, matrix composition 3 denotes mixtures of both 1 and 2. Due to the inability for cohesive flows to effectively bulk with underlying material (Scott et al., 1995), facies Gms deposits are interpreted to have entrained their matrix during flow initiation, however this may be an oversimplified explanation due to morphing flow dynamics and is discussed later. The depositional sub-environment of this facies typically belongs on the active lobe of the alluvial fan, the most boulder-rich, uneven textured alluvial fan surfaces.

Facies Gmsc (matrix- to clast-supported gravel). Facies Gmsc consists of ungraded to coarse-tail inverse (i) or normally (n) graded, very poorly- to moderately-

sorted, dominantly clast-supported, pebble to boulder-sized framework grains with silt to granule-sized matrix. Typical clast sizes are 3-35 cm in diameter, though larger (<50 cm) clasts are abundant. Matrix texture varies from very poorly-sorted silt to granules (1), to well sorted silt to very-fine sand (2), and mixtures of both (3). Facies Gmsc lacks internal stratification (Figures 2.11, 2.12, 2.13). Upper boundaries of Gmsc typically grade into other gravel or sand facies. Lower boundaries on top of sandy facies are abrupt and range from planar to low and high amplitude wavy. These lower boundaries often incorporate material from sandy horizons below as oversized rip-up clasts with minimal internal deformation or transition to Gmsc as lenses within sandy facies. Upper boundaries typically transition into other facies gradually. Specific occurrences of Gmsci facies, where beds are typically 10 cm thick and in successions of multiple bedsets with grading pattern up to 30 cm, display inverse coarse-tail graded, poorly to moderately-sorted, clast to matrix-supported, subangular to subround pebble-sized gravels. The base of beds consist of coarse-sand to granule-sized clasts that demonstrate inverse grading upward to angular to subangular small clast-supported pebbles. The upper portion of deposits transition to larger clast-supported subround to subangular pebbles, as granule to medium-sized sand matrix content increases upward with grading.

Interpretation. Facies Gmsc represents deposition of non-cohesive debris flow. Unlike cohesive debris flow, non-cohesive debris flow allows for internal movement (Pierson and Scott, 1985; Scott et al., 1995) and deposits show evidence of normal grading due to turbulent flow or inverse grading produced from grain-collision dispersive pressure (Nemec and Steel, 1984). The same numeric system described for the matrix

composition variation in Gms facies is applied herein. With facies Gmsc, the difference in matrix composition reflects not only the potential initial matrix source material, but the provenance of bulking and entrainment during flow (Iverson, 2011). For example, a flow that originates within the catchment and traverses down-fan over eolian sand deposits, may be bulked by these sands, ultimately recording a type 2 matrix upon deposition. Matrix type 2 can also be from debris flow originating in sandy deposits on the fan. Matrix composition 3 (mixtures of both 1 and 2) represent smaller flows with limited entraining ability of a flow or limited supply of eolian material on fan surface (Iverson, 2011). The depositional sub-environment of this facies is typically the active lobe of the alluvial fan, the most boulder-rich, unevenly textured of alluvial fan surfaces.

Facies Gm (massive gravel). This facies comprises ungraded to weakly inversely or normally graded, moderately to well-sorted, clast-supported, angular to subround granule to pebble-sized, tightly packed gravels. Matrix content is typically medium to coarse-grained sand. Facies Gm lacks internal stratification. Deposits are typically 10 to 200 cm thick and are laterally continuous on the observable order of up to ~50 m. Lower boundaries of Gm are typically clear and wavy to semi-planar with diffuse, gradational, or abrupt upper boundaries.

Interpretation. Gm facies is interpreted to result from fluid-gravity flow, reworking of surface material on fans by water as overland flow. This facies can also represent the fluid phase of primary deposition as hyperconcentrated flow. Hyperconcentrated flow events that deposit facies Gm either occur directly before or after

the debris flow surge (Pierson, 2005; Pierson and Costa, 1987; Costa, 1984). Without the concordant debris flow, facies Gm can be interpreted merely as a reworking agent (overland flow). The-clast supported framework grains and sorting of both framework clasts and matrix indicate that this facies was deposited by differential settling of the sediment load in a fluid-gravity flow or a fluid-rich phase of hyperconcentrated flow. Contextual sedimentary architecture is central when interpreting the depositional setting of this facies. Potential clues may reside in the underlying deposits. For example, if facies Gm is located immediately below facies Gms or Gmsc (debris-flow), Gm likely represents the fluid-rich phase of a hyperconcentrated flow and could indicate deposition on the depositional lobe sub-environment. If facies related to primary processes are absent near facies Gm, it may more likely be telling of modifying fluid processes. Facies Gm is not diagnostic of specific depositional sub-environment, as it can occur most places on the fan.

Facies Gl (low-angle stratified gravel). Facies Gl is composed of crudely stratified, fining upward, low-angle stratified (<20°), moderately to well-sorted, clast-supported, angular to subround granule to pebble-sized gravel. Matrix content is medium to coarse, angular sand. Beds are typically 5 to 10 cm thick and bedsets of an entire deposit are generally lenticular with a maximum thickness up to ~ 30 cm. These beds are commonly interbedded with mud.

Interpretation. Gl facies is interpreted to represent hyperconcentrated flow but can also indicate reworking of fan material by overland flow. Hyperconcentrated flow

deposits material through suspension fall-out and transport the coarser material at the base of the flow with finer sediment suspended higher up and at lower concentrations generating fining upward deposits, like facies Gl (Pierson, 2005; Calhoun and Clague, 2018). Fluid-gravity flows like overland flow can also produce these characteristics, which make the distinction challenging. Facies Gl alone is not the most helpful in identifying the depositional sub-environment, though the surrounding facies assemblage and sedimentological features can advance interpretation. When reasonably clear in the field, the amount of clay-sized material along with surrounding facies may assist in distinguishing between hyperconcentrated or overland flow processes. For example, hyperconcentrated flows are likely to occur either directly after or just before debris flow surge as a transitional deposit between debris flow and fluid-gravity flow and typically have a higher clay content (≥3%) (Fisher, 1983; Costa, 1988; Pierson, 2005). Conversely, overland flow reworks fan-surface material regardless of sedimentary transport sourced from the catchment, will typically have less clay (≤3%) and can occur with considerable time (up to 10^6s of years) since debris flow (Blair and McPherson, 1994; Blair and McPherson, 2009; de Haas et al., 2014). The depositional sub-environment for facies Gl can be either the abandoned lobe of a debris-flow alluvial fan, the area dominated by secondary modifying processes, or the active depositional lobe.

Facies GlSl (low-angle stratified, sandy matrix-supported gravel). Facies GlSl is low-angle stratified, poorly sorted, matrix-supported granules to pebbles in medium to course sand. Framework clasts are subround to subangular and typically 2 mm to 3 cm. Beds dip at approximately 20 degrees with wavy upper and lower truncation surfaces.

Beds of facies GlSl are typically 15 cm thick and are laterally continuous on the order of 1 to 2 meters.

Interpretation. Like facies Gl, GlSl facies can represent secondary reworking of fan material by overland flow or the hyperconcentrated flow phase transforming from debris flow directly before or after deposition of debris flow facies (Gms, Gmsc). As mentioned above, differentiating between hyperconcentrated flow and overland flow may be difficult and it is important to consider architectural context and the amount of clay-sized material where possible. The depositional sub-environments are both the abandoned lobes and the active depositional lobe of debris-flow alluvial fans.

Facies Gh (horizontally stratified gravel). This facies is composed of fining upward, horizontally stratified, moderately to well-sorted, clast-supported, angular to subround granule to pebble-sized gravels. Planar beds of Gh are 3-20 cm thick and exist in lenses generally an observed maximum lateral extent of 2 m.

Interpretation. Facies Gh is interpreted to be deposited as fluid-gravity flow (overland flow) during upper-flow regime plane-bed conditions. Flows may have been channelized in areas, as deposits exist as lenses (Blair and McPherson, 1994; Smith, 2000; Blair and McPherson, 2009). Gh facies may be few due to the obliteration of previous deposits from lateral channel migration, which could occur within a singular event in the upper flow regime in plane bed conditions (Smith, 2000). Planar deposits have commonly been described as laterally extensive (Blair, 1987; Blair, 1999; Bull, 1972). Gh facies here are not observed as laterally extensive, likely because they were

recoded mostly in exposures located at the distal end of the fans, where flows were probably channelized (Blair, 1987). The typical depositional sub-environment for facies Gh is the abandoned lobes of a debris-flow alluvial fan, the area dominated by secondary modifying processes.

Facies Smps (massive sand, poorly sorted). Facies Smps comprises ungraded, massive to very crudely stratified, poorly sorted fine to coarse sand. This facies is commonly ~50-125 cm thick and laterally pinches out into coarser-grained facies. Smps facies is often interbedded with low-angle stratified sand (Sl), horizontally stratified sand (Sh), ripple cross-laminated sand (Sr), and matrix-supported gravel (Gms) single beds and lenses. Lower boundaries of Smps are generally clear and smooth, though upper contacts are chaotic and are incorporated as large (~50 cm-long) rip-ups in overlying facies, which generally lack internal deformation.

Interpretation. Smps is interpreted to record the hyperconcentrated flow, runout phase of a debris flow (Calhoun and Clague; 2018; Pierson and Scott, 1985; Pierson, 2005; Scott et al., 1995). Hyperconcentrated flows frequently reach the distal extent of alluvial fans. In fact, runout distances have been recorded up to 70 km subsequent to flow transition from larger noncohesive debris flows (Scott et al., 1995). Smps facies express typical hyperconcentrated flow features of this grain size such as poor sorting and lack of stratification (Pierson and Scott, 1985; Calhoun and Clague; 2018). The typical depositional sub-environment for facies Smps is the depositional lobe of debris-flow alluvial fans, still these deposits can also occur on the abandoned lobes.

Facies Smws (massive sand, well sorted). Facies Smws comprises ungraded, unstratified (massive), very well-sorted silt to very fine sand. This facies is commonly ~30-100 cm thick and are extensively laterally continuous (as extensive as exposure, up to 100 m). Smws facies is often interbedded with low-angle stratified sand (Sl), horizontally stratified sand (Sh), ripple cross-laminated sand (Sr), and matrix-supported gravel (Gms) single beds.

Interpretation. Facies Smws is interpreted as wind-blown material that has been deposited on a fan; both as a primary eolian deposit and as reworked, secondarily transported eolian sediment. The absence of bedding in fine-grained sands generally has been attributed to be caused by heavy bioturbation (Freyberger et al., 1979; Bateman et al., 2003; Bateman et al., 2007). However, the lack of sedimentary structures here is prescribed to be concealed by the high degree of sorting and fine-grained nature of Smws facies. Smsw denotes the active portion of a mobile sand sheet on the fan (Bertran, 2011), a portion of the eolian deposit reworked by water or deposited in wet areas atop the fan (Schokker and Koster, 2004), or wind-blown sediment remobilized as a hyperconcentrated flow (Sweeney and Loope, 2001). Regardless, the presence of Smws signifies an eolian-influenced environment on the abandoned lobe of a debris-flow alluvial fan.

Facies Sl (low-angle stratified sand). This facies is composed of normally graded low-angle stratified (5-20°), moderately to well-sorted, very fine to medium sand. Deposit thickness is typically <10 cm and laterally pinches out in lenses typically <80 cm

long. This facies is commonly interbedded with silt-sized laminae, coarse sand, and granule stringers. Sl facies are typically at the upper-most section of sand facies just below Gms and Gmsc facies or atop Gms facies.

Interpretation. Facies Sl is interpreted to be formed through reworking of eolian sand by overland flow. Sl can signify high-velocity reworking of eolian sand as antidunes (Southard and Boguchwal, 1990; Miall, 1977) or fill of low-relief scours (Miall, 1977; Baas, 2016). The relative position of Sl facies, on the top of other sand facies and just below Gms and Gmsc facies or atop Gms facies, represents fluid-gravity flow surge (hyperconcentrated flow) directly before or after debris flow events (Iverson, 2011; Postma, 1986; Pierson and Scott, 1985). The frequency of facies that indicate debris-flow deposits (Gms, Gmsc) concordant with Sl can either signify debris-flow occurring on the abandoned lobes (low frequency) or an active depositional lobe environment (high frequency). However, due to the makeup of facies Sl as eolian sand, the typical depositional sub-environment is interpreted as the abandoned lobe of a debris-flow alluvial fan, the area dominated by secondary modifying processes.

Sh (horizontally stratified sand). This facies includes fining and coarsening upward, coarse-tail sequences with well-defined to crude horizontal stratification. Facies Sh ranges from poorly to well-sorted, fine to very coarse sand with occasional outsized (granule to small pebble) clasts. Beds are commonly 3-15 cm and are occur in lenses or layers with limited lateral continuity (1-2 m) in lower horizons with more extensive (10^1s of meters) lateral continuity in upper-most exposed horizons.

Interpretation. Facies Sh is interpreted as reworking of on-fan material by water, typically overland flow and hyperconcentrated flow (Sweeney and Loope, 2001). The degree of sorting and grain-size is dictated by the material being reworked. Sh facies composed of well-sorted fine sand results from the reworking of eolian material (Sweeney and Loope, 2001; Schokker and Koster, 2004), whereas the more poorly sorted facies are likely hyperconcentrated flow deposits (Pierson and Scott, 1985; Scott et al., 1995; Pierson, 2005; Calhoun and Clague; 2018). The depositional sub-environment for facies Sh is both the abandoned lobes and the active depositional lobe of debris-flow alluvial fans.

Facies Sr (ripple cross-laminated sand). Sr is ripple cross-laminated, poorly to very well-sorted, silt to coarse grained sand with frequent outsized granule clasts in the more poorly-sorted phases. Laminae sets are approximately 5 cm and cosets up to 50 cm. Both erosional truncation surfaces and gradational ripples exist in Sr facies.

Interpretation. Much like the other sand facies, facies Sr represents reworking of fan material by overland flow. The sedimentary structures in this facies are evident of migrating ripple bedforms. Facies characteristics such as grain size and sorting were inherited by eolian deposition prior to the material being reworked. Just as Sh, Sr facies composed of well-sorted fine sand results from the reworking of eolian material (Schokker and Koster, 2004). The depositional sub-environment for facies Sr is typically the abandoned lobe of a debris-flow alluvial fan, the area dominated by secondary modifying processes.

Facies, Forms, and Depositional Histories of Southern Fans (South Zapata, Pioneer, and Holbrook)

Active depositional lobe. The active depositional lobes of the southern fans occupy the youngest, topographically lowest, surfaces of each fan among more diffuse surfaces of older relative age (Figure 2.14a-f).

Deposit morphology

Deposit morphologies of the active depositional lobes of fans exhibit high-relief local topography dominated by boulders. These deposits display lobe morphology, with down-fan trending lobes ranging in width from approximately 1 to 10 meters and height from approximately 1 to 3 meters. Upper-fan levées are often paired, with distance between conjugate pairs typically about 1-4 meters. Elongate, boulder-rich deposits are oriented along the down-fan direction. Deposits are poorly sorted and range from matrix-supported to open-matrix texture. Boulders are sub-round to round and angular when fractured.

The most recently active areas of the active depositional lobes show very little weathering and faint oxidation on a minority of boulders, no soil, only minor lichen development on clasts, and little vegetation other than trees. In these areas, trees show scaring up to a meter from top of deposit in the expression of bark removal and trapping of woody debris on uphill side of trunks (Figure 2.15). Mature juniper trees show evidence of debris bombardment through irregular growth. Additionally, some elongate trees are up-rooted and aligned parallel with channel flow direction. Pebble-sized gravels are in swales and piled up on levées with coarse sand. Silt deficient, fine to coarse sand

and grus fill interstices between gravels and boulders on levées and lobes (Figure 2.16). Boulders are fresh, lack weathering rinds, and are interlocked in a clast-supported framework. In some cases, boulder arrangements display arcuate frontal lobes perpendicular to slope. These lobes display high local relief and are composed of large boulders, some lichen-covered and others lichen-void (Figure 2.17).

The active depositional lobe areas with less-recent activity show slightly smoothed, weathered, and overall generally subdued fan surfaces (Figure 2.10). In these areas, minor portions (<5%) of boulders are fractured from weathering and <10% boulders display weathering rinds with thickness of <1 mm. Overall, these surfaces are stabilized by soil, mosses, shrub layer, and piñion-juniper forest. Trees are buried at their base by duff and soil. Surfaces without boulder-cover consists of coarse sand to granules from grussified granite, silt, very fine to coarse sand, and pebble-sized gravel between boulder levées. Boulder levées range from clast-supported with point and long contacts to floating where matrix-supported.

Facies assemblage

The facies assemblage that represents the active depositional lobes of the southern fans includes facies that signify primary depositional processes like debris-flow, hyperconcentrated flow, and modification processes (Table 2.2). These facies are Gms (matrix-supported gravel), Gmsc (matrix- to clast-supported gravel), Smps (poorly-sorted massive sand), and unexclusively Gm (massive gravel), Gl (low-angle stratified gravel), GlSl (low-angle stratified, sandy matrix-supported gravel), and Sh (horizontally stratified sand).

Depositional process/interpretation

The characteristic coarse-grained, massive form, poorly-sorted, pebble to boulder-sized texture, and slope-parallel orientation of these deposits is consistent with features and facies observed and described for the primary depositional processes of debris flow (Pierson and Costa, 1987; Costa, 1988; Scott et al., 1995; Blair and McPherson, 1998; Coe, 2008). Facies are consistent with both cohesive debris flow, which often display massive, matrix-supported texture (Gms) non-cohesive debris flow with massive, poorly sorted, matrix supported facies (Gmsc), and hyper concentrated flow deposits expressed by poorly-sorted massive sand (Smps), massive gravel (Gm), low-angle stratified gravel (Gl), low-angle stratified gravel, supported by a sandy matrix (GlSl), and horizontally stratified sand (Sh). Differential areas of reworking on the active depositional lobe are due to individual debris flow-scale (levées and individual flow-lobes) avulsion cycles, similar to the larger, fan-scale topographic compensation cycles that dictate the location of the active depositional lobe (de Haas et al., 2016). Although debris flow deposition is the most apparent process on the active depositional lobe, reworking processes are acting on the fan surface regardless of flow recency, most readily recorded in the deposits as overland flow (Table 2.2).

Abandoned surfaces.

Deposit morphology

Abandoned lobe surfaces have a wide range of deposit morphologies that vary with topographic position—from diffuse and smooth surfaces with no remnant of boulder lobes (Qao surfaces), to uneven surfaces with recognizable, yet weathered pairs of levées

(Qay-Qai). Boulders on abandoned surfaces are consistently at least partially buried by fine-grained sediment (<2 mm), increasing with time (relative topographic position) since abandonment, and range from angular to subangular due to spalling and fracturing. Many boulders have weathering rinds, carbonate rinds, and lichen cover that increase in thickness and abundance with age since abandonment and topographic position. Silt to coarse sand, granule-sized grus and angular pebble-sized gravel are present in the interstitial space between and burying boulders, generally filling in topographic lows (Figure 2.18). Boulder concentrations on surfaces that have been abandoned for the longest spans of time are not necessarily the highest relief features on those surfaces. Tree bases on surfaces of all ages are buried to some degree (Figure 2.19). The oldest surfaces are smooth, relatively flat, and have sand and angular gravel-sheet cover (Figure 2.20).

Facies assemblage

The facies assemblage that represents the abandoned lobes of the southern fans is generally limited to the facies that signify secondary modifying processes (Table 2.2). These facies include Gh (horizontally stratified gravel), Smws (well-sorted massive sand), Sl (low-angle stratified sand), Sr (ripple cross-laminated sand), and, though not diagnostic, Gm (massive gravel), Gl (low-angle stratified gravel), GlSl (low-angle stratified, sandy matrix-supported gravel), Sh (horizontally stratified sand), and rarely matrix-supported gravels (Gms).

Modification Processes

Deposit morphologies of abandoned fan surfaces display varying degrees of reworking, which mask evidence of primary debris flow (McFadden, 1989; Blair and McPherson, 1994; Blair and McPherson, 2009; de Haas et al., 2014). These deposits display characteristics of water-lain deposition, such as sorting and stratification, producing secondary deposits from the reworking of material already on the fan. Overland flow remobilizes material with water, which can produce several stratified sand facies and gravel facies (Sh, Sr, Sl, GlSl, Gm, Gl, and Gh) (Figures 2.21 and 2.22). Secondary modifying processes do not exclusively rework fan material but can also deposit material onto the fan. For example, Smws facies is interpreted to be eolian-sourced sand, blown onto fan surfaces (Blair and McPherson, 1994; Blair and McPherson, 2009). Wind-blow material reworked by overland flow results in facies Sh, Sr, and Sl and by hyperconcentrated flow, facies Smws. Secondary modifying process can be difficult to distinguish between fluid-rich primary processes, such as hyperconcentrated flow. For this reason, caution must be taken when prescribing sedimentary facies to associated sediment transport mechanism. Using surrounding facies for context can aid these interpretations.

Facies, Forms, and Depositional Histories of Northern Fans (7, 8, 9, and 15)

Active depositional lobe.

Deposit morphology

In general, active surfaces of the northern fans are similar to those on southern fans with boulder levée, lobe, and swale topography. A fresh boulder-rich deposit sourced from the drainage of Fan 9 extends a distance of approximately 1.75 km, from the apex of Fan 9 nearly to the toe of the fan (Figure 2.23). This deposit is as wide as 30 m in the proximal reaches of the fan and approximately 10 m at its distal extent. The top-most portion of this deposit (upper ~0.5m) is open framework gravel and the underlying portion is matrix-rich and only in places supported by the matrix. This deposit is composed of subangular to angular boulder and large cobbles, similar to other active deposits.

Swales are smoothed from aggradation of duff and fine-grained sediment, are narrow, and outer levées are commonly touching, impinging the swales. Boulder lobes are approximately 4-7 meters wide. Lithology of boulders is intermediate to mafic Proterozoic crystalline basement and Pennsylvanian and Permian sedimentary rocks. Boulder levees are infilled by angular pebble-sized gravel. Many boulders are rotting, oxidized, fractured, and have weathering rinds that range from 1-3 mm. About half of boulders are buried on high points of lobes where most boulders are in point contact. The bases of lobes have a higher abundance of fine sand to pebble-sized matrix and boulders are matrix-supported. The trunks of the piñon-juniper trees are buried by fines and duff, some with boulders butting up to trunk.

Facies assemblage

The same facies assemblage that represents the active depositional lobes of the southern fans is applied to the northern fans and includes facies that signify primary depositional processes like debris-flow (Table 2.2). These facies are Gms (matrix-supported gravel), Gmsc (matrix- to clast-supported gravel), Smps (poorly-sorted massive sand), and unexclusively Gm (massive gravel), Gl (low-angle stratified gravel), GlSl (low-angle stratified, sandy matrix-supported gravel), and Sh (horizontally stratified sand).

Depositional process

Given the similar facies and deposit morphologies of the northern fans to the southern fans, the depositional processes on the active depositional lobe surfaces of the northern fans have the same interpretation as the southern fans. Despite morphometric and drainage basin glacial history differences, these fans are both formed through the similar process of debris flow.

The primary distinction between the northern fans and southern fans is in clast morphology. In the most-recent deposits of each, the northern fans have more angular and weathered clasts. This is likely because they are sourced from unglaciated drainages, where weathering dictates sediment supply (Blair and McPherson, 1994; Blair and McPherson, 2009). The southern fans, on the other hand, have sediment produced by glacial erosion, resulting in relatively more-rounded and less weathered boulders. The deposit described from Fan 9 is interpreted as a debris flow deposit from a single event, illustrating that a single flow can run out from the apex to nearly the toe of the fan.

Abandoned surfaces.

Deposit morphology

Deposits on abandoned surfaces display uneven levée and lobe topography with incised channels. Boulder levées are diffuse and buried yet are still decipherable. The crests of levées and lobes are prominent and composed of un-buried boulders (Figure 2.24). Boulder levées are infilled with compact sandy silt. Clasts in these deposits are mostly boulder-sized gravel, but range in size from pebbles to boulders. Boulders have rough, granular surface texture, are round to angular, and are rotten from weathering with occasional 1-3 mm weathering rinds. Packages of angular to round pebble-sized gravels (Gm) with interstitial fines create an immature desert pavement texture (McFadden et al. 1989; Wells et al., 1995) (Figure 2.25). Most boulders are at least half buried with the exception for those on crests of lobes. The abandoned fan surfaces commonly have moss, shrub layer and canopy cover. Some piñon trees have fines and duff burying their bases, while others have boulders resting against them.

Facies assemblage

The facies assemblage that represents the abandoned lobes of the northern fans is identical to the assemblage of the southern fans' abandoned lobes. This assemblage is also limited to the facies that signify secondary modifying processes (Table 2.2). These facies include Gm (massive gravel), Gl (low-angle stratified gravel), Gh (horizontally stratified gravel), Smws (well-sorted massive sand), Smps (poorly-sorted massive sand), Sl (low-angle stratified sand), Sh (horizontally stratified sand), and Sr (ripple cross-laminated sand).

Modification processes

Modification processes on the northern fans are interpreted as the same processes acting on the southern fan surfaces. Secondary modifying processes operate across all fan surfaces in a similar manner regardless of drainage basin glacial history.

Discussion

Alluvial fans along the western range front of the Sangre de Cristo Mountains south of Great Sand Dunes National Park are formed by primary debris-flow processes, with subsequent secondary modifying processes acting on surfaces of all ages to varying degrees in different areas. Sedimentary facies, deposit morphologies, and landform-scale features represent the duality of primary deposition and secondary modification. Both primary processes and secondary modification are evident in the sedimentary facies within exposures associated with the northern and southern fans. Primary debris-flow deposit morphologies that exhibit progressively muted features from young to old surfaces also demonstrate the role of secondary modification in obscuring primary deposits. Furthermore, landscape-scale smoothing resulting in degradation of alluvial fan surfaces is commonly illustrated by modification of initial rough topography, created by primary debris flow deposition (individual levées and lobes), by secondary processes operative in smoothing the surfaces (e.g. McFadden, 1989; Mushkin, 2005; Frankel and Dolan, 2007; Johnstone et al., 2018). Overall, features of fan-building primary depositional processes and secondary modification processes are recorded on the fan surface by deposit morphology, in the vertical exposures by sedimentary facies, and in the landscape at a landform-scale through textual characteristics.

A translatable and comprehensive evaluation of this debris-flow alluvial fan system is made through integrating geomorphic features, characteristics of deposit morphologies, and sedimentary facies data. These data and characteristic features are useful when working with systems that do not have all dimensions available for analysis. Applications include 1) using fan surfaces as proxy for timing, process, and cause of depositional activity for hazard mitigation, 2) identifying, interpreting, and correlating deposits as event horizons for paleoseismic investigations, 3) utilizing a holistic approach and perspective to understand results and target appropriate sites for various geochronologic investigations and techniques, and 4) more accurately interpreting paleoenvironmental conditions and landscapes from the sedimentary record. By applying this multidimensional approach to the more complete systems, those with missing components can be more accurately interpreted (Ventra and Clark, 2018).

The reported properties of the alluvial fans and their deposits on the western range front of the Sangre de Cristo are consistent with previous research of ancient, historical, and experimental debris-flow deposits and forms (Fisher, 1983; Nemec and Steel, 1984; Pierson and Scott, 1985; Postma, 1986; Costa, 1988; Druitt, 1995; Sohn, 1997; Lowe and Guy, 2000). Figure 2.26 displays a general overview of the major sediment transport processes on debris-flow alluvial fans as primary depositional and secondary modifying processes, the deposit morphologies they produce, and sedimentary facies associated with each process.

The primary sediment transport processes of both the northern and southern fans, most unobscured on the active depositional lobes, are debris flow. Debris flow processes

are represented by deposits of boulder-rich levées and lobes with high-relief (~0.5-2 m) morphologies (Figure 2.26). Levées are positive topographic features that form as accumulation of material on the edges of the flow (Blair and McPherson, 1998). Lobes define the extent of the frontal-most trajectory of a flow, or pulse of flow. Lateral lobes represent avulsions from the main flow and terminal lobes deposit once the flow ceases to move.

Debris flow processes are also represented in facies where distinctive deposits give insight to flow dynamics. Debris flows are described as both cohesive and non-cohesive flow, nomenclature aimed to reflect the behavioral differences in matrix cohesiveness (Costa, 1984; Pierson and Costa, 1987; Scott et al., 1995). Cohesive debris flow deposits are ungraded due to the cohesive behavior of the matrix inhibiting differential movement of coarse particles. Non-cohesive debris flow facies, however, do display both inverse and normal grading due to the ability for coarse particles to remain mobile in a non-cohesive matrix (Figure 2.26).

Hyperconcentrated flow is an intermediate phase between sediment-gravity and fluid-gravity flow that often occurs in company with non-cohesive debris flow and sometimes with cohesive debris flow (Pierson, 2005). These rheological differences produce distinguishable facies but because of the inconsistent nature of flow transformation within debris flow, representative characteristics are not always exclusively illustrative (Scott et al., 1995) (Figure 2.26). Although hyperconcentrated flow can act as a modifying process, remobilizing sediment already present on the fan surface (e.g. eolian material), it is also included in primary processes because of its 1)

aggradational effectiveness and 2) tendency to contemporaneously deposit with and evolve from non-cohesive debris flow through flow transformations.

Fan-scale shifting of the locus of primary deposition occurs when vertically accumulated material reaches a topographic threshold and forces a lateral avulsion of the sediment flow path, compensating accommodation space by directing flow to a topographically lower area. The abandonment of active deposition from this area of the fan allows for secondary modifying processes to become the relatively dominant (by volume) sediment transport processes (Denny, 1967; Bull, 1977; de Haas et al., 2018). Secondary modifying processes are responsible for the most common activity on western Sangre de Cristo alluvial fans, a function of frequency and duration of processes acting on surfaces. As seen on these fans, the majority of secondary modification is due to reworking by fluid-gravity flow, and by the addition and subsequent reworking of wind-blown material (Figure 2.26).

McCalpin (1982) previously explained the western Sangre de Cristo alluvial fans as glacial outwash fans that aggraded during their associated glacial stade. Inherent in this interpretation is that these fans were deposited by braided stream networks, or sandurs, thus precluding them as debris-flow alluvial fans (Zelinski, 2002; Zelinski, 2003). Similarly, the Trollheim fan model by Miall (1977) originated from interpretation of the Trollheim fan in Saline Valley, California as dominantly fluvial (Hooke, 1967), where surficial deposits were interpreted to represent a braided fluvial network interrupted by debris flow (Miall, 1977). However, it has been more recently recognized that the primary depositional mechanisms of debris flow fans (debris flow) are masked by surface

reworking processes and gullying, making interpretation by deposit morphology alone rather misleading (Figure 2.27a-d) (Blair and McPherson, 1992; Hooke, 1993; Blair and McPherson, 1994; Blair and McPherson, 2009; de Haas et al., 2014). The facies that record formation and modification of the alluvial fans on the western Sangre de Cristo are similar to those reported in Miall's 1977 Trollheim fan model. Thus, an interpretation of fluvially-formed fan with the occasional debris flow (Hooke, 1967; Miall, 1977; Hooke, 1993), is dismissed. Applying both geomorphic and sedimentological analysis, this study demonstrates formation of the western Sangre de Cristo fans, and other similar fans, by debris flow accompanied by secondary modification, largely fluid-gravity flow.

Although this model is broadly applicable to many different debris-flow fans, there are intrinsic limitations in practice. As demonstrated (and summarized in Table 2.2), not all facies are diagnostic of specific depositional sub-environment and require contextual information and sedimentological features to differentiate. This is especially important when addressing fluid flows such as hyperconcentrated flow and overland flow. Where practical in the field, the amount of clay-sized material and surrounding facies may assist in distinguishing between hyperconcentrated or overland flow processes. Hyperconcentrated flows are likely to occur either directly after or just before debris flow surge as a transitional deposit between debris flow and fluid-gravity flow and typically have a higher clay content (≥3%) (Fisher, 1983; Costa, 1988; Pierson, 2005). Conversely, overland flow reworks fan-surface material regardless of sedimentary transport sourced from the catchment, will typically have less clay (≤3%) and can occur with considerable time (up to 10^6s of years) since debris flow (Blair and McPherson,

1994; Blair and McPherson, 2009; de Haas et al., 2014). Inopportunely, the depositional sub-environment for these facies alone can be either the abandoned lobe of a debris-flow alluvial fan, the area dominated by secondary modifying processes, or the active depositional lobe, so numerous observations must be used thoughtfully for interpretation.

Conclusion

There are clear associations between facies, surface deposit morphologies, and interpretation of specific processes inherent to the depositional and abandoned lobes on the debris-flow dominated alluvial fans. The sedimentary facies, depositional morphologies, and sediment transport processes represented on the active depositional lobe of the debris-flow alluvial fans are distinguishable from the surficial characteristics of the relict deposits on abandoned surfaces on the western range front of the Sangre de Cristo Mountains. These relict deposits have been modified from their primary deposit morphology by sediment transport processes that act on the abandoned lobe surfaces.

Literature Cited

Aschoff, J. L., and Schmitt, J. G., 2008, Distinguishing syntectonic unconformity types to enhance analysis of growth strata: an example from the Cretaceous, southeastern Nevada, USA: Journal of Sedimentary Research, v. 78, p. 608-623.

Baas, J. H., Best, J. L., and Peakall, J., 2016, Predicting bedforms and primary current stratification in cohesive mixtures of mud and sand: Journal of the Geological Society, v. 173, p. 12-45.

Barbeau, D. L., 2003, A flexural model for the Paradox Basin: implications for the tectonics of the Ancestral Rocky Mountains, Basin Research, v. 15, p. 97-115.

Bateman, M. D., Frederick, C. D., Jaiswal, M. K., and Singhvi, A. K, 2003, Investigations into the potential effects of pedoturbation on luminescence dating: Quaternary Science Reviews, v. 22, p. 1169-1176.

Bateman, M. D., Boulter, C. H., Carr, A. S., Frederick, C. D., Peter, D., and Wilder, M., 2007, Preserving the palaeoenvironmental record in drylands: bioturbation and its significance for luminescence-derived chronologies: Sedimentary Geology, v. 195, p. 5-19.

Beaty, C.B., 1961, Topographic effects of faulting: Death Valley, California: Annals of the Association of American Geographers, v. 51, p. 234-240.

Beaty, C. B., 1963, Origin of alluvial fans, White Mountains, California and Nevada: Annals of the Association of American Geographers, v. 53, p. 516-535.

Bertran, P., Bateman, M. D., Hernandedz, M., Mercier, N., Millet, D. Sitzia, L. and Tastet, J.-P., 2011, Inland aeolian deposits of south-west France: facies, stratigraphy and chronology: Journal of Quaternary Science, v. 26, p. 374-388.

Blair, T. C., 1987, Sedimentary processes, vertical stratification sequences, and geomorphology of the Roaring River Alluvial Fan, Rocky Mountain National Park, Colorado: Journal of Sedimentary Petrology, v. 57, p. 1-18.

Blair, T.C., 1999, Cause of dominance by sheetflood vs. debris flow processes on two adjoining alluvial fans, Death Valley, California: Sedimentology, v. 46, p. 1015-1028.

Blair, T. C., 2000, Sedimentology and progressive tectonic unconformities of the sheetflood-dominated Hell's Gate alluvial fan, Death Valley, California: Sedimentary Geology, v. 132, p. 233-262.

Blair, T.C., and McPherson, J. G., 1992, The Trollheim alluvial fan and facies model revisited: Geological Society of America Bulletin, v. 104, p. 726-769.

Blair, T.C., and McPherson, J. G., 1994, Alluvial fan processes and forms, *in* Parsons, A.J., and Abrahams, A.D., eds., Geomorphology of desert environments: London, Chapman & Hall, p. 354-402.

Blair, T. C., and McPherson, J. G., 1998, Recent debris-flow processes and resultant form and facies of the Dolomite alluvial fan, Owens Valley, California: Journal of Sedimentary Research, v. 68, p. 801-818.

Blair, T.C., and McPherson, J. G., 2009, Alluvial fan processes and forms, *in* Parsons, A.J., and Abrahams, A.D., eds., Geomorphology of desert environments, 2nd Edition: Berlin, Springer, p. 413-467.

Brubaker, K. M., Myers, W. L., Drohan, P. J., Miller, D. A., and Boyer, E. W., 2013, The use of LiDAR terrain data in characterizing surface roughness and microtopography: Applied and Environmental Soil Science, pp. 13.

Bull, W. B., 1977, The alluvial fan environment, Bull, W. B: Progress in Physical Geography: Earth and Environment, p. 222–270.

Calhoun, N. C., and Clague, J. J., 2018, Distinguishing between debris flows and hyperconcentrated flows: an example from the eastern Swiss Alps: Earth Surface Processes and Landforms, v. 43, p. 1280-1294.

Coe, J. A., Kinner, D. A., and Godt, J. W., 2008, Initiation conditions for debris flows generated by runoff at Chalk Cliffs, central Colorado: Geomorphology, v. 96, p. 270-297.

Costa, J. E., 1984, Physical geomorphology of debris flows, *in* Costa, J. E. and Fleisher, P. J., eds., Developments and applications of geomorphology, p. 268-317.

Costa, J. E., 1988, Rheologic, geomorphic, and sedimentologic differentiation of water floods, hyperconcentrated flows, and debris flows: Flood Geomorphology, p. 113-122.

D'Arcy, M., Whittaker, A. C., and Roda-Boluda, D. C., 2017 Measuring alluvial fan sensitivity to past climate changes using a self-similarity approach to grain-size fining, Death Valley, California: Sedimentology, v. 64, p. 388-424.

de Haas, T., Ventra, D., Carbonneau, P. E., and Kleinhans, M. G., 2014, Debris-flow dominance of alluvial fans masked by runoff reworking and weathering: Geomorphology, v. 217, p. 165-181.

de Haas, T., L. Braat, J. R. F. W. Leuven, I. R. Lokhorst, and M. G. Kleinhans, 2015, Effects of debris flow composition on runout, depositional mechanisms, and deposit morphology in laboratory experiments: Journal of Geophysical Research: Earth Surface, v. 120, 1949-1972

de Haas, T., van den Berg, W., Braat, L., and Kleinhans, M. G., 2016, Autogenic avulsion, channelization and backfilling dynamics of debris-flow fans: Sedimentology, v. 63, p. 1596-1619.

de Haas, T., Densmore, A. L., Stoffel, M., Suwa, H., Imaizumi, F., Ballesteros-Cánovas, J. A., and Wasklewicz, T., 2018, Avulsions and the spatio-temporal evolution of debris-flow fans: Earth-Science Reviews, v. 177, p. 53-75.

de Haas, T., Densmore, A. L., den Hond, T., and Cox, N. J., 2019, Fan-surface evidence for debris-flow avulsion controls and probabilities, Saline Valley, California: Journal of Geophysical Research: Earth Surface, v. 124, p.1118-1138.

Denny, C. S., 1967, Fans and pediments: American Journal of Science, v. 265, p. 81-105.

Druitt, T. H., 1995, Settling behaviour of concentrated dispersions and some volcanological applications. Journal of Volcanology and Geothermal Research, v. 65, p. 27-39.

Dühnforth, M., Densmore, A. L., Ivy-Ochs, S., Allen, P. A., and Kubik, P. W., 2007, Timing and patterns of debris flow deposition on Shepherd and Symmes creek fans, Owens Valley, California, deduced from cosmogenic 10Be: Journal of Geophysical Research: Earth Surface, v. 112(F3).

Fisher, R. V., 1983, Flow transformations in sediment gravity flows: Geology, v. 11, p. 273-274.

Frankel, K. L., and Dolan, J. F., 2007, Characterizing arid region alluvial fan surface roughness with airborne laser swath mapping digital topographic data. Journal of Geophysical Research: Earth Surface, v. 112(F2).

Fryberger, S. G., Ahlbrandt, T. S., and Andrews, S., 1979, Origin, sedimentary features, and significance of low-angle eolian ‘sand-sheet’ deposits, Great Sand Dunes National Monument and vicinity, Colorado: Journal of Sedimentary Petrology, v. 49, p. 733-746.

Harvey, A.M., 2011, Dryland alluvial fans, *in* Thomas, D.S.G., ed., Arid zone geomorphology: Process, form and change in drylands, Wiley, Chichester, p. 333-371.

Hooke, R. L., 1967, Processes on arid-region alluvial fans: The Journal of Geology, v. 75, p. 438-460.

Hooke, R. L., Blair, T. C., and McPherson, J. G., 1993, The Trollheim alluvial fan and facies model revisited: Discussion and reply. Geological Society of America Bulletin, v. 105, p. 563-567.

Horton, B. K., and Schmitt, J. G., 1996, Sedimentology of a lacustrine fan-delta system, Miocene Horse Camp Formation, Nevada, USA: Sedimentology, v. 43, p. 133-155.

Iverson, R. M., 1997, The physics of debris flows: Reviews of Geophysics v. 35, p. 245-296.

Iverson, R. M., Reid, M. E., Logan, M., LaHusen, R. G., Godt, J. W., and Griswold, J. P., 2011, Positive feedback and momentum growth during debris-flow entrainment of wet bed sediment: Nature Geoscience, v. 4, p. 116.

Kellogg, K., 1999, Neogene basins of the northern Rio Grande Rift-partitioning and asymmetry inherited from Laramide and older uplifts: Tectonphysics, v. 305, p. 141-152.

Lindsey, D. A., 1998, Laramide structure of the central Sangre de Cristo Mountains and adjacent Raton basin, southern Colorado: The Mountain Geologist, v. 35.

Lowe, D. R. and Guy, M., 2000. Slurry-flow deposits in the Britannia Formation (Lower Cretaceous), North Sea; a new perspective on the turbidity current and debris flow problem. Sedimentology v. 47, p. 31-70.

Machette, M.N., Marchetti, D.W., and Thompson, R.A., 2007, Ancient Lake Alamosa and the Pliocene to middle Pleistocene evolution of the Rio Grande, in Machette, M.N., Coates, M.M., and Johnson, M.L., eds., 2007 Rocky Mountain Section Friends of the Pleistocene Field Trip—Quaternary geology of the San Luis Basin of Colorado and New Mexico, September 7-9, 2007: U.S. Geological Survey Open-File Report 2007-1193, p. 157-167.

McCalpin, J.P., 1982, Quaternary geology and neotectonics of the west flank of the northern Sangre de Cristo Mountains, south-central Colorado: Colorado School of Mines Quarterly, n. 77, p. 97.

McCalpin, J., 1986, Quaternary tectonics of the Sangre de Cristo and Villa Grove fault zones: Contributions to Colorado seismicity and tectonics—A: p. 59-64.

McCalpin, J.P., 2006, Active faults and seismic hazards to infrastructure at Great Sand Dunes National Monument and Preserve: Crestone, Colorado: unpublished report by GEO-HAZ Consulting, Inc., 49 p., 1 oversize plate.

McFadden, L.D., Wells, S.G., and Jercinovich, M.J., 1987, Influences of eolian and pedogenic processes on the origin and evolution of desert pavements: Geology, v. 15, p. 504-508.

McFadden, L. D., Ritter, J. B., and Wells, S. G., 1989, Use of multiparameter relative-age methods for age estimation and correlation of alluvial fan surfaces on a desert piedmont, eastern Mojave Desert, California: Quaternary Research, v. 32, p. 276-290.

Meyer, G. A., Wells, S. G., Balling Jr, R. C., and Jull, A. T., 1992, Response of alluvial systems to fire and climate change in Yellowstone National Park: Nature, v. 357, p. 147.

Miall, A. D., 1978, Lithofacies and vertical profile models in braided river deposits: a summary: Geological Survey of Canada, p. 597-604.

Mushkin, A. and Gillespie, A. R., 2005, Estimating sub-pixel surface roughness using remotely sensed stereoscopic data: Remote Sensing of Environment, v. 99, p. 75-83.

Nemec, W., and Steel, R., 1984, Alluvial and coastal conglomerates: their significant features and some comments on gravelly mass-flow deposits: *in* Koster, E. H. and Steel, R. J., eds., Sedimentology of Gravels and Conglomerates. Canadian Society of Petroleum Geologists, Memoir 10, 1984, p. 1-31.

Owen, L. A., Finkel, R. C., Haizhou, M., and Barnard, P. L., 2006, Late Quaternary landscape evolution in the Kunlun Mountains and Qaidam Basin, Northern Tibet: a framework for examining the links between glaciation, lake level changes and alluvial fan formation: Quaternary International, v. 154, p. 73-86.

Palmquist, R. C., 2019, Alluvial fan sediments and surface ages resulting from differing climatic and tectonic conditions in Star Valley, Wyoming, USA: Catena, v. 181, 104050.

Pierson, T. C., Costa, J. E., and Vancouver, W., 1987, A rheologic classification of subaerial sediment-water flows. Debris flows/avalanches: process, recognition, and mitigation: Reviews in Engineering Geology, v. 7, p. 1-12.

Pierson, T. C., 2005, Hyperconcentrated flow—transitional process between water flow and debris flow: *in* Jakob, M. and Hungr, O., eds., Debris-flow hazards and related phenomena. Springer, Berlin, Heidelberg, 2005, p. 159-202.

Postma, G., 1986, Classification for sediment gravity-flow deposits based on flow conditions during sedimentation: Geology v. 114, p. 291-294.

Ritter, J. B., Miller, J. R., Enzel, Y., Howes, S. D., Nadon, G., Grubb, M. D., and Summa, C. L., 1993, Quaternary evolution of Cedar Creek alluvial fan, Montana: Geomorphology, v.8, 287-304.

Ritter, J. B., Miller, J. R., Enzel, Y., Howes, S. D., Nadon, G., Grubb, M. D., and Summa, C. L., 1993, Quaternary evolution of Cedar Creek alluvial fan, Montana: Geomorphology, v. 8, p. 287-304.

Ruleman, C.A., and Machette, M.N, 2007, An overview of the Sangre de Cristo fault system and new insights to interactions between Quaternary faults in the Northern Rio Grande Rift: *in* Machette, M.N., Coates, M.M., and Johnson, M.L., eds., 2007 Rocky Mountain Section Friends of the Pleistocene Field Trip—Quaternary geology of the San Luis Basin of Colorado and New Mexico, September 7-9, 2007: U.S. Geological Survey Open-File Report 2007-1193, p. 187-197.

Schokker, J. and Koster, E. A., 2004, Sedimentology and facies distribution of Pleistocene cold-climate aeolian and fluvial deposits in the Roer Valley Graben (southeastern Netherlands): Permafrost and Periglacial Processes, v. 15, p. 1-20.

Scott, K. M., Vallance, J. W., and Pringle, P. T., 1995, Sedimentology, behavior, and hazards of debris flows at Mount Rainier, Washington: US Geological Survey Open-File Report, n. 1547, 106 p.

Smith, G. A., 2000, Recognition and significance of streamflow-dominated piedmont facies in extensional basins: Basin research, v. 12, p. 399-411.

Sohn, Y.K., 1997. On traction-carpet sedimentation: Journal of Sedimentary Research. v. 67, p. 502-509.

Southard, J.B. and Boguchwal, L.A., 1990, Bed configurations in steady unidirectional water flows. Part 2. Synthesis of flume data: Journal of Sedimentary Petrology, v. 60, p. 658–679.

Sweeney, M. R., and Loope, D. B., 2001, Holocene dune-sourced alluvial fans in the Nebraska Sand Hills: Geomorphology, v. 381, p. 31-46.

Ventra, D., and Clarke, L. E., 2018, Geology and geomorphology of alluvial and fluvial fans: current progress and research perspectives: Geological Society, London, Special Publications, v. 440, p. 440-16.

Ventra, D., Abels, H. A., Hilgen, F. J., & de Boer, P. L., 2018, Orbital-climate control of mass-flow sedimentation in a Miocene alluvial-fan succession (Teruel Basin, Spain): Geological Society, London, Special Publications, v. 440, p. 129-157.

Ventra, D., and Nichols, G. J., 2014, Autogenic dynamics of alluvial fans in endorheic basins: outcrop examples and stratigraphic significance: Sedimentology, v. 61, p. 767-791.

Wallace, A. R., 2004, Evolution of the southeastern San Luis basin margin and the Culebra embayment, Rio Grande rift, southern Colorado in Geology of the Taos Region: New Mexico Geological Society 55th Fall Field Conference Guidebook

Wells, S. G., McFadden, L. D., Poths, J., and Olinger, C. T., 1995, Cosmogenic 3He surface-exposure dating of stone pavements: Implications for landscape evolution in deserts: Geology, v. 23, p. 613-616.

Zielinski, T., and Van Loon, A. J., 2002, Present-day sandurs are not representative of the geological record: Sedimentary Geology v. 152, p. 1-5.

Zielinski, T., and Van Loon, A. J., 2003, Pleistocene sandur deposits represent braidplains, not alluvial fans: Boreas v. 32, p. 590-611.

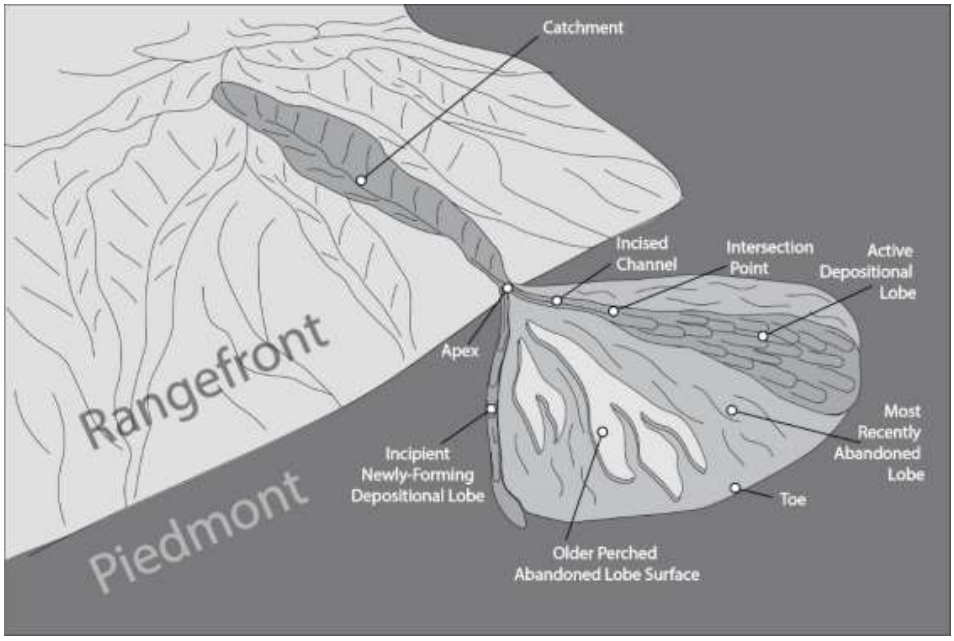

Figure 2.1. Schematic diagram for generic make-up of fan surfaces due to autogenic fan-lobe switching. Primary processes are dominant on the active depositional lobe, while older surfaces of the abandoned lobes are subject to secondary modification.

Figure 2.2. Stark juxtaposition of fresh boulder debris-flow deposit filling incision into older surface. Reference location 13 (Figure 2.5) on proximal Holbrook fan surface. Note dog and human for scale in red circle.

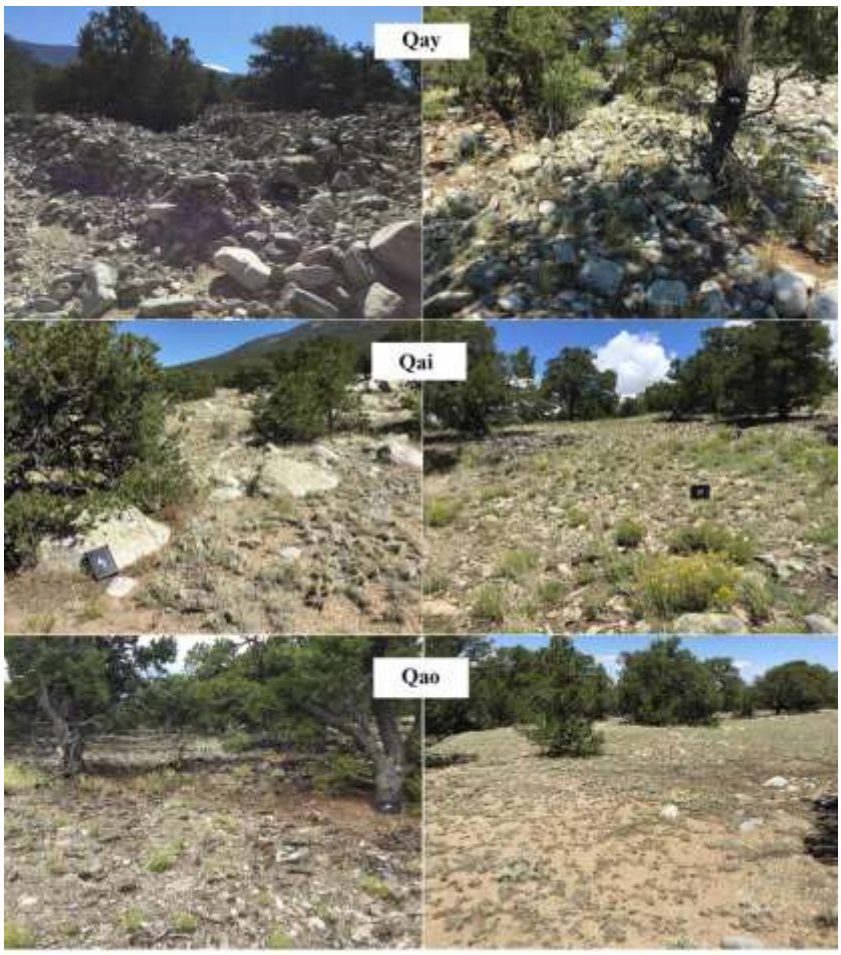

Figure 2.3. Varying surface texture of stages of young (Qay), intermediate (Qai), and old (Qao) alluvial fan surfaces within the study area. Sequence reads left to right starting with fresh, primary depositional fabric in Qay, through consecutively older surfaces. Oldest Qao (lower right) represents heavily reworked and smoothed alluvial fan surface with very minimal to no relicts of primary depositional fabric.

Figure 2.4. Alluvial fans and catchments of the western rangefront of the Sangre de Cristo Mountains.

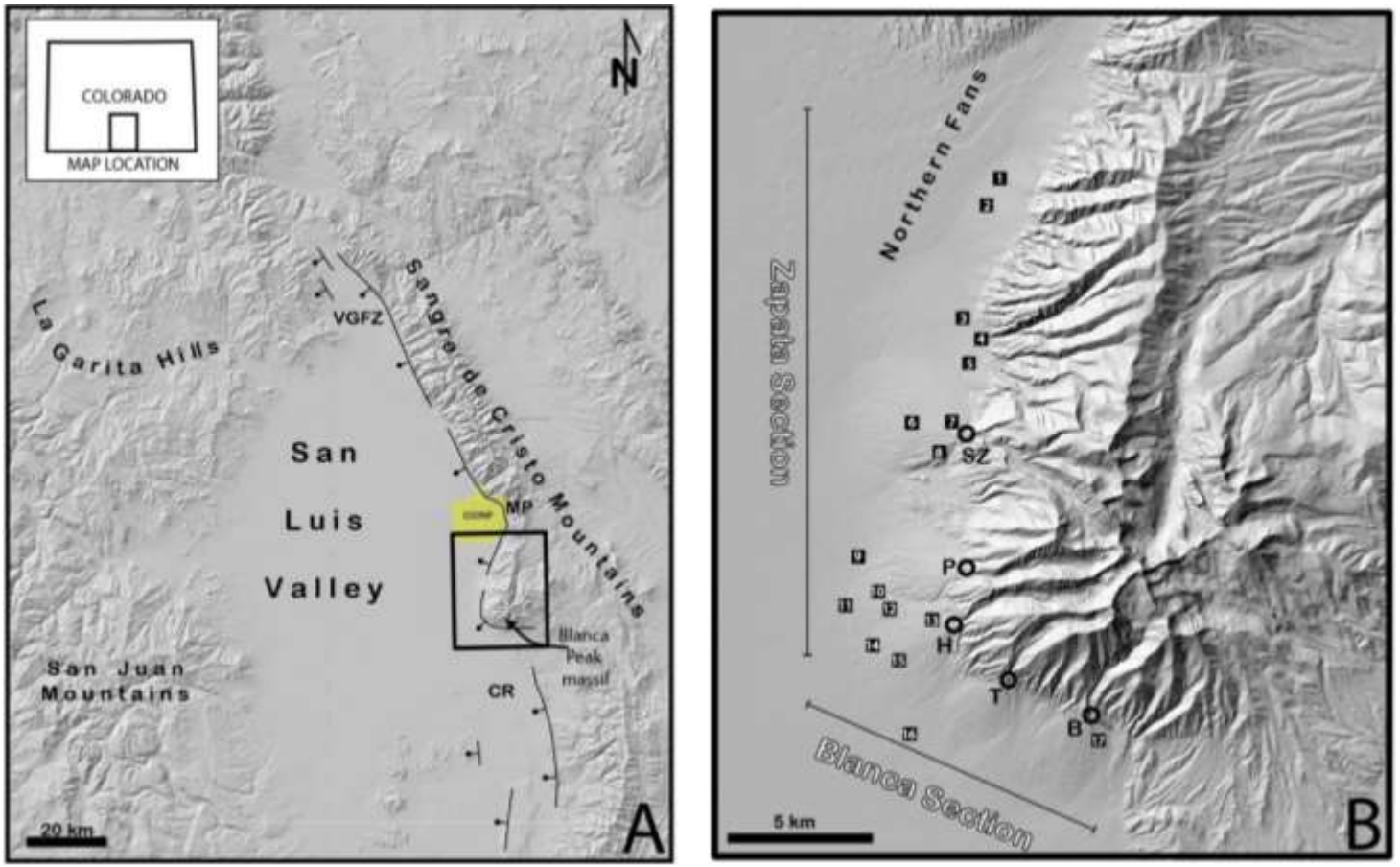

Figure 2.5. Physiographic map of the northern San Luis Valley in southcentral, CO. (A) VGFZ- Villa Grove fault zone, MP- Medano Pass, CR- Culebra reentrant. Inset box is shown on right (B). The alluvial fans of the western rangefront of the Sangre de Cristo mountains. Zapata and Blanca sections show boundaries of the specific sections of the Sangre de Cristo normal fault system. Numbered boxes denote picture site locations. Fans are represented by circle at apex; SZ-South Zapata alluvial fan, P-Pioneer alluvial fan, H-Holbrook alluvial fan, T-Tobin alluvial fan, B- Blanca alluvial fan.

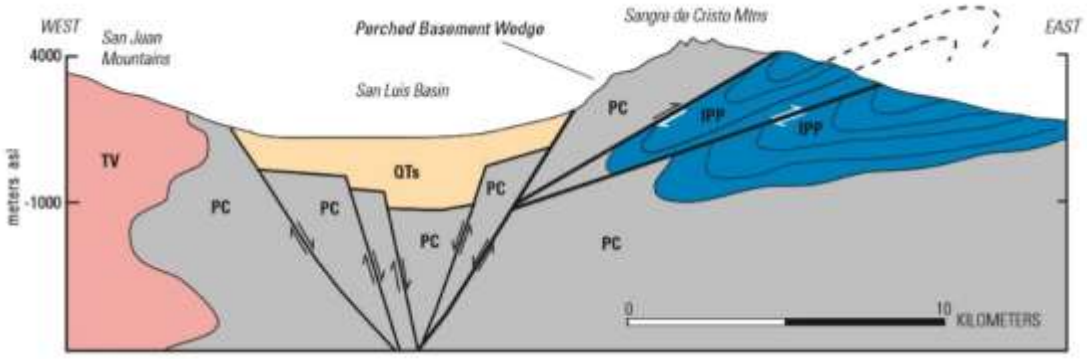

Figure 2.6. Schematic cross-section of the San Luis Valley from Ruleman and Machette (2007). PC- Precambrian (Paleoproterozoic) basement. |PP- Pennsylvanian-Permian sedimentary rocks, TV-Tertiary volcanic rocks QTs- Quaternary and Tertiary basin fill.

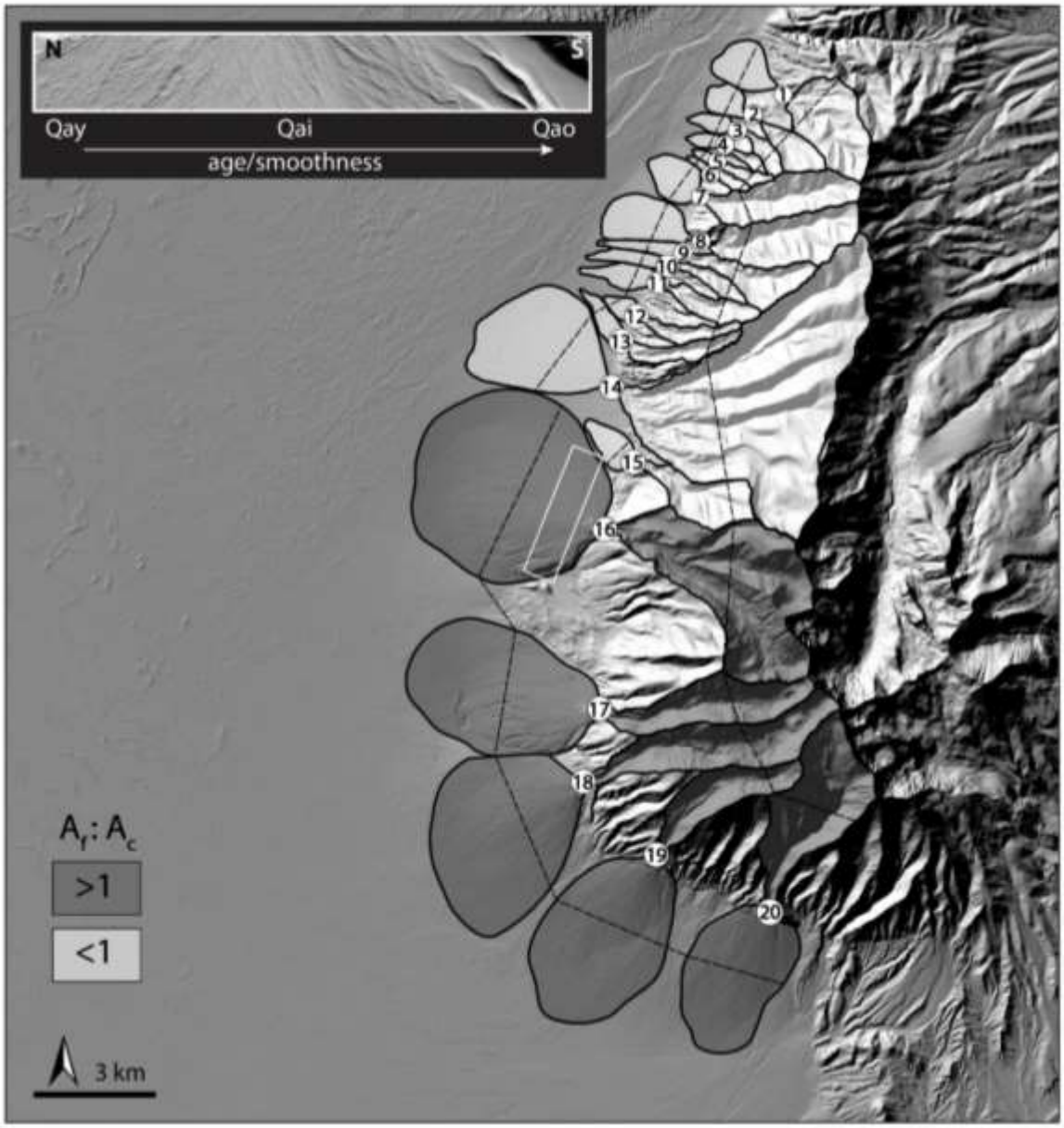

Figure 2.7. Map depicting alluvial fan and catchment area. Dark grey signifies fan-area to catchment-area ratios larger than 1 and light grey denotes ratios less than 1. Dashed lines show cross sectional profiles of fans and catchments shown in Figure 2.9 with corresponding representative numbers. The inset upper left box shows a blow-up of the white rectangle on the proximal portion on the Zapata fan (16) to display the different surface roughness of surfaces of varying age.

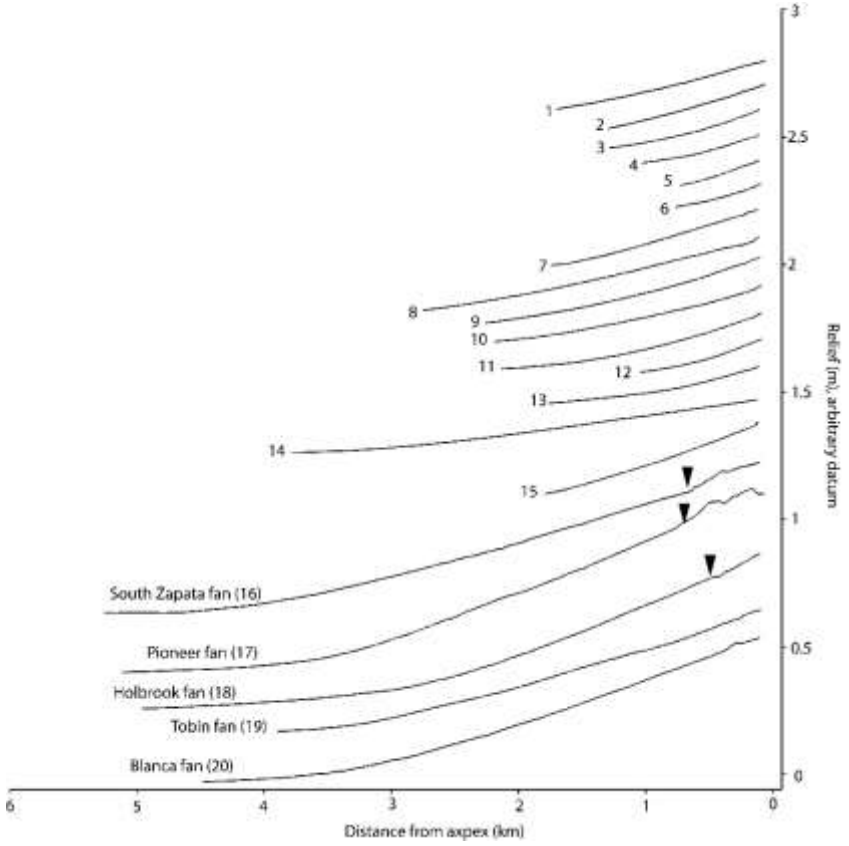

Figure 2.8. Radial profiles of alluvial fans that correspond to fan numbers in Figure 2.7. Radii extend west from fan apexes at the mountain front. Black triangles indicate western terminus of glacial moraines.

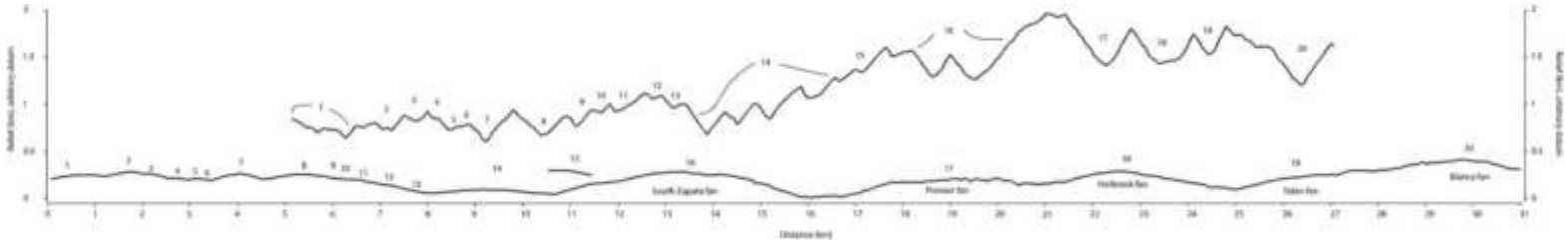

Figure 2.9. Cross-profile of alluvial fans and drainage basins that correspond to profile line in Figure 2.7. Fans and catchments are labeled by corresponding number. Note the U-shape cross section of glaciated catchments 16-20 and the sharp V-shape of non-glaciated catchments 1-15.

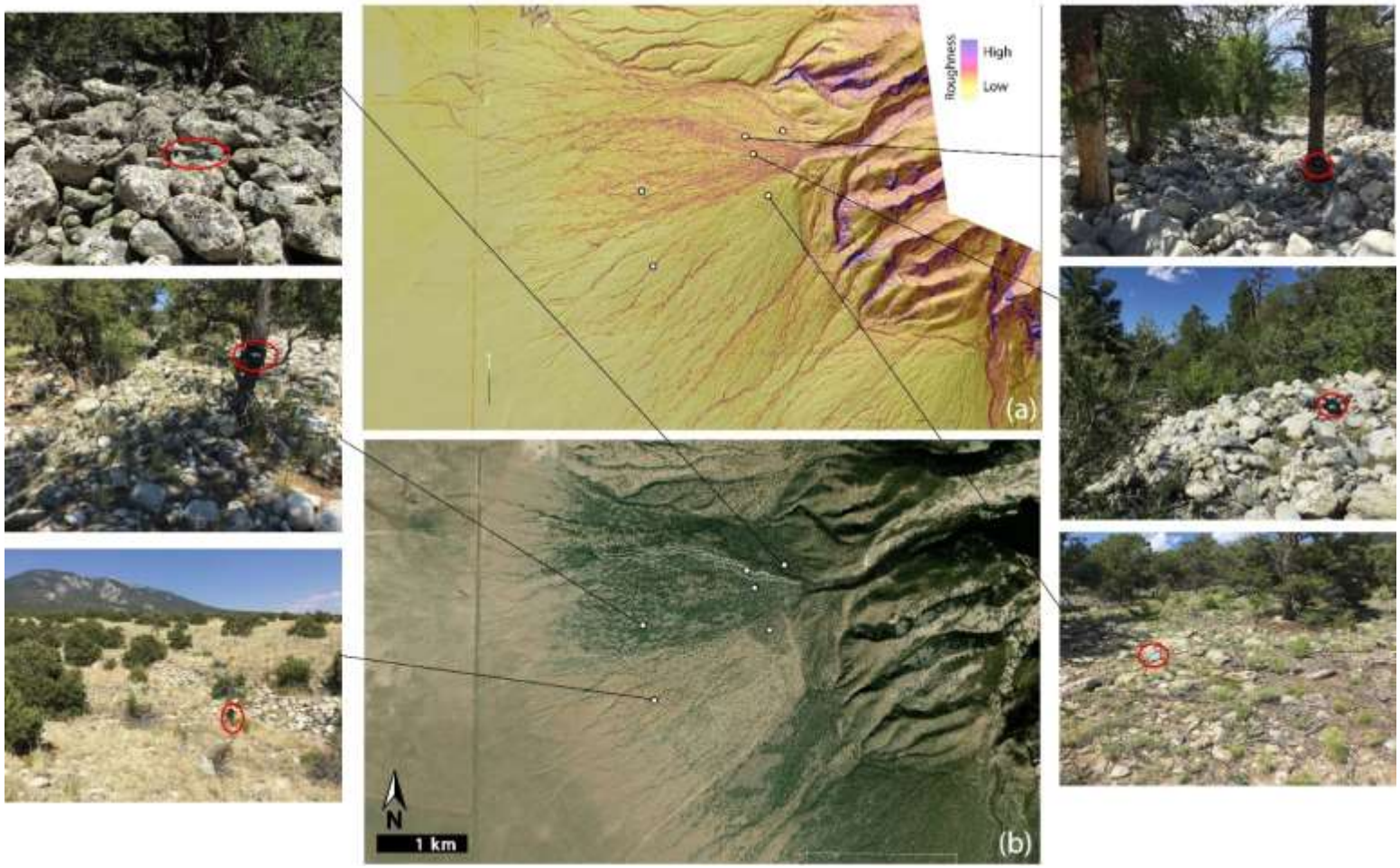

Figure 2.10. Roughness displayed as standard deviation of slope for Holbrook fan (a). Satellite image of Holbrook fan and outlined most-recent debris flow in white (b). White dots tied to pictures at location showing deposit morphologies belonging to relative roughness values (standard deviation of slope). Red circles highlight scale.

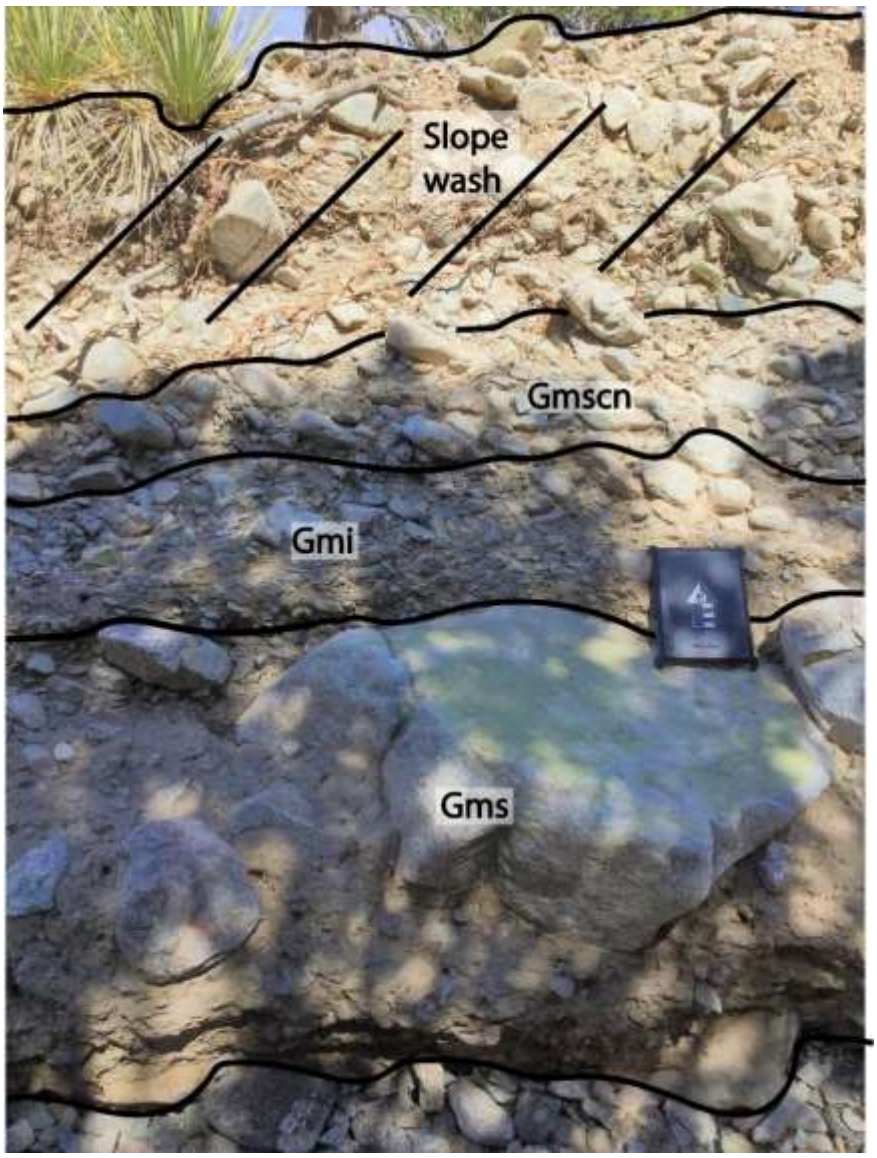

Figure 2.11. Reference location 1 (Figure 2.5) in incision of northern fan 7 represents a suite of primary processes. A large boulder resides in matrix-supported debris-flow deposit (Gms), overlain by inversely graded hyperconcentrated flow deposit (Gmi), and normally graded clast-supported debris-flow deposit (Gmscn). Scale-arrow is 10 cm.

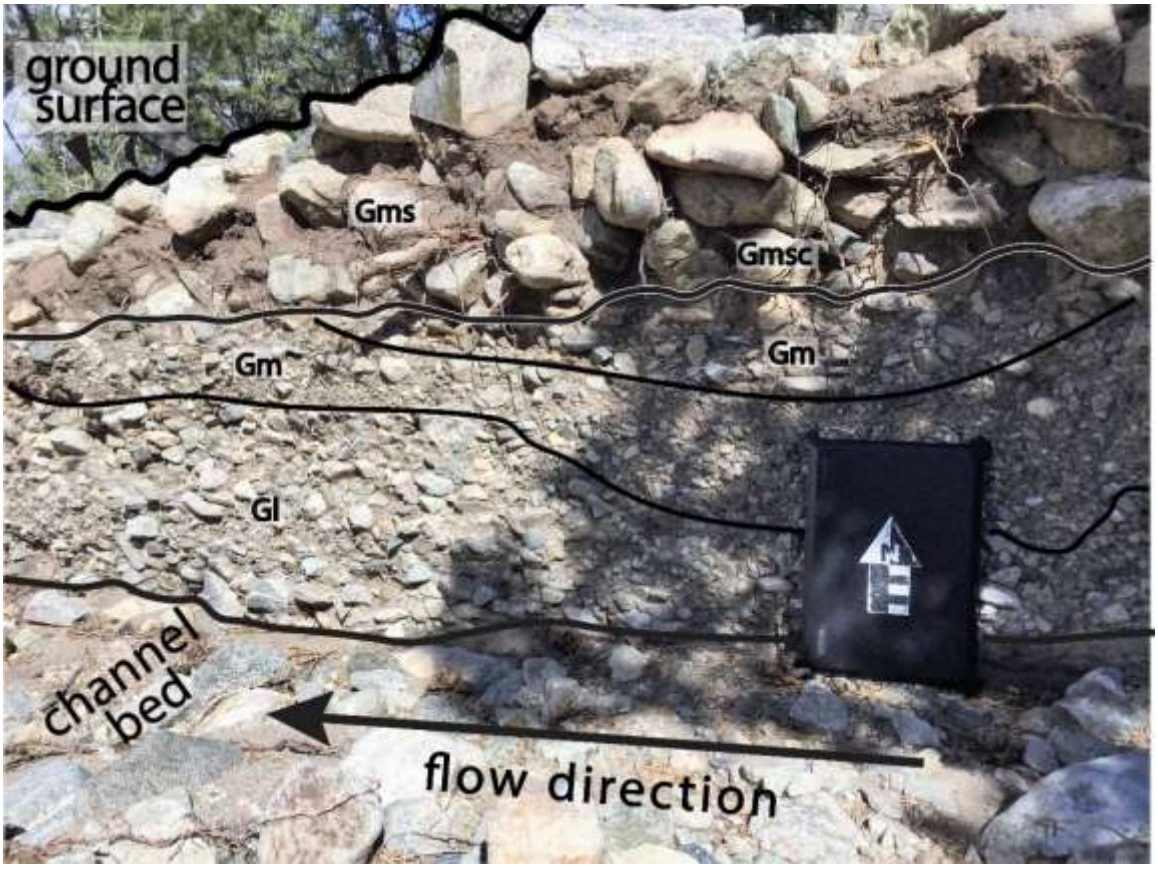

Figure 2.12. Reference location 1 (Figure 2.5) from incision of northern fan 7. Gl and Gm facies are deposits of hyperconcentrated flow. The trough-shape bounding surface separating the two Gm facies likely records sufficient time between the deposition of the lowest Gm facies and Gmsc and Gms above. Scale-arrow is 10 cm.

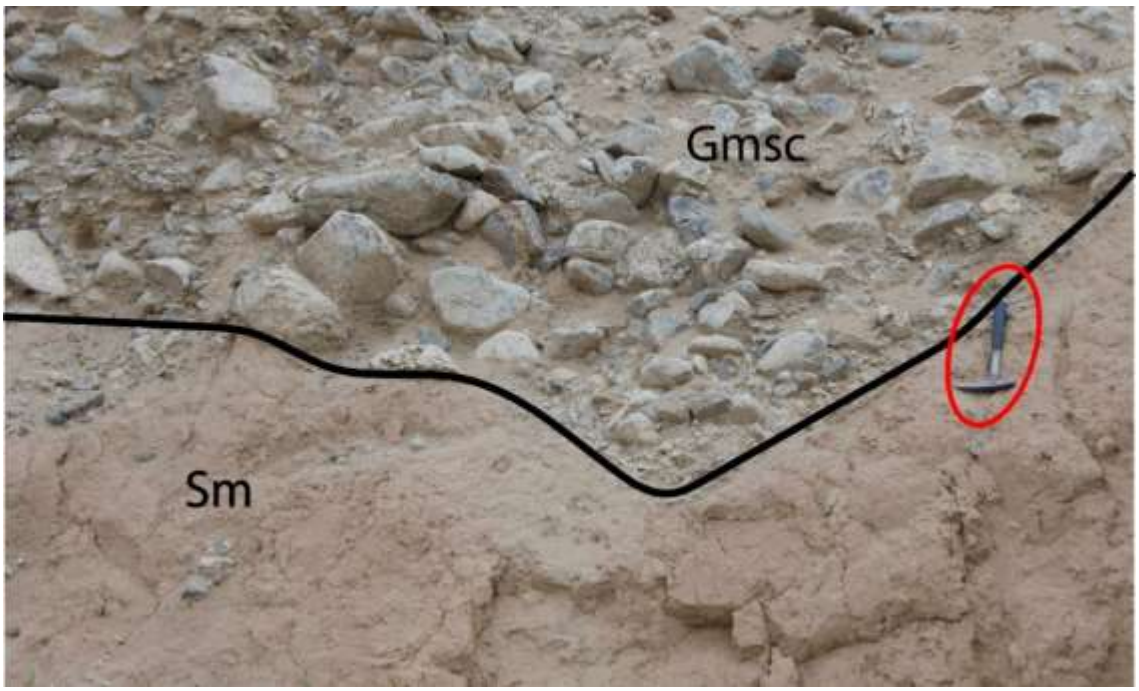

Figure 2.13. Massive sand (Sm) overlain by boulder-rich, clast-supported (Gmsc) debris-flow deposit. Note the wavy, erosion surface at the base of the debris-flow deposit. Reference location 9 (Figure 2.5) at the Pioneer fan quarry.

Figure 2.14. A) Reference location 17 (Figure 2.5) on the proximal portion of the Blanca fan. Debris-flow levees are marked by white dots on crest. Picture taken in up-flow direction. Note the person for scale circled in red. B) Terminal debris-flow lobe. Stadia rod is 9 feet long (~3 m). Reference location 14 on distal reaches of the Holbrook fan. C) Boulder-rich clast-supported fresh debris flow deposits that form rough surface texture of young surface. Reference location 13 on proximal Holbrook fan. Scale-arrow is 10 cm and oriented north. D) Moderately diffuse boulder-rich debris-flow levees at reference location 12, on the Holbrook fan. White arrow shows flow direction. Stadia rod is 9 feet (~3 m) in red circle. E) Terminal lobes of boulder-rich, matrix-deprived, debris flow deposit. Reference location 2 on distal reach of northern fan 8. Note human, Andy, and dog, Flysch, in red circle. F) Matrix to clast-supported right-lateral levee from recent debris flow at reference location 2. Top arrow points to levee crest and bottom arrow shows subsequent flow-scour of levee, black arrow with tail points in flow direction. Stadia rod is 9 feet (~3 m).

Figure 2.15. Woody debris incorporated as clasts and buried tree in most-recent flow on Holbrook fan (site 13, Figure 2.5).

Figure 2.16. Recent debris flow deposit on Holbrook fan (site 13, Figure 2.5) showing fresh boulders with pebble-sized gravel filling interstitial space. Ruler is 10 cm.

Figure 2.17. Variation of lichen cover on boulders of active depositional lobe of Zapata fan (site 7, Figure 2.5).

Figure 2.18. Sand sheet burying boulder-sized clasts. Reference location 16 (Figure 2.5), distal toe of the Tobin fan. Scale arrow is 10 cm.

Figure 2.19. Tree trunks partially buried by eolian and reworked eolian material. Bottom left shows small hand-dug entrenchment into deposit. Reference locations 7 and 4 (Figure 2.5), scale-arrow is 10 cm.

Figure 2.20. Pebble-sized overland flow deposits shown collected behind woody debris. Reference location 8 (Figure 2.5) on the oldest surface on the South Zapata fan. Flow direction is from left to right. Hammer for scale.

Figure 2.21. Water-lain sand and flotsam (white triangle) atop pebble-sized surficial sheet. Black arrow points in flow direction. Scale-arrow is 10 cm and oriented north. Reference location 3 (Figure 2.5), on northern fan 14.

Figure 2.22. Moderately to well sorted pebble-sized sheet. Arrow in the down-fan direction. Scale-arrow is 10 cm and oriented north. Reference location 7 (Figure 2.5) on the proximal portion of the South Zapata fan.

Figure 2.23. Debris-flow lateral lobe at proximal reach of Fan 9. Stadia rod for scale.

Figure 2.24. Deposit morphology of abandoned lobes of the norther fans (location 3 on Figure 2.5).

Figure 2.25. Angular to round pebble and cobble-sized gravels with interstitial fines creating immature desert pavement (location 5 on Figure 2.5).

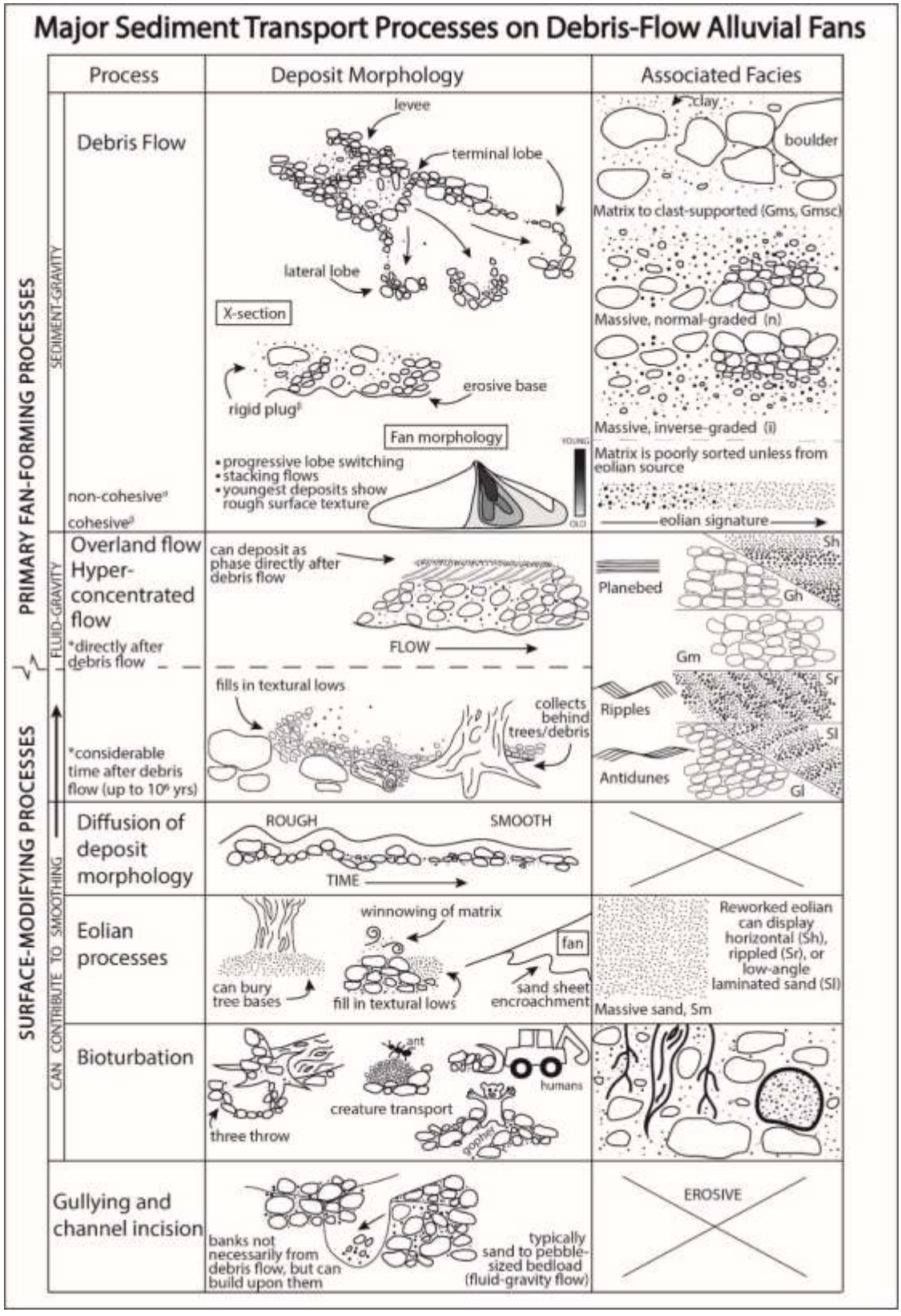
Major Sediment Transport Processes on Debris-Flow Alluvial Fans
Process
Deposit Morphology
Associated Facies
PRIMARY FAN-FORMING PROCESSES
SURFACE-MODIFYING PROCESSES
SEDIMENT-GRAVITY
FLUID-GRAVITY
CAN CONTRIBUTE TO SMOOTHING
Debris Flow
non-cohesive[a]
cohesive[b]
levee
terminal lobe
lateral lobe
X-section
rigid plug[b]
erosive base
Fan morphology
• progressive lobe switching
• stacking flows
• youngest deposits show rough surface texture
YOUNG
OLD
clay
boulder
Matrix to clast-supported (Gms, Gmsc)
Massive, normal-graded (n)
Massive, inverse-graded (i)
Matrix is poorly sorted unless from eolian source
eolian signature
Overland flow
Hyper-concentrated flow
*directly after debris flow
*considerable time after debris flow (up to 10[6] yrs)
can deposit as phase directly after debris flow
FLOW
fills in textural lows
collects behind trees/debris
Planebed
Sh
Gh
Gm
Ripples
Sr
Antidunes
Sl
Gl
Diffusion of deposit morphology
ROUGH
SMOOTH
TIME
Eolian processes
winnowing of matrix
fan
can bury tree bases
fill in textural lows
sand sheet encroachment
Reworked eolian can display horizontal (Sh), rippled (Sr), or low-angle laminated sand (Sl)
Massive sand, Sm
Bioturbation
ant
humans
creature transport
three throw
Gullying and channel incision
banks not necessarily from debris flow, but can build upon them
typically sand to pebble-sized bedload (fluid-gravity flow)
EROSIVE

Figure 2.26. Major sediment transport processes on debris-flow alluvial fans. Processes are divided into the two main categories of primary fan-forming and secondary surface-modifying processes. Facies are represented on the left. Gms-gravel, matrix supported; Gmsc, gravel, clast-supported. Matrix varieties are shown in reference to amount of eolian-sourced material. Modifiers to describe grading; n, normal grading and i for inverse grading. Primary processes are dominantly sediment-gravity debris-flow, but fluid-gravity flow also contribute to fan aggradation and are therefore included in the primary processes. Hyperconcentrated flow is often a phase that occurs simultaneously or just after debris flow. Fluid-gravity flow can also be a modifying agent (secondary processes). Overland flow remobilizes material already on the fan and can produce facies with similar characteristics as hyperconcentrated flow (Gm, Gl, Gh, Sh, Sr, Sl, Sh). Eolian processes deposit massive sand (Sm) that can be subsequently reworked by water to display Sh, Sl, or Sr facies.

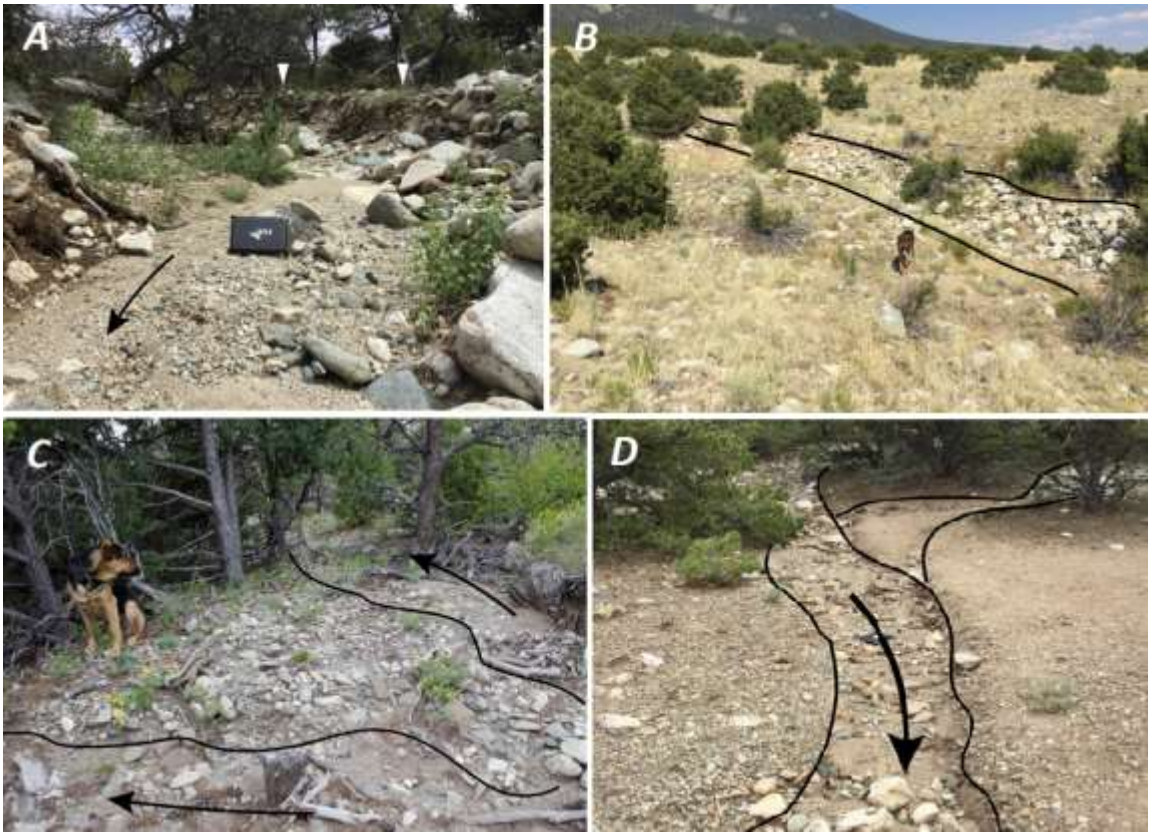

Figure 2.27. A) Reference location 10 on Figure 2.5, near the distal junction of the Pioneer and Holbrook fans. White arrows show incised surface exposing debris-flow deposits. Bed-load of channel consists of coarse-grain lag from primary deposits along with pebbles and sand mobilized by fluid flow. Black arrow indicates flow direction. Scale-arrow is 10 cm and oriented north. B) Incised channel on Holbrook fan, reference location 15 on Figure 2.5. Dog for scale. C) Gullying (arrow) into pebble to cobble-sized deposit. Arrow is in down-fan direction, reference location 7 on Figure 2.5 on the proximal portion of the South Zapata fan. Dog for scale. D) Gullying into pebble-sized sheet to expose underlying boulder-rich deposit. Arrow is in down-fan direction, reference location 7 on Figure 2.5 on the proximal portion of the South Zapata fan.

Table 2.1. Alluvial fan morphometrics

#	Fan Area (km^2)	Catchment Area (km^2)	Fan Area/ Catment Area	Maximum Width (m)	Radial Length (m)	Average Slope	Proximal interval (m along radial profile)	Proximal Slope	Middle Interval (m along radial profile)	Mid Slop	Distal Interval (m along radial profile)	Distal Slope	Radial Descent (m)
1	1.46	3.60	0.40	1332	1654	6.1	0 - 535	7.5	535 - 1179	6.0	1179 - 165	4.8	178
2	0.70	1.13	0.62	905	1339	7.4	0 - 515	8.8	515 - 875	7.3	875 - 1339	6.0	175
3	0.42	0.52	0.81	518	1157	6.9	0 - 295	10.0	295 - 659	7.5	659 - 1157	4.6	140
4	0.24	0.27	0.89	390	923	6.5	0 - 255	9.1	255 - 615	6.9	615 - 923	4.0	106
5	0.13	0.38	0.35	293	622	8.4	0 - 151	9.4	151 - 373	9.3	373 - 622	6.9	92
6	0.11	0.25	0.42	194	685	7.2	0 - 218	10.1	218 - 441	6.8	441 - 685	5.0	87
7	1.26	3.44	0.37	1131	1591	7.2	0 - 423	8.3	423 - 977	8.1	977 - 1591	5.6	201
8	2.17	4.04	0.54	1109	2397	6.6	0 - 819	8.4	819 - 1534	6.6	1534 - 239	4.9	277
9	0.57	2.07	0.28	398	2139	6.4	0 - 578	9.2	578 - 1295	6.5	1295 - 213	4.5	242
10	0.60	0.67	0.89	352	2077	5.8	0 - 590	8.5	590 - 1324	5.6	1324 - 207	3.8	210
11	0.86	1.17	0.74	692	2024	5.7	0 - 552	9.1	552 - 1132	6.4	1132 - 202	3.1	202
12	0.39	0.82	0.48	613	941	7.3	0 - 257	10.4	257 - 586	7.6	586 - 941	4.7	120
13	0.64	1.18	0.54	533	1641	4.7	0 - 466	8.0	466 - 883	4.7	883 - 1641	2.7	136
14	7.32	22.66	0.32	2803	3469	3.2	0 - 1367	3.8	1367 - 231	3.6	2313 - 346	2.0	191
15	0.96	2.55	0.38	870	1657	8.7	0 - 534	10.1	534 - 991	9.0	991 - 1657	7.3	252
16	19.12	11.95	1.60	4783	5130	5.5	525 - 1807	7.9	1807 - 3366	6.9	3366 - 513	2.5	445
17	12.38	4.58	2.70	3221	5021	6.9	690 - 1983	10.8	1983 - 338	8.9	3386 - 502	2.0	524
18	13.39	6.11	2.19	3818	4371	6.9	0 - 1241	10.0	1241 - 265	8.2	2654 - 437	3.6	532
19	11.53	3.39	3.41	3205	4899	6.7	0 - 1529	11.4	1529 - 311	7.4	3111 - 489	1.8	572
20	7.77	6.76	1.15	2509	3837	6.7	0 - 977	8.9	977 - 2086	8.0	2086 - 383	4.7	451

Table 2.2. Facies of western Sangre de Cristo alluvial fans. Facies codes are modified from Miall (1977).

Debris-Flow Alluvial Fan				
Facies	**Description**	**Interpretation**	**Typical Sub-Environment**	**Picture**
Gms	Matrix-supported gravel:Poorly sorted, granule to boulder gravel deposit, unstratified	Sediment-gravity flow (debris flow) deposits	Active depositional lobe	
Gmsc	Matrix- to clast-supported gravel: Poorly sorted, granule to boulder gravel deposit, unstratified	Sediment-gravity flow (debris flow) deposits	Active depositional lobe	
Gm	Massive gravel: Moderately to well-sorted, clast-supported pebble-sized gravel	Fluid-gravity flow (overland flow/ hyperconcentrated flow)	Both depositional and abandoned lobes	
Gl	Low-angle stratified gravel: Moderately to well-sorted, clast-supported granule to pebble-sized gravel	Fluid-gravity flow (overland flow/ hyperconcentrated flow)	Both depositional and abandoned lobes	
Gls	Low-angle stratified, sandy matrix-supported gravel: Poorly sorted, matrix-supported granules to pebbles in medium to coarse-sand.	Fluid-gravity flow (overland flow/ hyperconcentrated flow)	Both depositional and abandoned lobes	
Gh	Horizontally stratified gravel: Moderately to well-sorted, plane-bedded, clast-supported pebble-sized gravel	Fluid-gravity flow (overland flow)	Abandoned lobes	
Smps	Massive sand, poorly sorted: Massive to very crudley stratified, poorly sorted fine to coarse sand.	Fluid-gravity flow (hyperconcentrated flow)	Active depositional lobe	
Smws	Massive sand, well sorted: Well to very well sorted, massive, silt to very fine sand	Eolian deposition/reworked eolian sediment by hyperconcentrated flow	Abandoned lobes	
Sl	Low-angle stratified sand: Normally graded, moderately to well-sorted, very fine to medium sand	Reworked eolian material by fluid-gravity flow (overland flow/ hyperconcentrated flow)	Abandoned lobes	
Sh	Horizontally stratified sand: Crudely stratified, poorly to well-sorted, plane-laminated, fine to very coarse sand	Fluid-gravity flow (overland flow/ hyperconcentrated flow)	Both depositional and abandoned lobes	
Sr	Ripple cross-laminated sand: Poorly to very well-sorted, silt to coarse sand	Reworked eolian material by fluid-gravity flow (overland flow)	Abandoned lobes	

CHAPTER THREE

LATE PLEISTOCENE RECORD OF SURFACE-MODIFYING PROCESSES ON THE PIONEER DEBRIS-FLOW ALLUVIAL FAN, SAN LUIS VALLEY, COLORADO

Contribution of Authors and Co-Authors

Manuscript in Chapter 3

Author: Sylvia Nicovich

Contributions: Conceived the study, performed the analyses, interpreted results, and wrote the manuscript.

Co-Author: James Schmitt

Contributions: Conceived the study, assisted the analysis, discussed results and implications, and edited earlier manuscripts.

Co-Author: Ralph Klinger

Contributions: Assisted in description of soil profiles and soil properties.

Co-Author: Shannon Mahan

Contributions: Major assistance of obtaining optically stimulated luminescence age data.

Manuscript Information

Sylvia Nicovich, Jim Schmitt, Ralph Klinger, Shannon Mahan

Geological Society of America Bulletin

Status of Manuscript:
_X_ Prepared for submission to a peer-reviewed journal
____ Officially submitted to a peer-reviewed journal
____ Accepted by a peer-reviewed journal
____ Published in a peer-reviewed journal

Abstract

Alluvial fans and fan deposits in the stratigraphic record are often used as indicators of landscape dynamics, yet the sedimentological signature of depositional and surface-modifying processes is poorly understood. Integrative sedimentological and geomorphic analyses, applied facies and soils mapping along with infrared stimulated luminescence (IRSL) geochronology were applied to document timing of fan construction and modification processes recorded over the last ~100 ky in deposits of the Pioneer alluvial fan sourced from the extensively glaciated Pioneer drainage, located on the western range front of the Sangre de Cristo Mountains in southern Colorado. The Pioneer fan was constructed mostly by debris-flow deposition on the active depositional lobe, with progressive lateral lobe switching due to autogenic topographic compensation. Debris-flow activity on adjacent surfaces of abandoned fan lobes is minimal with modifying processes dominating the abandoned lobe surfaces. Both constructive and modifying processes are recorded in a 16-meter vertical quarry exposure at the fan toe that constitute intervals of depositional lobe activity and abandoned lobe modification, respectively. Matrix- to clast-supported gravels (facies assemblage A) represent primary debris-flow deposition (the depositional lobe sub-environment). Surface reworking by overland flow is represented by facies assemblage B—massive gravel, horizontally-stratified gravel, low-angle cross-stratified sand, and horizontally-stratified sand. Modification periods with strong eolian influence are also represented by facies assemblage B, by massive sand and include surficial water modification of eolian deposits represented by horizontally and low-angle laminated sand. Three well-developed

buried soils are exposed in a quarry at the toe of the Pioneer fan, yielding IRSL ages of 77.1±5.3 ka, 61.8±6.2 to 54.4±7.0 ka, and 37.3±2.7 ka, that define three periods of relatively long-duration surface stability. More poorly developed soils are also exposed in the quarry, defining two periods of relatively short-duration surface stability with IRSL ages of 100±10.2 to 96.3±8.7 ka, and 84.3±6.7 ka. Accompanying each soil is a facies association that originates with a constructive facies assemblage A (debris flow) and transitions upward to modifying facies assemblage B indicative of surficial water reworking, capped by eolian-influenced facies comprising windblown and water-reworked sand/silt. Periods of long-duration surface stability reflect autogenic depositional lobe switching and periods of short-duration surface stability reflect time gaps in debris-flow deposition on active depositional lobe surfaces. On the Pioneer fan, and likely other debris-flow alluvial fans, eolian-influenced facies are associated with periods of abandoned lobe surface stability as shown by soil horizons. This suggests that eolian deposition, water reworking of eolian sediment, and pedogenesis are important processes on the abandoned lobe surfaces of debris-flow alluvial fans.

Introduction

Alluvial fans encompass active and inactive surfaces resulting in contemporaneous periods of fan building and surface development. Progressive lobe switching produces multi-leveled topographic surfaces that constitute the greater alluvial fan systems. Fan building processes are distinct to the depositional lobe while all other surfaces are dominated by secondary processes (Figure 3.1). Surface development includes secondary modifying processes that occur during breaks in primary depositional activity (Blair and McPherson 1994; Blair and McPherson,2009; de Haas et al., 2014). The relative duration of hiatus in primary deposition is often demonstrated by the formation of soils due to time and surface stability (Bockheim, 1980; Birkeland, 1984; Berry, 1987; Birkeland and Burke, 1988; Reheis et al., 1989; Harden, 1990).

Research on alluvial fans has largely been approached through the context of surficial analysis (Hooke, 1967; Bull, 1977; Wells and McFadden, 1987; Ritter et al., 1993). The concept of surface development within modern alluvial fan settings creates a framework primed for enhancing recognition of unconformities in fan deposits. To demonstrate, surface smoothing with time has been widely recognized to initiate when a fan lobe surface becomes abandoned (McFadden et al., 1989; Hsu and Pelletier, 2004; Matmon et al., 2006; Frankle and Dolan, 2007; Johnstone et al., 2018). This smoothing is due to secondary modifying processes that degrade primary deposit morphology, rock and mineral weathering, reworking of material by overland flow, and introduction of windblown sediment (Blair and McPherson, 1994; Blair and McPherson, 2009). Most researchers focus on surficial characteristics involving texture. However, the processes

that contribute to smoothing are also recorded in the stratigraphic succession of alluvial fan deposits. Therefore, their stratigraphic characteristics help define criteria useful for recognition of periods of surface formation or gaps in time recorded in the sedimentary record. Processes acting during periods of surface formation that simultaneously contribute to fan smoothing include reworking of material by overland flow, the addition of eolian material, and over-all gravitational collapse of the originally rough surface (McFadden et al., 1989; Blair and McPherson, 1994; Blair and McPherson, 2009)

Understanding the features of surface modification that represent hiatuses in primary deposition preserved in alluvial fan deposits is significant for the use of alluvial fan interpretation as an indicator in landscape evolution (i.e. periods of surface stability as an indicator for changes in climate, base level, tectonic activity, and over-all fan lobe switching). Recognition of sedimentary facies that represent surface formation is necessary when interpreting rock-record and modern system deposits that illuminate syntectonic unconformities or growth strata, especially less obvious, subtle-type unconformities (Riba, 1976; Suppe et al., 1997; Aschoff and Schmitt, 2008). These data coupled with the analysis of soil development, buried soils, and/or paleosols, are the record for systems with complex histories of surface stability and landscape evolution (Kraus, 1999; Demko et al., 2004).

Surface modification on debris-flow alluvial fans occurs inverse to deposition on fans. Periods of deposition and conversely, surface-forming periods, exist on two distinct spaciotemporal scales dictated by the lateral and vertical autogenic dynamics of alluvial fan sediment accumulation and avulsion (Ventra and Nichols, 2013). Short-duration

surface development occurs on the depositional lobe during relatively short-lived hiatuses in debris-flow deposition, which reflect the recurrence period of the primary processes (debris flow) generally 10^1s to 10^3s of years (Costa, 1988; Scott et al., 1995). These lulls are due to lateral autogenic dynamics that concern individual debris-flow deposits and avulsions to adjacent areas on the active depositional lobe of a fan. On the other hand, long-duration surface development occurs when the depositional lobe switches to an adjacent area of the fan because of vertical autogenic dynamics or topographic compensation. This process occurs over time scales on the order of tens of events (10^3s to 10^4s of years) and involves generations of flows stacking atop one another until a threshold is passed and a new, topographically lower depositional lobe is occupied (Ventra and Nichols, 2013; de Haas et al., 2018).

So, what is the stratigraphic expression of these periods of surface development and can they be distinguish? This study puts interactions of surface development, erosion, and sedimentation into context with the combined use of sedimentary facies indicative of surface formation, soil morphology, and geochronologic methods to establish that there are representative sedimentary facies for periods of surface stability demonstrated by the pedogenic processes. In fact, the duration of surface development can be interpreted through the development of soils and thus pin-point the spaciotemporal style and scale of surface-forming mechanisms.

Setting of the Pioneer Alluvial Fan

The Pioneer alluvial fan emanates from the extensively glaciated Pioneer Creek drainage on the Blanca Peak massif within the Sangre de Cristo Mountains into the San Luis Valley of south-central Colorado (Figure 3.2). The Holocene-active Sangre de Cristo normal fault system bounds the western range front, creating the high-topography necessary for glaciation (Ruleman and Machette, 2007). Debris flow is the primary process characterizing deposition of the Pioneer and adjacent fans of the Blanca Peak massif. Debris-flow processes are evident though levée and lobe morphology and rough fabric of the youngest surfaces. The older surfaces show signs of smoothing and incision due to modifying processes. The approximate area of the Pioneer fan is 12 km^2 while the catchment occupies about 5 km^2. Unequal fan-area to catchment-area ratio is due to the U-shaped geometry of the catchment formed through glacial scour. Sediment supplied to the fan is largely of glacial origin. Previous studies (McCalpin, 1982) have interpreted the Pioneer fan and adjacent alluvial fans as outwash-plains, yet the sedimentary facies and surface morphology indicative of debris-flow processes contradict this interpretation, and these fans are likely a result of persistent debris-flow processes.

Surfaces of the fan can be separated into three broad groups; old, intermediate, and young and are capped by glacial moraines from Bull Lake and Pinedale glacial periods (McCalpin, 1982; Pierce, 2003) (Figure 3.3). Old surfaces are smooth, incised, relict fan surfaces, where modifying processes of overland flow, addition of eolian sediment, and incision control the dominant morphologies rather than primary processes like debris flow. Intermediate surfaces are somewhat smoothed and modified by

secondary processes, but still maintain discernable evidence of primary deposition such as boulder trains from debris flow levees and lobes. The youngest surfaces display the most defined evidence of debris flow processes and minimal reworking as these surfaces have experienced the most recent debris-flow deposition in the fan complex. Primary and secondary sediment transport processes that create and modify original deposit morphology, respectively, are illustrated in Figure 3.4.

The Pioneer fan is selected for this study from its adjoining range front fans due to the opportune exposure in a gravel quarry excavated into its distal reaches (Figures 3.3 and 3.5). Moreover, the Pioneer and adjacent fans sourced from glaciated catchments exhibit similar surface morphologies and catchment characteristics, therefore making the Pioneer fan a reasonable analogue to neighboring fans as well as other debris-flow dominated alluvial fans.

Methods

The approach used to distinguish periods of surface development are two-fold; 1) identification of sedimentary facies that represent secondary (surface-modifying) processes distinguished from primary processes and, 2) extent of soil development in representative surface-forming sedimentary facies. Infrared-stimulated luminescence (IRSL) was used on feldspar grains within sandy deposits to determine numerical-age context for sequences representing surface stability (Appendix B). Sedimentary facies were described by sedimentary structures, deposit texture, and matrix composition. Interpretive facies associations were made by comparing sedimentary facies' characteristics to the alluvial fan surfaces characteristics and deposit morphologies.

Facies analysis was conducted on accessible deposits and projected to inaccessible portions of the approximately 16-meter quarry exposure (Figure 3.6). Complete descriptions of soil profiles are made where safely accessible. In precarious areas, identified horizons were sampled for in-house descriptions. Unreachable soils are purely visually described. IRSL samples are collected from the accessible portions of sand beds exposed in the quarry (Figure 3.7).

Soils as an Indicator of Surface Stability

Soil formation is a function of climate, biota, topography, parent material, time, and other factors that vary locally or regionally (Jenny, 1941; 1980). Soils that form on similar landscape and parent material and differ only in development as a function of time represent what is referred to as a soil chronosequence (Vreeken, 1975; Markewich, 2017). The soils exposed in the Pioneer quarry represent a time-transgressive chronosequence without historical overlap (nomenclature of Vreeken, 1975), a vertical stacking of sediments and soil development where the soils represent periods of non-deposition (Vreeken, 1975; Birkeland, 1999).

A soil profile develops from the ground surface downward into the unweathered parent material of rock or deposit it is formed on. Soil profiles comprise a series of horizons distinguished by zones of accumulated organic and eolian material (A horizon), changes in parent material since deposition (B horizon), and parent material (C horizon) (Birkeland, 1999). Subdivisions of B horizons are based on the specific material changes that have occurred since deposition. Subdivisions common in this study area are Bk and Bt. Bk is the annotation for the accumulation of calcium carbonate in the B horizon and

Bt for the accumulation of clay. Soil notation consists of; 1) horizon (and subdivision if necessary), 2) change in parent material (pretext to horizon), and 3) burial sequence (Birkeland, 1999). For example, the first buried soil exposed in the quarry is represented by Btb/2Bkb and the second by 3Btb1/4Bkb1. B in front of a t or a k denotes the B horizon with t (clay) or k (carbonate) subdivision. b denotes that this horizon is buried and the number after b records the buried sequence with depth. The number in front of B denotes a change in parent material, in this case from sand to gravel and vice versa.

Documenting the chronosequence at the Pioneer quarry creates a context for understating relative duration of periods of non-deposition within the alluvial fan system. Three distinctive buried soils were analyzed in this study. Figure 3.6 shows the exposure in the northern extent of the quarry and type-locality soil profile labels (e.g., SDA, SDRZ, etc.). Soils SDRU and SDRL were measured from the apparent upper-most extent of the visible soil profile and delineated between horizons. Each horizon was sampled for in-house soil characteristic descriptions. The complete profile of SDA was delineated in the field and each horizon was sampled for in-house description of soil characteristics.

Stratigraphic Framework

To understand the associated processes with sedimentary facies, sedimentary structures, deposit texture, and matrix composition were catalogued and compared with alluvial fan surface characteristics. Secondary modifying processes were determined by categorization of surficial deposit morphologies of various ages, ranging from fresh, primary debris-flow deposits to degrade, smoothed surfaces. Geomorphic surface age-relations of the Pioneer alluvial fan were determined initially using high-precision

LiDAR data based on characteristics of roughness and topographic position. These age relations were used as the framework for how deposit morphologies and sedimentological characteristics develop on each surface through time.

Sedimentological facies that represent these secondary (surface modifying) processes exposed in the vertical exposure at the quarry signify periods of surface stability (periods of non-primary deposition). Recognition of sediment transport processes and surficial characteristics is critical when interpreting representative signatures of surface stability within stratigraphic successions of the dispositional system. Facies associations were made for the exposure at the Pioneer quarry, which is oriented parallel to the fan radius, approximately 3.5 km from the fan apex.

Infrared-Stimulated Luminecese (IRSL)

Sandy deposits were targeted to sample for luminescence dating. Because luminescence methods rely on the post-burial dosimetric signal acquired when a deposit becomes blocked from the sun, all samples must be collected without exposure to light. Samples were collected by either driving metal pipes into deposits or by breaking off a cohesive sandy block and spray painting the outer portion to indicate the grains exposed to light. Luminescence samples are labeled 1 through 5 and A through E (Figure 3.6).

Luminescence samples were processed and measured at the United States Geological Survey Luminescence Laboratory in Lakewood, Colorado. Conditions used to model age are described in Appendix B.

Results

Two discrete facies assemblages and soil morphologies are present in the 16-meter quarry exposure. Figure 3.8 is a stratigraphic column that illustrations facies, soils, and geochronology of the quarry exposure. The two major facies assemblages within the quarry are grouped based on their interpreted distinction as either primary deposition or secondary modification. Facies assemblage A is the coarsest (up to large boulders) grouping of facies and represents primary debris-flow deposition. Facies assemblage B contains smaller clasts-size, from layers of well-sorted silt and sand to cobble-sized clasts, and represent fan surface-modifying processes, namely overland flow and eolian deposition. Each soil demarcated in the soils column corresponds with deposits of Facies assemblage B and represents a period of surface stability. Deposits within Facies assemblage B were targeted for geochronology because they represent periods of surface stability resulting in their fine-grained texture (specifically facies B1 and B2). Ages of each sampled deposit are reported in the age column of the stratigraphic section (Figure 3.8).

Facies Assemblage A

Description. Facies assemblage A contains the thickest and coarsest-grained deposits exposed in the Pioneer fan quarry (Figure 3.9). Facies assemblage A comprises three typical facies. Facies A1 is a poorly-sorted, matrix-to clast-supported, unstratified, ungraded, inversely, and normally-graded, sub-angular to round, pebble- to boulder-sized gravel. Matrix texture ranges from; 1) coarse-grained, poorly-sorted sand to granules, 2)

silt to very fine-grained, well-sorted sand, 3) mixtures of both 1 and 2. Facies A2 is poorly-sorted, matrix-supported, unstratified, ungraded, sub-angular to round, pebble- to boulder-sized gravel. Like facies A1, Facies A2 also has matrix variation distilled into the three categories. Facies A3 is clast-supported, moderately-sorted, unstratified, ungraded to inversely- or normally-graded, sometimes matrix-deprived, pebble- to cobble-sized gravel. Clast lithology in all three facies is predominantly Paleoproterozoic gneiss, granodiorite, and quartz monzonite.

Lower contacts for Facies A1 and A2 are abrupt, wavy to straight. Facies A1 and A2 range in thickness from 1 up to approximately 3 meters and are typically intermingled or stacked. Deposits commonly exhibit laterally discontinuous geometries. Facies A3 is typically 1 meter or less thick and often present above Facies A1 and A2.

Interpretation. Facies assemblage A is interpreted to represent primary deposition within the debris-flow alluvial fan system. Facies A1 and A2 represent deposition by debris flow. In debris flow, the cohesive versus noncohesive flow behavior is largely dictated by matrix characteristics. In cohesive flows, the matrix cushions the grain interaction, which reduces erosion potential at the flow boundaries and prohibits coarse particle settling and differential movement of all coarse particles (Scott et al., 1995). This is inverse for noncohesive flows, where large particles are able to differentially move through the cohesionless matrix, therefore producing well-developed normal and inverse grading (Scott et al., 1995). The clast-rich, poorly sorted, chaotic fabric of Facies A1 is consistent with deposition of non-cohesive debris-flow deposits (Costa, 1988; Scott et al., 1995; Iverson, 1997; de Haas, 2014). The lack of matrix allows

for grain interaction and the ability for the flow to mix and change form, resulting in crude stratification (Scott et al., 1995). Facies A2 represents cohesive debris-flows. The abundant matrix and massive fabric are evident of limited grain-grain interaction and deposition as a solitary mass (Scott et al., 1995; Iverson, 1997). Cohesion in debris flow is generally attributed to the volume percent of clay- or silt-sized (~3%) material present in the matrix (Scott et al., 1995). Facies A3 characterizes the water-rich, matrix poor, transitional phase, following the initial debris-flow charge. Facies A3 is likely derived from the flow transformation of Facies A1, non-cohesive flows. Non-cohesive flows are more readily mixed and therefore have a greater potential to change into hyperconcentrated flow (Scott et al., 1995; Sohn et al., 1999). Facies assemblage A is consistent with sedimentology of surficial deposits on surfaces with relatively recent debris-flow activity (the depositional lobe sub-environment). Cobble and boulder-rich debris-flow levees and lobes are sedimentologically similar to facies A1 and A2. Given the properties of its matrix, Facies A2 is likely characteristic of debris-flow plug and tail (Iverson, 1997).

Facies Assemblage B

Description. Facies assemblage B is the finer-grained assemblage of the quarry exposure and comprises three distinct facies (Figure 3.9). Facies B1 is massive, well-sorted, silt to very fine-grained sand. Facies B2 consist of low-angle laminated, ripple cross-laminated, well-sorted silt to very fine sand with occasional coarse sand to granule stringers along laminae. Facies B3 is made up of massive, low-angle, and horizontally bedded, moderately sorted, clast-supported pebble to cobble-sized gravel. Like in facies

assemblage A, clast lithology of grains larger than sand size in Facies B2 and B3 is predominantly Paleoproterozoic gneiss, granodiorite, and quartz monzonite.

Lower contacts of facies assemblage B are generally abrupt and smooth. Deposits of Facies B1 are as thick as 2 meters, while B2 and B3 are generally thinner with a maximum thickness of about 1 meter. Facies B1 is typically overlain by Facies B2; B3 is often present atop Facies assemblage A.

Interpretation. Facies assemblage B is interpreted to represent the secondary processes that modify and rework the material of alluvial fan surfaces, both on depositional and abandoned lobes. Facies assemblage B is characteristic of periods of stability and non-primary aggradation on alluvial fan surfaces and should be considered as unconformities.

Massive silt to very fine sand of Facies B1 is consistent with eolian material introduced to the fan surface during times of minimal or no primary deposition. These deposits are well sorted and are within the grain-size fraction that is transportable by wind (Reheis, 1995; Pye, 1995). Facies B2 represent eolian deposits reworked by overland flow, producing lamination and incorporation of coarser-grained material from remobilization by water (Blair and McPherson, 1992; Blair and McPherson, 1994; Blair and McPherson, 2009; de Haas et al., 2014). These deposits maintain a dominance of the grain-size distribution recorded in facies B1, but with modification of the depositional fabric. B3 represents coarser-grained overland flow transport of gravely materials already present on fan surface, but with sedimentary architecture more typical of fluid flow (Scott et al., 1995; de Haas et al., 2014).

Soil Development

Soil morphology demonstrated in the Pioneer fan quarry can be broadly divided into two groups; strongly-developed soils and weakly-developed soils. Three buried soils, visually qualified by red (Bt) horizons atop white (Bk) horizons, exist within the exposure at the Pioneer quarry. From top to bottom they are labeled SDRZ, SDRU, and SDRL, respectively (Figure 3.10). These three buried soils exhibit red (~7.5YR6/3-5/4) Bt horizons within sand (Facies B1 and B2) above white (~10YR8/1-7/2) Bk horizons within gravel deposits (Facies assemblage A and Facies B3). The topmost buried soils (SDRZ) was not sampled due to inaccessibility, but visually reflect similar texture and color values for SDRU and SDRL, reported in Table 3.1.

Bk horizons of all three soils are characterized as Stage II development, meaning that within the gravely parent material (Facies assemblage A and Facies B3), clasts are coated by carbonate and the matrix has accumulated enough carbonate to display whitened appearance, yet remains loose (Gile et al, 1981; Machette, 1985). Soil structure of both SDRU and SDRL Bt horizons are similar—very coarse to coarse, subangular blocky peds. With depth, clay films in these two horizons become more apparent. SDRU Bt clay films are faint, few, and only on ped faces. In contrast, SDRL Bt clay films are common, distinct, and occur on ped faces and colloid coats on mineral grains. The Bt horizon of SDRL has a relatively greater clay content and an effervescent reaction to HCl while the Bt of SDRU has a relatively lower clay content and does not react to HCl.

Figure 3.11 shows a more detailed soil profile at sample site SDA within Facies B1. Soil SDA shows strong development with a minimum B horizon thickness of 163 cm. The SDA profile does not show a change in parent material, which is a thick very

fine to fine sand deposit. There is no A horizon present on this buried soil, most likely due to erosion. SDA soil characteristics are shown in Table 3.1.

Geochronology

Six sand beds were sampled for IRSL geochronological analysis. Ages range from 100±10.2 ka to 5.8±0.42 ka and follow the order of super position. Sample data used to calculate dose rate are reported in Table 3.2 and luminescence ages in Table 3.3. Ages reported follow the Minimum Age Model (MAM, Table 3.3). Stratigraphic context of each age, associated soil, and facies are illustrated in Figure 3.8. Each period of surface stability has an estimated maximum time of non-deposition, calculated from the time difference between each measured sample. Long-duration periods range from roughly 19 to 31 ky and short-duration periods range from roughly 7 to 14 ky (Figure 3.8).

Discussion

Periods of surface stability are interpreted through multiple lines of evidence. Sedimentary facies within the Pioneer fan quarry exposure that represent surface formation (Facies assemblage B) account for periods of non-primary deposition. When these facies, specifically Facies B1, coincide with soil development, duration of surface stability can be implied through comparison of the soil chronosequence. Paleo surfaces represented by reworked fan sediment are punctuated by periods of active primary deposition shown by debris-flow deposits (Facies assemblage A).

The interaction of these two types of processes within the Pioneer alluvial fan system produce deposits similar to those previously interpreted as braided river deposits

influenced by debris-flow (Miall, 1978). Miall (1978) framed the Trollheim alluvial fan deposits, described by Hooke (1967), as a type facies model for braided rivers. As pointed out by Blair and McPherson (1992), the facies exposed in the Trollheim alluvial fan reflect debris-flow deposits with a reworked top. Facies recorded by Hooke (1967) and reported by Miall (1978) for the Trollheim fan are strikingly similar to the facies of the Pioneer alluvial fan. However, rather than a braided stream system influenced by debris flow, the depositional system represented by the Pioneer fan supports the Trollheim fan interpretation by Blair and McPherson (1992); debris-flow dominated primary deposition with reworking of fan material by overland flow. This example highlights the importance of careful sedimentological analysis of debris-flow alluvial fan systems and what water-lain facies record in terms of fan-surface process dynamics (i.e. secondary modification versus fluvial processes).

From these recognized hiatuses of primary deposition, two separate scales of surface formation are interpreted from both development of soils and facies types with time-context through IRSL geochronology. Long-duration and short-duration periods of surface stability signify the dually varying dynamics of debris-flow alluvial fan deposition: lobe avulsion/switching and single-debris-flow-deposit recurrence. For example, evidence for long-duration surface stability can aid the interpretation of avulsion of the depositional lobe whereas short-duration surfaces stability may represent debris-flow variability on the deposition lobe.

Long-Duration Surface Stability (Abandoned Lobe)

Layers with sedimentary facies indicative of surface modification (Facies Assemblage B) in conjunction with strong soil development are interpreted as long-duration stages of surface stability. Long-duration phases void of primary deposition (debris-flow) can represent periods where the depositional lobe is occupying an adjacent area of the alluvial fan due to vertical autogenic dynamics, occurring at time scales on the order of tens of debris-flow events (Ventra and Nichols, 2013; de Haas et al., 2018). This temporal extent of surface stability before subsequent burial permits pedogenic and secondary sediment transport processes to modify the surface to the developmental stage observed in the quarry.

In this case, a single chronostratigraphic package that includes facies that represent surface stability (Assemblage B) and soil development, represents a cycle of deposition across a large-scale compensational unit (entire fan complex) comprised of small-scale compensational units (depositional lobe), which is made up of a series of compensational beds (debris-flows) (Straub et al., 2009; Straub and Pyles, 2012; Hajek and Straub, 2017). Assuming a single chronostratigraphic package represents one full compensational scale, then long-duration surface stability indicators are key in understanding the autogenic dynamics of topographic compensational stacking. An impediment to this simplistic interpretation, however, is the path of the depositional loci on the fan during one cycle of compensation. Even still, greater understanding of compensational organization of debris-flow alluvial fan sedimentation will lead to clearer interpretations of allogenic signals that may or may not be recorded in the sedimentary

record (Swanson-Hysell and Barbeau, 2007; Straub et al., 2009; Wang, et al., 2011; Straub and Pyles, 2012; Tipper, 2014; Trampush and Hajek, 2017; Hajek and Straub; 2017)

Short-Duration Surface Stability (Depositional Lobe)

Conversely, sedimentary facies indicative of surface modification paired with week to moderately developed soils are interpreted as short-duration stages of surfaces stability. We interpret these periods to represent quiescence in active deposition while the surface continues to occupy the loci of active deposition. Hiatuses in deposition in this case are due to both the recurrence interval of debris flow and/or the deposit extent in reference to the active surface.

Short-duration periods of surface stability are similar to long-duration periods of surface stability in concept yet represent one fractal step lower in the compensational processes (Straub and Pyles, 2012). Debris-flow alluvial fans are fractal, scale-invariant compensational systems, but these fractal scales yield separate processes. The scale at which short-duration periods of surface stability occur represent lulls due to lateral autogenic dynamics involving the specific depositional pathways for a single flow (i.e. debris-flow) and flow recurrence periods (Ventra and Nichols, 2014; de Haas et al., 2018). In these cases, pedogenic and secondary sediment transport processes have only the time interval between debris-flow events and their spatial extent to modify the surface.

Chronology

Geomorphic variation of alluvial fan surfaces along with the eolian deposits within alluvial fan coarse-grain strata have often been attributed to climatic shifts (Machette, 1978; McFadden et al., 1986; Reheis et al., 1995; Ballantyne, 2002; Muhs et al., 2003; Sheppard et al., 2018). Within the conceptual framework of climate-driven fan dynamics, avulsion of the loci of alluvial deposition and mobilization of fine-grained sediments by wind, are controlled by climate changes (Clarke, 1994; Lancaster, 1996).

Two periods of short-duration surface stability followed by three periods of long-duration surface stability are captured in the Pioneer fan quarry buried by the modern surface (Figures 3.8 and 3.10). In context of global climatic stades, the chronology obtained within Facies assemblage B—which represent periods of surface stability, eolian deposition, and potentially depositional lobe avulsion events—are not correlated to any particular pattern (i.e. colder periods, warmer periods, or transitional periods) (Railback, 2015). This implies that alluvial fan geomorphic and sedimentologic records are complex beyond attribution to a singular control (e.g. climate) and are influenced by a myriad of external and internal factors.

Conclusion

Periods of surface stability and surface formation are evident within the stratigraphic succession of alluvial fan deposits through specific sedimentary facies and pedogenic characteristics. Stratigraphic facies of secondary sediment transport processes that modify the surface during periods of non-primary deposition are recorded in the alluvia fan deposits. Facies assemblage B represents these modifying processes, where

B2 and B3 display sedimentary structures indicative of overland flow represented by horizontally and low-angle laminated sand, rippled sand, and horizonal, low-angle bedded, and massive gravels. Eolian input is represented as a dominant process during periods of surface stability, evident in Facies B1 by massive sand and shown as reworked by water in Facies B2 by horizontally and low-angle laminated sand, and rippled sand.

The intensity of soil formation within the chronosequence recorded in the Pioneer quarry exposure corelates to duration of surface stability and therefore specific autogenic dynamics controlling periods of non-deposition on a given surface. Two periods of short-duration surface stability followed by three periods of long-duration surface stability are captured in the Pioneer fan quarry in Facies assemblage B (Figure 3.8). Stratigraphic and pedogenic analysis and the contextualization of these two methods with geochronology show that poor soil formation represents relatively short quiescence in primary deposition on the depositional lobe and strong soil development reflects switching of active depositional lobe elsewhere, allowing prolonged exposure of the newly-formed abandoned lobe, consistent with the autogenic dynamics of alluvial fans. Furthermore, reworking of surface materials by water, addition of wind-blown sediment, and pedogenesis are important processes on all surfaces of alluvial fans, both on the depositional and abandoned lobes.

Literature Cited

Aschoff, J. L., and Schmitt, J. G., 2008, Distinguishing syntectonic unconformity types to enhance analysis of growth strata: an example from the Cretaceous, southeastern Nevada, USA: Journal of Sedimentary Research, v. 78, p. 608-623.

Ballantyne, C. K., 2002, Paraglacial geomorphology: Quaternary Science Reviews, v. 21, p. 1935-2017.

Berry, M. E., 1987, Morphological and chemical characteristics of soil catenas on Pinedale and Bull Lake moraine slopes in the Salmon River Mountains, Idaho: Quaternary Research, v. 28, p. 210-225.

Birkeland, P. W., 1984, Holocene soil chronofunctions, Southern Alps, New Zealand: Geoderma, v. 34, p. 115-134.

Birkeland, P. W. and Burke, R. M., 1988, Soil catena chronosequences on eastern Sierra Nevada moraines, California, USA: Arctic and Alpine Research, v. 20, p. 473-484.

Birkeland, P. W., 1999, Soils and geomorphology, third edition. Oxford University Press.

Blair, T. C. and McPherson, J., 1992, The Trollheim alluvial fan and facies model revisited. Geological Society of America Bulliten, v. 104, p. 762-769.

Blair, T.C., and McPherson, J. G., 1994, Alluvial fan processes and forms, *in* Parsons, A.J., and Abrahams, A.D., eds., Geomorphology of desert environments: London, Chapman & Hall, p. 354-402.

Blair, T.C., and McPherson, J. G., 2009, Alluvial fan processes and forms, *in* Parsons, A.J., and Abrahams, A.D., eds., Geomorphology of desert environments, 2nd Edition: Berlin, Springer, p. 413-467.

Bockheim, J. G., 1980, Solution and use of chronofunctions in studying soil development: Geoderma, v. 24, p. 71-85.

Bull, W. B., 1977, The alluvial fan environment, Bull, W. B: Progress in Physical Geography: Earth and Environment, p. 222–270.

Clarke, M. L., 1994, Infra-red stimulated luminescence ages from aeolian sand and alluvial fan deposits from the eastern Mojave Desert, California. Quaternary Science Reviews, v. 13, p. 533-538.

Costa, J. E., 1988, Rheologic, geomorphic, and sedimentologic differentiation of water floods, hyperconcentrated flows, and debris flows: Flood Geomorphology, p. 113-122.

de Haas, T., Ventra, D., Carbonneau, P. E., and Kleinhans, M. G., 2014, Debris-flow dominance of alluvial fans masked by runoff reworking and weathering: Geomorphology, v. 217, p. 165-181.

de Haas, T., Densmore, A. L., Stoffel, M., Suwa, H., Imaizumi, F., Ballesteros-Cánovas, J. A., and Wasklewicz, T., 2018, Avulsions and the spatio-temporal evolution of debris-flow fans: Earth-Science Reviews, v. 177, p. 53-75.

Demko, T. M., Currie, B. S., and Nicoll, K. A., 2004, Regional paleoclimatic and stratigraphic implications of paleosols and fluvial/overbank architecture in the Morrison Formation (Upper Jurassic), Western Interior, USA: Sedimentary Geology, v. 167, p. 115-135.

Durcan, J. A., King, G. E., and Duller, G. A. T., 2015, DRAC: Dose rate and age calculator for trapped charge dating: Quaternary Geochronology, v. 28, p. 54-61.

Frankel, K. L., and Dolan, J. F., 2007, Characterizing arid region alluvial fan surface roughness with airborne laser swath mapping digital topographic data. Journal of Geophysical Research: Earth Surface, v. 112(F2).

Gile, L. H., 1981, Soils and geomorphology in the Basin and Range area of southern New Mexico: Guidebook to the Desert Project, New Mexico: Bureau of Mines and Mineral Resources Memoir v. 39, 222 p.

Hajek, E. A., and Straub, K. M., 2017, Autogenic sedimentation in clastic stratigraphy: Annual Review of Earth and Planetary Sciences, v. 45, p. 681-709.

Harden, J. W., 1990, Soil development on stable landforms and implications for landscape studies: Geomorphology, v. 3, p. 391-398.

Hooke, R. L., 1967, Processes on arid-region alluvial fans: The Journal of Geology, v. 75, p. 438-460.

Hsu, L. and Pelletier, J. D., 2004, Correlation and dating of Quaternary alluvial-fan surfaces using scarp diffusion: Geomorphology v. 60, p. 319-335.

Iverson, R. M., 1997, The physics of debris flows: Reviews of Geophysics v. 35, p. 245-296.

Jenny, H., 1941, factors of soil formation. McGraw-Hill, New York, 281 p.

Jenny, H. 1980, The soil resource —origin and behavior, Springer-Verlag, New York, 377 p.

Jerolmack, D. J., and Paola, C., 2010, Shredding of environmental signals by sediment transport: Geophysical Research Letters, v. 37, doi:10.1029/2010GL044638.

Johnstone, S. A., Hudson, A. M., Nicovich, S., Ruleman, C. A., Sare, R. M., and Thompson, R. A., 2018, Establishing chronologies for alluvial-fan sequences with analysis of high-resolution topographic data: San Luis Valley, Colorado, USA: Geosphere, v. 14, p. 2487-2504.

Kraus, M. J., 1999, Paleosols in clastic sedimentary rocks: their geologic applications: Earth-Science Reviews, v. 47, p. 41-70.

Lancaster, N., 1996, Response of eolian geomorphic systems to minor climate change: examples from the southern California deserts: Geomorphology, v. 19, p. 333-347.

Machette, Michael N., 1978, Dating Quaternary faults in the southwestern United States by using buried calcific paleosols: Journal of Research of the United States Geological Survey, v. 6, p. 369-382.

Machette, M. N., 1985, Calcific soils of the southwestern United States. Soils and Quaternary geology of the southwestern United States: Geological Society of America Special Paper, v. 203, p. 1-21.

Markewich, H. W., Pavich, M. J., and Wysocki, D. A., 2016, Soils as Relative-Age Dating Tools. International Encyclopedia of Geography: People, the Earth, Environment and Technology: People, the Earth, Environment and Technology, p. 1-14.

Matmon, A., Nichols, K., and Finkel, R., 2006, Isotopic insights into smoothening of abandoned fan surfaces, Southern California: Quaternary Research, v. 66, p. 109-118.

McCalpin, J.P., 1982, Quaternary geology and neotectonics of the west flank of the northern Sangre de Cristo Mountains, south-central Colorado: Colorado School of Mines Quarterly, n. 77, p. 97.

McFadden, L. D., Wells, S. G., and Dohrenwend, J. C., 1986, Influences of Quaternary climatic changes on processes of soil development on desert loess deposits of the Cima volcanic field, California: Catena, v. 13, p. 361-389.

McFadden, L.D., Wells, S.G., and Jercinovich, M.J., 1987, Influences of eolian and pedogenic processes on the origin and evolution of desert pavements: Geology, v. 15, p. 504-508.

McFadden, L. D., Ritter, J. B., and Wells, S. G., 1989, Use of multiparameter relative-age methods for age estimation and correlation of alluvial fan surfaces on a desert piedmont, eastern Mojave Desert, California: Quaternary Research, v. 32, p. 276-290.

Miall, A. D., 1978, Lithofacies and vertical profile models in braided river deposits: a summary: Geological Survey of Canada, p. 597-604.

Muhs, D. R., Bettis, E. A., Chan, M. A., and Archer, A. W., 2003, Quaternary loess-paleosol sequences as examples of climate-driven sedimentary extremes: Geological Society of America Special Paper 370, p. 53-74.

Pierce, K.L., 2003, Pleistocene glaciation of the Rocky Mountains, in Gillespie, A.R., Porter, S.C., and Atwater, B.F., eds., The Quaternary Period in the United States: Amsterdam, Elsevier, p. 63–76.Quigley, M.C., Sandiford, M., and Cupper, M.L., 2007, Distinguishing tectonic from climatic controls on range-front sedimentation: Basin Research, v. 19, p. 491-505.

Pye, K., 1996, Nature, origin, and accumulation of loess: Quaternary Science Reviews, v. 15, p. 653-667.

Railback, B.L., Gibbard, P.L., Head, M.J., Voarintsoa, N.R.G., Toucanne, S., 2015, An optimized scheme of lettered marine isotope substages for the last 1.0 million years, and the climatostratigraphic nature of isotope stages and substages: Quaternary Science Reviews, v. 111, p. 94-106.

Reheis, M. C., Goodmacher, J. C., Harden, J. W., McFadden, L. D., Rockwell, T. K., Shroba, R. R., Sowers, J. M., and Taylor, E. M., 1995, Quaternary soils and dust deposition in southern Nevada and California. Geological Society of America Bulletin, v. 107, p. 1003-1022.

Riba, O., 1976, Syntectonic unconformities of the Alto Cardener, Spanish Pyrenees: a genetic interpretation: Sedimentary Geology, v. 15, p. 213-233.

Ritter, J. B., Miller, J. R., Enzel, Y., Howes, S. D., Nadon, G., Grubb, M. D., and Summa, C. L., 1993, Quaternary evolution of Cedar Creek alluvial fan, Montana: Geomorphology, v. 8, p. 287-304.

Ruleman, C.A., and Machette, M.N, 2007, An overview of the Sangre de Cristo fault system and new insights to interactions between Quaternary faults in the Northern Rio Grande Rift: *in* Machette, M.N., Coates, M.M., and Johnson, M.L., eds., 2007 Rocky Mountain Section Friends of the Pleistocene Field Trip—Quaternary geology of the San Luis Basin of Colorado and New Mexico, September 7-9, 2007: U.S. Geological Survey Open-File Report 2007-1193, p. 187-197.

Scott, K. M., Vallance, J. W., and Pringle, P. T., 1995, Sedimentology, behavior, and hazards of debris flows at Mount Rainier, Washington: US Geological Survey Open-File Report, n. 1547, 106 p.

Shepard, C., Pelletier, J. D., Schaap, M. G., and Rasmussen, C., 2018, Signatures of obliquity and eccentricity in soil chronosequences: Geophysical Research Letters, v. 45, p. 11-147.

Sohn, Y. K., Rhee, C. W., and Kim, B. C., 1999, Debris flow and hyperconcentrated flood-flow deposits in an alluvial fan, northwestern part of the Cretaceous Yongdong Basin, Central Korea: The Journal of Geology, v. 107, p. 111-132.

Straub, K. M., and Pyles, D. R., 2012, Quantifying the hierarchical organization of compensation in submarine fans using surface statistics: Journal of Sedimentary Research, v.82, p. 889-898.

Suppe, J., Sàbat, F., Munoz, J. A., Poblet, J., Roca, E., and Vergés, J., 1997, Bed-by-bed fold growth by kink-band migration: Sant Llorenç de Morunys, eastern Pyrenees: Journal of Structural Geology, v. 19, p. 443-461.

Swanson-Hysell, N., and Barbeau, D. L. Jr., 2007, The diachroneity of alluvial-fan lithostratigraphy? A test case from southeastern Ebro basin magnetostratigraphy: Earth and Planetary Science Letters, v. 262, p. 343-362.

Tipper, J. C., 2014, The importance of doing nothing: stasis in sedimentation systems and its stratigraphic effects: Geological Society of London, Special Publications, v. 404, doi:10.1144/SP404.6

Trampush, S. M. and Hajek, E. A., 2017, Preserving proxy records in dynamic landscapes: Modeling and examples from the Paleocene-Eocene Thermal Maximum: Geology, v. 45, p. 967-970.

Ventra, D., and Nichols, G. J., 2014, Autogenic dynamics of alluvial fans in endorheic basins: outcrop examples and stratigraphic significance: Sedimentology, v. 61, p. 767-791.

Vreeken, W.J., 1975, Principal kinds of chronosequences and their significance in soil history: Journal of Soul Science, v. 26, p. 378-394

Wang, Y., Straub, K. M., and Hajek, E. A., 2011, Scale-dependent compensational stacking: an estimate of autogenic time scales in channelized sedimentary deposits: Geology, v. 39, p. 811-814.

Wells, S.G., McFadden, L.D., and Dohrenwend, J.C., 1987, Influence of late Quaternary climatic changes on geomorphic and pedogenic processes on a desert piedmont, eastern Mojave Desert, California: Quaternary Research, v. 27, p. 130-146.

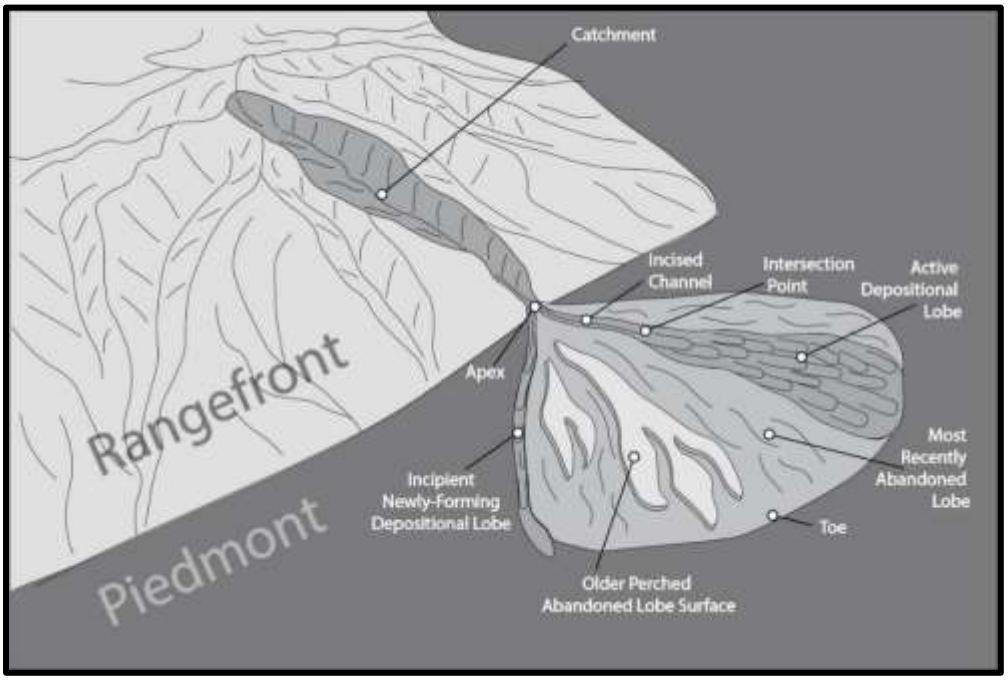

Figure 3.1. Schematic for generic architecture of fan surfaces due to autogenic fan-lobe switching. Primary processes are dominant on the active depositional lobe, while older surfaces are subject to secondary modification.

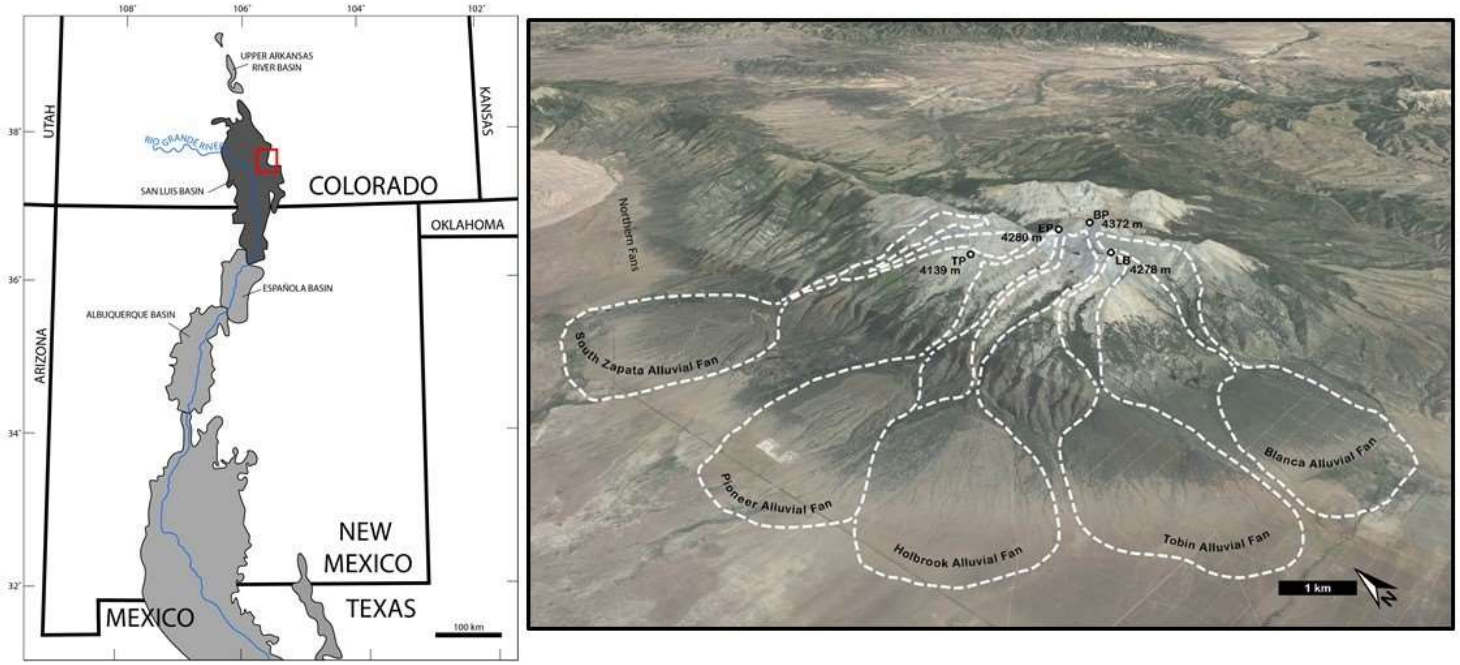

Figure 3.2. Left—Location of the San Luis Basin (dark grey) within Rio Grande Rift. Location of Blanca Peak Massif and approximate area of image to right is within red box. Adapted from Grauch and Hundson, 2013. Right- Oblique Google Earth image of Blanca Peak Massif outlining glacially-influenced catchments and the alluvial fans emanating from them. Note the quarry on the distal extent of the Pioneer alluvial fan.

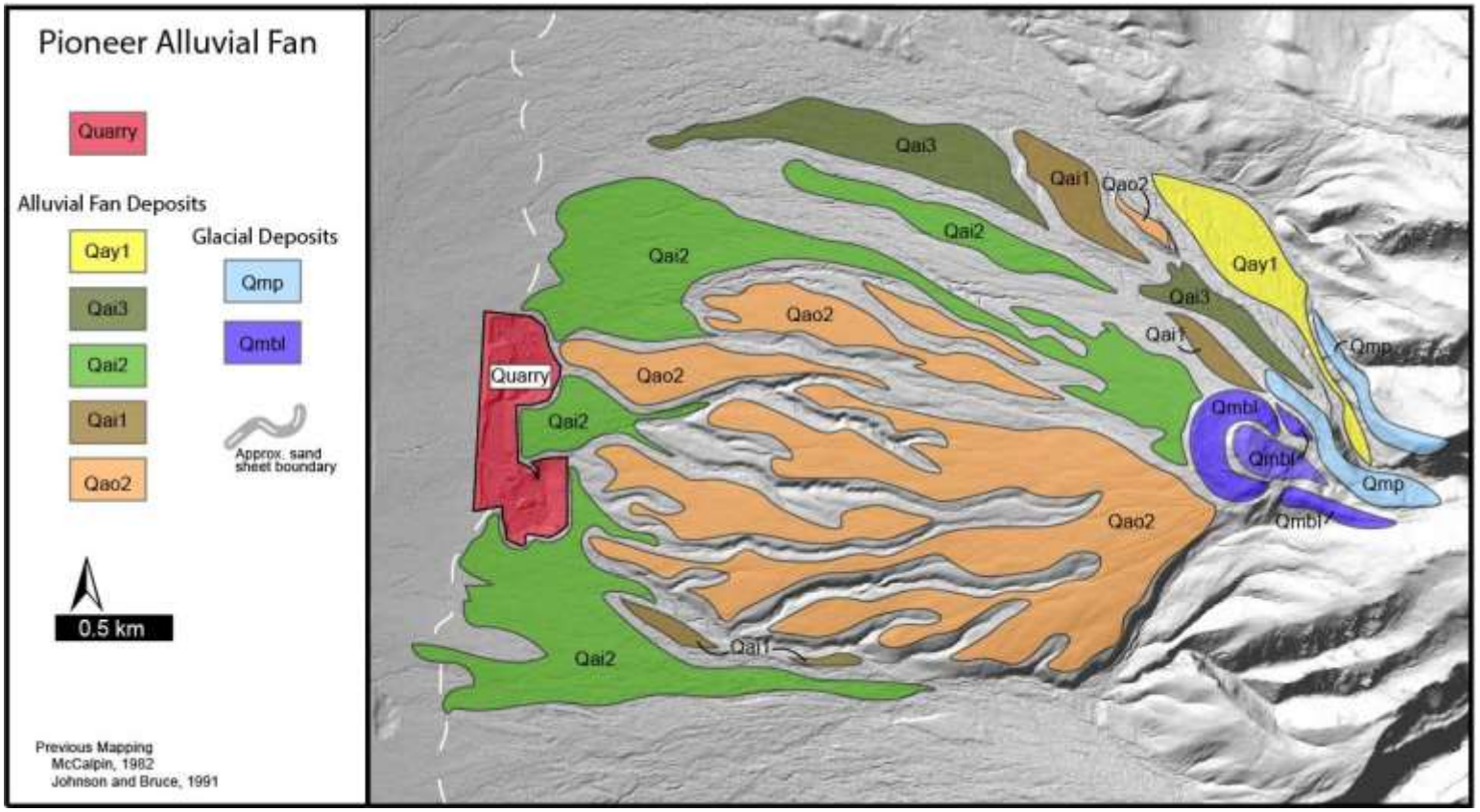

Figure 3.3. Surficial map of the Pioneer alluvial fan on 1-meter digital elevation model.

Figure 3.4. Deposit morphologies of primary and secondary processes that occur on debris flow alluvial fans. A) Debris flow in distal reaches of alluvial fan that exhibits terminal and lateral lobes, human for scale. B) Rough topography showing fresh debris flow levees in proximal reach of alluvial fan. C) Diffused debris-flow lobe morphology. D) Sand, pebble-sized gravel, and flotsam moved by overland-flow. E) Pebble-sized gravel sheet mobilized by overland flow. F) Channel incision, white arrows show fan surface. G) Tree trunks buried by wind-blown silt and fine sand.

Figure 3.5. Eastern view of the Pioneer alluvial fan showing location of gravel quarry.

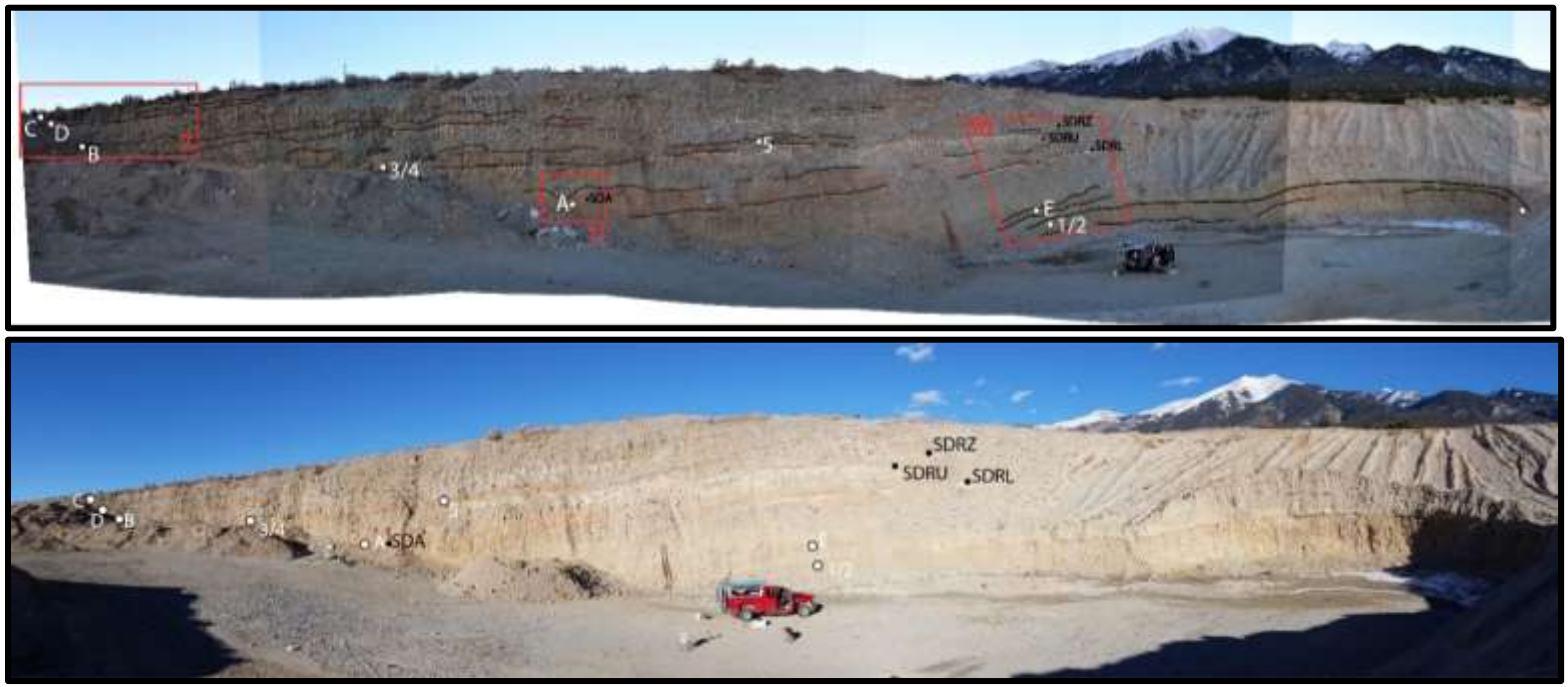

Figure 3.6. Panoramic view to the north of quarry exposure. Upper photo highlights sand beds and shows locations of Figures 3.7(7), 3.10(10), and 3.11(11) in red boxes (west to east, respectively). Lower highlights buried soils. Soil desctiption locations SDA, SDRL, SRDU, and SDRZ are denoted by black dots and black text and IRSL samples 1-5 and A-E by shown by white dots and white text.

Figure 3.7. Locations of accessible IRSL samples C, D, and B.

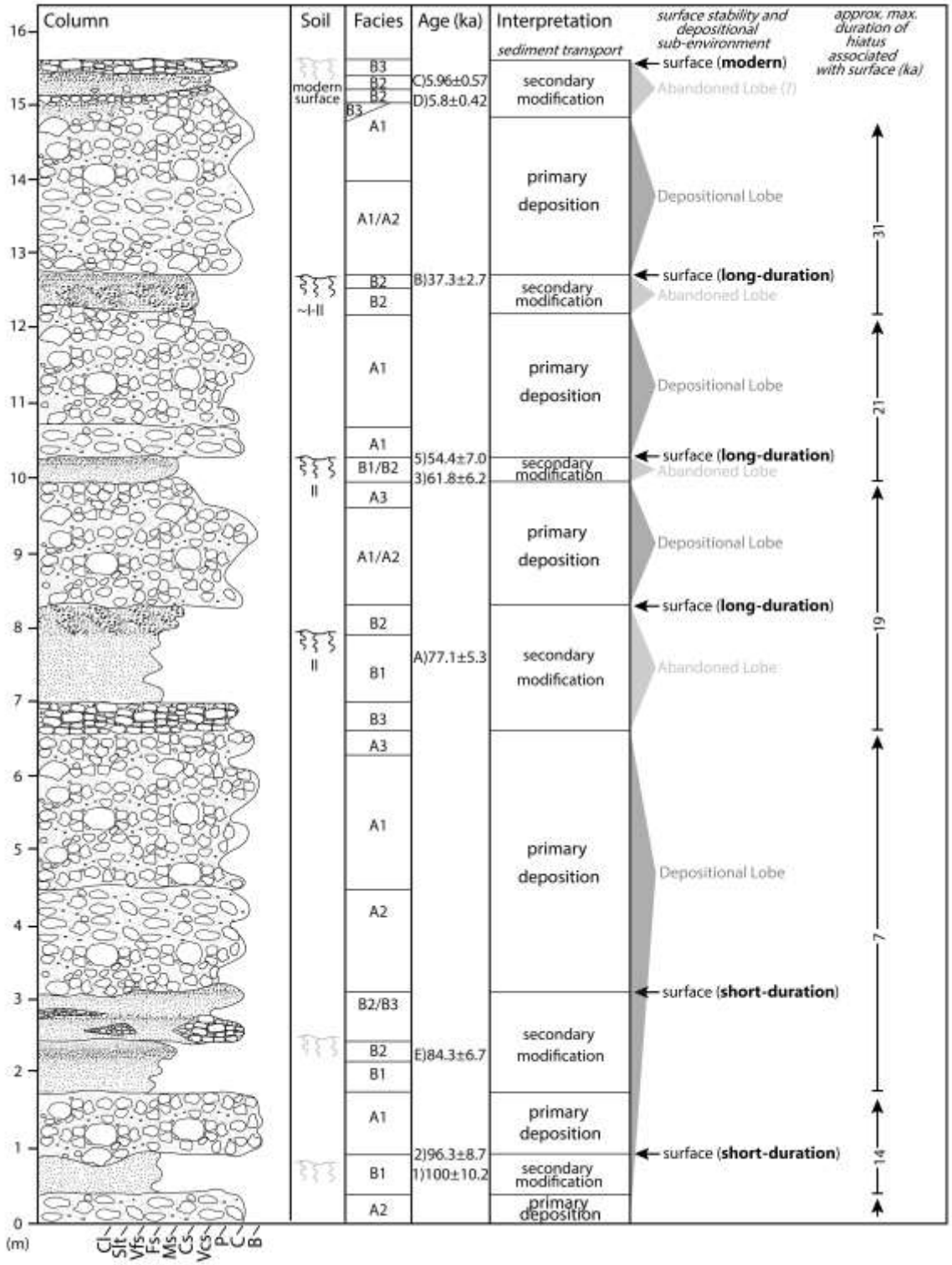
Column
Soil
Facies
Age (ka)
Interpretation
sediment transport
surface stability and depositional sub-environment
approx. max. duration of hiatus associated with surface (ka)
modern surface
~I-II
II
II
B3
B2
B2
B3
A1
A1/A2
B2
B2
A1
A1
B1/B2
A3
A1/A2
B2
B1
B3
A3
A1
A2
B2/B3
B2
B1
A1
B1
A2
C)5.96±0.57
D)5.8±0.42
B)37.3±2.7
5)54.4±7.0
3)61.8±6.2
A)77.1±5.3
E)84.3±6.7
2)96.3±8.7
1)100±10.2
secondary modification
primary deposition
secondary modification
primary deposition
secondary modification
primary deposition
secondary modification
primary deposition
secondary modification
primary deposition
surface (modern)
Abandoned Lobe (?)
Depositional Lobe
surface (long-duration)
Abandoned Lobe
Depositional Lobe
surface (long-duration)
Abandoned Lobe
Depositional Lobe
surface (long-duration)
Abandoned Lobe
Depositional Lobe
surface (short-duration)
surface (short-duration)
31
21
19
7
14
16
15
14
13
12
11
10
9
8
7
6
5
4
3
2
1
0
(m)
Cl
Slt
VFs
Fs
Ms
Cs
VCs
P
C
B

Figure 3.8. Generalized stratigraphic column of quarry exposure showing relation of facies, soil development, and IRSL geochronology samples. Height is in meters and horizontal axis shows grain size; Cl–clay, Slt–silt, Vfs–very-fine sand, Fs–fine sand, Ms–medium sand, Cs–coarse sand, Vcs–very-coarse sand, P–pebbles, C–cobbles, B–boulders. Interpretation includes catagorized sediment transport within the dichotomy of primary deposition versus secondary modification. The relative duration of surface stability and interpreted depositional sub-environment (i.e. depositional vs. abandoned lobe) are shown with the duration of time inbetween each interpreted period of surface stability (ka).

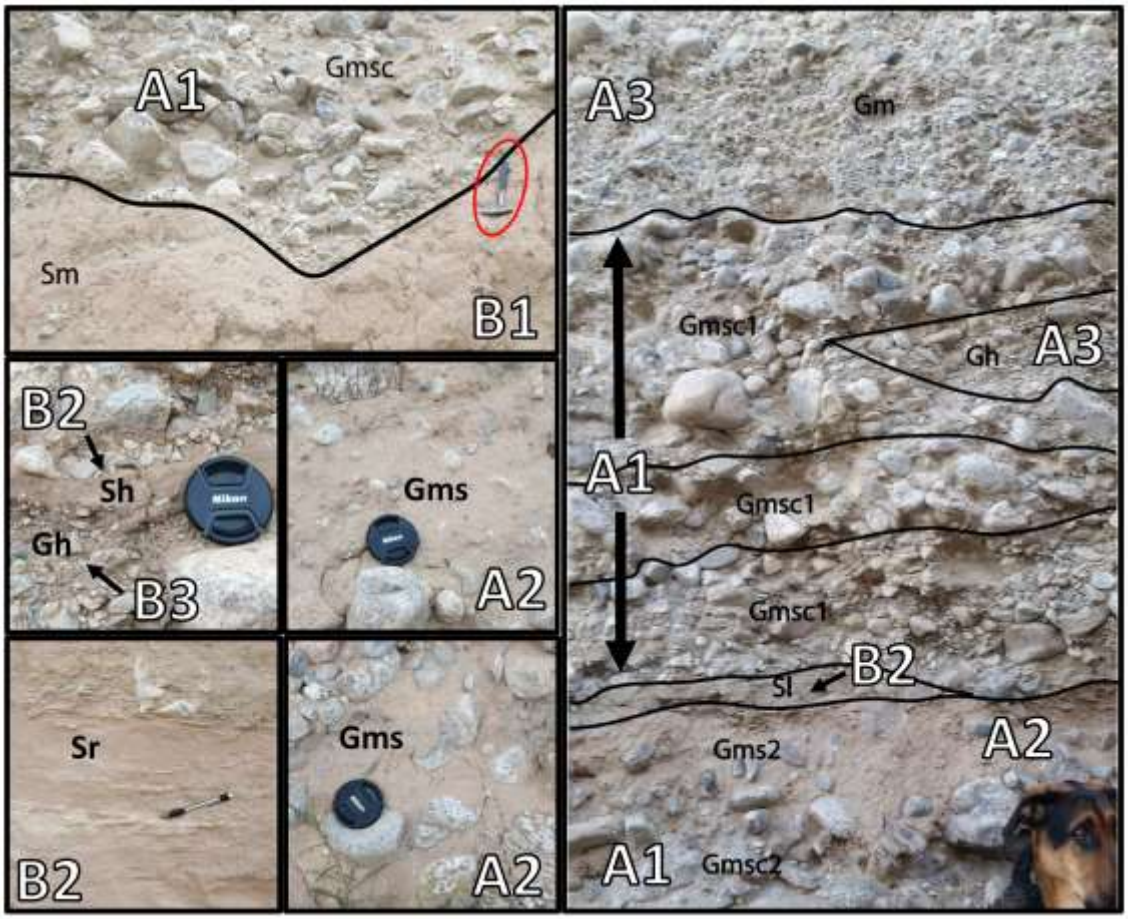

Figure 3.9. Facies that compose facies assemblages A and B. Gravel facies—Gmsc: gravel, matrix- to clast-supported, Gms: gravel, matrix-supported, Gh: gravel, horizontal, Gm: gravel, massive. Sand facies—Sh: sand, horizontal, Sl: sand, low-angle laminated, Sr: sand, ripple cross-laminated, Sm: sand, massive. Matrix—1: medium-grained sand to granule-sized matrix, 2: silt to very fine-grained sandy matrix, 3: silt to granule-sized matrix (mix of 1 and 2).

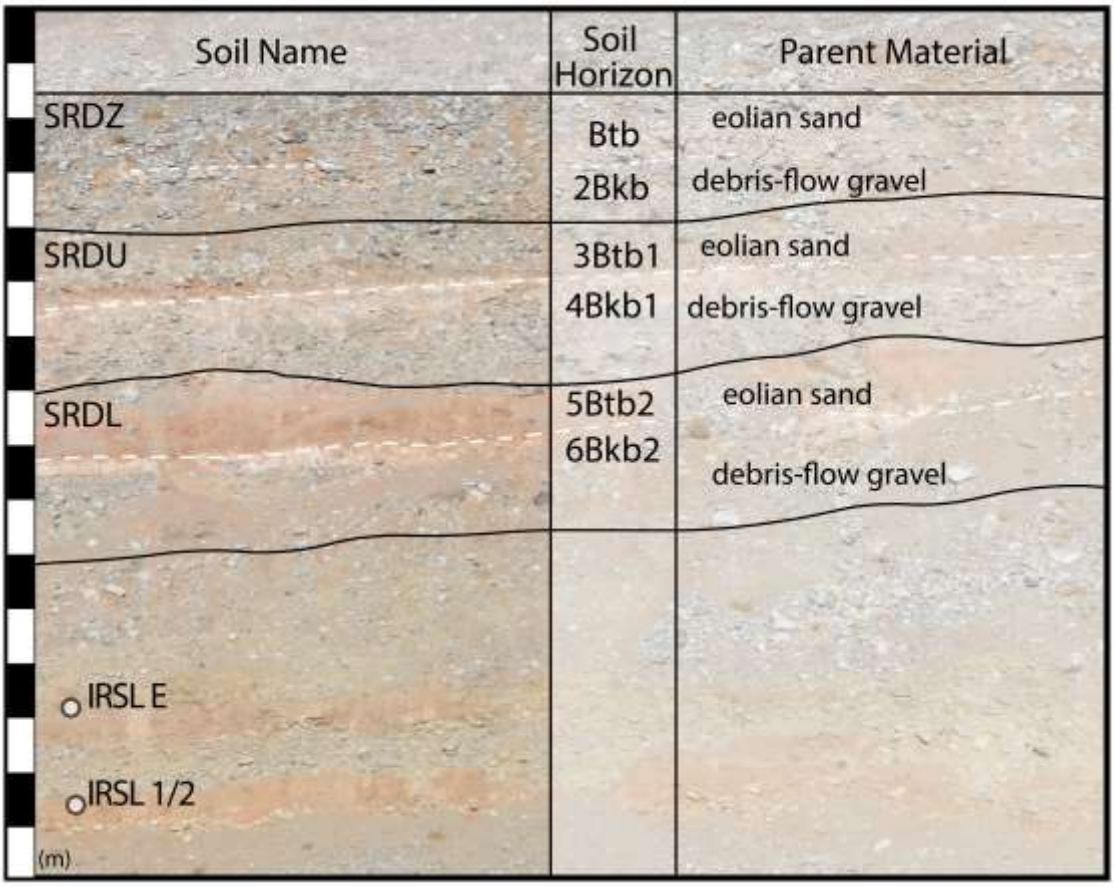

Figure 3.10. Three buried strongly-developed soils packages composed of Bt and Bk pairs. White dotted line denotes boundaries of each Bt/Bk pair within same soil. Location is shown in Figure 3.6.

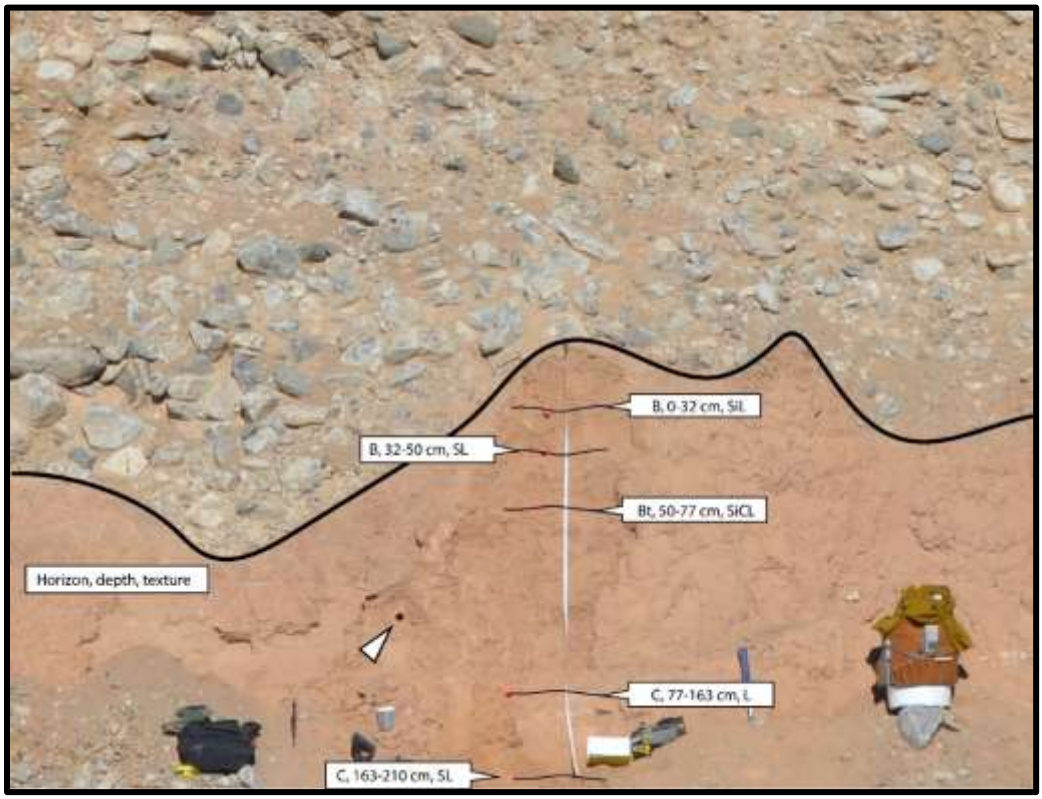

Figure 3.11. Soil SDA. Labels are at each horizon and represent horizon notation, depth, and soil texture. Location is shown in Figure 3.6.

Table 3.1 Soil Properties

Soil	horizon	depth (cm)	bouldaries	structure	clay films	consistence	texture	gravel %	CaCO3	Color	notes
SDA											
	B	0-32	c,s	1, m, abk	x	ss, ps, sh	vf SiL	trace	x	7.5YR4/3M, 7.5YR5/3D	
	B	32-50	c,s	m-1, c, abk-sbk	x	ss, ps, so	vf-f SL	trace	x	7.5YR4/3M, 7.5YR6/4D	similar texture to 0-32, but can feel sand grains
	Bt	50-77	c,s	1, c, sbk	x	ss-s, ps, sh	SiCL	trace	x	7.5YR5/3M, 7.5YR6/4D	
	C	77-163	c,s	2-3, vc, abk	x	so-ss, po-ps, sh-h	vf-f L	trace	x	7.5YR4/3M, 7.5YR6/4D	
	C	163-210	a,w	m	x	so, po, so	vf-f SL	trace	x	10YR5/4M, 10YR6/4D	Iron staining
SDRU*											
	Bt	0-50	x	vc, sbk	1, f, pf	ss, ps, sh-h	L	25	no rxn	7.5YR5/3W, 7.5YR5/4D	
	Bk	50-100	x	x	x	so, po, x	LS	75	es, ll	10YR6/2W, 10YR7/2D	
SDRL*											
	Bt	0-40	x	c, sbk	2, d, pf, co	ss, po, so	vf-c L	25	e	7.5YR4/3M, 7.4YR6/3D	some carbonate filiments
	Bk	40-60	x	x	x	so, po, x	LS	50	ev, ll	10YR6/2W, 10YR8/1D	

* profile depths measured from top of soil profile, not ground surface

Table 3.2 Sample data used to calculate dose rates

Lab Code	Eleveation (m)	Depth (m)	Water Content[a]	K[b] (%)	U[b] (ppm)	Th[b] (ppm)	D_R[c] (Gray/ka)
SRN-C-IRSL	2362	0.25	1 (30) [5]	2.08 ± 0.04	2.04 ± 0.227	6.34 ± 0.34	2.95 ± 0.08
SRN-D-IRSL	2362	1	2 (30) [5]	2.31 ± 0.04	2.92 ± 0.23	8.07 ± 0.355	3.92 ± 0.09
SRN-B-IRSL	2362	3	2 (32) [5]	2.77 ± 0.04	2.69 ± 0.233	8.92 ± 0.37	4.37 ± 0.1
SRN-05-IRSL	2366	5	0 (31) [5]	1.87 ± 0.03	2.44 ± 0.15	7.08 ± 0.21	3.43 ± 0.2
SRN-03-IRSL	2362	6.1	0 (25) [4]	1.73 ± 0.05	1.97 ± 0.227	5.75 ± 0.33	3.12 ± 0.2
SRN-A-IRSL	2362	8	12 (50) [6]	2.34 ± 0.05	2.94 ± 0.227	9.06 ± 0.44	3.98 ± 0.1
SRN-E-IRSL	2362	13	7 (37) [5]	2.70 ± 0.09	2.23 ± 0.165	8.03 ± 0.845	4.12 ± 0.1
SRN-01-IRSL	2360	15.5	1 (37) [5]	1.97 ± 0.1	2.02 ± 0.317	6.21 ± 0.41	3.36 ± 0.3
SRN-02-IRSL	2360	15.5	4 (39) [6]	2.72 ± 0.07	2.46 ± 0.207	8.12 ± 0.475	4.27 ± 0.3

[a]Percent water content of field sample used for age calculation, number in parentheses represents the saturated water content, square brackets shows modeled water content (Nelson and Rittenour, 2015).

[b]Method used to determine elemental concentrations given in Table 3.

[c]Calculated using the Dose Rate Age Calculator (Durcan et al., 2015).

Table 3.3. Sample data used to calculate luminescence ages

Lab Code	n[a]	CAM Over-dispersion[b]	CAM D_e[c] (Gray)	MAM D_e[c] (Gray)	CAM Age[c] (Gray)	MAM Age[c] (Gray)
SRN-C-IRSL	18 (25)	28	23.6 ± 1.6	17.6 ± 1.6	8 ± 0.6	**5.96 ± 0.6**
SRN-D-IRSL	23 (33)	22	26 ± 1.3	22.7 ± 1.6	6.62 ± 0.4	**5.8 ± 0.4**
SRN-B-IRSL	14 (20)	17	192 ± 8.8	163 ± 11.4	44 ± 2.2	**37.3 ± 2.7**
SRN-05-IRSL	5 (10)	9	193 ± 11.1	187 ± 20	56.2 ± 5.2	**54.4 ± 7**
SRN-03-IRSL	10 (10)	7	193 ± 5.9	193 ± 11.4	61.8 ± 5.3	**61.8 ± 6.2**
SRN-A-IRSL	14 (21)	14	357 ± 13.5	307 ± 19.9	89.8 ± 4	**77.1 ± 5.3**
SRN-E-IRSL	8 (8)	17	392 ± 23.3	347 ± 26.2	95.2 ± 6.2	**84.3 ± 6.7**
SRN-01-IRSL	15 (15)	14	369 ± 14.4	338 ± 22.3	110 ± 9.6	**100 ± 10.2**
SRN-02-IRSL	13 (15)	12	443 ± 16.6	411 ± 27.1	104 ± 7.5	**96.3 ± 8.7**

[a]number of aliquots meeting acceptance criteria, parentheses indicate total number of aliquots measured

[b]Defined as the statistical dispersion beyond what would be expected for a perfectly bleached sample.

[c]Determined using the function calc CentralDose from the R-Luminescence package. Uncertainty is 2 σ.

[d]Determined using the function calc MinDose from the R-Luminescence package. Uncertainty is 2 σ.

CHAPTER FOUR

IMPACT OF WIND-BLOWN SEDIMENT ON THE PIONEER DEBRIS-FLOW ALLUVIAL FAN, SOUTH-CENTRAL COLORADO: CONCEPTS OF FAN ACTIVITY

Contribution of Authors and Co-Authors

Manuscript in Chapter 4

Author: Sylvia Nicovich

Contributions: Conceived the study, performed the analyses, interpreted results, and wrote the manuscript.

Co-Author: James Schmitt

Contributions: Conceived the study, assisted the analysis, discussed results and implications, and edited earlier manuscripts.

Manuscript Information

Sylvia Nicovich, Jim Schmitt

Geosphere

Status of Manuscript:
_X_ Prepared for submission to a peer-reviewed journal
____ Officially submitted to a peer-reviewed journal
____ Accepted by a peer-reviewed journal
____ Published in a peer-reviewed journal

Abstract

Debris flow alluvial fans comprise suites of depositional lobes characterized by rough, *active* surfaces and abandoned lobes characterized by smooth, *inactive* surfaces. Activity is generally defined by the most recent locus of sediment derived from a common drainage basin, while surfaces are deemed abandoned and inactive once removed from the drainage basin-sourced sediment. Used commonly to describe primary sedimentary processes, this dichotomy between active and inactive surfaces neglects to recognize sedimentation sourced beyond the catchment. Wind-blown sediment is ubiquitous atop alluvial fan surfaces regardless of primary depositional activity, and is commonly sourced from the fan itself and an adjacent playa basin. Impact of eolian material is frequently unaddressed when considering working processes on alluvial fan surfaces. This case study of the Pioneer alluvial fan within the San Luis Valley of southern Colorado reports the role of wind-blown sediment on alluvial fan surfaces and stratigraphy while revisiting the concept of activity on fan surfaces, complications of provenance analysis, and climatic interpretations. Analysis of surface geomorphology, facies assemblages, and particle size distributions of matrix from various facies of exposed alluvial fan deposits suggest that wind-blown material plays a significant part in the sedimentary processes that operate on alluvial fan surfaces. These data may require a conceptual reevaluation of how surfaces are classified as active and inactive independent from connectivity to drainage basin sedimentation.

Introduction

Debris-flow alluvial fans are commonly used as geomorphic indicators of tectonic and climatic activity both by their stratigraphic features in the rock record and their geomorphic surface expression (Ritter et al., 1995; Dühnforth, 2007). The landform's fan shape develops through progressive switching of depositional activity across its areal extent through time (Figure 4.1) (Hooke, 1967; Ritter et al., 1995; Blair and McPherson, 2009). Primary processes (i.e. debris flow) deliver sediment from the catchment to the active depositional lobe of the fan. When the locus of deposition moves from one area of the fan to another, through the process of lobe avulsion, the abandoned lobe surface is considered inactive and processes that contribute to surface development dominate (Blair and McPherson, 1994; Blair and McPherson, 2009; de Haas et al., 2014). These secondary modifying processes include reworking of surface material by overland flow, weathering and erosion, pedogenesis, bioturbation, and the introduction of eolian sediment.

Research exploring the topic of eolian influence on fans has largely focused on post-abandonment surface modification including surface smoothing and the amount of wind-blown accumulated sediment as a function of the age since abandonment (McFadden et al., 1987; McFadden et al., 1989; Pelletier, 2006; Pelletier, 2007), leaving the significant impact on debris-flow alluvial fan processes overlooked. Some studies have addressed the impact of encroaching dune fields on debris-flow fan system's geomorphic form, creating dune-impounded debris-flow benches (Anderson and Anderson, 1990), and even alluvial fans sourced entirely from eolian sand, forming from

incision and erosion of stabilized dune fields (Sweeney and Loope, 2001), but not specifically the interplay that eolian material has on debris-flow processes. Eolian material (dust/loess) itself has been widely studied in arid environments that often feature alluvial fans, though this work largely has focused on dust source and accumulation rates (Reheis, 2006; Sweeney et al., 2011).

The impact wind-blown material has on sediment transport processes working on depositional and abandoned lobes of alluvial fans and its recognition within fan facies is poorly documented. The lack of attention is illustrated by the pervasive historic uses of the terms “inactive” and “active” for the abandoned and depositional lobes, respectively (Wells and Dohrenwend, 1985; Ritter et al., 1995; Harvey et al., 2003; de Haas et al., 2014). Eolian processes are active on abandoned lobes of debris-flow alluvial fans and can influence other sediment transport resulting in the smoothing of the abandoned lobes. This study focuses on the influence that wind-blown material has on fan surfaces and how eolian activity modifies depositional processes on debris-flow alluvial fans as demonstrated by sedimentary facies.

Major sediment transport processes on alluvial fan surfaces are largely dependent on where a given surface exists within a fan complex (Blair and McPherson, 2009). Regions of the fan connected to the drainage basin are controlled by different processes than areas that are cut off from the catchment sediment source. Although both primary and secondary processes may occur within any lobe and on any surface, it is the connection to the drainage basin that ultimately controls which processes hold the chief influence on the morphology of a given lobe. On the active depositional lobe, primary

processes are the major sediment transport mechanism while the abandoned lobes are dominated by secondary modifying processes. Therefore, depositional lobes have rougher surfaces due to debris flow dominance and abandoned lobes have smoother surfaces due to the addition of eolian sediment and reworking processes.

This concept is important when assessing the relative impact of eolian deposition on alluvial fans (here regarded as the focus secondary process), mainly in the sense of which transport processes contribute the highest relative volume of sediment. On the depositional lobe, the major contributors are debris flow and hyper-concentrated flow—all primary process. Although eolian sedimentation also occurs on the active depositional lobe surfaces, the relative volume of sediment from primary processes sourced from the drainage basin is the highest. Conversely, the major sediment source on abandoned lobes is from eolian deposition. This includes eolian material being incorporated in debris flow, hyper-concentrated flow, and overland flow, which are sourced from the fan surfaces rather than the catchment, as these lobes are cut off from the drainage basin sediment supply.

The objective of this work is to recognize the influence that eolian sediment has on debris flow fan surface processes through surface characteristics, stratigraphy, and ultimately grain-size distribution analysis, emphasizing the recorded importance of post-surface abandonment activity on debris-flow alluvial fans. The Pioneer alluvial fan in the San Luis Valley of southcentral Colorado exhibits an excellent site for exploring these dynamics through its extensive surface access and exposure for sedimentary facies examination. Furthermore, a greater understanding of eolian processes on alluvial fans

may illuminate appropriate caution needed when making tectonic and or climatic interpretations from alluvial fan surfaces and deposits, and when assessing sediments from provenance analysis. This paper presents results of grain size distribution data aimed to distinctly specify the signature of eolian influence on debris flow alluvial fans. In the following sedimentological report, surface geomorphologies and deposit morphologies, facies descriptions and associations were analyzed along with quantitative grain size data for these purposes.

Pioneer Alluvial Fan

Geologic Setting

The Pioneer alluvial fan emanates from the western range front of the Sangre de Cristo Mountains in southcentral Colorado's San Luis Valley (Figure 4.2). It is flanked by the Holbrook alluvial fan to the south and is unbound by the Uracca Creek drainage landslide complex to the north, neighbor to the Zapata alluvial fan (Figure 4.3). Though this study focuses on the Pioneer alluvial fan, specifically facies exposed in a quarry on the fan's toe, a few deposits are also examined from the near northern Zapata and southern Holbrook alluvial fans.

The San Luis Valley is an asymmetric extensional half-graben system of the southern Rio Grande rift (Wallace, 2004; Lipman, 2007). The northern extent of the San Luis Valley is just south of the Arkansas River basin at the Villa Grove fault zone and extends south to the Española basin bound by the Embudo accommodation zone near Taos, NM (Wallace, 2004) (Figure 4.2). The uppermost Eocene to Miocene volcanic San Juan Mountains bound the valley to the west and the Sangre de Cristo Mountains to the

east (Lipman, 2007). The steep western range front of the Sangre de Cristo Mountains is controlled by the Holocene-active Sangre de Cristo normal fault system (Figure 4.4) (McCalpin, 1982; McCalpin, 1986; McCalpin, 2006). The Blanca Peak and Sangre de Cristo horsts make up the extensional footwall, which include Laramide thrust sheets of Paleoproterozoic basement rock in fault and depositional contact with Pennsylvanian-Permian terrigenous rocks associated with the Ancestral Rocky Mountain orogeny (Lindsey, 1998; Kellogg, 1999; Barbeau, 2003; Ruleman and Machette, 2007).

The San Luis Valley was host to the long-lived Plio-Pliestocene Lake Alamosa (Figure 4.4) (Machette et al., 2007). Lake Alamosa contracted and expanded for approximately 3 million years before it overtopped a low-elevation sill in the San Luis Hills to the south around 440 ka (Machette et al., 2007). As lake Alamosa drained, it incised the Rio Grande Gorge, integrating the San Luis Valley into the Rio Grande drainage basin. The evacuation of Lake Alamosa from the San Luis Valley at ~440 ka partially provided the sediment supply of the Great Sand Dunes—an active dune field that rests just north of the study area (Madole et al., 2008).

Evidence for at least three major Pleistocene glaciations is present at the Blanca Peak massif, including the glacially carved catchments of the Pioneer and neighboring alluvial fans (Figure 4.3). Pre-Bull Lake, Bull Lake, and Pinedale moraines are present within catchments and cap the proximal reaches of these fans (McCalpin, 1982).

Geomorphology and Processes

The Pioneer alluvial fan is a debris-flow fan characterized by a series of surfaces separated into three broad groups based on geomorphic position and relative age; old,

intermediate, and young. In general, the topographically lowest surfaces with the roughest relative surface topography, and no dissection, are considered the youngest, most active surfaces. In contrast, the topographically highest, most dissected surfaces, with the smoothest relative surfaces, are considered the oldest, abandoned surfaces. The intermediate surfaces rest in-between these two end members as slightly rougher, and less dissected than the oldest surfaces but smoother and more dissected than the youngest.

Relative age relations correspond with the types of lobes where each surface occurs. The youngest surfaces are on the depositional lobe and the intermediate and old surfaces are on abandoned lobes. The coincidence of surfaces and lobes also has consistencies with the processes that dominate. Major processes on the youngest surfaces on the depositional lobe are primary processes—mainly debris flow. Eolian processes are also active on these surfaces but with a minor relative contribution of sediment. Major processes on the intermediate and oldest surfaces on the abandoned lobes are secondary modifying processes, of which eolian processes are the largest contributor of sediment with minor occurrences of debris flow.

Surface morphology evident of eolian sedimentation support these interpretations (Lancaster and Tchakerian, 1996). Well-sorted fine sand accumulations are present at tree bases and in low points on most all alluvial fan surfaces (Figure 4.6a-e). On the oldest (highest elevation, smoothest) fan surfaces, well-sorted silt and sand fill the interstitial spaces of gravels (Figure 4.6b and c). Eolian sand sheets ramp up on toes of fans, covering the rough texture from cobble- and boulder-sized clasts to smoother infilled surfaces, and associated deposits are visible in some incised areas (Figure 4.6d, e, and f).

Finally, moderately to well-sorted sand occurs as bars and small-scale terraces in minor channels on fan surfaces showing reworking by water (Figure 4.6g).

Sedimentology

The Pioneer alluvial fan exhibits deposits derived from both primary and secondary modifying processes (as described in Chapter 2). Facies included in this analysis are poorly sorted, matrix-supported, unstratified gravel (Gms); poorly sorted, matrix- to clast-supported, unstratified gravel (Gmsc); moderately to well-sorted, horizontally stratified, very coarse silt to very fine sand (Sh); and very well to well sorted, massive, very coarse silt to fine sand (Sm). The matrix components from gravel facies (Gms and Gmsc) are sub-divided into three distinct field-classification variations of matrix texture 1) poorly-sorted silt to medium sand, 2) moderately to well-sorted silt to very fine sand, and 3) poorly- to moderately-sorted silt to medium sand.

Methods

Investigation of the eolian impact on the Pioneer fan includes description of geomorphic surface features, facies descriptions and association with geomorphic features, and grain-size distribution analysis of facies with field-described eolian characteristics. Surface features demonstrate the presence of eolian material on fan surfaces and sedimentary facies exhibit the incorporation of eolian material within the sedimentary transport processes that they represent. Grain-size distribution analysis helps to verify the genetic interpretations.

Geomorphic Features/Surfaces

Geomorphology of the Pioneer fan was initially contextualized using high-resolution topographic data. Relative topographic position, relation to other geomorphic features (e.g. moraines and fault scarps), and surface texture were used to delineate age relations of surfaces. These surfaces were subsequently described in the field, based on the remote mapping, characterizing deposit morphologies. Descriptions for each fan surface class were developed into relative chronology of oldest fan surfaces (Qao), intermediate relative age surfaces (Qai) and the youngest surfaces (Qay). The older and intermediate surfaces rest on the abandoned lobes of the fan and the youngest surfaces occupy areas of the active depositional lobe.

Sedimentary Facies

Facies were described and mapped on vertical exposures within the Pioneer quarry located at the toe of the Pioneer alluvial fan (Figure 4.3). Facies were delineated by sedimentary structures, deposit texture, and matrix composition. Interpretive facies associations were made in comparison between alluvial fan surface characteristics and deposit morphologies, and sedimentary facies preserved in vertical exposures (Chapter 2). The textual features of sand facies and the wide range in matrix-texture in gravel facies observed in the field inspire motivation to test the hypothesis that sediment with grain-size populations characterized by eolian texture is present in different facies types.

Grain-Size Distribution

Analysis of grain size distributions has been applied in many environments and has been used broadly to interpret distinct depositional environments based on

entrainment capabilities and sediment transport processes (Folk and Ward, 1957; Visher, 1969; Blot and Pye, 2012; Vandenberghe, 2013). The application herein is to aid interpretation of eolian influenced material within facies of the Pioneer debris flow and associated fans.

Sample selection. Fourteen deposits of multiple facies were sampled for grain-size analysis (Figure 4.5). Because of the available extensive vertical exposure, the primary site of sample collection is the gravel quarry located at the toe of the Pioneer alluvial fan, though samples were also collected from the Zapata and Holbrook fans (Figure 4.3). Samples were taken from the active depositional lobe of the Zapata fan (Gmsc1) and the eolian sand sheet encroaching on the toe of the Holbrook fan (Sm) to cross-check grain-size distribution with facies samples from vertical exposure. Sampled facies within the Pioneer quarry and on the Zapata and Holbrook fan surfaces are shown in Figure 4.5. Sand facies (Sh and Sm) were sampled along with matrix-types 1, 2, and 3 from gravel facies (Gms and Gmsc). Three matrix-type 1 samples were taken from Gmsc faces within the vertical exposure in the Pioneer quarry and one sample from the active depositional lobe of the Zapata fan. Three matrix-type 2 facies were sampled, two from Gms and one Gmsc facies, and one matrix-type 3 from was sampled from Gmsc facies. Three Sh facies were sampled from the Pioneer quarry and two Sm facies—one from the quarry and one from the toe of the Holbrook fan. Table 4.1 denotes sample number, facies, location, and sample preparation details.

Material was removed from the vertical exposure or surficial deposit and placed in plastic bags. Care was taken to collect the material around larger, gravel-sized

particles, which in the Gms and Gmsc facies meant sampling the matrix only. The sediment samples were then left to dry for sample preparation.

Sample preparation. Sample preparation of collected silt/sand deposits began with sieving 200 grams of each sample using a 2 mm sieve to remove particles larger than sand. If samples showed no visible grains over 2 mm, they were not sieved. Samples with aggregated particles were broken up in a mortar and pestle (noted in Table 4.1). Sub samples of each sieved sample were then disaggregated in hexametaphosphate. Of these samples, three sub-samples were used for analysis in the Malvern Mastersizer 3000 laser diffraction particle size analyzer at Montana State University's Environmental Analytical lab.

Grain Size Measurement. The Malvern Mastersizer 3000 measures particle sizes of dispersed particles using laser diffraction and Mie theory (Fu and Sun, 2001). The size of the scattering angle changes with the size of the particle, which is measured to calculate the particle size distribution of a sample (Loizeau et al., 1994). Laser diffraction grain size measurements are an efficient way to measure particle size distributions and capture the fine-grain fraction of deposits(Varga et al., 2019).

Statistical analysis. Data from the Mastersizer was delivered as percent volume of each grain size fraction (Appendix C). The GRADISTAT Macro by Blott and Pye (2001) was used to calculate statistical parameters of these data including, modal properties, mean, sorting, skewness, kurtosis (Appendix C). Modifications were made in determining numerical and verbal sorting to the macro and calculated for 1 sigma

standard deviation rather than 2 sigma in order to capture intended verbal description of the scale (Folk, 1964). Grain-size distributions are graphically displayed as probability distributions.

Results

Descriptions and numerical values for each deposit were produced from the grain size data gathered by the laser diffraction particle analyzer. Grain size data are reported in groups of each matrix type (1, 2, and 3) and each sand facies (Sm and Sh). Table 4.2 summarizes the verbal descriptions and numeric values in phi of mean, sorting, skewness, and kurtosis for the average of each sample type. Notice that the standard deviation of the mean grain size, and therefore the sorting value, is largest among matrix type 1 and smallest in the Sm facies. Grain size analysis of the three variations of matrix texture within gravel facies are described as 1) poorly to moderately-sorted fine silt to medium sand, 2) moderately-sorted, very coarse silt to very fine sand, and 3) moderately-sorted, very coarse silt to fine sand. Horizontally stratified sand (Sh) is well to moderately-sorted coarse silt to very fine sand and the massive sand (Sm) as very well to well sorted very coarse silt to very fine sand.

Grain-size distributions expressed in phi are graphically represented as frequency plots in Figure 4.7. Matrix type 1 is the most poorly sorted, has a fine-grained tail, and the coarsest mode around 2 phi. Matrix type 2 shows a much more sorted signature, with a poorly defined fine-grained tail, and a finer modal grain size, closer to 4 phi, the sand-silt boundary. Distributions of matrix type 3 have intermediate characteristics between matrix type 1 and 2, which align with its classification. Facies Sm samples are the most

well-sorted samples with a modal peak near the mean graze size at about 3 phi (Figure 4.7 and Table 4.2). Finally, facies Sh is also well sorted, but has a finer-grained mode, just under 4 phi, a mean of 4.3 phi, and exhibits a fine-grained tail (Figure 4.7 and Table 4.2). Distributions are reported as percentages of sand, silt, and clay in Figure 4.8. Sand composition is reported in terms of quartz, feldspar, and lithic-fragment abundances in Figure 4.9. There is no obvious correlation between composition and faces.

Interpretation

Primary and secondary process relations within the sandy facies and three matrix types of debris-flow facies are substantiated by the interpretation of corresponding grain-size distributions. Grain-size distributions are used as a tool to understand sediment transport processes in addition to contextual indicators of the deposit in situ, like textual properties, sedimentary structures, and neighboring facies. The behavior that particles have in fluids (both gas and liquid) is influenced strongly by the particle size. In turn, the mechanisms of settling can be narrowed by examining grain populations (Middleton, 1976). Using both grain-size measurements and facies analysis can help understand the complicated genesis that the sediment has experienced prior to its last deposit. Table 4.3 summarizes facies descriptions and interpretations.

Grain-size distributions as cumulative plots, where the subpopulations are represented as a series of straight lines, suggest formation from a combination of sedimentary mechanisms (Visher, 1969), as do frequency plots with multiple modal curves (Middleton, 1976; Ashley, 1978; Sun et al., 2002). Consequently, frequency distributions that exhibit a smooth, unimodal distribution, can be attributed to a single

sedimentary mechanism. Distributions of matrix types 1-3, and facies Sm and Sh, are shown as frequency plots in terms of phi versus weight percent and are compared in Figure 4.7.

Debris-flow facies (Gms and Gmsc) with matrix-type 1 are typified by poorly to moderately-sorted, sometimes bimodal, fine silt to medium sand. The moderately to poorly-sorted texture of matrix type 1 is demonstrated by an overall wide and ununiform distribution with a fine-grained tail (Figure 4.7). This is expected for a debris-flow deposit that originated from sedimentation en masse, and supports the interpretation of drainage basin origin, or rather, no eolian influence. The more well-sorted and finer-grain texture seen in matrix type 2 is attributed to its eolian origin (Anderson and Haff, 1988; Pye, 1995). The moderately sorted, very coarse silt to fine sand of matrix type 3 is interpreted as an intermediate of type 1 and 2. The distinction of matrix type 3 as having only partial eolian influence is largely from field-observation of matrix texture.

Very well to well-sorted, unimodal, very coarse silt to very fine sand is indicative of wind-blown processes, as shown by sampled facies Sm (Pye, 1995; Sun et al., 2002), though the lack of structure and massiveness of Sm also suggests reworking of eolian sand by hyperconcentrated flow (Sweeney and Loope, 2001). The very-well sorted, yet bi-modal grain-size distribution of Sh suggests water reworked eolian material (Sweeney and Loope, 2001; Sun et al., 2002).

The most consistently unimodal sample group is from facies Sm, where the interpretation is purely eolian deposition. Because there is not a phase of reworking by overland flow where new grain sizes could be introduced or sorted, the original eolian

grain-size distribution remains, even if reworked by hyperconcentrated flow (Sweeney and Loope, 2001; Sun et al., 2002). Facies Sm consists of well-sorted fine sand, likely mobilized by saltation, also with a silt-sized particles that are interpreted to have settled from near-surface, short-term suspension (Vandenberghe, 2013). Finally, facies Sh indicates eolian material with subsequent reworking by water by its well-sorted distribution and a fine-grain tail. This bulk of fines likely reflects suspension by water during ultimate deposition in contrast to a distribution with no-fines, likely removed from the system by wind (Anderson and Haff, 1988; Pye, 1995).

Discussion

The results of this study show that eolian sediment on debris flow alluvial fans leaves a significant and recognizable impact on fan surface texture, deposit morphologies and sedimentary facies, and is detectable by signature grain-size distributions. Differences in geomorphic expression and related deposit morphologies of fan surfaces varying in age exemplify the significance of sedimentation by eolian processes recorded in stratigraphic successions of debris-flow alluvial fans.

Surface development atop of lobes within the alluvial fan complex varies according to the connectivity of the lobe to the catchment and depends on time since the lobe has been cut off from catchment-sourced sediment. Dominant processes acting on fan surfaces hinge on these lobe dynamics and are also influenced by neighboring geomorphic systems. The older, smooth, incised, relict fan surfaces are on the older abandoned lobes. This is where modifying processes of overland flow, addition of eolian sediment, and incision control the dominant morphologies rather than primary processes

like debris flow. The intermediate, somewhat smoothed surfaces are modified by secondary processes but still maintain discernable evidence of primary deposition such as boulder trains from debris flow levees and lobes. The youngest surfaces display the most defined evidence of debris flow processes and minimal reworking because these surfaces have experienced the most recent debris-flow deposition in the fan complex. Regardless of age, wind-blown sediment impacts all alluvial fan surfaces. Evidence of wind-blown sand atop surfaces includes tree-bases buried by well sorted silt to fine-grained sand. Sand is also observable covering the distal reaches of fans as eolian sand sheets.

It is the collective work of adding sediment to the system by eolian processes and degrading deposit morphologies through gravitational, biological, and fluvial processes responsible for fan surface smoothing with time (McFadden et al., 1989; Hsu and Pelletier, 2004; Matmon et al., 2006; Frankel and Dolan, 2007; de Hass et al., 2014; Johnstone et al., 2018). Post lobe-avulsion surface abandonment eolian processes effectively fill in micro-, meso-, and macro-scale topographic lows with sediment, which is also readily reworked on the surface by water.

Eolian sediment effects process on depositional and abandoned lobes of debris-flow alluvial fans. Relatively, eolian sediment is a more significant source of sediment on abandoned lobes than the depositional lobes, contributing to surface modification and smoothing, since debris flows are less frequent there. When considering processes that target all fan surfaces indiscriminate of age, like eolian processes, the conception of what an “active” alluvial fan surface is versus an “inactive” surface may require reevaluation. Both the depositional lobe and abandoned lobes are impacted by depositional processes.

Debris flow deposition dominates depositional lobes and eolian sedimentation dominates abandoned lobes. So, if the criteria for a surface to be active is sediment transport and deposition, then all surfaces of alluvial fans are active, just in different ways. Therefore, there is no such thing as an "inactive" surface relative to deposition and the term should be abandoned.

On alluvial fans, primary processes operate dominantly on the active depositional lobe surface (Blair and McPherson, 1994; Blair and McPherson, 2009; de Haas et al., 2014). These are mostly constructive processes, like debris flow. However, secondary modifying processes are also acting on this surface. These processes include the introduction of eolian sand and general surface reworking by overland flow as demonstrated by facie Sh (Blair and McPherson, 1994; Blair and McPherson; de Haas et al., 2014). Secondary modifying processes dominate abandoned lobe surfaces, masking the surface morphology created by primary processes (Blair and McPherson, 1994; Blair and McPherson, 2009; de Haas et al., 2014). These processes include pedogenesis, weathering, reworking of material by water, bioturbation, incision, and introduction of eolian sediment. So, eolian processes affect the entire collection of fan surfaces, both considered active or inactive, and lobes, both depositional and abandoned.

Transient and accumulating eolian sand is active on fan surfaces of varying age and atop both depositional and abandoned lobes. Facies that represent debris flow with eolian influenced matrix illustrate the effect secondary processes have on primary processes. For example, packages of eolian sediment stored on the fan surfaces can serve to prompt processes that are usually primary by bulking debris-flow slurries,

incorporating sediment into flow via an erosional flow boundary, as they move down fan (Scott, 1988; Scott et al., 1995; Scott and Vallance, 1995; Cannon et al., 2003; Shroba et al., 2007; Frank et al., 2014). This is evident by the preservation of grain-size population characterized by eolian texture in facies that represent the primary process of debris-flow. Thus, sediment supply that contributes to debris flow activity can be derived from the fan surface itself, not only drainage basin. Also, sand can be remobilized by water more readily than the gravel-sized particles on the fan surface. Consequentially, debris-flow activity on abandoned lobes can be facilitated by eolian sediment input to the lobe surface. Debris flows that originate from the fan surface rather than the catchment are likely bulked with fine sand as matrix contribution as shown in Gms and Gmsc facies with matrix type 2. Because there are debris flow facies with a dominant eolian signal, the debris-flow activity could have occurred while a surface was abandoned from the drainage basin sediment supply.

When consulting the stratigraphic record to understand past fan dynamics and activity, one must rely on sedimentary facies and whether they represent primary versus secondary processes. In this case, debris flow are the primary depositional processes whose deposits generally build the active depositional lobe. Given what we know of the introduction of eolian material on fan surfaces regardless of age or connectivity to the drainage basin, the incidence of debris flow facies alone is not necessarily sufficient evidence to deem a depositional package to represent an active (connected to drainage basin) system.

A caveat to this research is that the area of focus was principally at the toe of the Pioneer alluvial fan. Distal areas of alluvial fans usually experience more eolian activity than proximal areas of the fan (Reheis and Kihl, 1995; Sweeney et al., 2011). For this reason, the occurrence of facies influenced by eolian input reported herein is likely more frequent than what is actual on other areas of the fan.

Moreover, understanding sediment recycling through the interactions between eolian and primary processes on debris-flow alluvial fans can serve useful for many other interpretations. Numerous studies have used wind-blown deposits as indicators of climate (McFadden et al., 1987; Wells et al., 1987; Clarke, 1994; Reheis and Kihl, 1995; Harrison et al., 2001; Pelletier, 2006; Urban et al., 2009; Reheis and Urban, 2011). If wind-blown sand can be attributed to discrete climatic events, the attention to eolian signatures within the matrix of debris-flow deposits is imperative when making these interpretations, rather than sand facies alone.

Secondly, eolian sediment in arid regions is sourced from playas, distal reaches of fans, and dry washes (Gillette et al., 1980; Reheis and Kihl, 1995; Goudie and Middleton, 2006; Sweeney et al., 2011). It is important to understand these provenance relations when evaluating deposits within alluvial fan systems that represent the primary mechanism of deposition (i.e. debris flow). If the matrix of certain deposits is largely derived from windblown sources (e.g. Gmsc2 and Gms2), then caution must be used during provenance analysis (e.g. detrital zircon studies). For example, wind-blown sediment of the Great Sand Dunes is largely sourced from Lake Alamosa sediments (Madole et al., 2008), and is likely the dominant contributor to much of the eolian sand in

the Pioneer fan deposits. Lake Alamosa sediment chiefly originated from the San Juan Mountains by the Rio Grande River, Alamosa River, and Saguache Creek to the west (Lipman, 1975; Madole et al., 2008; Machette et al., 2013). Therefore, a provenance analysis using the matrix of these deposits to understand the origin of debris-flow facies might be misleading, as the primary deposits are derived from the Sangre de Cristo Mountains.

Conclusion

Surface characteristics, strata, and grain-size distributions of facies within debris-flow alluvial fan systems distinctly indicate the influence of eolian processes on alluvial fan surfaces. Eolian sediment addition is evident in the grain-size distribution of sand facies and matrices of gravel facies that record debris-flow processes in the sedimentary record. The presence of sediment that indicates modification or secondary processes (eolian derived sand) incorporated within the facies of primary process deposits shows an interplay between the binary of processes we consider on alluvial fans. Deposition and reworking of eolian material can be an important controlling factor governing surficial processes on the abandoned lobes of debris-flow fans. Delivery of eolian material is especially significant on abandoned lobes detached from their accompanying mountain catchment sediment source, leading to continuous sediment transport and aggradation. Therefore, characterization of abandoned fan lobes in such a way that suggests the inactivity of sediment transport is misleading.

Literature Cited

Anderson, R. S. and Anderson, S. P., 1990, Debris-flow benches; dune-contact deposits record paleo-sand dune positions in North Panamint Valley, Inyo County, California: Geology, v. 18, p. 524-527.

Anderson, R. S. and Haff, P. K., 1988, Simulation of eolian saltation: Science, v. 241, p. 820-823.

Ashley, G.M., 1978. Interpretation of polymodal sediments: Journal of Geology, v. 86, p. 411 – 421.

Barbeau, D. L., 2003, A flexural model for the Paradox Basin: implications for the tectonics of the Ancestral Rocky Mountains, Basin Research, v. 15, p. 97-115.

Blair, T.C., and McPherson, J. G., 1994, Alluvial fan processes and forms, *in* Parsons, A.J., and Abrahams, A.D., eds., Geomorphology of desert environments: London, Chapman & Hall, p. 354-402.

Blair, T.C., and McPherson, J. G., 2009, Alluvial fan processes and forms, *in* Parsons, A.J., and Abrahams, A.D., eds., Geomorphology of desert environments, 2nd Edition: Berlin, Springer, p. 413-467.

Blott, S. J., and Pye, K., 2001, GRADISTAT: a grain size distribution and statistics package for the analysis of unconsolidated sediments: Earth surface processes and Landforms, v. 26, p. 1237-1248.

Blott, S. J., and Pye, K., 2012, Particle size scales and classification of sediment types based on particle size distributions: Review and recommended procedures: Sedimentology, v. 59, p. 2071-2096.

Cannon, S. H., Gartner, J. E., Parrett, C., and Parise, M., 2003, Wildfire-related debris-flow generation through episodic progressive sediment-bulking processes, western USA, *in* Rickenmann, D. and Chen-lung, C., eds., Debris-flow hazards mitigation: mechanics, prediction, p. 71-82.

Clarke, M. L., 1994, Infra-red stimulated luminescence ages from aeolian sand and alluvial fan deposits from the eastern Mojave Desert, California. Quaternary Science Reviews, v. 13, p. 533-538.

de Haas, T., Ventra, D., Carbonneau, P. E., and Kleinhans, M. G., 2014, Debris-flow dominance of alluvial fans masked by runoff reworking and weathering: Geomorphology, v. 217, p. 165-181.

Dühnforth, M., Densmore, A. L., Ivy-Ochs, S., Allen, P. A., and Kubik, P. W., 2007, Timing and patterns of debris flow deposition on Shepherd and Symmes creek fans, Owens Valley, California, deduced from cosmogenic 10Be: Journal of Geophysical Research: Earth Surface, v. 112(F3).

Folk, R. L., and Ward, W. C., 1957, Brazos River bar [Texas]; a study in the significance of grain size parameters: Journal of Sedimentary Research, v. 27, p. 3-26.

Folk, R. L., 1964, A review of grain-size parameters: Sedimentology, v. 6, p. 73-93.

Frank, F., McArdell, B. W., Huggel, C., and Vieli, A., 2015, The importance of entrainment and bulking on debris flow runout modeling: examples from the Swiss Alps: Natural Hazards and Earth System Sciences, v. 15, p. 2569-2583.

Frankel, K. L., and Dolan, J. F., 2007, Characterizing arid region alluvial fan surface roughness with airborne laser swath mapping digital topographic data. Journal of Geophysical Research: Earth Surface, v. 112(F2).

Fu, Q. and Sun, W., 2001, Mie theory for light scattering by a spherical particle in an absorbing medium: Applied Optics, v. 40, p. 1354-1361.

Gillette, D.A., Adams, J., Endo, A., Smith, D., and Kihl, R., 1980, Threshold velocities for input of soil particles into the air by desert soils: Journal of Geophysical Research v. 85 (C10), p. 5621–5630.

Goudie, A.S., Middleton, N.J., 2006, Desert Dust in the Global System. Springer, Berlin.

Harrison, S.P., Kohfeld, K.E., Roelandt, C., and Claquin, T., 2001, The role of dust in climate changes today, at the last glacial maximum and in the future: Earth-Science Reviews v. 54, p. 43–80.

Harvey, A. M., and Wells, S. G., 2003, Late Quaternary variations in alluvial fan sedimentologic and geomorphic processes, Soda Lake basin, eastern Mojave Desert, California. Special Papers-Geological Society of America, p. 207-230.

Hsu, L. and Pelletier, J. D., 2004, Correlation and dating of Quaternary alluvial-fan surfaces using scarp diffusion: Geomorphology v. 60, p. 319-335.

Hudson, M. R., and Grauch, V. J. S., 2013, New Perspectives on Rio Grande Rift Basins: From Tectonics to Groundwater: Geological Society of America Special Paper, v. 494.

Johnstone, S. A., Hudson, A. M., Nicovich, S., Ruleman, C. A., Sare, R. M., and Thompson, R. A., 2018, Establishing chronologies for alluvial-fan sequences with analysis of high-resolution topographic data: San Luis Valley, Colorado, USA: Geosphere, v. 14, p. 2487-2504.

Kellogg, K., 1999, Neogene basins of the northern Rio Grande Rift-partitioning and asymmetry inherited from Laramide and older uplifts: Tectonphysics, v. 305, p. 141-152.

Lancaster, N., and Tchakerian, V. P., 1996, Geomorphology and sediments of sand ramps in the Mojave Desert: Geomorphology, v. 17, p. 151-165.

Lindsey, D. A., 1998, Laramide structure of the central Sangre de Cristo Mountains and adjacent Raton basin, southern Colorado: The Mountain Geologist, v. 35.

Lipman, P. W., 1975, Evolution of the Platoro caldera complex and related volcanic rocks, southeastern San Juan Mountains, Colorado: U.S. Geological Survey Professional Paper, v. 852, no. 128, p. 197.

Lipman, P. W., 2007, Incremental assembly and prolonged consolidation of Cordilleran magma chambers: Evidence from the Southern Rocky Mountain volcanic field: Geosphere, v. 3, p. 42-70.

Loizeau, J. L., Arbouille, D., Santiago, S., and Vernet, J. P., 1994, Evaluation of a wide range laser diffraction grain size analyzer for use with sediments: Sedimentology, v. 41, p. 353-361.

Machette, M.N., Marchetti, D.W., and Thompson, R.A., 2007, Ancient Lake Alamosa and the Pliocene to middle Pleistocene evolution of the Rio Grande, in Machette, M.N., Coates, M.M., and Johnson, M.L., eds., 2007 Rocky Mountain Section Friends of the Pleistocene Field Trip—Quaternary geology of the San Luis Basin of Colorado and New Mexico, September 7-9, 2007: U.S. Geological Survey Open-File Report 2007-1193, p. 157-167.

Machette, M. N., Thompson, R. A., Marchetti, D. W., and Smith, R. S., 2013, Evolution of ancient Lake Alamosa and integration of the Rio Grande during the Pliocene and Pleistocene: Geological Society of America Special Papers, v. 494, p. 1-20.

Madole, R. F., Romig, J. H., Aleinikoff, J. N., VanSistine, D. P., and Yacob, E. Y., 2008, On the origin and age of the Great Sand Dunes, Colorado: Geomorphology, v. 99, p. 99-119.

Matmon, A., Nichols, K., and Finkel, R., 2006, Isotopic insights into smoothening of abandoned fan surfaces, Southern California: Quaternary Research, v. 66, p. 109-118.

McCalpin, J.P., 1982, Quaternary geology and neotectonics of the west flank of the northern Sangre de Cristo Mountains, south-central Colorado: Colorado School of Mines Quarterly, n. 77, p. 97.

McCalpin, J., 1986, Quaternary tectonics of the Sangre de Cristo and Villa Grove fault zones: Contributions to Colorado seismicity and tectonics—A: p. 59-64.

McCalpin, J.P., 2006, Active faults and seismic hazards to infrastructure at Great Sand Dunes National Monument and Preserve: Crestone, Colorado: unpublished report by GEO-HAZ Consulting, Inc., 49 p., 1 oversize plate.

McDonald, R. R. and Anderson, R., 1996, Constraints on eolian grain flow dynamics through laboratory experiments on sand slopes: Journal of Sedimentary Research, v. 66, p. 642–653.

McDonald, E.V., McFadden, L.D., Wells, S.G., 2003. Regional response of alluvial fans to the Pleistocene–Holocene climatic transition, Mojave Desert, California, *in* Enzel, Y., Wells, S.G., Lancaster, N., eds., Paleoenvironments and Paleohydrology of the Mojave and Southern Great Basin Deserts: Geological Society of America Special Paper, 368, p. 189–205.

McFadden, L.D., Wells, S.G., and Jercinovich, M.J., 1987, Influences of eolian and pedogenic processes on the origin and evolution of desert pavements: Geology, v. 15, p. 504-508.

McFadden, L. D., Ritter, J. B., and Wells, S. G., 1989, Use of multiparameter relative-age methods for age estimation and correlation of alluvial fan surfaces on a desert piedmont, eastern Mojave Desert, California: Quaternary Research, v. 32, p. 276-290.

Middleton, G.V., 1976. Hydraulic interpretation of sand size distributions: Journal of Geology, v. 84, p. 405-426.

Pelletier, J.D., 2006, Sensitivity to playa windblown-dust emissions to climatic and anthropogenic change: Journal of Arid Environments, v. 66, p. 62–75.

Pelletier, J. D., 2007, Cantor set model of eolian dust deposits on desert alluvial fan terraces: Geology, v. 35, p. 439-442.

Pye, K., 1995, The nature, origin and accumulation of loess: Quaternary Science Reviews, v. 14, p. 653-667.

Reheis, M.C., Kihl, R., 1995, Dust deposition in southern Nevada and California, 1984–1989: relations to climate, source area, and source lithology: Journal of Geophysical Research v. 100 (D5), p. 8893-8918.

Reheis, M. C., 2006, A 16-year record of eolian dust in Southern Nevada and California, USA: Controls on dust generation and accumulation: Journal of Arid Environments, v. 67, p. 487-520.

Reheis, M.C., Urban, F.E., 2011, Regional and climatic controls on seasonal dust deposition in the southwestern U. S: Aeolian Research, v. 3, p. 3-21.

Ritter, J.B., Miller, J.R., Enzel, Y., and Wells, S.G., 1995, Reconciling the roles of tectonism and climate in Quaternary alluvial fan evolution: Geology, v. 23, p. 245-248.

Ruleman, C.A., and Machette, M.N, 2007, An overview of the Sangre de Cristo fault system and new insights to interactions between Quaternary faults in the Northern Rio Grande Rift: *in* Machette, M.N., Coates, M.M., and Johnson, M.L., eds., 2007 Rocky Mountain Section Friends of the Pleistocene Field Trip—Quaternary geology of the San Luis Basin of Colorado and New Mexico, September 7-9, 2007: U.S. Geological Survey Open-File Report 2007-1193, p. 187-197.

Scott, K. M., 1988, Origin, behavior, and sedimentology of prehistoric catastrophic lahars at Mount St. Helens, Washington: Geological Society of America Special Papers 229, p. 23-36.

Scott, K. M., and Vallance, J. W., 1995, Debris flow, debris avalanche and flood hazards at and downstream from Mount Rainier, Washington: USGS Hydrologic Investigations Atlas 729: 2 sheets and accompanying pamphlet, US Geological Survey, Reston, VA.

Scott, K. M., Vallance, J. W., and Pringle, P. T., 1995, Sedimentology, behavior, and hazards of debris flows at Mount Rainier, Washington: US Geological Survey Open-File Report, n. 1547, 106 p.

Shroba, R. R., Thompson, R. A., and Ruleman, C., 2007, Possible role of eolian sediment in the genesis of boulder debris-flow deposits on the lower flanks of Ute Mountain, northern Taos Plateau volcanic field, New Mexico, *in* Machette, M.N., Coates, M.M., and Johnson, M.L., eds., 2007 Rocky Mountain Section Friends of the Pleistocene Field Trip—Quaternary geology of the San Luis Basin of Colorado and New Mexico, September 7-9, 2007: U.S. Geological Survey Open-File Report 2007-1193, p. 181-185.

Sun, D., Bloemendal, J., Rea, D. K., Vandenberghe, J., Jiang, F., An, Z., and Su, R., 2002, Grain-size distribution function of polymodal sediments in hydraulic and aeolian environments, and numerical partitioning of the sedimentary components: Sedimentary Geology, v. 152, p. 263-277.

Sweeney, M. R., and Loope, D. B., 2001, Holocene dune-sourced alluvial fans in the Nebraska Sand Hills: Geomorphology, v. 381, p. 31-46.

Sweeney, M. R., McDonald, E. V., and Etyemezian, V., 2011, Quantifying dust emissions from desert landforms, eastern Mojave Desert, USA: Geomorphology, v. 135, p. 21-34.

Tsoar, H. and Pye, K., 1987, Dust transport and the question of desert loess formation: Sedimentology, v. 34, p. 139-153.

Urban, F.E., Reynolds, R.L. and Fulton, R., 2009, The dynamic interaction of climate, vegetation, and dust emission, Mojave Desert, USA *in* Fernandez-Bernal, A., De La Rosa, M.A., eds., Arid Environments and Wind Erosion: NOVA Science Publishers, Inc., p. 243–267.

Vandenberghe, J., 2013, Grain size of fine-grained windblown sediment: A powerful proxy for process identification: Earth-Science Reviews, v. 121, p. 18-30.

Varga, G., Újvári, G., Kovács, J., and Szalai, Z., 2015, Effects of particle optical properties on grain size measurements of aeolian dust deposit: EGU General Assembly Conference Abstracts, v. 17.

Wallace, A. R., 2004, Evolution of the southeastern San Luis basin margin and the Culebra embayment, Rio Grande rift, southern Colorado, *in* Geology of the Taos Region: New Mexico Geological Society 55th Fall Field Conference Guidebook

Wells, S. G., and Dohrenwend, J. C., 1985, Relict sheetflood bed forms on late Quaternary alluvial-fan surfaces in the southwestern United States: Geology, v. 13, p. 512-516.

Wells, S.G., McFadden, L.D., and Dohrenwend, J.C., 1987, Influence of late Quaternary climatic changes on geomorphic and pedogenic processes on a desert piedmont, eastern Mojave Desert, California: Quaternary Research, v. 27, p. 130-146.

Zarate, M., and Blasi, A., 1991, Late Pleistocene and Holocene loess deposits of the southeastern Buenos Aires province, Argentina: Geojournal, v. 24, p. 211-220.

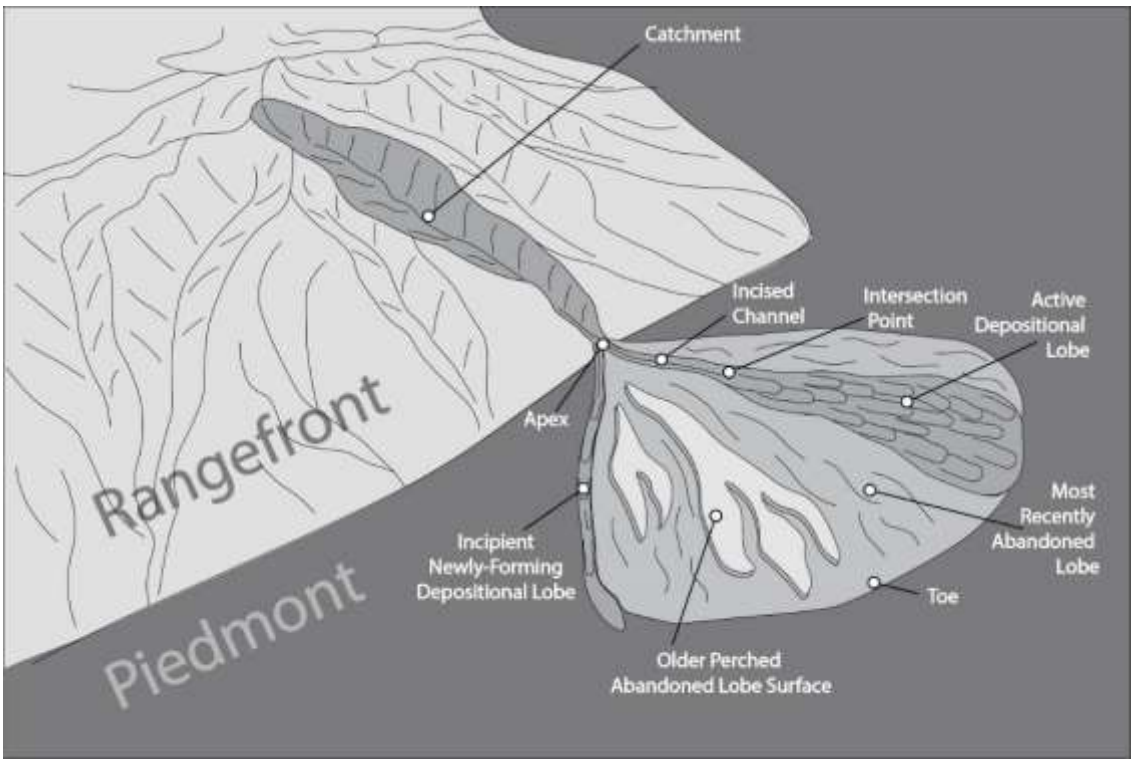

Figure 4.1. Schematic architecture of composite surfaces and associated processes on alluvial fans. Older surfaces are elevated and dissected while younger, active surfaces are inset into fan complex and are dominated by primary processes.

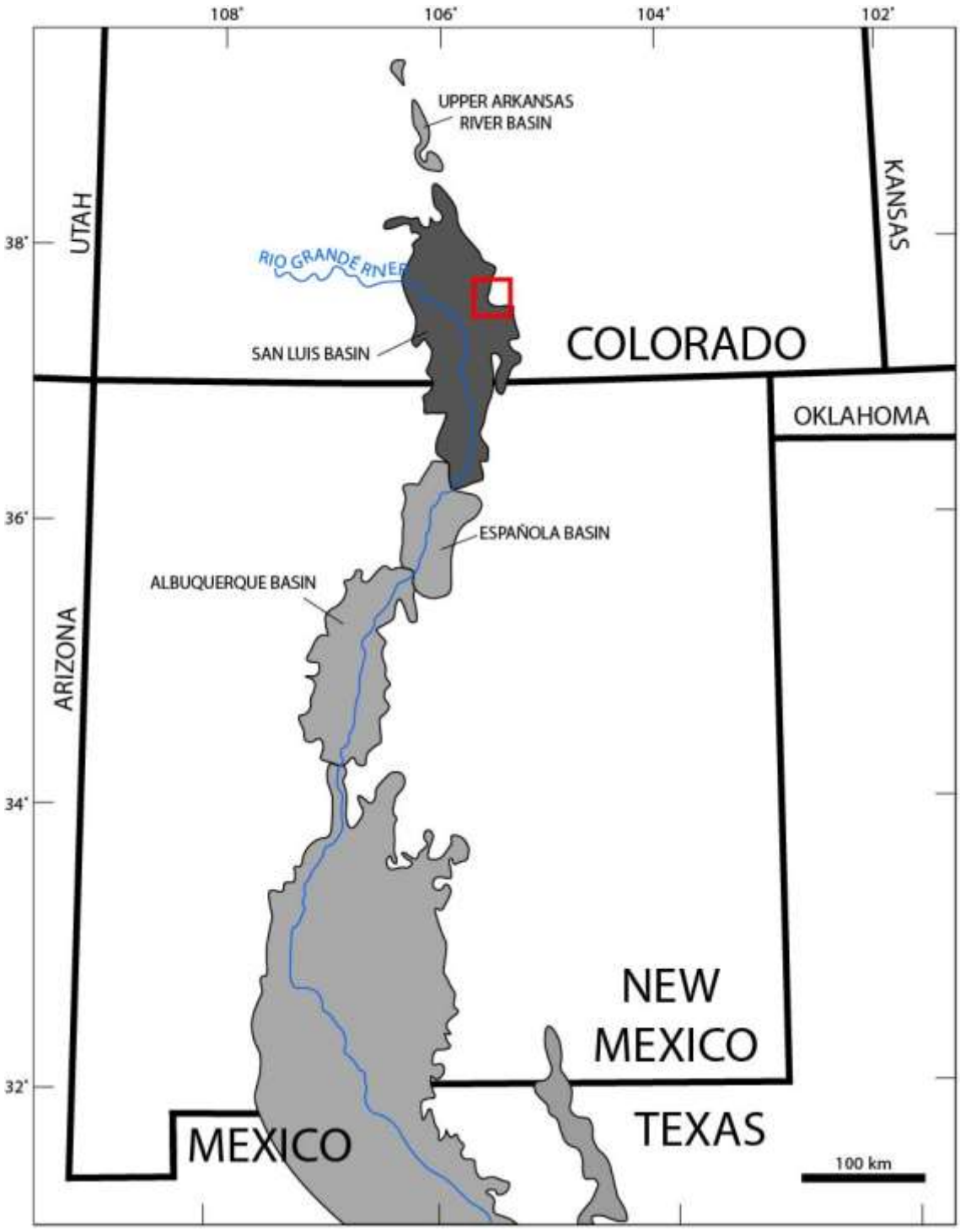

Figure 4.2. Basins of the Rio Grande Rift after Hudson and Grauch (2013). The San Luis Valley extends from south-central Colorado into northern New Mexico and is highlighted in dark grey. The Rio Grande River is shown in blue. The red box denotes study area and location of Figure 4.3.

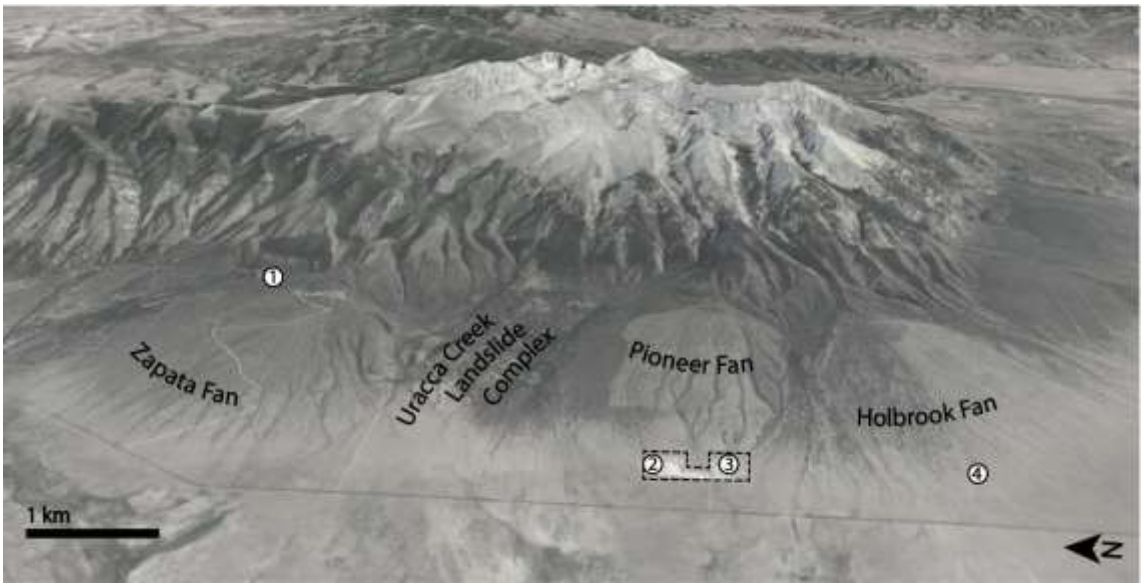

Figure 4.3. Oblique eastward Google Earth Image of the extensively glaciated Blanca Massif. The Pioneer fan extends westward between the Holbrook fan to the south and Uracca drainage and Zapata fan to the north. Dotted line outlines the quarry at the toe of the Pioneer fan and numbers in circles are locations of samples taken shown in Figure 4.5. Zapata fan active depositional lobe (1), northern quarry (2), southern quarry (3), and toe of Holbrook fan (4).

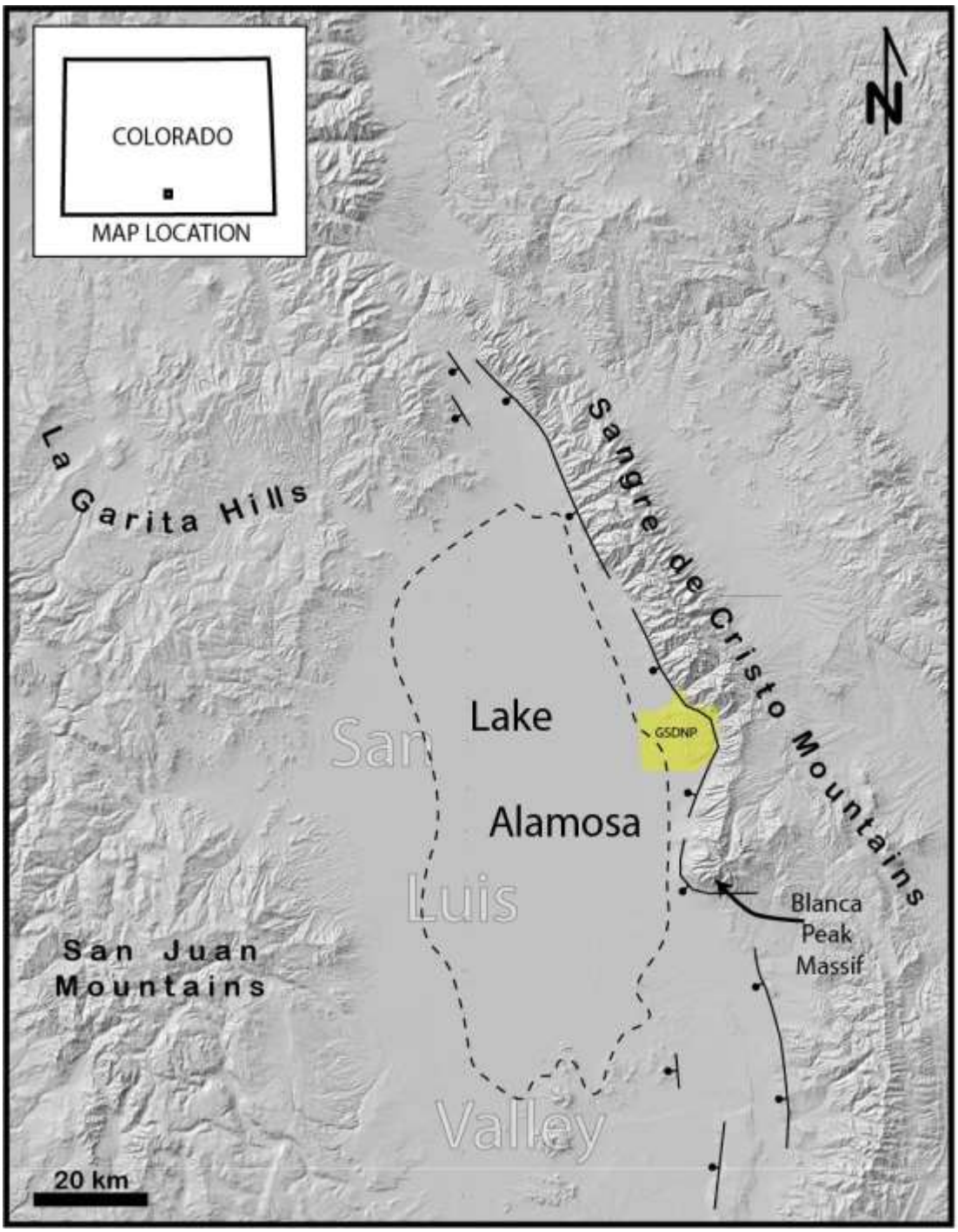

Figure 4.4. Hillshade of the northern portion of the San Luis Valley. The Sangre de Cristo normal fault flanks the western rangefront of the Sangre de Cristo Mountains, denoted by black line with bar and ball. The ball is on the downthrown side of the fault. Great Sand Dunes National Park is shown in yellow. The high stand extent of Lake Alamosa is shown by the black dotted line, after Machette et al. (2013).

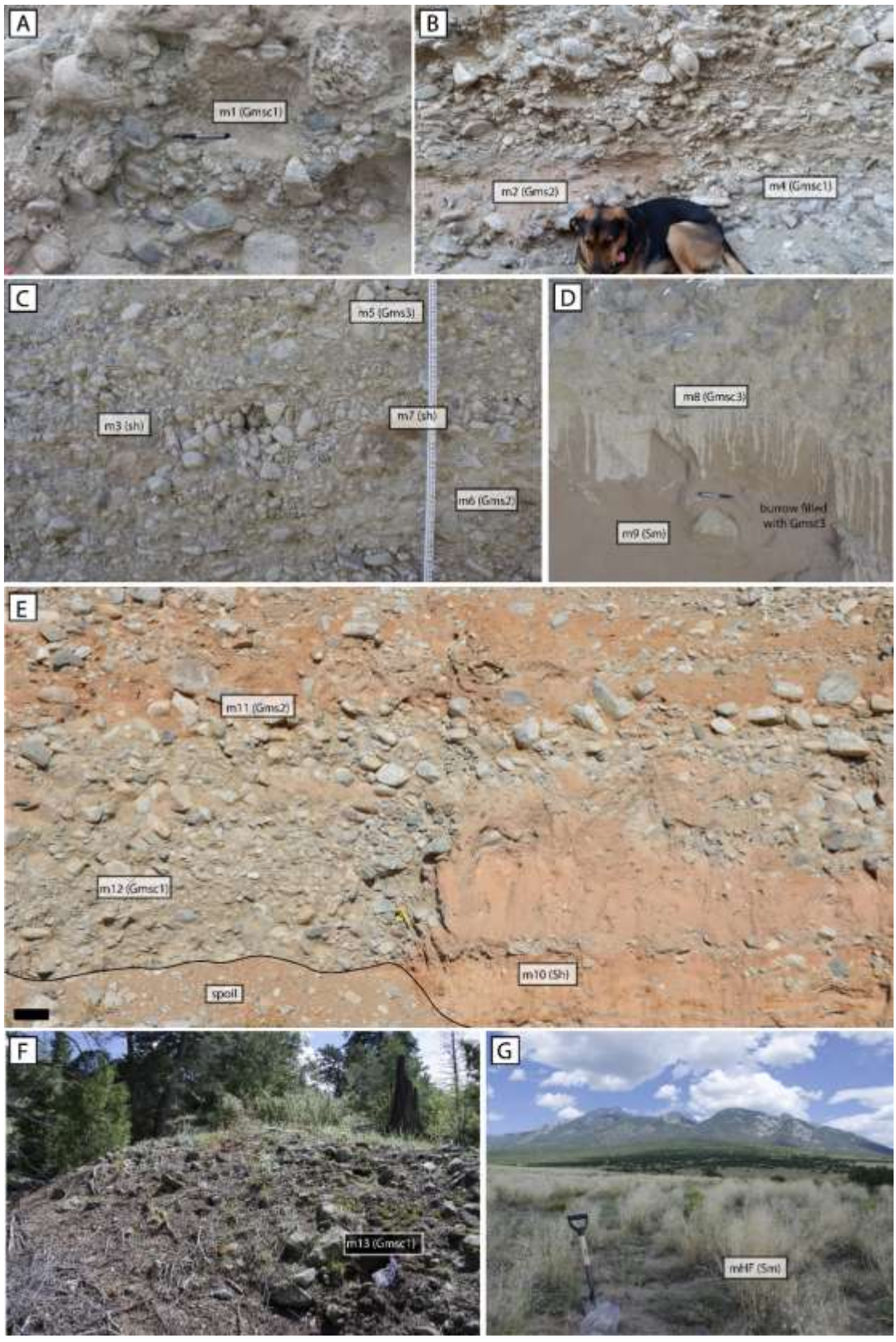
A
m1 (Gmsc1)
B
m2 (Gms2)
m4 (Gmsc1)
C
m5 (Gms3)
m3 (sh)
m7 (sh)
m6 (Gms2)
D
m8 (Gmsc3)
burrow filled with Gmsc3
m9 (Sm)
E
m11 (Gms2)
m12 (Gmsc1)
m10 (Sh)
spoil
F
m13 (Gmsc1)
G
m14F (Sm)

Figure 4.5. Sample locations, names, and associated facies used in this study. Location of each sample is reported in Table one and corresponding Figure 4.3. A) Sample m1 from facies Gmsc1, pencil for scale, B) sample m2 from facies Gms2 and sample m4 from facies Gmsc1, hound for scale, C) sample m3 and m7 from facies Sh, sample m5 from facies Gms3, and sample m6 from facies Gms2, stadia rod for scale (width is 4.6 cm), D) sample m8 from facies Gmsc3, and sample m9 from facies Sm, pen for scale. E) sample m10 from facies Sh, sample m11, from facies Gms2, and sample m12 from facies Gmsc1, black bar for scale (approximately 10 cm long), F) m13 from facies Gmsc1 on debris flow levee of Zapata fan surface Qay 3 (youngest), gallon zip-lock bag for scale, G) sample mHF from sand sheet (facies Sm) on toe of Holbrook alluvial fan, shovel for scale.

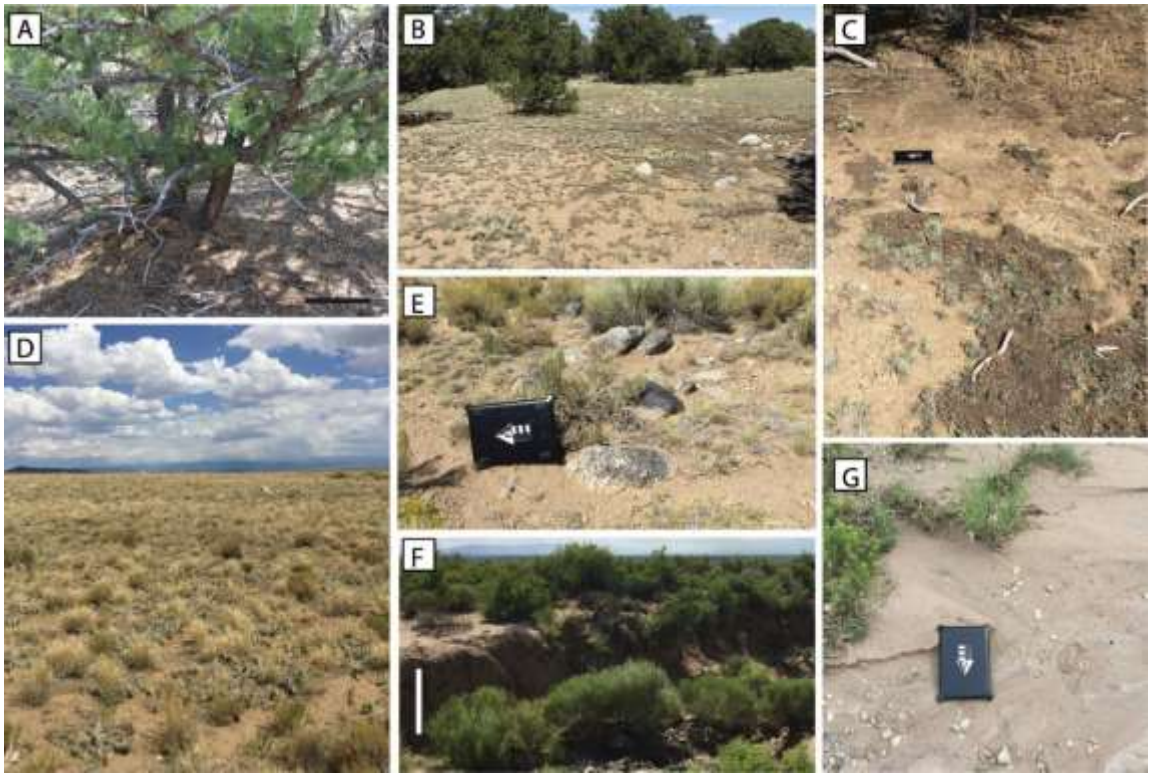

Figure 4.6. Deposit morphologies of alluvial fans that display evidence of eolian input. Photos A through C are taken at proximal to medial reach of fan and D through G were taken at distal reaches of fan. A) Base of Juniper tree buried by eolian and reworked fine-grained sediment. Black bar is ~50 cm. B) Smooth Qai surface with many fines filling spaces between boulder and cobble-sized clasts at. C) Fine sand, silt, and organic material mobilized by water on fan surface. Black case is 30 cm. D) Sand covered area of fan toe. E) Close up from photo D shown fine filling space in-between cobble and boulder-sized clasts at fan toe. Black case is 30 cm. F) Exposure of extensive fine sand/silt deposits on toe of fan. White bar is ~50 cm. G) Water reworked sand at toe of fan. Black case is 30 cm.

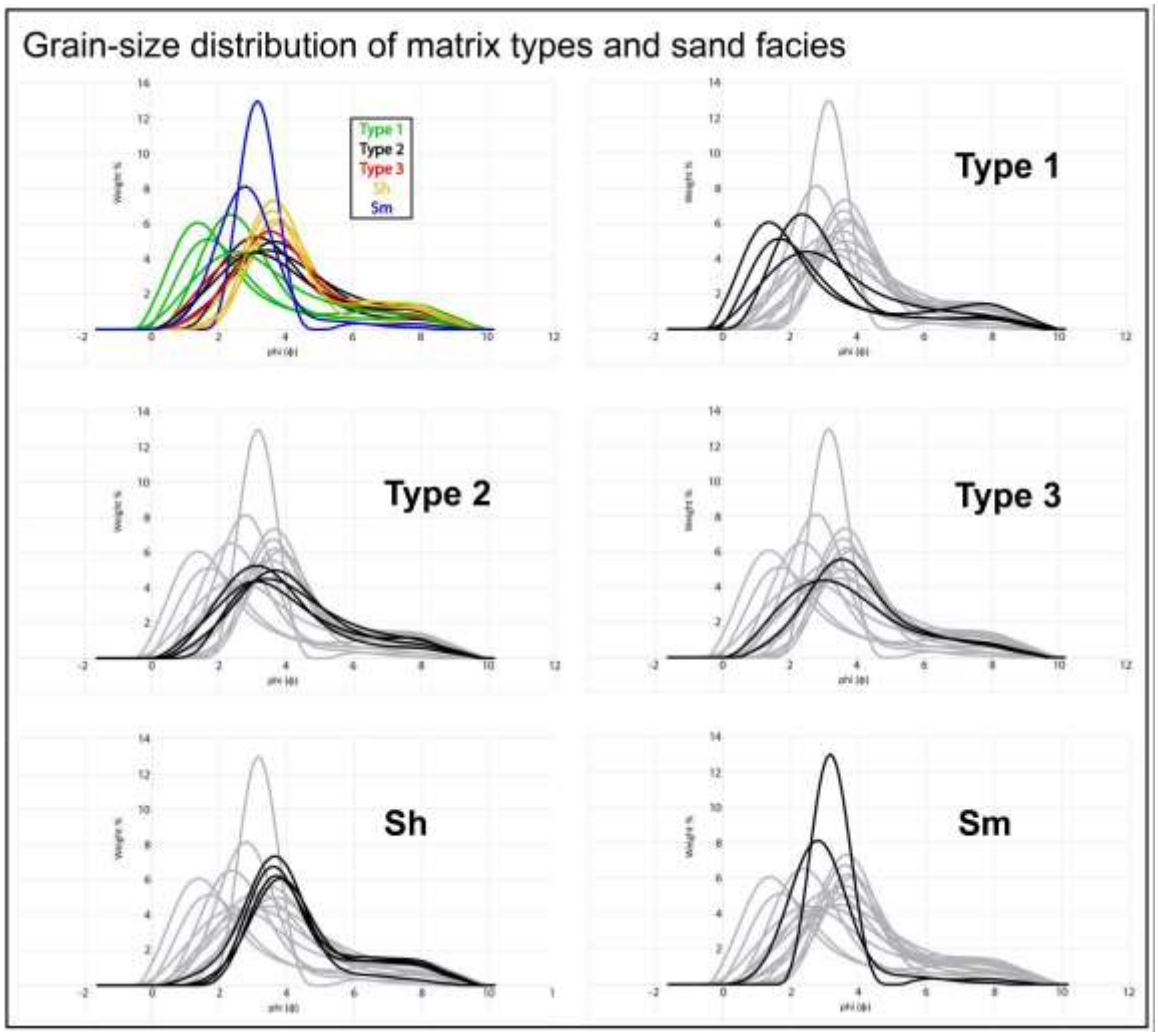

Figure 4.7. Grain-size plots of samples.

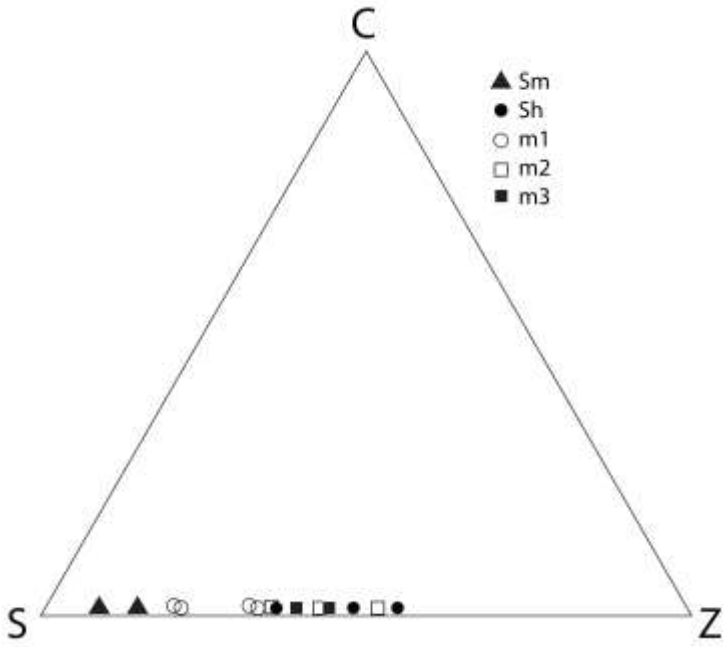

Figure 4.8. Sand (S)-silt (Z)-clay (C) ternary plot of samples from grain-size analysis.

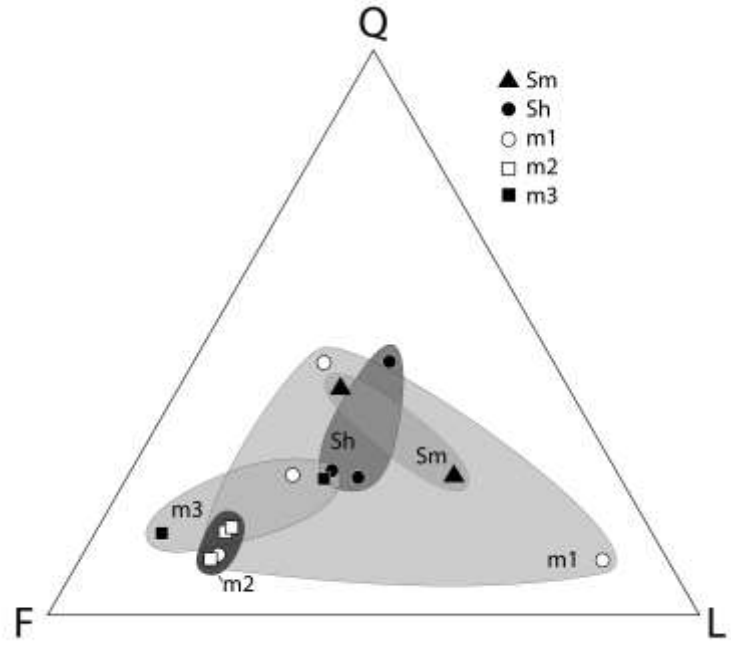

Figure 4.9. Quartz (Q)-feldspar (F)-lithic fragments (L) ternary plot of sample composition.

Table 4.1. Details of samples for grain-size analysis.

Sample	Facies	Fan (Location)[1]	Pre-seive weight (g)	Seived		total weight (g)	% <2 mm of total sample	Dissagregate peds	Number of runs through laser-analyzer
				<2 mm (g)	>2 mm (g)				
m-1	Gmsc1	Pioneer (2)	200	194.4	5.3	199.7	97.3	N/A	x3
m-2a*	Gmsc2	Pioneer (3)	47.2	39.7	7.4	47.1	84.3	Yes, > 2mm from m-2b	x2
m-2b	Gmsc2	Pioneer (3)	200	152.5	47.2	199.7	76.4	No	x2
m-3	Sh	Pioneer (3)	un-sieved						x2
m-4	Gmscn1	Pioneer (3)	200	177.1	24.1	201.2	88.0	N/A	x3
m-5	Gms3	Pioneer (3)	200	192.1	13.4	205.5	93.5	Yes	x3
m-6	Gms2	Pioneer (3)	un-sieved						x4
m-7	Sh	Pioneer (3)	un-sieved						x2
m-8	Gmsc3	Pioneer (2)	un-sieved						x2
m-9	Sm	Pioneer (2)	un-sieved						x2
m-10a	Sh	Pioneer (2)	un-sieved						x2
m-10b	Sh	Pioneer (2)	200	198.9	0.1	199	99.9	Yes	x2
m-11	Gms2	Pioneer (2)	200	178.7	21.3	200	89.4	Yes	x3
m-12	Gmsc1	Pioneer (2)	200	172.8	27.2	200	86.4	N/A	x2
m-13	Gmsc1	Zapata (1)	200	139.6	60	199.6	69.9	N/A	x2
m-HF	Sm	Holbrook (4)	200	196.6	3.6	200.2	98.2	N/A	x2

* this sample is the ped fraction of sample m-2b.

[1] location number corresponds with Figure 3.

Table 4.2. Verbal descriptions and grain-size statistics for each sample category. Values are averages with standard deviations for the number of samples reported in the count row.

		Matrix type 1	Matrix type 2	Matrix type 3	Sm	Sh
	SEDIMENT NAME	Fine silt to medium sand	Very coarse silt to very fine sand	Very coarse silt to fine sand	Very coarse silt to fine sand	Very coarse silt to very fine sand
	Sample count	4	4	2	2	4
FOLK AND WARD METHOD (ϕ)	MEAN (M_z):	3.02±0.48	3.97±0.33	3.83±0.18	3.0±0.2	4.28±0.46
	SORTING (σ_i):	1.03±0.28	0.88±0.08	0.87±0.13	0.4±0.1	0.76±0.18
	SKEWNESS (Sk_i):	0.42±0.11	0.25±0.02	0.25±0.01	0.1±0.1	0.33±0.15
	KURTOSIS (K_G):	1.19±0.29	1.09±0.10	1.12±0.07	1.2±0.3	1.14±0.13
FOLK AND WARD METHOD (Description)	MEAN:	Very fine to fine sand	Very coarse silt to very fine sand	Very fine sand	Fine to very fine sand	Very coarse silt to very fine sand
	SORTING:	Moderately to poorly sorted	Moderately sorted	Moderately sorted	Well to very well sorted	Moderately to well sorted
	SKEWNESS:	Very fine skewed	Fine skewed	Fine skewed	Fine skewed to symmetrical	Very fine to fine skewed
	KURTOSIS:	Leptokurtic to Platykirtic	Leptokurtic to Mesokurtic	Leptokurtic to Mesokurtic	Leptokurtic to Mesokurtic	Leptokurtic to Mesokurtic

Table 4.3. Generalized facies and matrix descriptions and interpretations.

Facies	Description	Interpretation
Gms	Poorly sorted, matrix-supported granule to boulder gravel deposit, unstratified	Sediment-gravity flow (debris flow) deposits
Gmsc	Poorly sorted, matrix- to clast-supported granule to boulder gravel deposit, unstratified	Sediment-gravity flow (debris flow) deposits
Matrix type 1	Moderately to poorly sorted fine silt to medium sand	Drainage basin derived matrix of debris flow
Matrix type 2	Moderately sorted very coarse silt to very fine sand	Significant eolian component, reworked into debris flow matrix
Matrix type 3	Moderately sorted very coarse silt to fine sand	Mixture of both drainage basin derived fines and eolian sediment
Sm	Well to very well sorted, massive, very coarse silt to fine sand	Eolian deposition
Sh	Moderately to well-sorted, horizonatally stratified, very coarse silt to very fine sand	Fluid-gravity flow (overland flow/ hyperconcentrated flow), reworked eolian sediment

CHAPTER FIVE

CONCLUSIONS

This dissertation examines the formative and modifying processes of debris-flow alluvial fans through sedimentological examination, both on the surface and in the sedimentary record, using the western rangefront of the Sangre de Cristo Mountains as a natural laboratory. These results provide improvements to the understanding of debris-flow alluvial fan formation and surface evolution, associating surface geomorphology and stratigraphic succession. The conclusions of this study address the objectives laid out in Chapter 1.

Sedimentary facies and surficial characteristics of primary deposition on debris-flow alluvial fans are discernable from those of secondary modifying processes. Sedimentary facies that record primary processes (debris flow) are matrix-supported gravel (Gms) and matrix- to clast-supported gravel (Gmsc). Primary processes also include hyperconcentrated flow deposits recorded in many facies that are more difficult to distinguish from secondary modifying processes, including massive gravel (Gm), low-angle stratified gravel (Gl), low-angle stratified, sandy matrix-supported gravel (GlSl), poorly-sorted massive sand (Smps), low-angle stratified sand (Sl), and horizontally stratified sand (Sh). Active depositional lobes are the loci of primary process sedimentation on debris-flow alluvial fans. Their surfaces are characterized by rough, boulder topography with distinctive debris-flow levees and lobes.

Sedimentary facies of secondary modifying processes on debris-flow alluvial fans are most commonly overland flow and include massive gravel (Gm), low-angle stratified gravel (Gl), low-angle stratified, sandy matrix-supported gravel (GlSl), and horizontally stratified gravel (Gh). Accumulation of wind-blown sediment is evident in facies that records its reworking by water. These facies include well-sorted massive sand (Smws), low-angle stratified sand (Sl), horizontally stratified sand (Sh), and ripple cross-laminated sand (Sr), and within the matrix of debris-flow facies (Gms and Gmsc, matrix type 2 and 3). Abandoned lobes of debris-flow alluvial fans are dominated by secondary modifying processes, though all areas of the fan are subject to reworking of sediment by overland flow and addition of eolian material. These surfaces are characterized by the degradation of original debris-flow deposit morphology, resulting in smoothing, and progressive incision on topographically higher surfaces.

Periods of surface development during phases of non-deposition are evident within the stratigraphic succession of alluvial fan deposits by representative sedimentary facies and pedogenic characteristics. The degree of soil development in combination with facies associations may provide information about the alluvial fan sub-environment (i.e. abandoned vs. depositional lobe) and insight to how long, relatively, a surface was stable. Additionally, infrared stimulated luminescence geochronology on facies that record periods of secondary modification offer numeric estimates to the fan dynamics that control surface development.

Input of eolian sediment on debris-flow alluvial fan surfaces has significant impact through surface smoothing. Here, it is shown that fan surface-smoothing involves

aggradation rather than exclusively erosional processes, illustrating that depositional and abandoned lobes are both characterized by deposition of different processes to different degrees.

Many sediment transport processes act on the debris-flow alluvial fans of the western Sangre de Cristo Mountains, the majority of which dominate the spaciotemporal extant of fans but are minor in fan aggradation (e.g. secondary modifying processes). Specific modifying processes are captured through facies and deposit morphology analysis with more precision than geomorphic expression alone. The significance of this approach is the application of these findings to fans and their deposits alike. Facies associated with specific surface processes provide insight to fan dynamics when working exclusively within the sedimentary record.

CUMULATIVE LITURATURE CITED

Anderson, R. S. and Anderson, S. P., 1990, Debris-flow benches; dune-contact deposits record paleo-sand dune positions in North Panamint Valley, Inyo County, California: Geology, v. 18, p. 524-527.

Anderson, R. S. and Haff, P. K., 1988, Simulation of eolian saltation: Science, v. 241, p. 820-823.

Aschoff, J. L., and Schmitt, J. G., 2008, Distinguishing syntectonic unconformity types to enhance analysis of growth strata: an example from the Cretaceous, southeastern Nevada, USA: Journal of Sedimentary Research, v. 78, p. 608-623.

Ashley, G.M., 1978. Interpretation of polymodal sediments: Journal of Geology, v. 86, p. 411 – 421.

Baas, J. H., Best, J. L., and Peakall, J., 2016, Predicting bedforms and primary current stratification in cohesive mixtures of mud and sand: Journal of the Geological Society, v. 173, p. 12-45.

Ballantyne, C. K., 2002, Paraglacial geomorphology: Quaternary Science Reviews, v. 21, p. 1935-2017.

Barbeau, D. L., 2003, A flexural model for the Paradox Basin: implications for the tectonics of the Ancestral Rocky Mountains, Basin Research, v. 15, p. 97-115.

Bateman, M. D., Frederick, C. D., Jaiswal, M. K., and Singhvi, A. K, 2003, Investigations into the potential effects of pedoturbation on luminescence dating: Quaternary Science Reviews, v. 22, p. 1169-1176.

Bateman, M. D., Boulter, C. H., Carr, A. S., Frederick, C. D., Peter, D., and Wilder, M., 2007, Preserving the palaeoenvironmental record in drylands: bioturbation and its significance for luminescence-derived chronologies: Sedimentary Geology, v. 195, p. 5-19.

Beaty, C.B., 1961, Topographic effects of faulting: Death Valley, California: Annals of the Association of American Geographers, v. 51, p. 234-240.

Beaty, C. B., 1963, Origin of alluvial fans, white mountains, California and Nevada: Annals of the Association of American Geographers, v. 53, p. 516-535.

Berry, M. E., 1987, Morphological and chemical characteristics of soil catenas on Pinedale and Bull Lake moraine slopes in the Salmon River Mountains, Idaho: Quaternary Research, v. 28, p. 210-225.

Bertran, P., Bateman, M. D., Hernandedz, M., Mercier, N., Millet, D. Sitzia, L. and Tastet, J.-P., 2011, Inland aeolian deposits of south-west France: facies, stratigraphy and chronology: Journal of Quaternary Science, v. 26, p. 374-388.

Birkeland, P. W., 1984, Holocene soil chronofunctions, Southern Alps, New Zealand: Geoderma, v. 34, p. 115-134.

Birkeland, P. W. and Burke, R. M., 1988, Soil catena chronosequences on eastern Sierra Nevada moraines, California, USA: Arctic and Alpine Research, v. 20, p. 473-484.

Birkeland, P. W., 1999, Soils and geomorphology, third edition. Oxford University Press.

Blair, T. C., 1987, Sedimentary processes, vertical stratification sequences, and geomorphology of the Roaring River Alluvial Fan, Rocky Mountain National Park, Colorado: Journal of Sedimentary Petrology, v. 57, p. 1-18.

Blair, T.C., 1999, Cause of dominance by sheetflood vs. debris-flow processes on two adjoining alluvial fans, Death Valley, California: Sedimentology, v. 46, p. 1015-1028.

Blair, T. C., 2000, Sedimentology and progressive tectonic unconformities of the sheetflood-dominated Hell's Gate alluvial fan, Death Valley, California: Sedimentary Geology, v. 132, p. 233-262.

Blair, T. C. and McPherson, J., 1992, The Trollheim alluvial fan and facies model revisited. Geological Society of America Bulliten, v. 104, p. 762-769.

Blair, T.C., and McPherson, J. G., 1994, Alluvial fan processes and forms, *in* Parsons, A.J., and Abrahams, A.D., eds., Geomorphology of desert environments: London, Chapman & Hall, p. 354-402.

Blair, T. C., and McPherson, J. G., 1998, Recent debris-flow processes and resultant form and facies of the Dolomite alluvial fan, Owens Valley, California: Journal of Sedimentary Research, v. 68, p. 801-818.

Blair, T.C., and McPherson, J. G., 2009, Alluvial fan processes and forms, *in* Parsons, A.J., and Abrahams, A.D., eds., Geomorphology of desert environments, 2nd Edition: Berlin, Springer, p. 413-467.

Blott, S. J., and Pye, K., 2001, GRADISTAT: a grain size distribution and statistics package for the analysis of unconsolidated sediments: Earth surface processes and Landforms, v. 26, p. 1237-1248.

Blott, S. J., and Pye, K., 2012, Particle size scales and classification of sediment types based on particle size distributions: Review and recommended procedures: Sedimentology, v. 59, p. 2071-2096.

Bockheim, J. G., 1980, Solution and use of chronofunctions in studying soil development: Geoderma, v. 24, p. 71-85.

Brister, B. S., and Gries, R. R., 1994, Tertiary stratigraphy and tectonic development of the Alamosa basin (northern San Luis Basin), Rio Grande rift, south-central Colorado, *in* Keller, G. R., and Cather, S. M., eds., Basins of the Rio Grande Rift: Structure, Stratigraphy, and Tectonic Setting: Boulder, Colorado, Geological Society of America Special Paper 291.

Brubaker, K. M., Myers, W. L., Drohan, P. J., Miller, D. A., and Boyer, E. W., 2013, The use of LiDAR terrain data in characterizing surface roughness and microtopography: Applied and Environmental Soil Science, pp. 13.

Bull, W.B., 1972, Recognition of alluvial-fan deposits in the stratigraphic record, *in* Rigby, J.K., and Hamblin, W.K., eds., Recognition of ancient sedimentary environments: Society of Economic Paleontologists and Mineralogists Special Publication 16, p. 63–83.

Bull, W. B., 1977, The alluvial fan environment, Bull, W. B: Progress in Physical Geography: Earth and Environment, p. 222–270.

Calhoun, N. C., and Clague, J. J., 2018, Distinguishing between debris flows and hyperconcentrated flows: an example from the eastern Swiss Alps: Earth Surface Processes and Landforms, v. 43, p. 1280-1294.

Cannon, S. H., Gartner, J. E., Parrett, C., and Parise, M., 2003, Wildfire-related debris-flow generation through episodic progressive sediment-bulking processes, western USA, *in* Rickenmann, D. and Chen-lung, C., eds., Debris-flow hazards mitigation: mechanics, prediction, p. 71-82.

Chapin, C. E. and Cather, S. M., 1994, Tectonic setting of the axial basins of the northern and central Rio Grande rift, *in* Keller, G. R., and Cather, S. M., eds., Basins of the Rio Grande Rift: Structure, Stratigraphy, and Tectonic Setting: Boulder, Colorado, Geological Society of America Special Paper 291.

Clarke, M. L., 1994, Infra-red stimulated luminescence ages from aeolian sand and alluvial fan deposits from the eastern Mojave Desert, California. Quaternary Science Reviews, v. 13, p. 533-538.

Coe, J. A., Kinner, D. A., and Godt, J. W., 2008, Initiation conditions for debris flows generated by runoff at Chalk Cliffs, central Colorado: Geomorphology, v. 96, p. 270-297.

Costa, J. E., 1984, Physical geomorphology of debris flows, *in* Costa, J. E. and Fleisher, P. J., eds., Developments and applications of geomorphology, p. 268-317.

Costa, J. E., 1988, Rheologic, geomorphic, and sedimentologic differentiation of water floods, hyperconcentrated flows, and debris flows: Flood Geomorphology, p. 113-122.

D'Arcy, M., Whittaker, A. C., and Roda-Boluda, D. C., 2017 Measuring alluvial fan sensitivity to past climate changes using a self-similarity approach to grain-size fining, Death Valley, California: Sedimentology, v. 64, p. 388-424.

de Haas, T., Ventra, D., Carbonneau, P. E., and Kleinhans, M. G., 2014, Debris-flow dominance of alluvial fans masked by runoff reworking and weathering: Geomorphology, v. 217, p. 165-181.

de Haas, T., L. Braat, J. R. F. W. Leuven, I. R. Lokhorst, and M. G. Kleinhans, 2015, Effects of debris flow composition on runout, depositional mechanisms, and deposit morphology in laboratory experiments: Journal of Geophysical Research: Earth Surface, v. 120, 1949-1972

de Haas, T., van den Berg, W., Braat, L., and Kleinhans, M. G., 2016, Autogenic avulsion, channelization and backfilling dynamics of debris-flow fans: Sedimentology, v. 63, p. 1596-1619.

de Haas, T., Densmore, A. L., Stoffel, M., Suwa, H., Imaizumi, F., Ballesteros-Cánovas, J. A., and Wasklewicz, T., 2018, Avulsions and the spatio-temporal evolution of debris-flow fans: Earth-Science Reviews, v. 177, p. 53-75.

de Haas, T., Densmore, A. L., den Hond, T., and Cox, N. J., 2019, Fan-surface evidence for debris-flow avulsion controls and probabilities, Saline Valley, California: Journal of Geophysical Research: Earth Surface, v. 124, p.1118-1138.

Demko, T. M., Currie, B. S., and Nicoll, K. A., 2004, Regional paleoclimatic and stratigraphic implications of paleosols and fluvial/overbank architecture in the Morrison Formation (Upper Jurassic), Western Interior, USA: Sedimentary Geology, v. 167, p. 115-135.

Denny, C. S., 1967, Fans and pediments: American Journal of Science, v. 265, p. 81-105.

Densmore, A. L., Philip, A. L., and Simpson, G., 2007, Development and response of a coupled catchment fan system under changing tectonic and climatic forcing: Journal of Geophysical Research, v. 112, F01002.

Druitt, T. H., 1995, Settling behaviour of concentrated dispersions and some volcanological applications. Journal of Volcanology and Geothermal Research, v. 65, p. 27-39.

Dühnforth, M., Densmore, A. L., Ivy-Ochs, S., Allen, P. A., and Kubik, P. W., 2007, Timing and patterns of debris flow deposition on Shepherd and Symmes creek fans, Owens Valley, California, deduced from cosmogenic 10Be: Journal of Geophysical Research: Earth Surface, v. 112(F3).

Dünforth, M., 2007, Sediment flux and deposition on arid-region fans, eastern California, USA [Ph.D. thesis]: Zurich, Swiss Federal Institute of Technology.

Fisher, R. V., 1983, Flow transformations in sediment gravity flows: Geology, v. 11, p. 273-274.

Folk, R. L., and Ward, W. C., 1957, Brazos River bar [Texas]; a study in the significance of grain size parameters: Journal of Sedimentary Research, v. 27, p. 3-26.

Folk, R. L., 1964, A review of grain-size parameters: Sedimentology, v. 6, p. 73-93.

Frank, F., McArdell, B. W., Huggel, C., and Vieli, A., 2015, The importance of entrainment and bulking on debris flow runout modeling: examples from the Swiss Alps: Natural Hazards and Earth System Sciences, v. 15, p. 2569-2583.

Frankel, K. L., and Dolan, J. F., 2007, Characterizing arid region alluvial fan surface roughness with airborne laser swath mapping digital topographic data. Journal of Geophysical Research: Earth Surface, v. 112(F2).

Fryberger, S. G., Ahlbrandt, T. S., and Andrews, S., 1979, Origin, sedimentary features, and significance of low-angle eolian ‘sand-sheet’ deposits, Great Sand Dunes National Monument and vicinity, Colorado: Journal of Sedimentary Petrology, v. 49, p. 733-746.

Fu, Q. and Sun, W., 2001, Mie theory for light scattering by a spherical particle in an absorbing medium: Applied Optics, v. 40, p. 1354-1361.

Gile, L. H., 1981, Soils and geomorphology in the Basin and Range area of southern New Mexico: Guidebook to the Desert Project, New Mexico: Bureau of Mines and Mineral Resources Memoir v. 39, 222 p.

Gillette, D.A., Adams, J., Endo, A., Smith, D., and Kihl, R., 1980, Threshold velocities for input of soil particles into the air by desert soils: Journal of Geophysical Research v. 85 (C10), p. 5621–5630.

Goudie, A.S., Middleton, N.J., 2006, Desert Dust in the Global System. Springer, Berlin.

Hajek, E. A., and Straub, K. M., 2017, Autogenic sedimentation in clastic stratigraphy: Annual Review of Earth and Planetary Sciences, v. 45, p. 681-709.

Harden, J. W., 1990, Soil development on stable landforms and implications for landscape studies: Geomorphology, v. 3, p. 391-398.

Harrison, S.P., Kohfeld, K.E., Roelandt, C., and Claquin, T., 2001, The role of dust in climate changes today, at the last glacial maximum and in the future: Earth-Science Reviews v. 54, p. 43–80.

Harvey, A. M., and Wells, S. G., 2003, Late Quaternary variations in alluvial fan sedimentologic and geomorphic processes, Soda Lake basin, eastern Mojave Desert, California. Special Papers-Geological Society of America, p. 207-230.

Harvey, A.M., 2011, Dryland alluvial fans, *in* Thomas, D.S.G., ed., Arid zone geomorphology: Process, form and change in drylands, Wiley, Chichester, p. 333-371.

Hooke, R. L., 1967, Processes on arid-region alluvial fans: The Journal of Geology, v. 75, p. 438-460.

Hooke, R. L., Blair, T. C., and McPherson, J. G., 1993, The Trollheim alluvial fan and facies model revisited: Discussion and reply. Geological Society of America Bulletin, v. 105, p. 563-567.

Horton, B. K., and Schmitt, J. G., 1996, Sedimentology of a lacustrine fan-delta system, Miocene Horse Camp Formation, Nevada, USA: Sedimentology, v. 43, p. 133-155.

Hoy, R. and Ridgeway, K., 2002, Syndepositional thrust-related deformation and sedimentation in an Ancestral Rocky Mountains basin, Central Colorado trough, Colorado, USA: GSA Bulletin, v. 144, no. 7, p. 804-828.

Hsu, L. and Pelletier, J. D., 2004, Correlation and dating of Quaternary alluvial-fan surfaces using scarp diffusion: Geomorphology v. 60, p. 319-335.

Hudson, M. R., and Grauch, V. J. S., 2013, New Perspectives on Rio Grande Rift Basins: From Tectonics to Groundwater: Geological Society of America Special Paper, v. 494.

Iverson, R. M., 1997, The physics of debris flows: Reviews of Geophysics v. 35, p. 245-296.

Iverson, R. M., Reid, M. E., Logan, M., LaHusen, R. G., Godt, J. W., and Griswold, J. P., 2011, Positive feedback and momentum growth during debris-flow entrainment of wet bed sediment: Nature Geoscience, v. 4, p. 116.

Jenny, H., 1941, factors of soil formation. McGraw-Hill, New York, 281 p.

Jenny, H. 1980, The soil resource —origin and behavior, Springer-Verlag, New York, 377 p.

Jerolmack, D. J., and Paola, C., 2010, Shredding of environmental signals by sediment transport: Geophysical Research Letters, v. 37, doi:10.1029/2010GL044638.

Johnstone, S. A., Hudson, A. M., Nicovich, S., Ruleman, C. A., Sare, R. M., and Thompson, R. A., 2018, Establishing chronologies for alluvial-fan sequences with analysis of high-resolution topographic data: San Luis Valley, Colorado, USA: Geosphere, v. 14, p. 2487-2504.

Kellogg, K., 1999, Neogene basins of the northern Rio Grande Rift-partitioning and asymmetry inherited from Laramide and older uplifts: Tectonphysics, v. 305, p. 141-152.

Kraus, M. J., 1999, Paleosols in clastic sedimentary rocks: their geologic applications: Earth-Science Reviews, v. 47, p. 41-70.

Lancaster, N., 1996, Response of eolian geomorphic systems to minor climate change: examples from the southern California deserts: Geomorphology, v. 19, p. 333-347.

Lancaster, N., and Tchakerian, V. P., 1996, Geomorphology and sediments of sand ramps in the Mojave Desert: Geomorphology, v. 17, p. 151-165.

Lecce, S. A, 1990, The alluvial fan problem in Alluvial fans: a field approach, v. 3, p. 24.

Lindsey, D. A., Johnson, B. R., and Andriessen, P. A. M., 1983, Laramide and Neogene structure of the northern Sangre de Cristo Range, south-central Colorado. Rocky Mountain foreland basins and uplifts: Denver, Colorado, Rocky Mountain Association of Geologists, p. 219-228.

Lindsey, D. A., Clark, R. F., and Soulliere, S. J., 1986, Minturn and Sangre de Cristo Formations of Southern Colorado: A Prograding Fan Delta and Alluvial Fan Sequence Shed from the Ancestral Rocky Mountains in Paleotectonics and sedimentation: AAPG, v. 41, p. 541-561.

Lindsey, D. A., 1998, Laramide structure of the central Sangre de Cristo Mountains and adjacent Raton basin, southern Colorado: The Mountain Geologist, v. 35.

Lipman, P. W., 1975, Evolution of the Platoro caldera complex and related volcanic rocks, southeastern San Juan Mountains, Colorado: U.S. Geological Survey Professional Paper, v. 852, no. 128, p. 197.

Lipman, P. W., 2007, Incremental assembly and prolonged consolidation of Cordilleran magma chambers: Evidence from the Southern Rocky Mountain volcanic field: Geosphere, v. 3, p. 42-70.

Loizeau, J. L., Arbouille, D., Santiago, S., and Vernet, J. P., 1994, Evaluation of a wide range laser diffraction grain size analyzer for use with sediments: Sedimentology, v. 41, p. 353-361.

Lowe, D. R. and Guy, M., 2000. Slurry-flow deposits in the Britannia Formation (Lower Cretaceous), North Sea; a new perspective on the turbidity current and debris flow problem. Sedimentology v. 47, p. 31-70.

Machette, Michael N., 1978, Dating Quaternary faults in the southwestern United States by using buried calcific paleosols: Journal of Research of the United States Geological Survey, v. 6, p. 369-382.

Machette, M. N., 1985, Calcific soils of the southwestern United States. Soils and Quaternary geology of the southwestern United States: Geological Society of America Special Paper, v. 203, p. 1-21.

Machette, M.N., Marchetti, D.W., and Thompson, R.A., 2007, Ancient Lake Alamosa and the Pliocene to middle Pleistocene evolution of the Rio Grande, in Machette, M.N., Coates, M.M., and Johnson, M.L., eds., 2007 Rocky Mountain Section Friends of the Pleistocene Field Trip—Quaternary geology of the San Luis Basin of Colorado and New Mexico, September 7-9, 2007: U.S. Geological Survey Open-File Report 2007-1193, p. 157-167.

Machette, M. N., Thompson, R. A., Marchetti, D. W., and Smith, R. S., 2013, Evolution of ancient Lake Alamosa and integration of the Rio Grande during the Pliocene and Pleistocene: Geological Society of America Special Papers, v. 494, p. 1-20.

Madole, R. F., Romig, J. H., Aleinikoff, J. N., VanSistine, D. P., and Yacob, E. Y., 2008, On the origin and age of the Great Sand Dunes, Colorado: Geomorphology, v. 99, p. 99-119.

Markewich, H. W., Pavich, M. J., and Wysocki, D. A., 2016, Soils as Relative-Age Dating Tools. International Encyclopedia of Geography: People, the Earth, Environment and Technology: People, the Earth, Environment and Technology, p. 1-14.

Matmon, A., Nichols, K., and Finkel, R., 2006, Isotopic insights into smoothening of abandoned fan surfaces, Southern California: Quaternary Research, v. 66, p. 109-118.

McCalpin, J.P., 1982, Quaternary geology and neotectonics of the west flank of the northern Sangre de Cristo Mountains, south-central Colorado: Colorado School of Mines Quarterly, n. 77, p. 97.

McCalpin, J., 1986, Quaternary tectonics of the Sangre de Cristo and Villa Grove fault zones: Contributions to Colorado seismicity and tectonics—A: p. 59-64.

McCalpin, J.P., 2006, Active faults and seismic hazards to infrastructure at Great Sand Dunes National Monument and Preserve: Crestone, Colorado: unpublished report by GEO-HAZ Consulting, Inc., 49 p., 1 oversize plate.

McDonald, R. R. and Anderson, R., 1996, Constraints on eolian grain flow dynamics through laboratory experiments on sand slopes: Journal of Sedimentary Research, v. 66, p. 642–653.

McDonald, E.V., McFadden, L.D., Wells, S.G., 2003. Regional response of alluvial fans to the Pleistocene–Holocene climatic transition, Mojave Desert, California, *in* Enzel, Y., Wells, S.G., Lancaster, N., eds., Paleoenvironments and Paleohydrology of the Mojave and Southern Great Basin Deserts: Geological Society of America Special Paper, 368, p. 189–205.

McFadden, L. D., Wells, S. G., and Dohrenwend, J. C., 1986, Influences of Quaternary climatic changes on processes of soil development on desert loess deposits of the Cima volcanic field, California: Catena, v. 13, p. 361-389.

McFadden, L.D., Wells, S.G., and Jercinovich, M.J., 1987, Influences of eolian and pedogenic processes on the origin and evolution of desert pavements: Geology, v. 15, p. 504-508.

McFadden, L. D., Ritter, J. B., and Wells, S. G., 1989, Use of multiparameter relative-age methods for age estimation and correlation of alluvial fan surfaces on a desert piedmont, eastern Mojave Desert, California: Quaternary Research, v. 32, p. 276-290.

Meyer, G. A., Wells, S. G., Balling Jr, R. C., and Jull, A. T., 1992, Response of alluvial systems to fire and climate change in Yellowstone National Park: Nature, v. 357, p. 147.

Miall, A. D., 1978, Lithofacies and vertical profile models in braided river deposits: a summary: Geological Survey of Canada, p. 597-604.

Middleton, G.V., 1976. Hydraulic interpretation of sand size distributions: Journal of Geology, v. 84, p. 405-426.

Moscariello, A., Marchi, L., Maraga, F., and Mortara, G., 2002, Alluvial fans in the Italian Alps: sedimentary facies and processes in Flood and Megaflood Processes and Deposits: Recent and Ancient Examples, p. 141-66.

Muhs, D. R., Bettis, E. A., Chan, M. A., and Archer, A. W., 2003, Quaternary loess-paleosol sequences as examples of climate-driven sedimentary extremes: Geological Society of America Special Paper 370, p. 53-74.

Mushkin, A. and Gillespie, A. R., 2005, Estimating sub-pixel surface roughness using remotely sensed stereoscopic data: Remote Sensing of Environment, v. 99, p. 75-83.

Mushkin, A., Sagy, A., Trabelci, E., Amit, R., and Porat, N., 2014, Measuring the time and scaledependency of subaerial rock weathering rates over geologic time scales with ground-based LiDAR: Geology, v. 42, no. 12, p. 1063–1066

Nemec, W., and Steel, R., 1984, Alluvial and coastal conglomerates: their significant features and some comments on gravelly mass-flow deposits: *in* Koster, E. H. and Steel, R. J., eds., Sedimentology of Gravels and Conglomerates. Canadian Society of Petroleum Geologists, Memoir 10, 1984, p. 1-31.

Owen, L. A., Finkel, R. C., Haizhou, M., and Barnard, P. L., 2006, Late Quaternary landscape evolution in the Kunlun Mountains and Qaidam Basin, Northern Tibet: a framework for examining the links between glaciation, lake level changes and alluvial fan formation: Quaternary International, v. 154, p. 73-86.

Palmquist, R. C., 2019, Alluvial fan sediments and surface ages resulting from differing climatic and tectonic conditions in Star Valley, Wyoming, USA: Catena, v. 181, 104050.

Pelletier, J.D., 2006, Sensitivity to playa windblown-dust emissions to climatic and anthropogenic change: Journal of Arid Environments, v. 66, p. 62–75.

Pelletier, J. D., 2007, Cantor set model of eolian dust deposits on desert alluvial fan terraces: Geology, v. 35, p. 439-442.

Pierce, K.L., 2003, Pleistocene glaciation of the Rocky Mountains, in Gillespie, A.R., Porter, S.C., and Atwater, B.F., eds., The Quaternary Period in the United States: Amsterdam, Elsevier, p. 63–76.Quigley, M.C., Sandiford, M., and Cupper, M.L., 2007, Distinguishing tectonic from climatic controls on range-front sedimentation: Basin Research, v. 19, p. 491-505.

Pierson, T. C., Costa, J. E., and Vancouver, W., 1987, A rheologic classification of subaerial sediment-water flows. Debris flows/avalanches: process, recognition, and mitigation: Reviews in Engineering Geology, v. 7, p. 1-12.

Pierson, T. C., 2005, Hyperconcentrated flow—transitional process between water flow and debris flow, *in* Jakob, M. and Hungr, O., eds., Debris-flow hazards and related phenomena. Springer, Berlin, Heidelberg, 2005, p. 159-202.

Postma, G., 1986, Classification for sediment gravity-flow deposits based on flow conditions during sedimentation: Geology v. 114, p. 291-294.

Pye, K., 1995, Nature, origin, and accumulation of loess: Quaternary Science Reviews, v. 15, p. 653-667.

Railback, B.L., Gibbard, P.L., Head, M.J., Voarintsoa, N.R.G., Toucanne, S., 2015, An optimized scheme of lettered marine isotope substages for the last 1.0 million years, and the climatostratigraphic nature of isotope stages and substages: Quaternary Science Reviews, v. 111, p. 94-106.

Reheis, M. C., Goodmacher, J. C., Harden, J. W., McFadden, L. D., Rockwell, T. K., Shroba, R. R., Sowers, J. M., and Taylor, E. M., 1995, Quaternary soils and dust deposition in southern Nevada and California. Geological Society of America Bulletin, v. 107, p. 1003-1022.

Reheis, M.C., Kihl, R., 1995, Dust deposition in southern Nevada and California, 1984–1989: relations to climate, source area, and source lithology: Journal of Geophysical Research v. 100 (D5), p. 8893-8918.

Reheis, M. C., 2006, A 16-year record of eolian dust in Southern Nevada and California, USA: Controls on dust generation and accumulation: Journal of Arid Environments, v. 67, p. 487-520.

Reheis, M.C., Urban, F.E., 2011, Regional and climatic controls on seasonal dust deposition in the southwestern U. S: Aeolian Research, v. 3, p. 3-21.

Riba, O., 1976, Syntectonic unconformities of the Alto Cardener, Spanish Pyrenees: a genetic interpretation: Sedimentary Geology, v. 15, p. 213-233.

Ritter, J. B., Miller, J. R., Enzel, Y., Howes, S. D., Nadon, G., Grubb, M. D., and Summa, C. L., 1993, Quaternary evolution of Cedar Creek alluvial fan, Montana: Geomorphology, v. 8, p. 287-304.

Ritter, J.B., Miller, J.R., Enzel, Y., and Wells, S.G., 1995, Reconciling the roles of tectonism and climate in Quaternary alluvial fan evolution: Geology, v. 23, p. 245-248.

Ruleman, C.A., and Machette, M.N, 2007, An overview of the Sangre de Cristo fault system and new insights to interactions between Quaternary faults in the Northern Rio Grande Rift: *in* Machette, M.N., Coates, M.M., and Johnson, M.L., eds., 2007 Rocky Mountain Section Friends of the Pleistocene Field Trip—Quaternary

geology of the San Luis Basin of Colorado and New Mexico, September 7-9, 2007: U.S. Geological Survey Open-File Report 2007-1193, p. 187-197.

Scheinert, C., Wasklewicz, T., and Staley, D., 2012, Alluvial fan dynamics—revisiting the field: Geography Compass, v. 6, p. 752-775.

Schokker, J. and Koster, E. A., 2004, Sedimentology and facies distribution of Pleistocene cold-climate aeolian and fluvial deposits in the Roer Valley Graben (southeastern Netherlands): Permafrost and Periglacial Processes, v. 15, p. 1-20.

Scott, K. M., 1988, Origin, behavior, and sedimentology of prehistoric catastrophic lahars at Mount St. Helens, Washington: Geological Society of America Special Papers 229, p. 23-36.

Scott, K. M., and Vallance, J. W., 1995, Debris flow, debris avalanche and flood hazards at and downstream from Mount Rainier, Washington: USGS Hydrologic Investigations Atlas 729: 2 sheets and accompanying pamphlet, US Geological Survey, Reston, VA.

Scott, K. M., Vallance, J. W., and Pringle, P. T., 1995, Sedimentology, behavior, and hazards of debris flows at Mount Rainier, Washington: US Geological Survey Open-File Report, n. 1547, 106 p.

Shaw, C., and Karlstrom, K. 1999, The Yavapai-Mazatzal boundary in the Southern Rocky Mountains: Rocky Mountain Geology, v. 34, p. 37-52.

Shepard, C., Pelletier, J. D., Schaap, M. G., and Rasmussen, C., 2018, Signatures of obliquity and eccentricity in soil chronosequences: Geophysical Research Letters, v. 45, p. 11-147.

Shroba, R. R., Thompson, R. A., and Ruleman, C., 2007, Possible role of eolian sediment in the genesis of boulder debris-flow deposits on the lower flanks of Ute Mountain, northern Taos Plateau volcanic field, New Mexico, *in* Machette, M.N., Coates, M.M., and Johnson, M.L., eds., 2007 Rocky Mountain Section Friends of the Pleistocene Field Trip—Quaternary geology of the San Luis Basin of Colorado and New Mexico, September 7-9, 2007: U.S. Geological Survey Open-File Report 2007-1193, p. 181-185.

Smith, G. A., 2000, Recognition and significance of streamflow-dominated piedmont facies in extensional basins: Basin research, v. 12, p. 399-411.

Sohn, Y.K., 1997. On traction-carpet sedimentation: Journal of Sedimentary Research. v. 67, p. 502-509.

Sohn, Y. K., Rhee, C. W., and Kim, B. C., 1999, Debris flow and hyperconcentrated flood-flow deposits in an alluvial fan, northwestern part of the Cretaceous Yongdong Basin, Central Korea: The Journal of Geology, v. 107, p. 111-132.

Southard, J.B. and Boguchwal, L.A., 1990, Bed configurations in steady unidirectional water flows. Part 2. Synthesis of flume data: Journal of Sedimentary Petrology, v. 60, p. 658–679.

Straub, K. M., Paola, C., Mohrig, D., Wolinsky, M. A., and George, T., 2009, Compensational stacking of channelized sedimentary deposits: Journal of Sedimentary Research, v. 79, p. 673-688.

Straub, K. M., and Pyles, D. R., 2012, Quantifying the hierarchical organization of compensation in submarine fans using surface statistics: Journal of Sedimentary Research, v.82, p. 889-898.

Sun, D., Bloemendal, J., Rea, D. K., Vandenberghe, J., Jiang, F., An, Z., and Su, R., 2002, Grain-size distribution function of polymodal sediments in hydraulic and aeolian environments, and numerical partitioning of the sedimentary components: Sedimentary Geology, v. 152, p. 263-277.

Suppe, J., Sàbat, F., Munoz, J. A., Poblet, J., Roca, E., and Vergés, J., 1997, Bed-by-bed fold growth by kink-band migration: Sant Llorenç de Morunys, eastern Pyrenees: Journal of Structural Geology, v. 19, p. 443-461.

Swanson-Hysell, N., and Barbeau, D. L. Jr., 2007, The diachroneity of alluvial-fan lithostratigraphy? A test case from southeastern Ebro basin magnetostratigraphy: Earth and Planetary Science Letters, v. 262, p. 343-362.

Sweeney, M. R., and Loope, D. B., 2001, Holocene dune-sourced alluvial fans in the Nebraska Sand Hills: Geomorphology, v. 381, p. 31-46.

Sweeney, M. R., McDonald, E. V., and Etyemezian, V., 2011, Quantifying dust emissions from desert landforms, eastern Mojave Desert, USA: Geomorphology, v. 135, p. 21-34.

Tipper, J. C., 2014, The importance of doing nothing: stasis in sedimentation systems and its stratigraphic effects: Geological Society of London, Special Publications, v. 404, doi:10.1144/SP404.6

Trampush, S. M. and Hajek, E. A., 2017, Preserving proxy records in dynamic landscapes: Modeling and examples from the Paleocene-Eocene Thermal Maximum: Geology, v. 45, p. 967-970.

Tsoar, H. and Pye, K., 1987, Dust transport and the question of desert loess formation: Sedimentology, v. 34, p. 139-153.

Tweto, O., 1978, Northern rift guide 1, Denver-Alamosa, Colorado, *in* Guidebook to the Rio Grande Rift: New Mexico Bureau of Mines and Mineral Resources Circular, v. 163, p. 13-28

Urban, F.E., Reynolds, R.L. and Fulton, R., 2009, The dynamic interaction of climate, vegetation, and dust emission, Mojave Desert, USA *in* Fernandez-Bernal, A., De La Rosa, M.A., eds., Arid Environments and Wind Erosion: NOVA Science Publishers, Inc., p. 243–267.

Vandenberghe, J., 2013, Grain size of fine-grained windblown sediment: A powerful proxy for process identification: Earth-Science Reviews, v. 121, p. 18-30.

Varga, G., Újvári, G., Kovács, J., and Szalai, Z., 2015, Effects of particle optical properties on grain size measurements of aeolian dust deposit: EGU General Assembly Conference Abstracts, v. 17.

Ventra, D., and Nichols, G. J., 2014, Autogenic dynamics of alluvial fans in endorheic basins: outcrop examples and stratigraphic significance: Sedimentology, v. 61, p. 767-791.

Ventra, D., and Clarke, L. E., 2018, Geology and geomorphology of alluvial and fluvial fans: current progress and research perspectives: Geological Society, London, Special Publications, v. 440, p. 440-16.

Ventra, D., Abels, H. A., Hilgen, F. J., and de Boer, P. L., 2018, Orbital-climate control of mass-flow sedimentation in a Miocene alluvial-fan succession (Teruel Basin, Spain): Geological Society, London, Special Publications, v. 440, p. 129-157.

Vreeken, W.J., 1975, Principal kinds of chronosequences and their significance in soil history: Journal of Soul Science, v. 26, p. 378-394

Wallace, A. R., 2004, Evolution of the southeastern San Luis basin margin and the Culebra embayment, Rio Grande rift, southern Colorado, *in* Geology of the Taos Region: New Mexico Geological Society 55th Fall Field Conference Guidebook

Wang, Y., Straub, K. M., and Hajek, E. A., 2011, Scale-dependent compensational stacking: an estimate of autogenic time scales in channelized sedimentary deposits: Geology, v. 39, p. 811-814.

Wells, S. G., and Dohrenwend, J. C., 1985, Relict sheetflood bed forms on late Quaternary alluvial-fan surfaces in the southwestern United States: Geology, v. 13, p. 512-516.

Wells, S.G., McFadden, L.D., and Dohrenwend, J.C., 1987, Influence of late Quaternary climatic changes on geomorphic and pedogenic processes on a desert piedmont, eastern Mojave Desert, California: Quaternary Research, v. 27, p. 130-146.

Wells, S. G., McFadden, L. D., Poths, J., and Olinger, C. T., 1995, Cosmogenic 3He surface-exposure dating of stone pavements: Implications for landscape evolution in deserts: Geology, v. 23, p. 613-616.

Yonkee, A. and Weil, A., 2015, Tectonic evolution of the Sevier and Laramide belts within the North American Cordillera orogenic system: Earth Science Reviews, v. 150, p. 531-593.

Zarate, M., and Blasi, A., 1991, Late Pleistocene and Holocene loess deposits of the southeastern Buenos Aires province, Argentina: Geojournal, v. 24, p. 211-220.

Zielinski, T., and Van Loon, A. J., 2002, Present-day sandurs are not representative of the geological record: Sedimentary Geology v. 152, p. 1-5.

Zielinski, T., and Van Loon, A. J., 2003, Pleistocene sandur deposits represent braidplains, not alluvial fans: Boreas v. 32, p. 590-611.

APPENDICES

APPENDIX A

GEOLOGIC MAP OF THE ZAPATA AND BLANCA SECTIONS OF THE NORTHERN SANGRE DE CRISTO RANGE-FRONT FAULT SYSTEM, SOUTH-CENTRAL COLORADO

197

GEOLOGIC MAP OF THE ZAPATA AND BLANCA SECTIONS OF THE NORTHERN SANGRE DE CRISTO RANGE-FRONT FAULT SYSTEM, SOUTH-CENTRAL COLORADO

by

SYLVIA NICOVICH

April 2017

Department of Earth Sciences, Montana State University, Traphagen Hall, Bozeman, MT, 59717

INTRODUCTION

The Zapata and Blanca sections of the Northern Sangre de Cristo fault-system mapping area constitutes the apex-to-toe widths of all alluvial fans along the range front extending from the Blanca massif salient north to the southern edge of Great Sand Dunes National Park. The total size of the map area is approximately equal to the area of two 7.5-minute quadrangles, comprising portions of the Zapata Ranch, Twin Peaks, Blanca Peak, Blanca, and Fort Garland 7.5.-minute quadrangles (**Fig. 1**). The purpose of this study is to create a surficial geologic framework for investigating piedmont development, along with a relative age context for alluvial fan development and modification.

The Blanca Massif encompasses a series of high-elevation, glaciated catchments and lower elevation, non-glaciated catchments. Five large alluvial fans (~5-6 km radii) are sourced from long, extensively glaciated drainage basins on the southern portion of the Blanca Massif. Fans to the north are much smaller (<3 km radii), sourced from shorter, steeper drainage basins that have no evidence of glaciation.

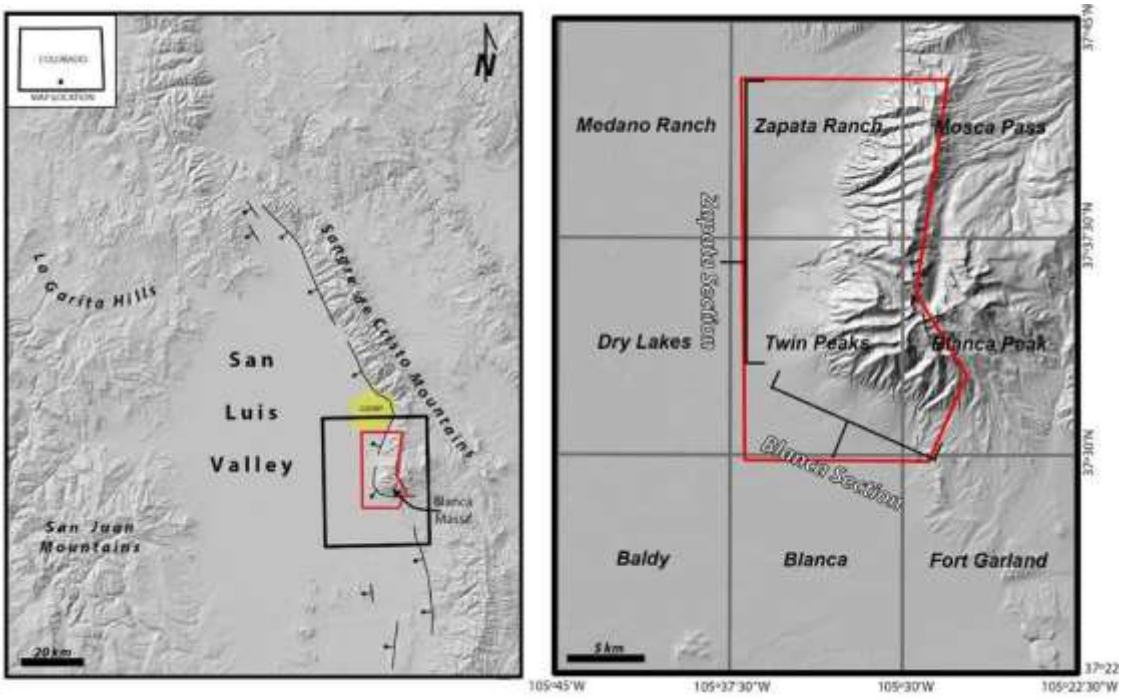

Figure 1. **Left-Map of the San Luis Valley within south-central Colorado. The San Juan Mountains and La Garita Hills mark the western edge of the valley with the Sangre de Cristo Mountains to the east. The Sangre de Cristo range-front fault system bounds the Sangre de Cristo Mountains western range-front. Black box displays map to the right and red outline shows the map extent. Great Sand Dunes National Park is highlighted in yellow. Right-Hillshade map of 7.5'quadrangles within the mapping area (red outline). Zapata and Blanca Sections of the Sangre de Cristo range-front fault system bracketed and labels.**

The western Sangre de Cristo Mountains within the San Luis Valley of southern Colorado serve as an exemplary field site for interpretations regarding the role of alpine glaciation on alluvial fan development. Detailed mapping of distinct alluvial fans that form at the piedmont junction of each drainage allow for such elucidations in addition to creating a relative-age sequence for the Quaternary deposits in the area.

The Sangre de Cristo fault system within the mapping area bounds the western flank of the range front. The Zapata section makes up the southernmost portion of the northern segment of the Sangre de Cristo fault system. The Zapata section trends north-south through the northern study until it terminates at the Blanca section of the central segment, where the trend of the fault system changes to east-west. The northeastern limit of the mapping area is defined by a series of barchan and parabolic sand dunes on the southern edge of Great Sand Dunes National Park. The northern edge of the range front piedmont is made up of numerous (~10), small, coalescing alluvial fans of relatively youngest age, sourced from short, steep drainage basins. These fans occur from North Zapata Creek north to the main Great Sand Dune dunefield. South of these smaller fans are five prominent large fans. The alluvial fans that propagate to the west are capped by glacial deposits extending from the confining drainage basins. The two south-facing fans are also sourced from glaciated drainages, but the glacial deposits do not extend past the fan apex.

Mapping was accomplished using a combination of high-resolution imagery, along with geomorphologic and sedimentological fieldwork. Newly acquired Light Detection and Ranging (LiDAR) data provided by the USGS was used to differentiate and preliminarily assign relative ages to fan surfaces, mainly based on topographic position and surface roughness. Precise field navigation of this heavily vegetated area was enabled by georeferenced imagery generated from the LiDAR data.
Sedimentary analyses of fan surfaces were conducted through fieldwork, and included cataloguing sedimentary texture, features, and degree of modification the surfaces have undergone during periods of non-deposition.

Given the juxtaposition of alluvial fans sourced from glaciated and non-glaciated drainage basins, the Zapata and Blanca sections of the western Sangre de Cristo Mountains within the San Luis Valley are an ideal setting to study the impact of mountain glaciation on alluvial fan development. This area provides an excellent opportunity to document and classify the spatial and temporal interplay of primary depositional and modifying processes on debris-flow alluvial fans.

GEOLOGIC SETTING

The Sangre de Cristo Mountains of southern Colorado comprise Laramide structures of Precambrian crystalline rocks thrust over folded Pennsylvanian and Permian deposits related ancestral rocky orogenic deposits (Lindsey et al., 1983; Lindsey, 1998; Kellogg, 1999; Hoy and Ridgway, 2002). Laramide structures are overprinted by Oligocene extension of the Rio Grande Rift, forming the San Luis Basin half-graben that accommodates Quaternary fill and Tertiary volcanics (Lindsey et al., 1983; Lindsey et al., 1986; Chapin and Cather, 1994; Brister

and Gries, 1994; Ruleman and Machette, 2007).

Widespread lacustrine deposits and landforms are evidence of a voluminous Plio-Pliestocene Lake Alamosa that once occupied the northern San Luis Basin. This lake expanded and contracted for probably hundreds of thousands of years while it filled the valley with sediment (Machette et al., 2007, Ruleman, 2012). Lake Alamosa began to overtop a low Oligocene volcanic topographic sill to the south at about <400 ka, which cut the Rio Grande Gorge over a period of ~200 ky (Ruleman, 2012). The evacuation of Lake Alamosa exposed sediments in the valley floor to aeolian processes, which have formed the Great Sand Dunes and continue to transport material throughout the valley.

The tectonically active Sangre de Cristo normal fault system bounds the range on the western front within the San Luis Valley, with obvious fault scarps cutting late-Pleistocene to Holocene deposits (McCalpin, 1982; Ruleman and Machette, 2007). This fault system is separated into three sections, the Northern, Central and Southern. The Blanca Massif encompasses the southern portion of the Northern Section (Zapata Section) and the northern-most portion of the Central Section (Blanca Section) where the range takes an eastward step (**Fig. 1**). The most recent event (MRE) along the Zapata section is estimated to have occurred at approximately 5.5-5.3 ka (McCalpin, 2006). The Blanca section, which defines the Blanca Massif salient, has only one post-35 ka MRE; one-half of the activity observed on the northern section (McCalpin, 1982).

Five large alluvial fans (~5-6 km radii) are sourced from long, extensively glaciated drainage basins on the southern portion of the Blanca Massif. From north to south they are the South Zapata, Pioneer, Holbrook, Tobin, and Blanca, named for the dominant watercourse of the catchment they are sourced from. Coalesced fans to the north are much smaller (<3 km radii), sourced from shorter, steeper drainage basins that have no evidence of glaciation.

Regardless of whether moving ice had occupied certain catchments of the Sangre de Cristo Mountains, all alluvial fans and associated drainage basins have been influenced by climate change of at least three Pleistocene glacial cycles (McCalpin, 1982; Pierce, 2003; Lindsey, 2010). Reconnaissance field mapping of fans in the Blanca and Zapata section reveal features such as boulder debris flow levees and lobes that suggest deposition by sediment-gravity flow with subsequent secondary modification.

DESCRIPTION OF MAP UNITS

Descriptions of surface roughness and shape in plan view were scrutinized through high-resolution imagery. Sedimentologic characteristics were described in the field, along with the was estimation of degree of weathering, soil horizonation, and surface modification.

QUATERNARY ALLUVIAL FAN DEPOSITS

Alluvial fan deposits have been differentiated into three main classes, **Qao** (old), **Qai** (intermediate), **Qay** (young). Each class has been subdivided into three sub-classes; 1 being

the oldest (stratigraphically lowest) and 3 the youngest (stratigraphically highest) (**Fig. 2**).

Alluvial fan deposits are pervasively built by sediment-gravity flow processes, specifically boulder-rich debris-flow. Clast lithology of fan deposits are dictated by their drainage basin geology. Most large particles that make up fans are Paleoproterozoic tonalite gneiss, gneiss, diorite, and quartz diorite, with minor addition of Pennsylvanian/Permian sedimentary rocks.

Primary debris flow deposits exhibit levees of poorly imbricated cobbles to large boulders varying from clast support to support by fine sand to pebble matrix. Lobes are generally composed of clast supported, sub-angular to round cobbles to large boulders, devoid of matrix. Fresh debris flow snouts contain similar sedimentologic features—clast-supported, sub-angular to rounded cobbles to large boulders, with varying matrix composition; from no matrix to fine sand to pebble matrix.

Besides topographic relations, diffusion of primary depositional morphology by processes including weathering, soil formation, and erosion are the dominant differentiating factors that allow distinguishing surfaces of different ages. These modifying processes are intrinsic in the smoothing of originally rough surface texture, another significant aspect of differentiation. Pedogenic carbonate is a useful indicator of relative age in aridisols that formed on fan surfaces. Stage of carbonate development referred to herein is based on Gile et al. (1966).

Reference to ridge and swale topography is applied to surfaces that have undergone sufficient modification of primary depositional features, but have not been smoothened to flatness. The ridges are relicts of debris flow levees and lobes, while the swales are relicts of channels between levees and channel incisions.

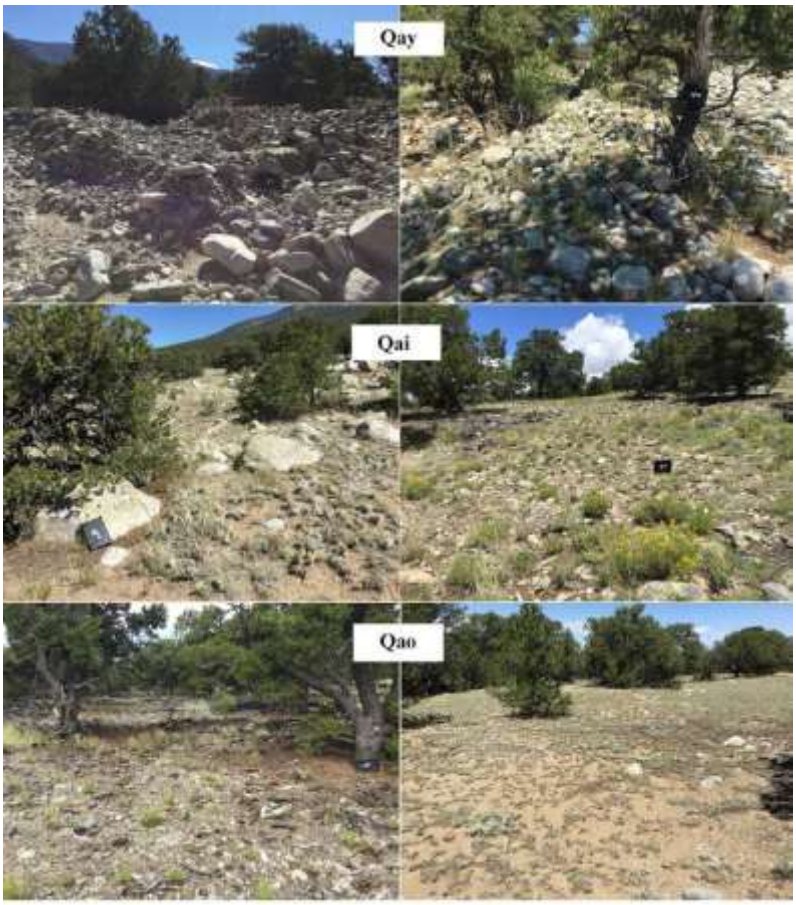

Figure 2. **Varying surface texture of stages of young (Qay), intermediate (Qai), and old (Qao) alluvial fan surfaces within the study area. Sequence reads left to right starting with fresh, primary depositional fabric in Qay, through consecutively older surfaces. Oldest Qao represents heavily reworked and smoothed alluvial fan surface with very minimal to no relicts of primary depositional fabric.**

Quaternary young alluvial fan deposits

The youngest alluvial fan surfaces display the freshest depositional fabric of boulder rich debris flow deposits (refer to **Fig. 2**). They are the lowest in elevation relative to other surfaces within fans, and occupy the most active depositional lobes that entrench older deposits. Debris flow levees, lobes, and snouts make up these youngest deposits. Qay deposits have not been subject to major pedogenic processes. Vegetation ranges from grasses and sages that grow on peaks of levees and lobes, piñon and juniper pine generally in the swales or channels, with occasional impact-removal of piñon and juniper pine bark evident on the freshest deposits.

Qay3 *Alluvium of the youngest fan surfaces*

The topographically lowest, undissected surfaces that encompass the most recent debris flow deposits on alluvial fans. Generally, occur as either lobes or channels within fan complexes. Rough surface morphology is produced by preservation of young to very young, fresh, unweathered boulder debris flow deposits. Boulder debris flow deposits comprise levees of poorly imbricated cobble to large boulders varying from clast support to support of fine sand to pebble matrix. Lobes are generally composed of clast-supported, sub-angular to round cobbles to large boulders, devoid of matrix. Cobbles and boulders display minimal to no weathering and primary depositional features display little to no signs of modification. Boulders are fresh and ring with strike of hammer.

Qay2 *Alluvium of the second youngest fan surfaces*

Deposits that are entrenched by and topographically above Qay3. Undissected to slightly dissected surfaces display rough primary depositional fabric. Generally, occur as segments within northern fan complexes or as individual depositional lobes of larger fan complex. Rough surface morphology is produced by preservation of young boulder debris flow deposits. Boulder debris flow deposits comprise levees of poorly imbricated cobble to large boulders varying from clast-support to support of fine sand to pebble matrix. Lobes are generally composed of clast supported, sub-angular to round cobbles to large boulders, devoid of matrix. Cobbles and boulders are minimally weathered, and primary depositional features display very minimal signs of modification.

Qay1 *Alluvium of the third youngest fan surfaces*

The topographically highest units of Qay subdivisions. Undissected to slightly dissected surfaces that display rough fabric. Occur as segments within northern fan complexes and as large individual depositional lobes of some larger fan complexes. Rough surface morphology is produced by preservation of young boulder debris flow deposits. Boulder debris flow deposits comprise levees of massive to poorly imbricated cobble to large boulders varying from clast-supported to support of fine sand to pebble matrix with minimal reworking. Lobes are generally composed of clast-supported, sub-angular to rounded cobbles to large boulders,

devoid of matrix. Cobbles and boulders are minimally weathered and primary depositional morphology display few signs of modification.

Quaternary intermediate alluvial fan deposits

Alluvial fan deposits of intermediate relative age are the dominant unit in the mapping area, especially in the southern portion. Primary depositional fabric has undergone significant winnowing of fine-grained matrix material. Surface displays rough fabric that ranges from discrete levees and lobes, to high amplitude ridge and swale morphology, but more subdued than in Qay (see **Fig. 2**). Piñon and juniper pine trees grow out of rough textured boulder deposits. Framework grains range from slightly weathered to rotten. Qai deposits have undergone pedogenic processes with carbonate horizons developed to stage I-III.

Qai3 *Alluvium of the youngest intermediate fan surfaces*

Lowest topographic position of the intermediate deposits that sit above Qay deposits. Rough surface texture from preserved primary depositional morphology. Significant winnowing of fine-grained material from matrix of debris flow levee and lobe deposits and variable aeolian input of silt within cobble to large boulder interstices. Diffusion of primary depositional morphology is evident by infilled topographic lows of fine-grained sand to cobble-sized particles.

Qai2 *Alluvium of the second youngest intermediate fan surfaces*

Surfaces are rough to moderately rough due to moderate disintegration of primary depositional morphology. Topographically below Qai1 and older deposits and perched above younger deposits. Most levee and lobe morphology of primary deposition is masked by diffusion of depositional morphology and input of aeolian fines. Boulders are sub-angular to round, and fresh to heavily weathered. Most heavily weathered boulders have disintegrated into angular fragments. Where large boulders are present, they thud with a hammer strike and display protruding mafic xenoliths. Vegetation grows pervasively throughout unit and includes pinon, juniper pines, sages, and grasses.

Qai1 *Alluvium of the oldest intermediate fan surfaces*

Topographically highest of intermediate deposits. The most significantly entrenched intermediate deposits. Moderately rough to somewhat smoothed surface texture from disintegration of primary depositional morphology. Occur as distinct fan lobes and as perched stand-alone surfaces. Levee and lobe morphology of primary depositional fabric has been diffused by structural collapse and aeolian input of fines. Stage II-III carbonate horizons and rinds formed in soil sequences. Cobbles to large boulders range from sub-angular to rounded, many are buried. Clasts range from slightly to heavily weathered and disintegrated.

Quaternary old alluvial fan deposits

Smooth surfaces punctuated and dissected by pervasive entrenchments and deep incised channels (refer to **Fig. 2**). Surfaces are the topographically highest of all other alluvial fan surfaces. Primary depositional features indicative of debris flow are masked by intense modification processes including disintegration of boulders into angular rock fragments. Strong carbonate soil horizons form up to stage IV.

Qao3 *Alluvium of the third oldest fan surfaces*

Smooth, segmented surfaces. Surfaces occur as both large depositional fan lobes and as fragmented, stand-alone, perched levels. Diffusion of primary depositional features evident by infilling of topographic lows and disintegration of levee and lobe highs. Smooth surfaces are made up of fragmented, rotten boulders with heavy aeolian input. Stage II to IV carbonate soil horizons occur with Qao3.

Qao2 *Alluvium of the second oldest fan surfaces*

Smooth to segmented surfaces with minimal to extensive incised channelization. Primary depositional features have been extensively reworked from heavily degraded debris flow levees and lobes to ridge and swale topography. Clasts are rotten and whole to fractured and angular with moderate to intense weathering.

Qao3 *Alluvium of the oldest fan surfaces*

The oldest surfaces at the highest elevation within individual alluvial fans. Deeply entrenched and segmented smooth surfaces. Primary depositional features are masked by substantial modification. Large boulders are heavily weathered and disintegrated. Clasts are fractured and angular due to weathering.

QUATERNARY ALLUVIUM/COLLUVIUM

Qc *Colluvium*

Poorly sorted, angular clasts supported by poorly sorted, course-grained matrix. Generally occur close to valleyward opening of drainage basins and on edges of segmented fan deposits.

Qal *Alluvium (undifferentiated)*

Active to inactive channelized deposits of undifferentiated alluvium.

Qic *Incised channel*

Headward eroding, channels incised into fan surfaces. Fan surfaces that have incised channels mappable at the 1:24,000 scale are predominantly the relatively oldest deposits.

Qtu *Fluvial terraces (undifferentiated)*

Flights of pebbles to large boulders in sandy matrix. Terraces make up nested suites propagating from glaciated drainage basins. These terraces occur atop and entrenched in alluvial fan surfaces.

Qog *Old gravel*

Angular to sub-round, boulder to large boulders buried by silt-medium sand. Makes up steeply sloping, flat surfaces.

Qdbu *Drainage basin deposits (undifferentiated)*

Includes talus cones and aprons, moraines, till, hillslope, fluvial, soil, regolith, and aeolian deposits.

QUATERNARY AEOLIAN DEPOSITS

Qdb *Barchan dunes*

Groups of, and individual crescent-shaped sand dunes.

Qdp *Parabolic dunes*

Parabolic dunes that have slip face facing dunefield.

Qss *Sand sheet*

Encompasses sandy grasslands, nebkah dunes that form around vegetation, transverse and parabolic dunes.

QUATERNARY LANDSLIDE DEPOSITS

Qls *Landslide deposits*

Mapped translational and rotational hillslope failure deposits are those that display scarp and toe**.**
Poorly sorted, matrix supported, angular to sub-round clasts make up this texturally immature deposit.

Qlso *Old landslide deposits and complexes*

Flat to hummocky topography of slightly to extensively weathered, cobbles to large boulders, within silt to coarse-sand matrix.

QUATERNARY GLACIAL DEPOSITS

Qmp *Pinedale-age moraine deposits*

Sharp-crested moraine deposits composed of poorly sorted cobbles to large boulders in a coarse- grained sand to pebble matrix.

Qmbl *Bull Lake-age moraine deposits*

Round-crested moraines built from slightly to heavily weathered, poorly sorted cobbles to large boulders in a coarse-grained sand to pebble matrix.

Qgft *Glacio-fluvial terrace*

Perched terraces of till above channels, within glaciated drainage basins, proximal to fan apex.

Qmu *Moraine diamict (undifferentiated)*

Undifferentiated moraine deposits and till.

TERTIARY (MIOCENE) SEDIMENTAY ROCKS LOWER SANTA FE GROUP

Tsf *Santa Fe Formation*

The Santa Fe Formation is the lower member of the Santa Fe Group sediments, overlain by the Alamosa Formation. The Santa Fe Formation is a volcaniclastic conglomerate interfingered by coarse- grained sand with carbonate cement. Conglomerate is matrix-supported by feldspathic litharenite, fine to coarse-grained sand. Framework grains are pebble to cobble-sized, sub-angular to sub-round volcanic rock fragments. Variegated color, generally pink, orange, light-brown, or tan. Induration varies upon location, as does attitude of beds that are commonly tilted ~14-45 degrees. In the mapping area, tilted Tsf underlies Qoa1 beneath an angular unconformity.

PALEOZOIC ROCKS

Paleozoic geology was not mapped in detail. Contacts are based on a compilation map published by the National Park Service in 2014; Geologic Map of Great Sand Dunes National Park and Preserve (includes; Lindsey et al., 1985; Lindsey et al., 1986; Johnson et al., 1989; Johnson and Bruce, 1991; Bruce and Johnson, 1991)

PPm *Pennsylvanian and Permian Minturn Formation*

Coarse-grained litharenite to polymict conglomerate. The Minturn formation represents sedimentation from the Ancestral Rocky orogen into the Central Colorado trough (Hoy and Ridgway, 2002).

PALEOPROTEROZOIC ROCKS

Paleoproterozoic geology was not mapped in detail. Contacts are based on a compilation map published by the National Park Service in 2014; Geologic Map of Great Sand Dunes National Park and Preserve (includes; Lindsey et al., 1985; Lindsey et al., 1986; Johnson et al., 1989; Johnson and Bruce, 1991; Bruce and Johnson, 1991).

Xgn *Mixed gneiss*

Xg *Metagabbro*

Xto *Tonalite gneiss*

Xhgn *Hornblende gneiss*

Xdi *Diorite*

Xqd *Quartz diorite*

REFFERENCES CITED

Brister, B. S., and Gries, R. R., 1994, Tertiary stratigraphy and tectonic development of the Alamosa basin (northern San Luis Basin), Rio Grande rift, south-central Colorado, *in* Keller, G. R,, and Cather, S. M. eds., Basins of the Rio Grande Rift: Structure, Stratigraphy, and Tectonic Setting: Boulder, Colorado, Geological Society of America Special Paper 291, p. 39-58.

Bruce, R. M., and Johnson, B. R., 1991, Reconnaissance Geologic Map of parts of the Zapata Ranch and Mosca Pass Quadrangles, Alamosa and Huerfano Counties, Colorado: U.S. Geological Survey, Miscellaneous Field Studies Map MF-2168, scale 1:24,000.

Chapin, C. E., and Cather, S. M., 1994, Tectonic setting of the axial basins of the northern and central Rio Grande rift, *in* Keller, G. R,, and Cather, S. M. eds., Basins of the Rio Grande Rift: Structure, Stratigraphy, and Tectonic Setting: Boulder, Colorado, Geological Society of America Special Paper 291, p. 5-26.

Gile, L.H., Frederick, F.P., Grossman, R. B., 1966, Morphological and genetic sequences of carbonate accumulation in desert soils: Soil Science, v. 101, p. 347-360.

Hoy, G.R. and Ridgway, K. D., 2002, Syndepositional thrust-related deformation and sedimentation in an Ancestral Rocky Basin, Central Colorado trough, Colorado, USA: Geological Society of America Bulletin, v. 144, p. 804-828.

Johnson, B. R., Bruce, R. M., and Lindsey, D. A., 1989, Reconnaissance Geologic Map of the Medano Pass Quadrangle and part of the Liberty Quadrangle, Alamosa, Huerfano, and Saguache Counties, Colorado: U.S. Geological Survey, Miscellaneous Field Studies Map MF-2089, scale 1:24,000.

Johnson, B. R., and Bruce, R. M., 1991, Reconnaissance Geologic Map of parts of the Twin Peaks and Blanca Peak Quadrangles, Alamosa, Costilla, and Huerfano Counties, Colorado: U.S. Geological Survey

Kellogg, K., 1999, Neogene basins of the northern Rio Grande Rift-partitioning and asymmetry inherited from Laramide and older uplifts: Tectonphysics, v. 305, p. 141-152.

Lindsey, D. A., Johnson, B. R., and Andriessen, P. A. M., 1983, Laramide and Neogene structure of the northern Sangre de Cristo Range, south-central Colorado. Rocky Mountain foreland basins and uplifts: Denver, Colorado, Rocky Mountain Association of Geologists, p. 219-228.

Lindsey, D. A., Soulliere, S. J., Hafner, K., and Flores, R.J., 1985, Geologic Map of Rio Alto Peak and Northeastern part of Mirage Quadrangles, Custer and Saguache Counties, Colorado: U.S. Geological Survey, Miscellaneous Field Studies Map MF-1787, scale 1:24,000.

Lindsey, D. A., Johnson, B. R., Soulliere, S. J., Bruce, R. M., and Hafner, K., 1986, Geologic

Map of the Beck Mountain, Crestone Peak, and Crestone Quadrangles, Custer, Huerfano, and Saguache Counties, Colorado: U.S. Geological Survey, Miscellaneous Field Studies Map MF-1878,1:24,000 scale.

Lindsey, D. A., Clark, R. F., and Soulliere, S. J., 1986, Minturn and Sangre de Cristo Formations of Southern Colorado: A Prograding Fan Delta and Alluvial Fan Sequence Shed from the Ancestral Rocky Mountains: Part IV. Southern Rocky Mountains.

Lindsey, D. A., 1998, Laramide structure of the central Sangre de Cristo Mountains and adjacent Raton basin, southern Colorado: The Mountain Geologist, v. 35, p. 55-70.

Lindsey, D.A., 2010, The geologic story of Colorado's Sangre de Cristo Range: U.S. Geological Survey Circular 1349, 14 p.

Machette, M.N., Marchetti, D.W., and Thompson, R.A., 2007, Ancient Lake Alamosa and the Pliocene to middle Pleistocene evolution of the Rio Grande, *in* Machette, M.N., Coates, M.M., and Johnson, M.L., eds., 2007 Rocky Mountain Section Friends of the Pleistocene Field Trip—Quaternary geology of the San Luis Basin of Colorado and New Mexico, September 7-9, 2007: U.S. Geological Survey Open-File Report 2007-1193, p. 187-197.

McCalpin, J.P., 1982, Quaternary geology and neotectonics of the west flank of the northern Sangre de Cristo Mountains, south-central Colorado: Colorado School of Mines Quarterly, n. 77, p. 97

McCalpin, J.P., 2006, Active faults and seismic hazards to infrastructure at Great Sand Dunes National Monument and Preserve: Crestone, Colorado: unpublished report by GEO-HAZ Consulting, Inc., 49 p., 1 oversize plate.

National Park Service, U.S. Department of the Interior, 2014, Geologic Map of Great Sand Dunes Park and Preserve: Geologic Resource Division.

Pierce, K. L., 2003, Pleistocene glaciations of the Rocky Mountains: Developments in Quaternary Sciences, v. 1, p. 63-76.

Ruleman, C.A., and Machette, M.N, 2007, An overview of the Sangre de Cristo fault system and new insights to interactions between Quaternary faults in the Northern Rio Grande Rift, in Machette, M.N., Coates, M.M., and Johnson, M.L., eds., 2007 Rocky Mountain Section Friends of the Pleistocene Field Trip—Quaternary geology of the San Luis Basin of Colorado and New Mexico, September 7-9, 2007: U.S. Geological Survey Open-File Report 2007-1193, p. 187-197.

Ruleman, C.A., 2012, Timing and rates of canyon incision and basin integration along the northern Rio Grande, San Luis Valley, New Mexico and Colorado: Geological Society of America Abstracts with Programs, vol. 44, p. 7

Plate A.1

Geologic Map of Alluvial Fans along the Zapata and Blanca Sections of the Northern Sangre de Cristo Range-Front Fault System, South-Central Colorado is provided as a supplementary document.

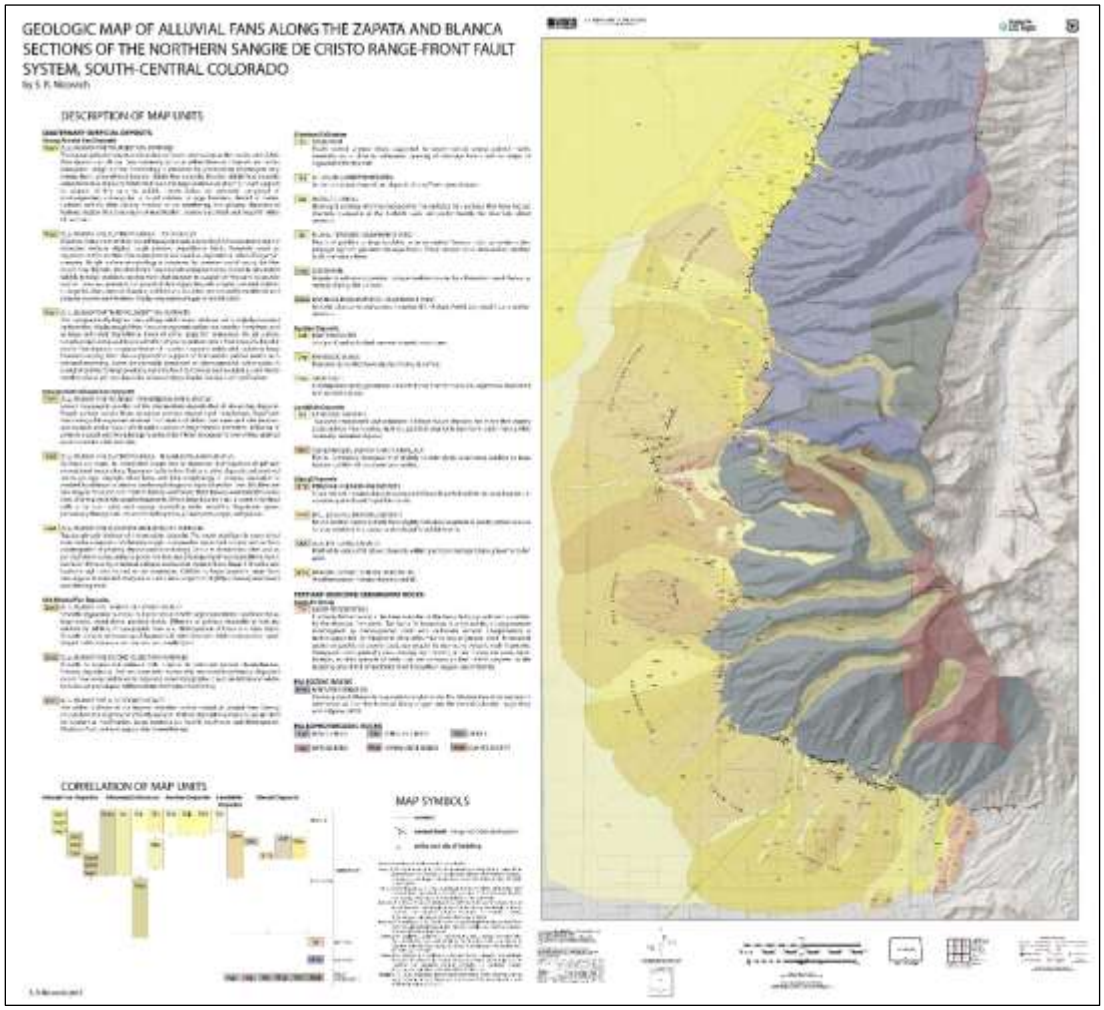

thumbnail

APPENDIX B

USGS LUMINESCENCE GEOCHRONOLOGY LABORATORY DATING REPORT

USGS Luminescence Geochronology Laboratory Dating Report

2017-2019 San Luis Valley - Pioneer Fan PI: Sylvia Nicovich

Report prepared by: Harrison J. Gray

Laboratory Director Shannon A. Mahan

May 24, 2019

Overview

The following report summarizes the dating results from the San Luis Valley - Pioneer Fan 2017-2019 dating project. Within this report, we detail the methodology used by the USGS Luminescence Geochronology Laboratory to obtain ages including sample preparation methods, luminescence measurement, equivalent dose determination, and dating-related calculations. We recommend that this report be included as the supplementary material for any publication(s) that use the ages within this report. This version supersedes all previous age estimates and reports.

This report contains:

1. A main report synthesizing the results (this document)
2. A .xlsx spreadsheet with the main summary table
3. A .xlsx file with all results in spreadsheet form with a definitions text file
4. A compressed folder containing:

a) .png versions of the figures in this report
b) .xlsx files with outputs from the code used for analysis

Contents

List of Tables

List of Figures

Lab Code	Elevation (m)	Depth (m)	Water Content[a]	K[b] (%)	U[b] (ppm)	Th[b] (ppm)	D_R[c] (Gray/ka)
SRN-C-OSL	2362	0.25	1 (30) [5]	2.08 ± 0.04	2.04 ± 0.23	6.34 ± 0.34	2.52 ±0.06
SRN-C-IRSL	2362	0.25	1 (30) [5]	2.08 ± 0.04	2.04 ± 0.23	6.34 ± 0.34	2.95 ±0.08
SRN-D-IRSL	2362	1.00	2 (30) [5]	2.31 ± 0.04	2.92 ± 0.23	8.07 ± 0.35	3.92 ±0.09
SRN-B-OSL	2362	3.00	2 (32) [5]	2.77 ± 0.04	2.69 ± 0.23	8.92 ± 0.37	3.92 ±0.08
SRN-B-IRSL	2362	3.00	2 (32) [5]	2.77 ± 0.04	2.69 ± 0.23	8.92 ± 0.37	4.37 ± 0.10
SRN-05-IRSL	2366	5.00	0 (31) [5]	1.87 ± 0.03	2.44 ± 0.15	7.08 ± 0.21	3.43 ± 0.25
SRN-03-IRSL	2362	6.10	0 (25) [4]	1.73 ± 0.05	1.97 ± 0.23	5.75 ± 0.33	3.12 ± 0.25
SRN-A-IRSL	2362	8.00	12 (50) [6]	2.34 ± 0.05	2.94 ± 0.23	9.06 ± 0.44	3.98 ± 0.10
SRN-E-IRSL	2362	13.00	7 (37) [5]	2.70 ± 0.09	2.23 ± 0.16	8.03 ± 0.85	4.12 ± 0.11
SRN-01-IRSL	2360	15.50	1 (37) [5]	1.97 ± 0.10	2.02 ± 0.32	6.21 ± 0.41	3.36 ± 0.26
SRN-02-IRSL	2360	15.50	4 (39) [6]	2.72 ± 0.07	2.46 ± 0.21	8.12 ± 0.57	4.27 ± 0.26

[a]Percent water content of field sample used for age calculation, number in parentheses represents the saturated water content, square brackets shows modeled water content (Nelson and Rittenour, 2015).
[b]Method used to determine elemental concentrations given in Table 3.
[c]Calculated using the Dose Rate Age Calculator (Durcan et al., 2015).

Table 1: Sample data used to calculate dose rates.

I Age Results

I.1 General Results

Debris flow is the primary fan-building process of the alluvial fans of the Blanca Peak massif. Primary processes are processes that move material from the drainage basin to the alluvial fan. The Pioneer Alluvial Fan is one of several forming the extensively glaciated western Sangre de Cristo piedmont of south-central Colorado. The Pioneer alluvial fan hosts a gravel quarry at its toe which exhibits excellent vertical exposure for facies analysis. Samples for OSL dating were collected from the toe of the alluvial fan in units that have been reworked fluvially into sand-sized material; thus we acknowledge that conditions at the distal end of the fan may be markedly different than the stratigraphic progressions at the proximal front, however we will speculate that both processes are equivalent for the purposes of our study. Three buried soils are exposed in the quarry, defining three periods of surface stability with IRSL ages of potassium feldspars of 75 ka, 60 ka, and 35 ka; there are also two less strong older soil developments (horizons) at 85 ka and 95 ka.

Associated with each soil is a facies assemblage that originates with constructive Gms and Gmsc facies (debris flow) and transitions upward to modifying Gm, Gh, Sl, Sh facies indicative of surficial water reworking, capped by eolian influenced Sm facies comprising windblown and water-reworked sand/silt. On the Pioneer Fan, and likely other debris-flow alluvial fans, eolian-influenced facies are associated with periods of inactive surface stability as shown by soil horizons. This suggests that eolian deposition, water reworking of eolian sediment, and pedogenesis are important processes on the inactive surfaces of debris-flow alluvial fans.

Lab Code	n[a]	CAM Over-dispersion[b]	CAM D_e[c] (Gray)	MAM D_e[d] (Gray)	CAM Age[c] (ka)	**MAM Age[d] (ka)**
SRN-C-OSL	27 (29)	34%	8.3 ± 0.5	4.95 ± 0.37	3.28 ± 0.23	**1.97 ± 0.14**
SRN-C-IRSL	18 (25)	28%	23.6 ± 1.6	17.6 ± 1.6	8.00 ± 0.59	**5.96 ± 0.57**
SRN-D-IRSL	23 (33)	22%	26.0 ± 1.3	22.7 ± 1.6	6.62 ± 0.4	**5.80 ± 0.42**
SRN-B-OSL	11 (23)	31%	99.2 ± 9.2	60.3 ± 5.6	25.3 ± 2.4	**15.4 ± 1.4**
SRN-B-IRSL	14 (20)	17%	192 ± 8.8	163 ± 11.4	44.0 ± 2.2	**37.3 ± 2.7**
SRN-05-IRSL	5 (10)	9%	193 ± 11.1	187 ± 20.0	56.2 ± 5.2	**54.4 ± 7.0**
SRN-03-IRSL	10 (10)	7%	193 ± 5.9	193 ± 11.4	61.8 ± 5.3	**61.8 ± 6.2**
SRN-A-IRSL	14 (21)	14%	357 ± 13.5	307 ± 19.9	89.8 ± 4.1	**77.1 ± 5.3**
SRN-E-IRSL	8 (8)	17%	392 ± 23.3	347 ± 26.2	95.2 ± 6.2	**84.3 ± 6.7**
SRN-01-IRSL	15 (15)	14%	369 ± 14.4	338 ± 22.3	110 ± 9.6	**100 ± 10.2**
SRN-02-IRSL	13 (15)	12%	443 ± 16.6	411 ± 27.1	104 ± 7.5	**96.3 ± 8.7**

[a]number of aliquots meeting acceptance criteria, parentheses indicate total number of aliquots measured [b]Defined as the statistical dispersion beyond what would be expected for a perfectly bleached sample. [c]Determined using the function calc CentralDose from the R-Luminescence package. Uncertainty is 2 σ. [d]Determined using the function calc MinDose from the R-Luminescence package. Uncertainty is 2 σ.

Table 2: Sample data used to calculate luminescence ages.

From analyses on the quartz separates for samples SRN-OSL-C and SRN-OSL-B, it appears that there is a medium component of OSL that interferes with the measurement of the fast component of OSL. The fast component of OSL (Singarayer and Bailey, 2004) is by far the dominant component in most of the worlds quartz and the component that all protocols for luminescence chronology are based on. Having an interference from a slower wavelength means that the quartz equivalent dose (and thus the age) will be underestimated (Steffen et al., 2009). We prefer to measure the quartz OSL if possible because the quartz resets much faster under conditions of turbid, fluvial flow much like the semi-debris flow methods that would have originally deposited the material that was sampled. Having ages from both feldspar (IRSL) and quartz (OSL) would give us some idea of the length and duration of the transport path of the particles. If the ages are within error of each other, we could be confident that the sediment was well bleached or zeroed before deposition. Thus, the problem of a slower OSL component in the quartz that underestimates the age doesnt allow us to use this valuable property and relegates us to "a slightly educated guess".

It is our best guess that the quartz OSL underestimates the true age but that partial bleaching is not a large issue because of the duplication of IRSL age in two separate samples (SRN-IRSL-C and SRN-IRSL-D) and because the sediment sampled is the finer grained portion that has been reworked. It is also our recommendation to use the minimum age model (the preferred ages are in bold) as this further reduces a partial bleaching bias by providing for an age taken from the measurements of the best bleached grains.

The method of choice for luminescence chronology was on potassium feldspar grains as they did not show unwanted luminescence components, did not show fade ratios, and did not saturate out with respect to old ages (i.e. >100,000 years). The feldspars were measured using post IRSL, a technique that reduces any anomalous fade associated with the artificial radiation and growth curves that laboratory measurements will necessarily been taken from.

For estimating the lifetime water content of the samples, we used the Nelson and Rittenour (2015) method. Effectively, this method estimates the matric potential of the sample based on approximate soil texture (loam, sand, etc.) and on the USDA soil moisture regime (Udic, Aridic, etc.). The method is appropriate for well-drained sediments above the water table, but does assume that current conditions are similar to lifetime water content conditions. This may or may not be appropriate for the Pioneer Fan. I assumed that the samples fell into the "Loamy Sand" category and that the soil moisture regime is "Aridic Ustic" based on the USDA Soil Moisture Regime Map for the contiguous United States. Alternative methods are to use either the Field, Saturated, or percent of saturation methods as outlined in the methods section. If you think another method is better, let's chat about it and decide what would work

Lab Code	Latitude (°)	Longitude (°)	Analysis Type	Grain Size (μm)	Water Content Method[a]	D_R Method[b]
SRN-C-OSL	37.580178	-105.593897	Quartz OSL	90 - 125	NelsonRittenour2015	Gamma
SRN-C-IRSL	37.580178	-105.593897	Feldspar pIRSL	90 - 125	NelsonRittenour2015	Gamma
SRN-D-IRSL	37.580178	-105.593897	Feldspar pIRSL	90 - 125	NelsonRittenour2015	Gamma
SRN-B-OSL	37.580178	-105.593897	Quartz OSL	90 - 125	NelsonRittenour2015	Gamma
SRN-B-IRSL	37.580178	-105.593897	Feldspar pIRSL	90 - 125	NelsonRittenour2015	Gamma
SRN-05-IRSL	37.580178	-105.593897	Feldspar pIRSL	90 - 250	NelsonRittenour2015	Gamma
SRN-03-IRSL	37.580178	-105.593897	Feldspar pIRSL	90 - 250	NelsonRittenour2015	Gamma
SRN-A-IRSL	37.580178	-105.593897	Feldspar pIRSL	90 - 125	NelsonRittenour2015	Gamma
SRN-E-IRSL	37.580178	-105.593897	Feldspar pIRSL	90 - 125	NelsonRittenour2015	Gamma
SRN-01-IRSL	37.580178	-105.593897	Feldspar pIRSL	90 - 250	NelsonRittenour2015	Gamma
SRN-02-IRSL	37.580178	-105.593897	Feldspar pIRSL	90 - 250	NelsonRittenour2015	Gamma

[a]Type of assumption used for water content history. F.Sat.Avg = average of field and saturated water contents. NelsonRittenour2015 = matric potential method (Nelson and Rittenour, 2015). Frac.Sat = fraction of saturation method.
[b]Method used for elemental concentrations of K, U, and Th. Gamma = high Resolution Germanium Gamma Spectrometry. ICP-MS = Inductively-Coupled Plasma Mass Spectrometry. All errors were obtained with calibration standards.

Table 3: Miscellaneous data used in age calculation. Part 1.

1.2 SRN-C-OSL Results

We analyzed SRN-C-OSL using Quartz OSL on 90-125 μm size grains. Out of 29 aliquots, 27 produced acceptable luminescence characteristics and passed acceptance criteria as listed in Table 7. Aliquots that passed acceptance criteria are plotted as a kernal density estimate and as a radial plot in Figure 1. Application of the central age model (CAM, Galbraith et al., 1999) produced an equivalent dose of 8.3 ± 0.5 Grays, which leads to a CAM age of 3.28 ± 0.2 ka. In contrast, application of the minimum age model (MAM, Galbraith et al., 1999) produces an equivalent dose of 5 ± 0.3 Gray, which leads to a MAM age of 1.97
± 0.1 ka.

Lab Code		G Value	(%) [a]	MAM: σ_b	MAM logged?	MAM: γ	MAM: σ	MAM: p_0	MAM: μ
SRN-C-OSL	±	0.00	0	0.08	TRUE	1.6	0.632	0.073	1.907
SRN-C-IRSL	±	0.00	0	0.08	TRUE	2.866	0.43	0.16	2.922
SRN-D-IRSL	±	0.00	0	0.08	TRUE	3.124	0.38	0.585	3.085
SRN-B-OSL	±	0.00	0	0.08	TRUE	4.1	0.603	0.078	4.36
SRN-B-IRSL	±	0.00	0	0.08	TRUE	5.093	0.242	0.169	5.107
SRN-05-IRSL	±	0.00	0	0.08	TRUE	5.229	0.046	0.095	5.189
SRN-03-IRSL	±	0.00	0	0.08	TRUE	5.262	0	0.879	5.187
SRN-A-IRSL	±	0.00	0	0.08	TRUE	5.727	0.191	0.037	5.83
SRN-E-IRSL	±	0.00	0	0.08	TRUE	5.85	0.252	0.408	5.814
SRN-01-IRSL	±	0.00	0	0.08	TRUE	5.823	0.194	0.445	5.781
SRN-02-IRSL	±	0.00	0	0.08	TRUE	6.02	0.161	0.435	6.009

[a]Determined from fading tests over three weeks. If a fading correction is not used, we show a value of 0.00 ± 0.

Table 4: Miscellaneous data used in age calculation. Part 2.

1.3 SRN-C-IRSL Results

We analyzed SRN-C-IRSL using Feldspar pIRSL on 90-125 μm size grains. Out of 25 aliquots, 18 produced acceptable luminescence characteristics and passed acceptance cri- teria as listed in Table 7. Aliquots that passed acceptance criteria are plotted as a kernal density estimate and as a radial plot in Figure 3. Application of the central age model (CAM, Galbraith et al., 1999) produced an equivalent dose of 23.6 ± 1.6 Grays, which leads to a CAM age of 8 ± 0.6 ka. In contrast, application of the minimum age model (MAM, Galbraith et al., 1999) produces an equivalent dose of 17.6 ± 1.6 Gray, which leads to a MAM age of 5.96 ± 0.6 ka.

-

1.4 SRN-D-IRSL Results

We analyzed SRN-D-IRSL using Feldspar pIRSL on 90-125 μm size grains. Out of 33 aliquots, 23 produced acceptable luminescence characteristics and passed acceptance cri- teria as listed in Table 7. Aliquots that passed acceptance criteria are plotted as a kernal density estimate and as a radial plot in Figure 5. Application of the central age model (CAM, Galbraith et al., 1999) produced an equivalent dose of 26 ± 1.3 Grays, which leads to a CAM age of 6.62 ± 0.4 ka. In contrast, application of the minimum age model (MAM, Galbraith et al., 1999) produces an equivalent dose of 22.7 ± 1.6 Gray, which leads to a

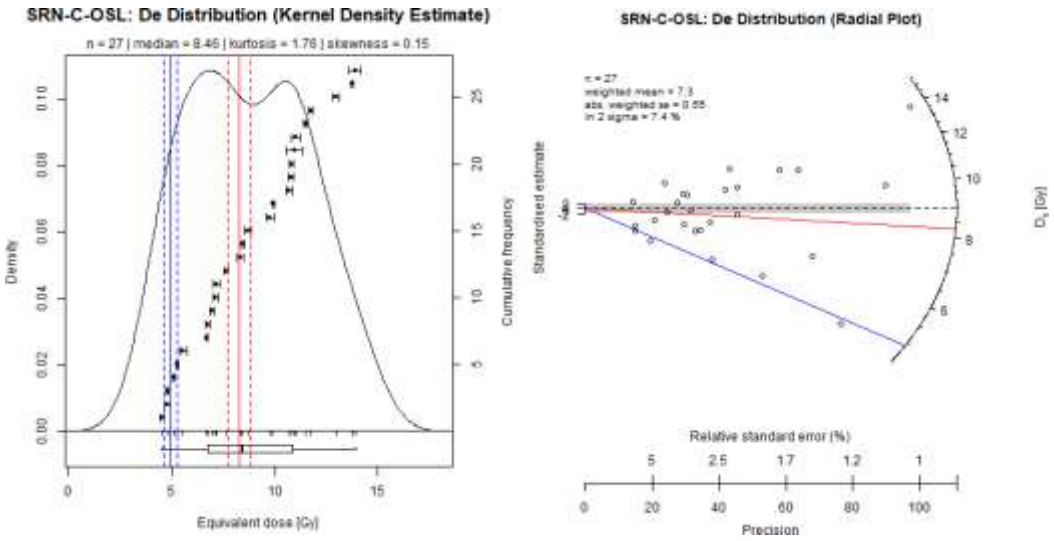

Figure 1: Plots of Equivalent Dose for SRN-C-OSL. Red lines shows CAM equivalent dose, blue lines show MAM equivalent dose, solid line shows the age, and dashed lines show uncertainty.

MAM age of 5.8 ± 0.4 ka.

-

1.5 SRN-B-OSL Results

We analyzed SRN-B-OSL using Quartz OSL on 90-125 μm size grains. Out of 23 aliquots, 11 produced acceptable luminescence characteristics and passed acceptance criteria as listed in Table 7. Aliquots that passed acceptance criteria are plotted as a kernal density estimate and as a radial plot in Figure 7. Application of the central age model (CAM, Galbraith et al., 1999) produced an equivalent dose of 99.2 ± 9.2 Grays, which leads to a CAM age of 25.3 ± 2.4 ka. In contrast, application of the minimum age model (MAM, Galbraith et al., 1999) produces an equivalent dose of 60.3 ± 5.6 Gray, which leads to a MAM age of 15.4 ± 1.4 ka.

-

1.6 SRN-B-IRSL Results

We analyzed SRN-B-IRSL using Feldspar pIRSL on 90-125 μm size grains. Out of 20 aliquots, 14 produced acceptable luminescence characteristics and passed acceptance cri-

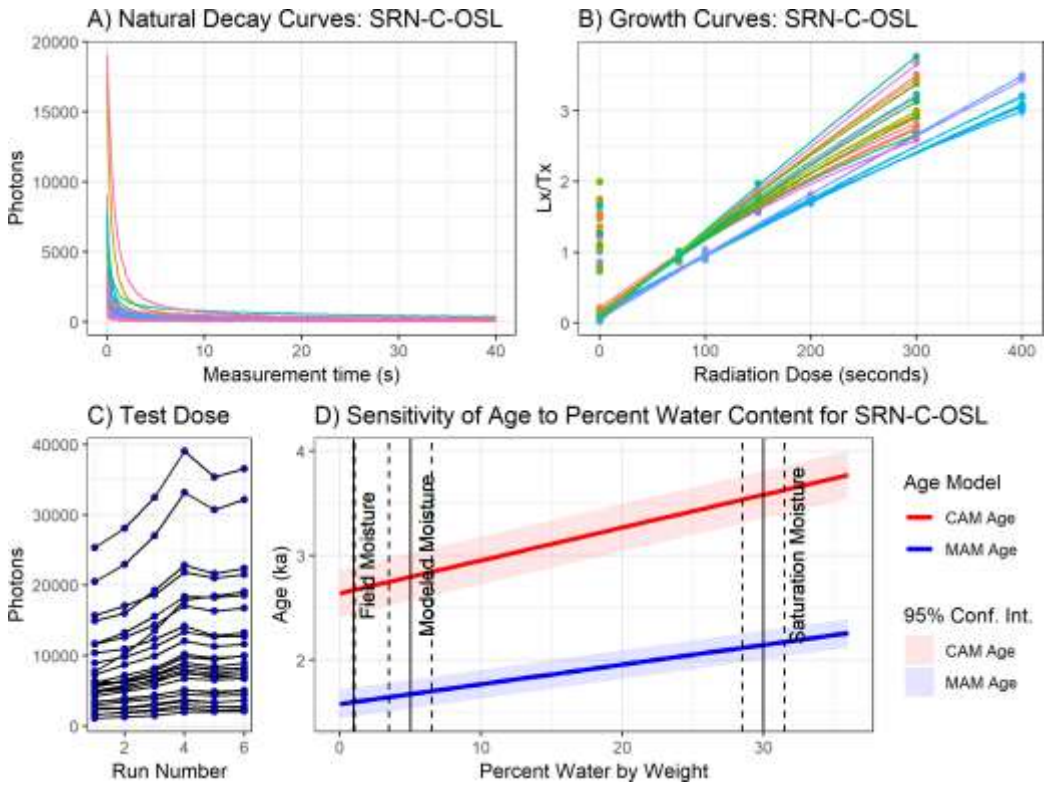

Figure 2: Plots of luminescence characteristics for SRN-C-OSL. A) Compilation of the natural luminescence decay curves for each aliquot. B) Compilation of the growth curves for each aliquot generated by the SAR protocol (Table 7). C) Magnitude of test dose response for each SAR cycle. D) Graph of CAM or MAM age as a function of water content. Note that for pre-2015 datasets, Plots A through C are not available and only Plot D will be present.

teria as listed in Table 7. Aliquots that passed acceptance criteria are plotted as a kernal density estimate and as a radial plot in Figure 9. Application of the central age model (CAM, Galbraith et al., 1999) produced an equivalent dose of 192 ± 8.8 Grays, which leads to a CAM age of 44 ± 2.2 ka. In contrast, application of the minimum age model (MAM, Galbraith et al., 1999) produces an equivalent dose of 163 ± 11.4 Gray, which leads to a MAM age of 37.3 ± 2.7 ka.

-

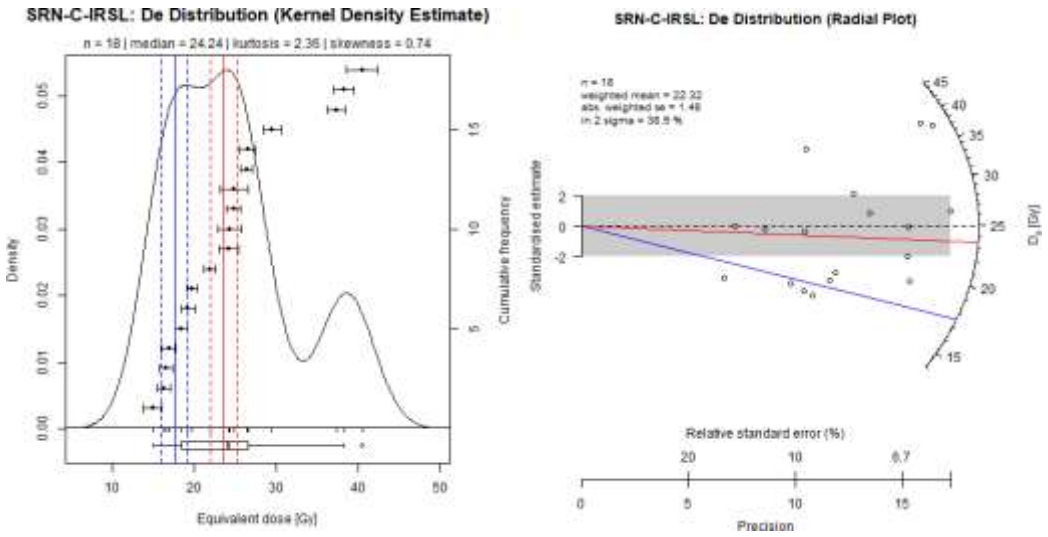

Figure 3: Plots of Equivalent Dose for SRN-C-IRSL. Red lines shows CAM equivalent dose, blue lines show MAM equivalent dose, solid line shows the age, and dashed lines show uncertainty.

1.7 SRN-05-IRSL Results

We analyzed SRN-05-IRSL using Feldspar pIRSL on 90-250 μm size grains. Out of 10 aliquots, 5 produced acceptable luminescence characteristics and passed acceptance criteria as listed in Table 7. Aliquots that passed acceptance criteria are plotted as a kernal density estimate and as a radial plot in Figure 11. Application of the central age model (CAM, Galbraith et al., 1999) produced an equivalent dose of 193 ± 11.1 Grays, which leads to a CAM age of 56.2 ± 5.2 ka. In contrast, application of the minimum age model (MAM, Galbraith et al., 1999) produces an equivalent dose of 187 ± 20 Gray, which leads to a MAM age of 54.4 ± 7 ka.

-

1.8 SRN-03-IRSL Results

We analyzed SRN-03-IRSL using Feldspar pIRSL on 90-250 μm size grains. Out of 10 aliquots, 10 produced acceptable luminescence characteristics and passed acceptance cri- teria as listed in Table 7. Aliquots that passed acceptance criteria are plotted as a kernal density estimate and as a radial plot in Figure 13. Application of the central age model (CAM, Galbraith et al., 1999) produced an equivalent dose of 193 ± 5.9 Grays, which leads

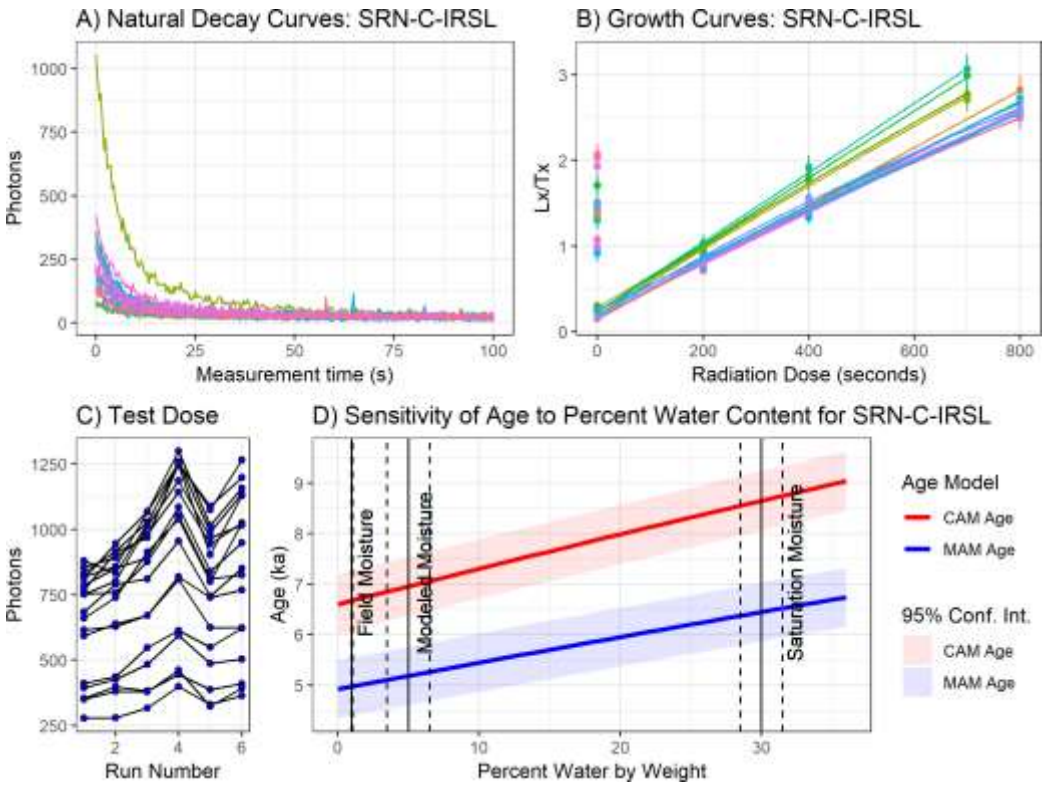

Figure 4: Plots of luminescence characteristics for SRN-C-IRSL. A) Compilation of the natural luminescence decay curves for each aliquot. B) Compilation of the growth curves for each aliquot generated by the SAR protocol (Table 7). C) Magnitude of test dose response for each SAR cycle. D) Graph of CAM or MAM age as a function of water content. Note that for pre-2015 datasets, Plots A through C are not available and only Plot D will be present.

to a CAM age of 61.8 ±5.3 ka. In contrast, application of the minimum age model (MAM, Galbraith et al., 1999) produces an equivalent dose of 193 ± 11.4 Gray, which leads to a MAM age of 61.8 ± 6.2 ka.

-

1.9 SRN-A-IRSL Results

We analyzed SRN-A-IRSL using Feldspar pIRSL on 90-125 μm size grains. Out of 21 aliquots, 14 produced acceptable luminescence characteristics and passed acceptance cri- teria as listed in Table 7. Aliquots that passed acceptance criteria are plotted as a kernal density estimate and as a radial plot in Figure 15. Application of the central age model

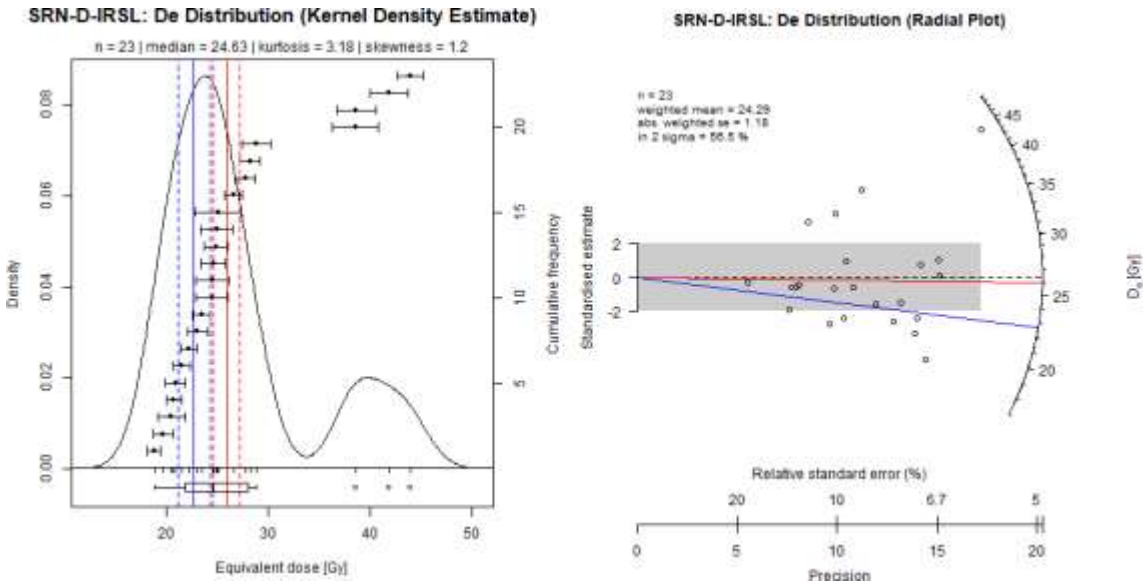

Figure 5: Plots of Equivalent Dose for SRN-D-IRSL. Red lines shows CAM equivalent dose, blue lines show MAM equivalent dose, solid line shows the age, and dashed lines show uncertainty.

(CAM, Galbraith et al., 1999) produced an equivalent dose of 357 ± 13.5 Grays, which leads to a CAM age of 89.8 ± 4 ka. In contrast, application of the minimum age model (MAM, Galbraith et al., 1999) produces an equivalent dose of 307 ± 19.9 Gray, which leads to a MAM age of 77.1 ± 5.3 ka.

-

1.10 SRN-E-IRSL Results

We analyzed SRN-E-IRSL using Feldspar pIRSL on 90-125 μm size grains. Out of 8 aliquots, 8 produced acceptable luminescence characteristics and passed acceptance criteria as listed in Table 7. Aliquots that passed acceptance criteria are plotted as a kernal density estimate and as a radial plot in Figure 17. Application of the central age model (CAM, Galbraith et al., 1999) produced an equivalent dose of 392 ± 23.3 Grays, which leads to a CAM age of 95.2 ± 6.2 ka. In contrast, application of the minimum age model (MAM, Galbraith et al., 1999) produces an equivalent dose of 347 ± 26.2 Gray, which leads to a MAM age of 84.3 ± 6.7 ka.

-

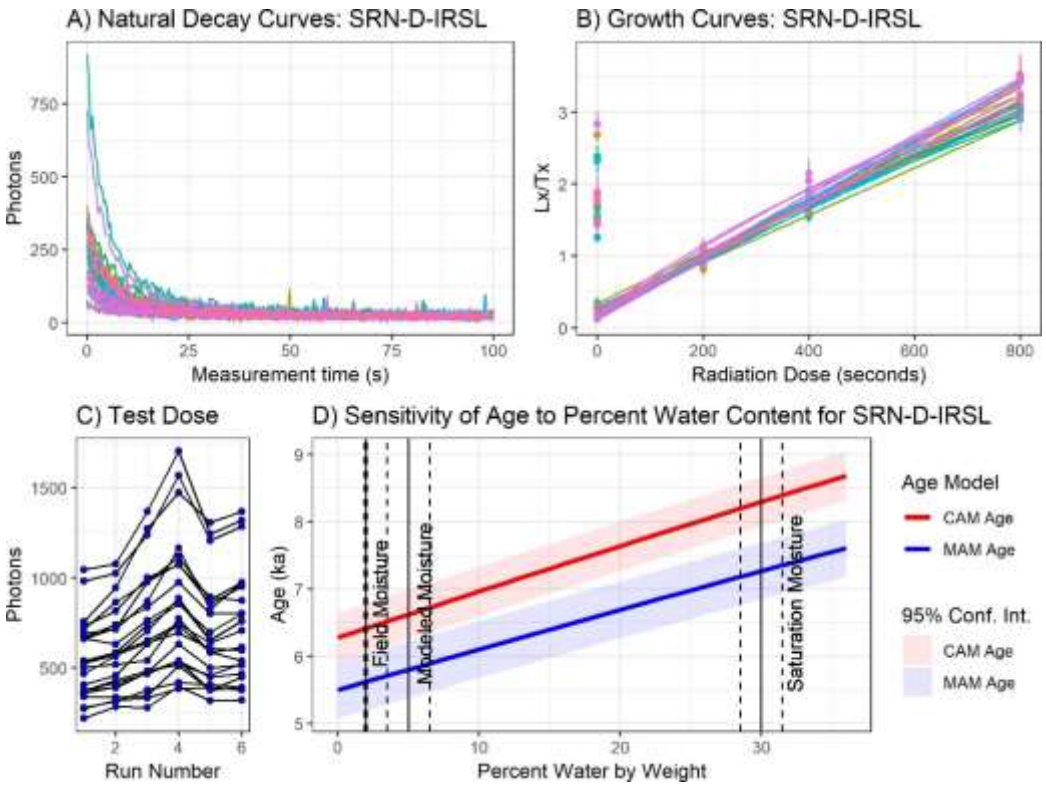

Figure 6: Plots of luminescence characteristics for SRN-D-IRSL. A) Compilation of the natural luminescence decay curves for each aliquot. B) Compilation of the growth curves for each aliquot generated by the SAR protocol (Table 7). C) Magnitude of test dose response for each SAR cycle. D) Graph of CAM or MAM age as a function of water content. Note that for pre-2015 datasets, Plots A through C are not available and only Plot D will be present.

I.11 SRN-01-IRSL Results

We analyzed SRN-01-IRSL using Feldspar pIRSL on 90-250 μm size grains. Out of 15 aliquots, 15 produced acceptable luminescence characteristics and passed acceptance cri- teria as listed in Table 7. Aliquots that passed acceptance criteria are plotted as a kernal density estimate and as a radial plot in Figure 19. Application of the central age model (CAM, Galbraith et al., 1999) produced an equivalent dose of 369 ± 14.4 Grays, which leads to a CAM age of 110 ± 9.6 ka. In contrast, application of the minimum age model (MAM, Galbraith et al., 1999) produces an equivalent dose of 338 ± 22.3 Gray, which leads to a MAM age of 100 ± 10.2 ka.

-

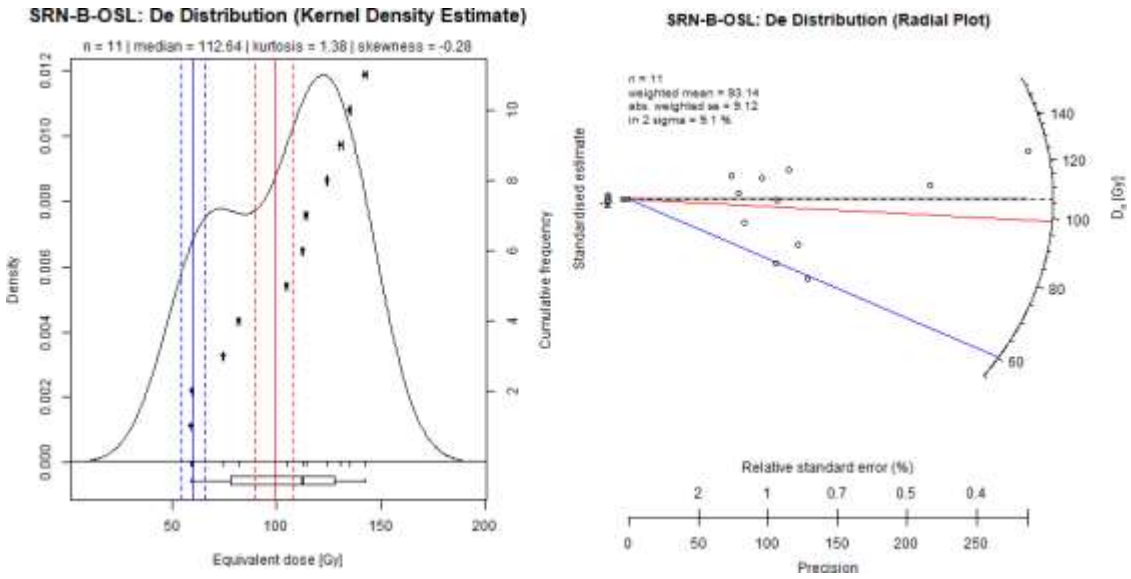

Figure 7: Plots of Equivalent Dose for SRN-B-OSL. Red lines shows CAM equivalent dose, blue lines show MAM equivalent dose, solid line shows the age, and dashed lines show uncertainty.

1.12 SRN-02-IRSL Results

We analyzed SRN-02-IRSL using Feldspar pIRSL on 90-250 μm size grains. Out of 15 aliquots, 13 produced acceptable luminescence characteristics and passed acceptance cri- teria as listed in Table 7. Aliquots that passed acceptance criteria are plotted as a kernal density estimate and as a radial plot in Figure 21. Application of the central age model (CAM, Galbraith et al., 1999) produced an equivalent dose of 443 ± 16.6 Grays, which leads to a CAM age of 104 ± 7.5 ka. In contrast, application of the minimum age model (MAM, Galbraith et al., 1999) produces an equivalent dose of 411 ± 27.1 Gray, which leads to a MAM age of 96.3 ± 8.7 ka.

-

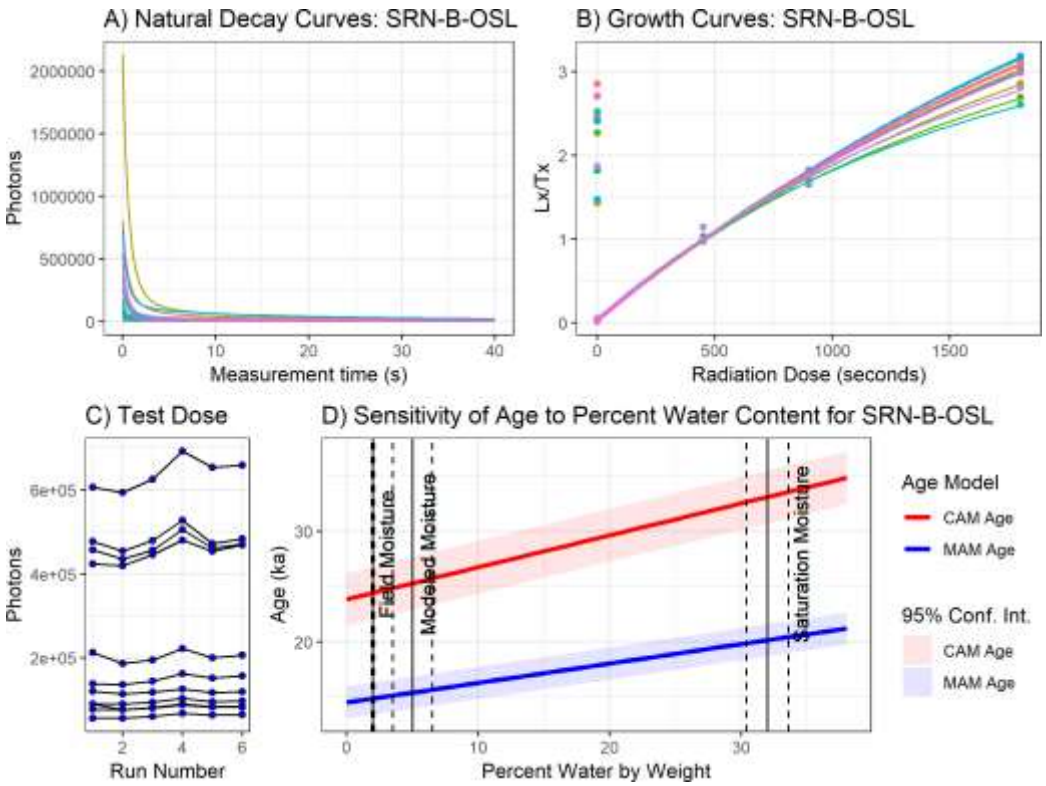

Figure 8: Plots of luminescence characteristics for SRN-B-OSL. A) Compilation of the natural luminescence decay curves for each aliquot. B) Compilation of the growth curves for each aliquot generated by the SAR protocol (Table 7). C) Magnitude of test dose response for each SAR cycle. D) Graph of CAM or MAM age as a function of water content. Note that for pre-2015 datasets, Plots A through C are not available and only Plot D will be present.

2 Methods

2.1 Luminescence dating background

A luminescence age dates the time since a sand grain or aliquot of grains was last exposed to sunlight. A luminescence age is calculated following the age equation:

$$Age = \frac{D_e}{D_R} \tag{1}$$

where D_e is the *equivalent dose* (units of Joules per kilogram, also written as units of Gray named after physicist Louis Harold Gray and *not* named after geochronologist Harrison James Gray), which is the equivalent amount of radiation needed to produce the observed

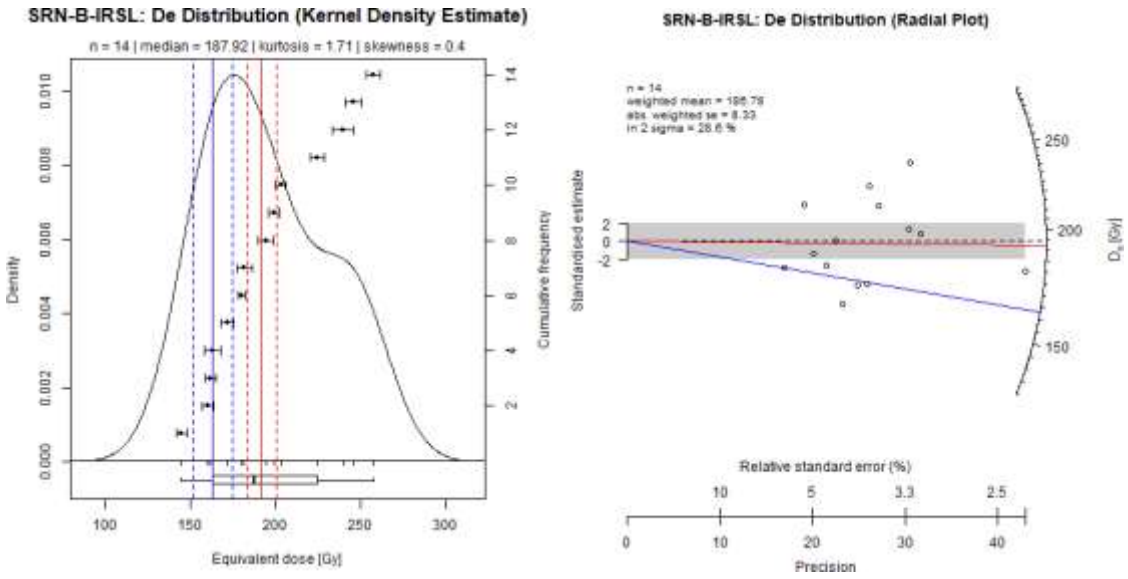

Figure 9: Plots of Equivalent Dose for SRN-B-IRSL. Red lines shows CAM equivalent dose, blue lines show MAM equivalent dose, solid line shows the age, and dashed lines show uncertainty.

natural luminescence, and D_R is the natural background radiation dose rate (in units of Gray per kiloannum, Gy/ka)). In luminescence dating, we determine the amount of luminescence as a function of absorbed radiation dose. When we measure the natural luminescence of a sand grain, or aliquots of grains, this provides the equivalent dose D_e. We determine the background dose rate, D_R, either through direct measurement or through measurement of radioactive elements in a given sample. The following paragraphs describe the results of determining both D_e and D_R and calculating an age following Equation 1 above. Extended details on how these numbers were obtained is given in the Methods section below.

2.2 Sample preparation

We obtained ages following the methods described in Nelson et al. (2015) and Gray et al. (2015), which are repeated here for convenience. We extracted both the light-exposed and light-protected sections of the sample. For tube-based samples, we extracted the outer 2cm from both ends of the tube and reserved this sample for water content determination and Inductively-Coupled Plasma Mass Spectrometry (ICP-MS) if needed. We then extract the inner contents of the tube for further preparation. For block samples, we spray painted

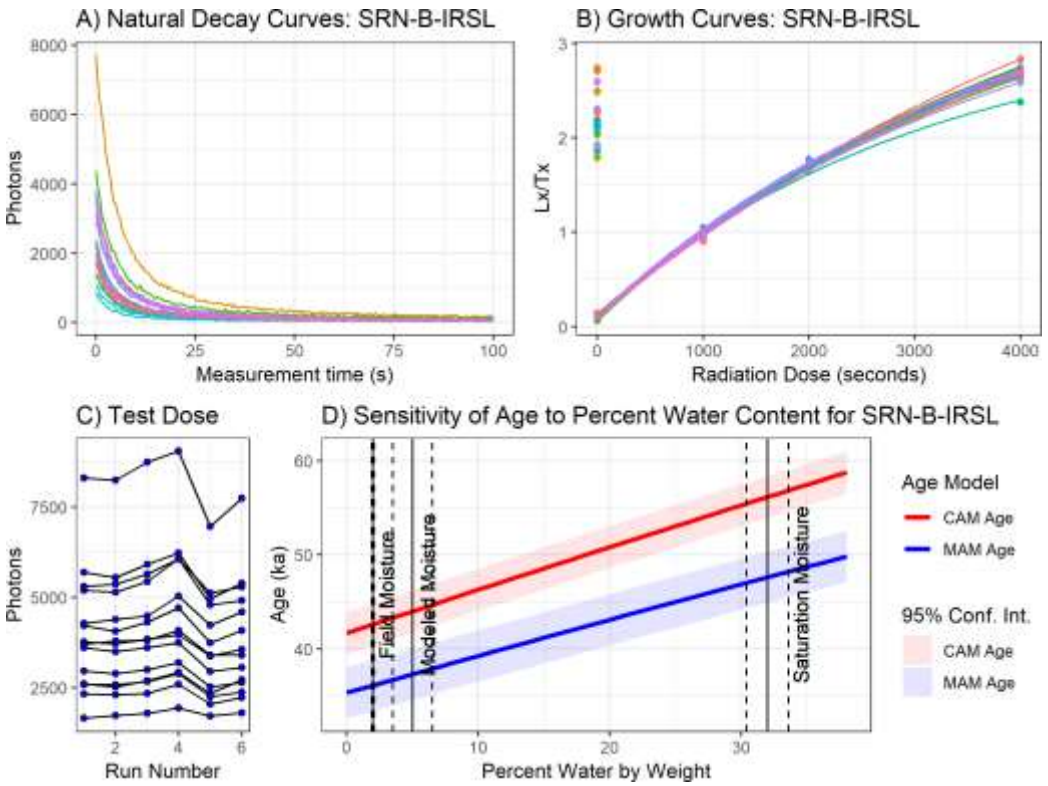

Figure 10: Plots of luminescence characteristics for SRN-B-IRSL. A) Compilation of the natural luminescence decay curves for each aliquot. B) Compilation of the growth curves for each aliquot generated by the SAR protocol (Table 7). C) Magnitude of test dose response for each SAR cycle. D) Graph of CAM or MAM age as a function of water content. Note that for pre-2015 datasets, Plots A through C are not available and only Plot D will be present.

the exterior of the block with black spray-paint to mark light exposed sediment. We then dismantle the block and reserve the outer 2cm radius of the block for water content and ICP-MS measurements. The inner contents of the block are then reserved for further preparation. For canister collected samples, the entire sample is used for further prep and additional canisters are used for water content. For all types of sample collection, we will use High Resolution Ge Gamma Spectrometry if the PI submits an additional 600 grams of bulk sample. Water content percents of the samples are measured and calculated using: (wet weight - dry weight)/(dry weight) for field obtained samples and again after samples are saturated with water in the laboratory to determine maximum water content.

We then treat light-protected extracts with a series of chemical and mechanical sepa-

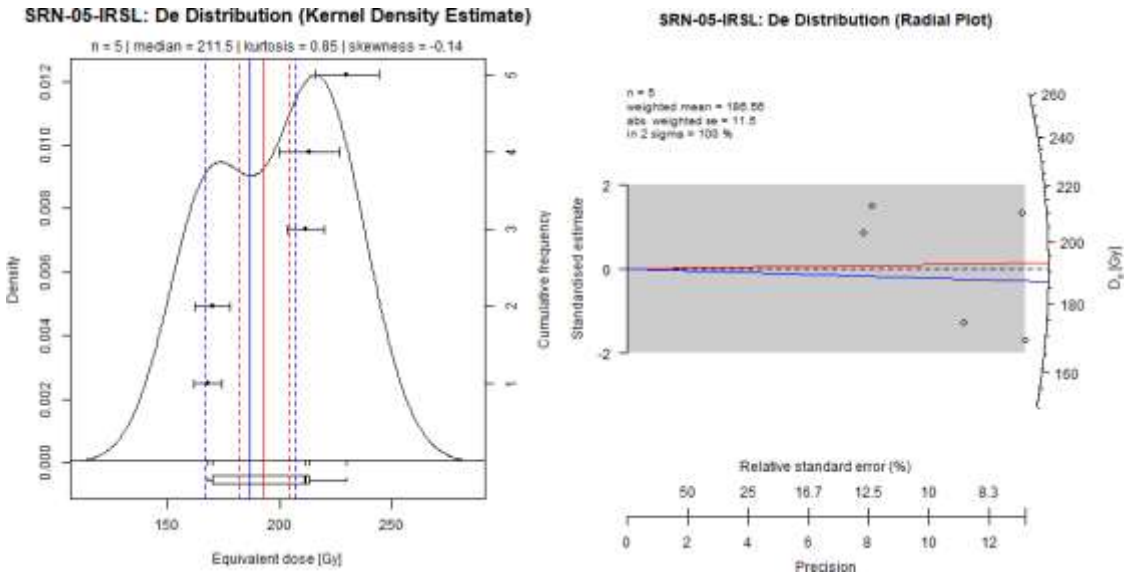

Figure 11: Plots of Equivalent Dose for SRN-05-IRSL. Red lines shows CAM equivalent dose, blue lines show MAM equivalent dose, solid line shows the age, and dashed lines show uncertainty.

rations. First, we submerge samples in a 5N hydrochloric acid solution for the greater of 4 hours or until the reaction follows to completion. We then rinse the sample and repeat the process with 30% hydrogen peroxide. We then apply 100 ml of sodium pyrophosphate, a deflocculant, to disperse clay particles. This sets the stage for our wet sieving process, where we separate the 90-250 μm grain size range in increments of 20 μm. After sepa- ration, we dry and weight the separations and select the dominant (by mass) grain size for further treatment. In the rare case that no size is dominant, or if less than 15g of sample is available, we combine the separations. We take this sieved separate and perform a magnetic separation with a Frantz Isodynamic Magnetic Separator (Model L-1) following the methods of Porat (2006). The non-magnetic fraction now contains mostly quartz and feldspar sand. To separate quartz from feldspar, we perform a density separation using lithium sodium polytungstate, a liquid with adjustable density such that quartz can sink and feldspars will float. The isolated quartz fraction is etched with a 49% hydroflouric solu- tion to remove feldspar inclusions and any accessory minerals. Finally, aliquots of quartz and/or feldspar are plated onto stainless steel discs using commercial silicone spray. The discs of quartz and/or feldspar are now ready for machine analysis.

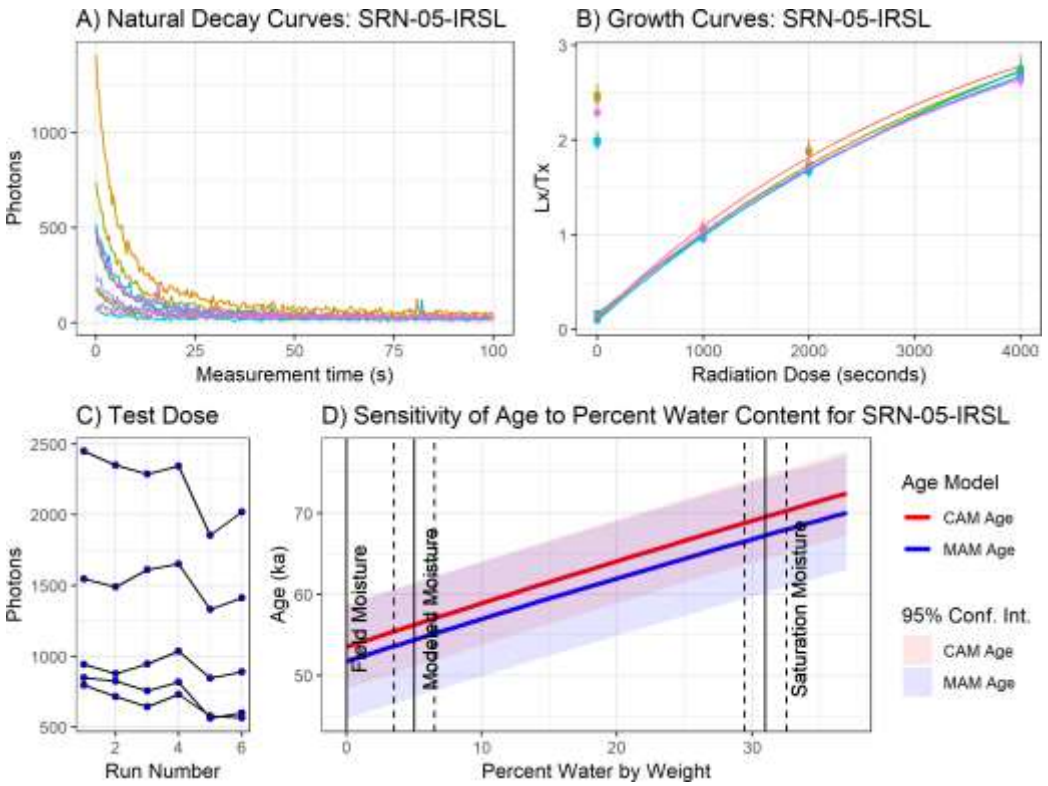

Figure 12: Plots of luminescence characteristics for SRN-05-IRSL. A) Compilation of the natural luminescence decay curves for each aliquot. B) Compilation of the growth curves for each aliquot generated by the SAR protocol (Table 7). C) Magnitude of test dose response for each SAR cycle. D) Graph of CAM or MAM age as a function of water content. Note that for pre-2015 datasets, Plots A through C are not available and only Plot D will be present.

2.3 Luminescence Machine Analysis

We measure the quartz OSL or feldspar IRSL using the single aliquot regeneration (SAR) protocol (Murray and Wintle, 2000; 2003) given in Table 5. See Table 6 for machine speci- fications. Decay curves showing the luminescence output during measurement and growth curves showing the relation between luminescence and equivalent dose are presented in the supplementary materials with this report. These graphs are examined by lab staff during measurement to check for signs of contamination by non quartz or feldspathic minerals or for evidence of luminescence saturation. We attempt to run between 30 to 48 aliquots per sample. However, factors such as sample availability can limit the number of runs performed or if laboratory staff determine that further aliquots are not necessary to calculate

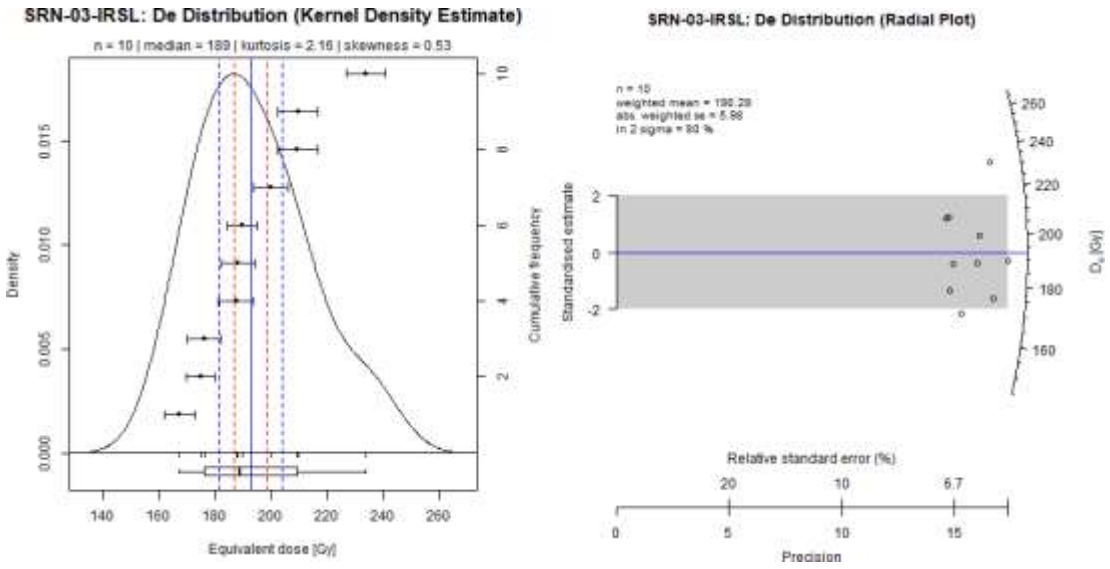

Figure 13: Plots of Equivalent Dose for SRN-03-IRSL. Red lines shows CAM equivalent dose, blue lines show MAM equivalent dose, solid line shows the age, and dashed lines show uncertainty.

an age. The number of aliquots that pass acceptance criteria (Table 7) depends on the mineralogy of the sample and the source geology. Often, samples that contain quartz and/or feldspar derived from volcanic or hydrothermal deposits will have unfavorable luminescence characteristics. The percentage of accepted aliquots varies greatly, but a lower percentage does not imply a inaccurate age. Rather, it indicates a longer sample measuring time as more aliquots are needed to improve age estimates and lower uncertainty. The number of aliquots measured is usually decided on a sample-by-sample basis by laboratory staff in consultation with the director.

2.4 Equivalent Dose Calculation and Age Models

After collecting data of the luminescence of plated aliquots, we analyze the results using the r-Luminescence package (Kreutzer et al., 2012; 2018) for the programming language **R** (R Core Team, 2018). The exact code used to produce this report is given in the Supplementary Materials at the end of this report. The general workflow is to import the machine files into **R**, process them using handling functions and analysis functions such as analyze SAR.CWOSL() to perform single aliquot regeneration and then driving the output into analysis functions such as calc CentralDose() and calc MinDose() to obtain the central

1. Preheat (225°C) for 60 seconds
2. Stimulation with blue (470 nm) at 225 °C for 100 seconds **(Ln)**
3. Test dose beta irradiation
4. Preheat (225 C) for 60 seconds
5. Stimulation with blue (470 nm) at 225 °C for 100 seconds **(Tn)**
6. Repeat steps 1-5 with beta regeneration doses **(Tx, Tn)**

Table 5: Single Aliquot Regeneration protocol for quartz OSL equivalent dose determination (Murray and Wintle, 2000, 2003).

Machine:	Automated Risø TL/luminescence-DA-15 and/or DA-20
Irradiation Source (β)	Sr^{90}/Y^{90} (0.845 Gy/s)
Stimulation source:	Blue diodes (quartz): emission centered on 470 nm
IR diodes (feldspar):	emission centered on 870 nm Power delivered
to aliquot:	136 mW/cm2 for quartz OSL (85% power)
	144 mW/cm2 for feldspar IRSL (90% power)
Photomultiplier:	Thorn-EMI 9235Q
Detection filters:	two Hoya U340 filters
Background evaluation:	black body counts <33 ct/sec, BG counts <41 ct/sec

Table 6: Machine parameters used in preparation and analyses of samples for quartz OSL, feldspar IRSL, and/or feldspar pIRIR.

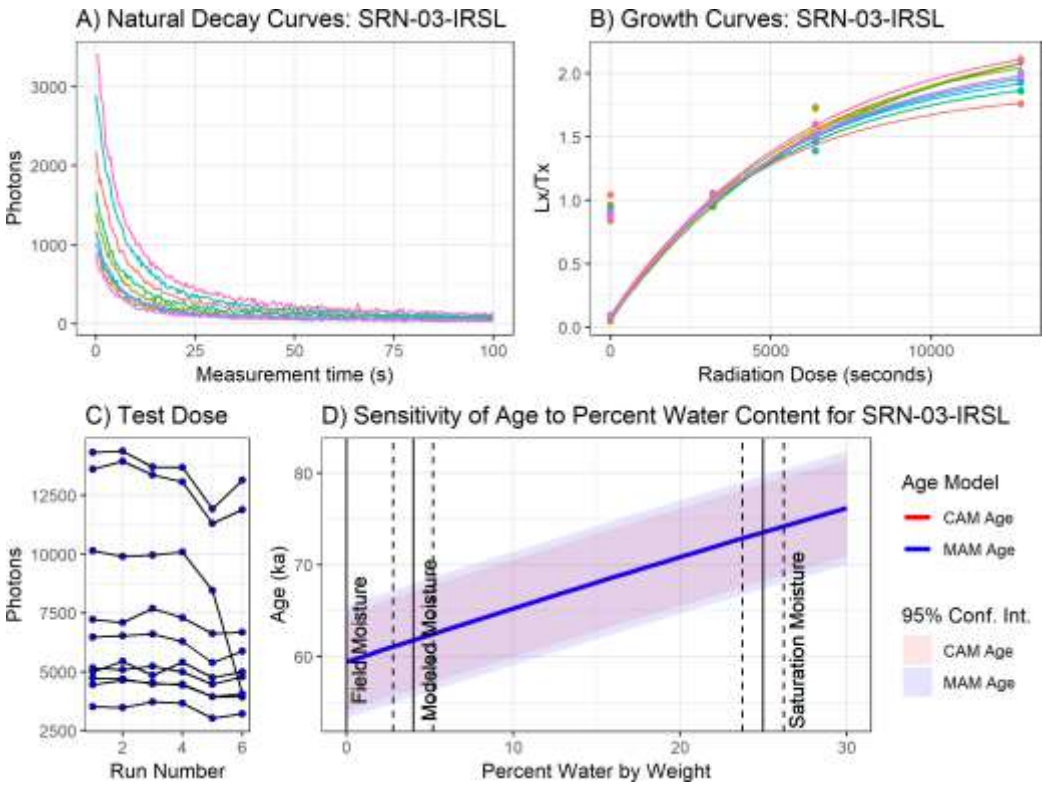

Figure 14: Plots of luminescence characteristics for SRN-03-IRSL. A) Compilation of the natural luminescence decay curves for each aliquot. B) Compilation of the growth curves for each aliquot generated by the SAR protocol (Table 7). C) Magnitude of test dose response for each SAR cycle. D) Graph of CAM or MAM age as a function of water content. Note that for pre-2015 datasets, Plots A through C are not available and only Plot D will be present.

age model and minimum age model results respectively. Various other parameters are estimated and can be seen in detail in the code below. The final output is the summary tables (Table 1 and Table 2) and the KDE/radial plots throughout this document.

The central age model (CAM) and minimum age model (MAM) used in this report are statistical tools specialized for luminescence dating (Galbraith et al., 1999; Galbraith and Roberts, 2012). They effectively solve for the dose that all grains received during burial. The central age model is analogous to a weighted average, but is different in that it accounts for the uncertainties associated with the doses received by grains during burial. When a sample has been fully bleached prior to deposition, the CAM will isolate the true burial dose. However, fully bleached samples can be rare in some depositional environments. In such cases where incomplete bleaching is expected, we use the minimum age model

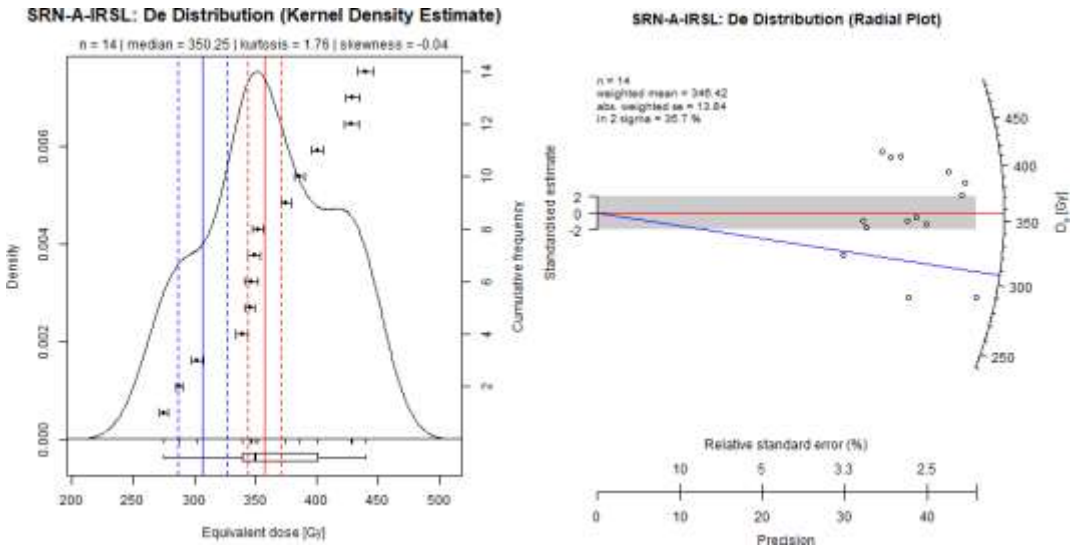

Figure 15: Plots of Equivalent Dose for SRN-A-IRSL. Red lines shows CAM equivalent dose, blue lines show MAM equivalent dose, solid line shows the age, and dashed lines show uncertainty.

(MAM). The MAM effectively weights the lower dose grains based on the idea that lower dosed grains are more likely to have been fully bleached prior to deposition. For fluvial and/or alluvial environments, the MAM is usually preferred. Note that in some cases, the CAM and MAM will produce overlapping results. This occurs when the statistical scatter of the sample is similar to the scatter expected for a well-bleached sample (20%, Cunningham and Wallinga, 2012). Both the CAM and MAM are identifying the central population as the population most likely to represent the true age. If there is overlapping results, we generally prefer the CAM. If they do not overlap, we generally prefer the MAM. However, the decision of which age model to prefer involves multiple factors and varies on

Recycling Ratio: 20%
Recuperation: 20%
Maximum Test Dose Error: 20%
Maximum Paleodose Error: 20%

Table 7: Acceptance criteria used to filter aliquots for equivalent dose determination. Aliquots passing these criteria are plotted in KDE and radial plots.

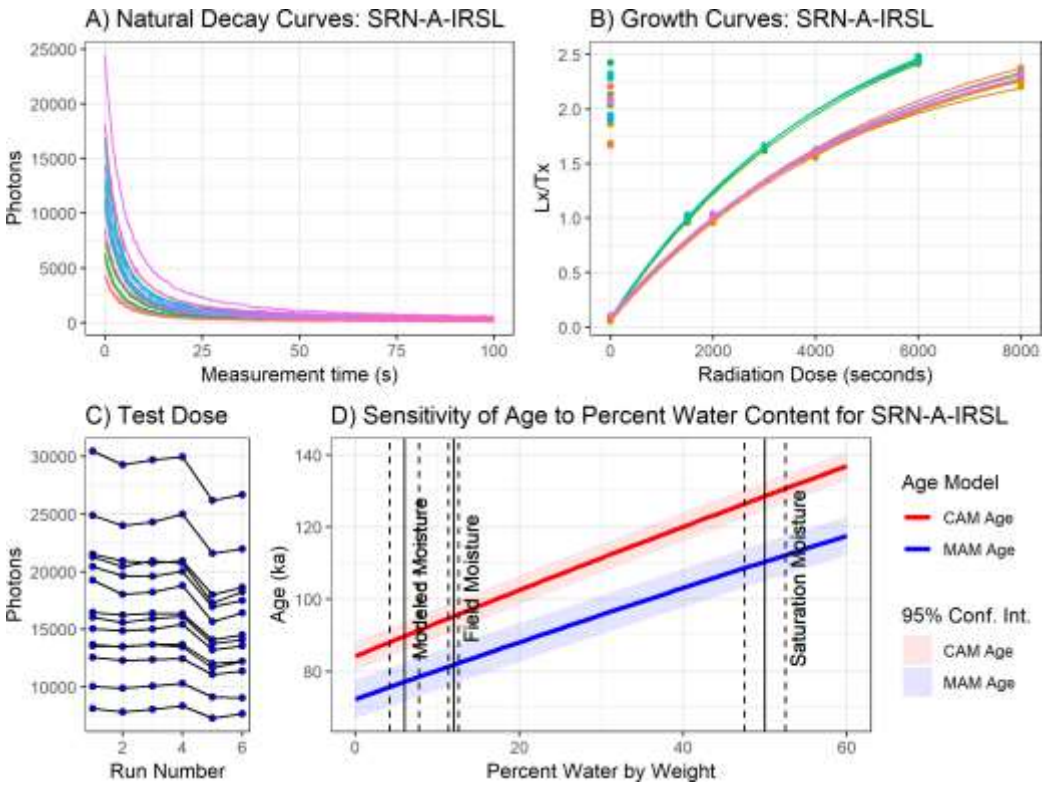

Figure 16: Plots of luminescence characteristics for SRN-A-IRSL. A) Compilation of the natural luminescence decay curves for each aliquot. B) Compilation of the growth curves for each aliquot generated by the SAR protocol (Table 7). C) Magnitude of test dose response for each SAR cycle. D) Graph of CAM or MAM age as a function of water content. Note that for pre-2015 datasets, Plots A through C are not available and only Plot D will be present.

a case-by-case basis.

2.5 Dose Rate Estimation, Age Calculation, and Water Content Modeling

To estimate the background dose rate (Table 1) we require measurements of the elemental concentrations of the weight percent of potassium (K%), and the parts per million (ppm) of Uranium (U) and Thorium (Th) as previously discussed. If only tube-based samples are provided, we will extract sample and submit for ICP-MS to determine K, U, and Th values. If we are provided with a large bulk sample of approximately 600 grams, we will use High Resolution Ge Gamma Spectrometry, which we find gives results with comparable or better precision/accuracy and has a faster turn-around time.

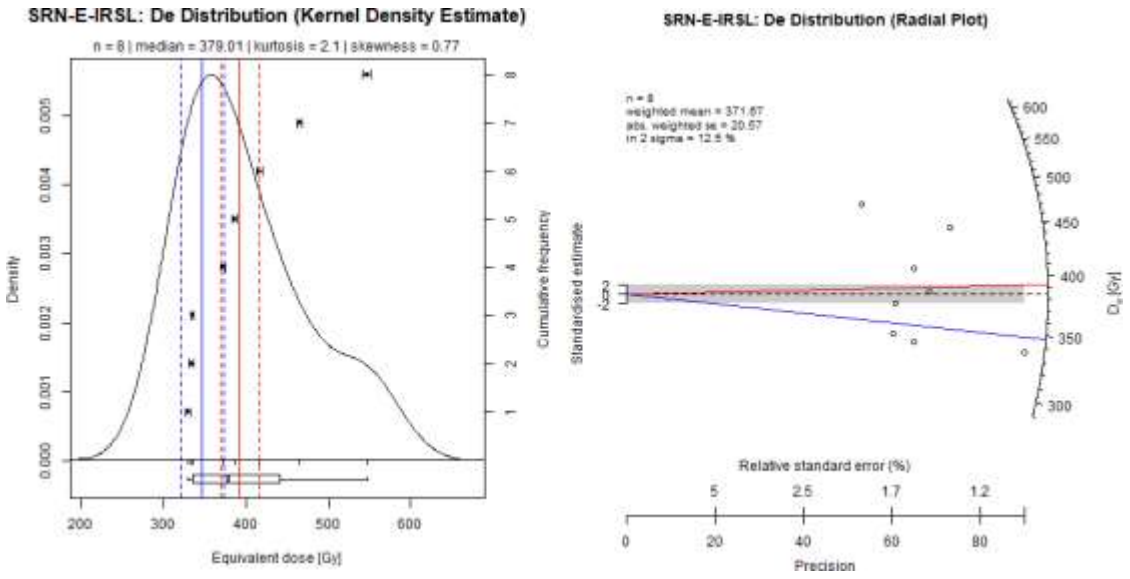

Figure 17: Plots of Equivalent Dose for SRN-E-IRSL. Red lines shows CAM equivalent dose, blue lines show MAM equivalent dose, solid line shows the age, and dashed lines show uncertainty.

We calculate dose rates (1) using the Dose Rate and Age Calculator (DRAC) by Durcan et al. (2015). We use DRAC as it is an open-source calculator that is continuously updated by the authors as improvements in luminescence dating develop. DRAC has been vetted by the community and also handles uncertainty propagation. Its use greatly minimizes the potential for calculation errors. DRAC takes inputs such as elemental concentrations of K, U, and Th, and other sample data and returns an estimate of the environmental dose rate. Our exact input and use of DRAC functions is demonstrated in the **R** code in the supplemental material. Finally, we calculate ages by using Equation 1 and propagating uncertainty using standard error propagation formulas (Table 2).

One of the largest sources of uncertainty in the dose rate calculation is an assumption of the water-content history of the sample over its burial lifetime. The water content, here defined as the water held in pore spaces within sediment, serves to lower the dose rate by absorbing radiation. This lowered dose rate leads to a decrease in luminescence generated per unit time. However, the water content of a sedimentary unit can change throughout time due to changes in water table height as a function of various processes such as climate change. There are three methods available to estimate the lifetime average water content of
a sample.

First, the *in-situ* water content of a sample can be used to estimate the lifetime water content. Another alternative used in luminescence dating is to choose a fraction of

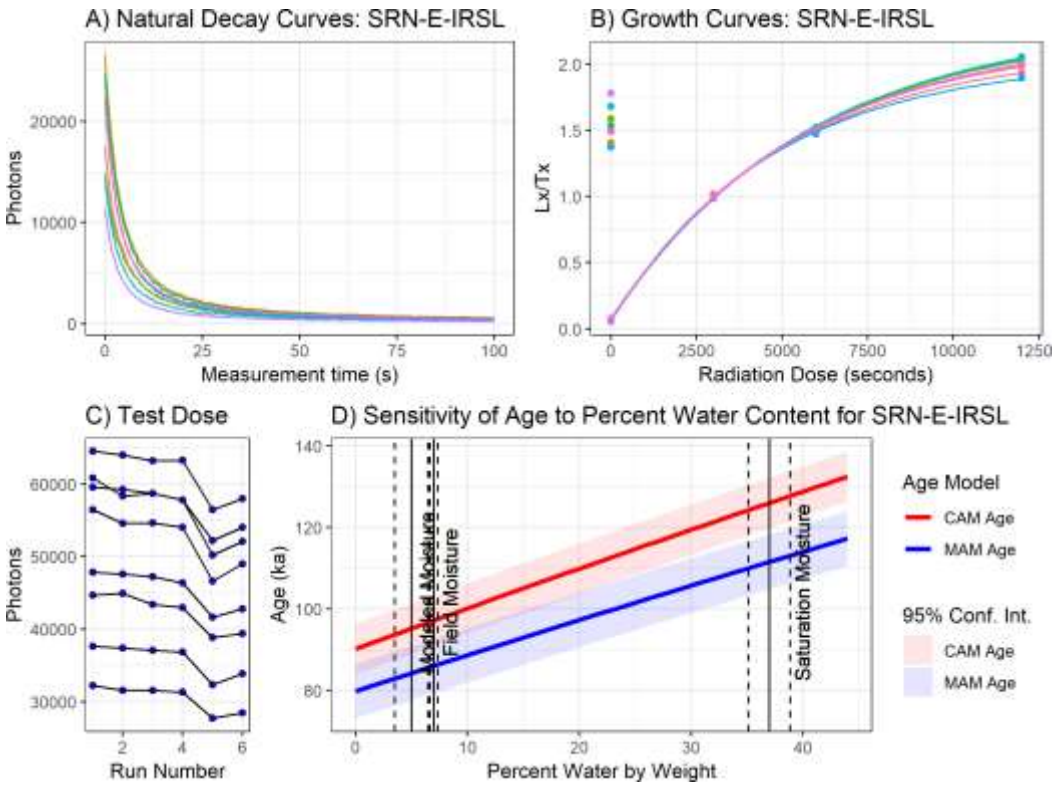

Figure 18: Plots of luminescence characteristics for SRN-E-IRSL. A) Compilation of the natural luminescence decay curves for each aliquot. B) Compilation of the growth curves for each aliquot generated by the SAR protocol (Table 7). C) Magnitude of test dose response for each SAR cycle. D) Graph of CAM or MAM age as a function of water content. Note that for pre-2015 datasets, Plots A through C are not available and only Plot D will be present.

saturated water content, e.g. 10%, 25%, etc. A third alternative we describe below is to model the lifetime water content following Nelson and Rittenour (2015).

We follow Nelson and Rittenour (2015) by constructing the model of the water content by using the van Genuchten (1980) water retention curve for each sample:

$$\theta(h) = \theta_r + \frac{\theta_s - \theta_r}{[1 + (\alpha|h|)^n]^{1-\frac{1}{n}}} \quad (2)$$

where $\theta(h)$ is the modeled volumetric water content (cm^3/cm^3), θ_r is the residual volumetric water content (cm^3/cm^3), θ_s is the saturated water content (cm^3/cm^3), α ($1/cm^3$) and n (dimensionless) are curve shape parameters, and h is the matric potential of the sediment (cm). We measure θ_s during sample preparation, and using soil texture class average

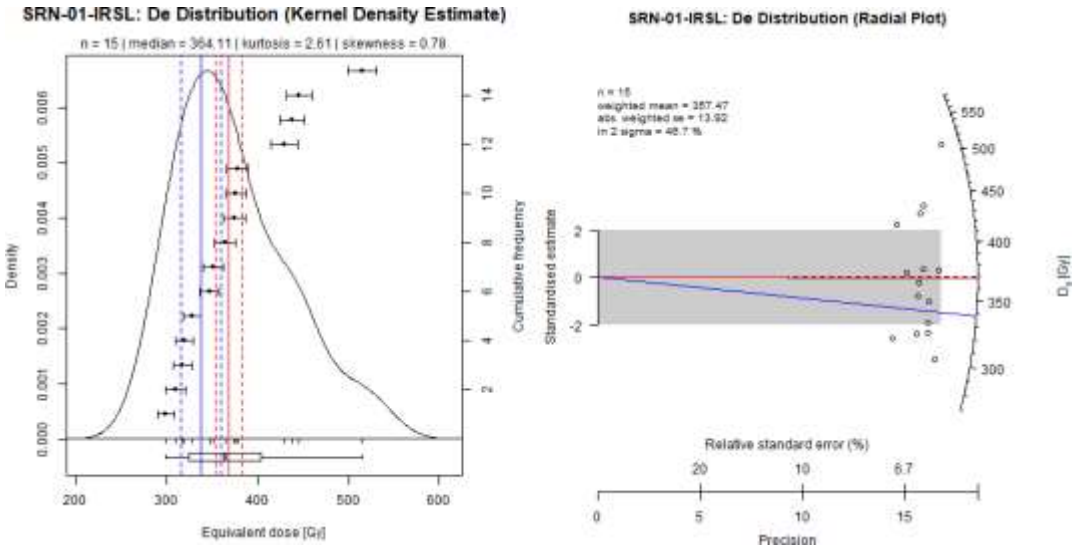

Figure 19: Plots of Equivalent Dose for SRN-01-IRSL. Red lines shows CAM equivalent dose, blue lines show MAM equivalent dose, solid line shows the age, and dashed lines show uncertainty.

values for θ_r, α, and n from the US Salinity Lab (https://www.ars.usda.gov/pacific-west- area/riverside-ca/us-salinity-laboratory/docs/rosetta-class-average-hydraulic-parameters/). We determine the soil texture class (sand, clay, loam, etc) using particle size measurements, laboratory evaluation, or client provided data. To estimate h, we follow Nelson and Rittenour (2015) and estimate the Mean Annual Water State (MAWS) matric potential using the USDA-NRCS Soil Moisture Regime Classification system. The USDA-NRCS Soil Moisture Regime Classification system provides estimates for the matric potential of a local soil, which can then be used with Equation 2 to provide a modeled water content value. See Nelson and Rittenour (2015) for detailed methodology.

The choice of water content method (*in-situ*, fraction of saturation, or modeling) depends on the applicability of the method for each sample. The *in-situ* method assumes

that the present water-content value is reflective of the average water content for the lifetime of a sample. In cases where the water content is not expected to have

changed significantly following deposition, the *in-situ* method is appropriate. Examples include samples obtained by coring more than a few meters below the surface or for samples below the water table. However, the *in-situ* can often be non-representative of the average water content over the life of sample prior to sampling (Nelson and Rittenour, 2015). For example, if one is sampling an escarpment, the recent exposure of the surface will lead to drying and a

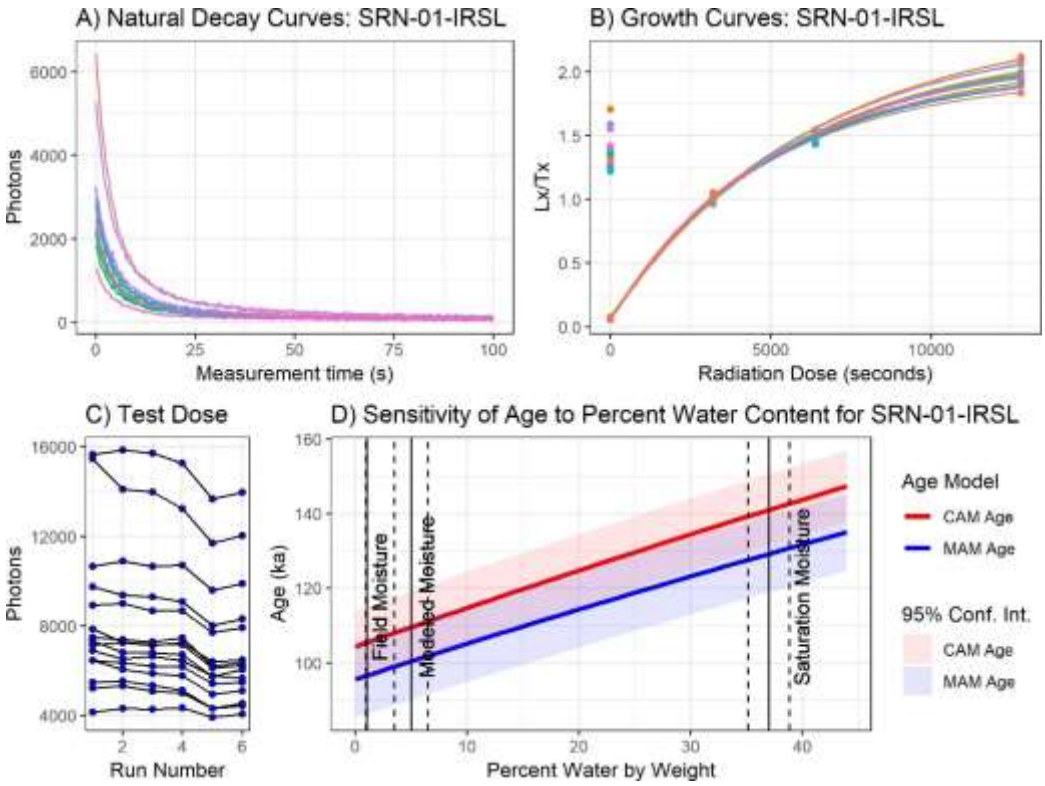

Figure 20: Plots of luminescence characteristics for SRN-01-IRSL. A) Compilation of the natural luminescence decay curves for each aliquot. B) Compilation of the growth curves for each aliquot generated by the SAR protocol (Table 7). C) Magnitude of test dose response for each SAR cycle. D) Graph of CAM or MAM age as a function of water content. Note that for pre-2015 datasets, Plots A through C are not available and only Plot D will be present.

lowering of the water table. An *in-situ* sample of water content in this environment may not be representative of the water conditions prior to erosion of the escarpment.

In contrast, the fraction of saturation method avoids the issue of the *in-situ* value being non-representative of the lifetime average value. The fraction of saturation method may be more appropriate when the water content history of a sample is

known or expected to have changed over time. An example may be paleo-lake deposits where the sample remained saturated following deposition until the lake dried up and the sample became desiccated for the rest of its history. However, the fraction of saturation method requires the user to assume some value and it may be difficult to robustly choose a value. Individual cases may require further analysis to estimate an appropriate fraction.
Finally, the modeling method, as described above, presents an alternative that seeks

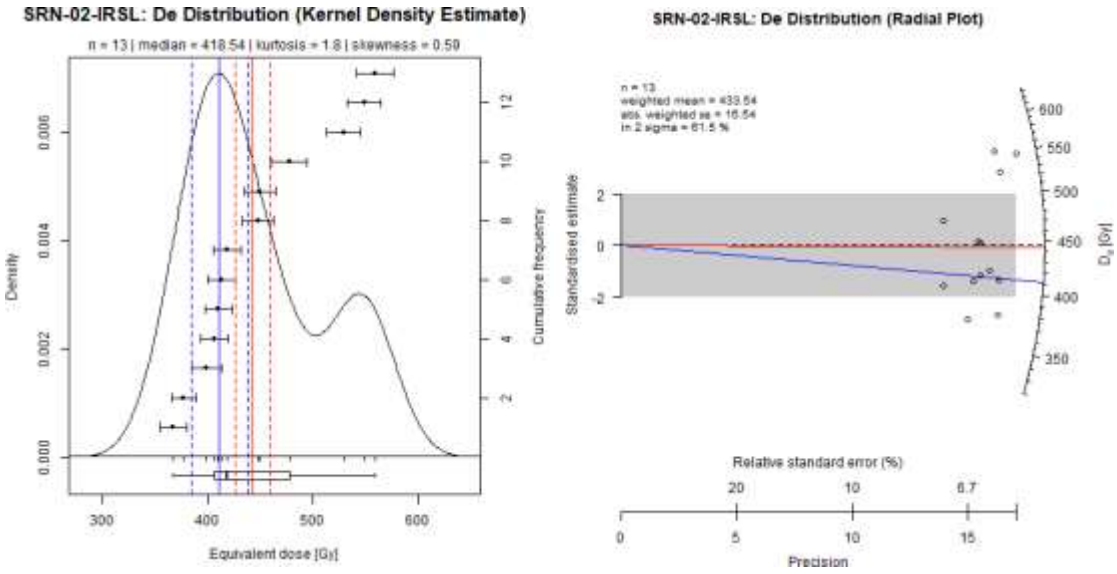

Figure 21: Plots of Equivalent Dose for SRN-02-IRSL. Red lines shows CAM equivalent dose, blue lines show MAM equivalent dose, solid line shows the age, and dashed lines show uncertainty.

to minimize subjectivity in the water content estimation. The modeling approach is appropriate for free-draining samples within 3 meters of the land surface and are not affected by perched or fluctuating water tables (Nelson and Rittenour, 2015). The modeling method assumes that group averages of hydraulic parameters (θ_r, α, and n) are reflective of the hydraulic parameters of the sample. As such, the uncertainty on the modeled water con- tent value is often large (30-50%). The use of class average hydraulic parameters is used heavily in soil science to general success (Vereecken et al., 2010). In additon, the method assumes that the Mean Annual Water State (MAWS) matric potential using the USDA- NRCS Soil Moisture Regime Classification system is approximately appropriate for the sample locations. The USDA-NRCS system is fairly coarse in resolution and may not capture local variations in sample matric potential. As with the *in-situ* and fraction of saturation methods, the modeling approach requires a consideration of its base assumptions and applicability on a sample-by-sample basis.

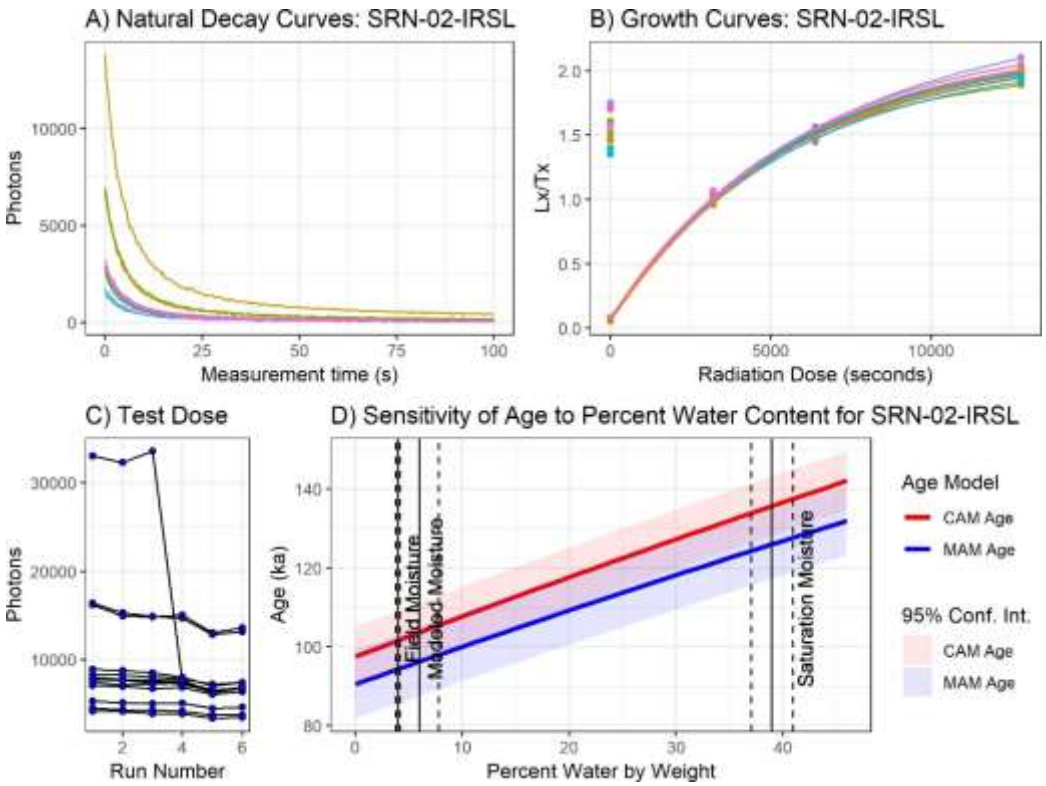

Figure 22: Plots of luminescence characteristics for SRN-02-IRSL. A) Compilation of the natural luminescence decay curves for each aliquot. B) Compilation of the growth curves for each aliquot generated by the SAR protocol (Table 7). C) Magnitude of test dose response for each SAR cycle. D) Graph of CAM or MAM age as a function of water content. Note that for pre-2015 datasets, Plots A through C are not available and only Plot D will be present.

3 References

Bell W (1979). Attenuation factors for the absorbed radiation dose in quartz inclusions for thermoluminescence dating. Ancient TL 8, 1-12.

Brennan B, Lyons R, Phillips S (1991). Attenuation of alpha particle track dose for spherical grains. International Journal of Radiation Applications and Instrumentation. Part D. Nuclear Tracks and Radiation Measurements, 18, 249-253.

Cunningham, A. C., & Wallinga, J. (2012). Realizing the potential of fluvial archives using robust OSL chronologies. Quaternary Geochronology, 12, 98-106.

Cunningham, A. C., Wallinga, J., & Minderhoud, P. S. (2011). Expectations of scatter in equivalent-dose distributions when using multi-grain aliquots for OSL dating. Geochronometria, 38(4), 424.

Durcan, J.A., King, G.E., and Duller, G.A.T., 2015. DRAC: Dose rate and age calculator for trapped charge dating. Quaternary Geochronology, 28, 54-61.

Galbraith, R. F., Roberts, R. G., Laslett, G. M., Yoshida, H., & Olley, J. M. (1999). Optical dating of single and multiple grains of quartz from Jinmium rock shelter, northern Australia: Part I, experimental design and statistical models. Archaeom- etry, 41(2), 339-364.

Galbraith, R. F., & Roberts, R. G. (2012). Statistical aspects of equivalent dose and error calculation and display in OSL dating: an overview and some recommendations. Quaternary Geochronology, 11, 1-27.

Gray, H. J., Mahan, S., Rittenour, T. M., & Nelson, M. S. (2015). Guide to luminescence dating techniques and their application for paleoseismic research. In Basin and Range Province Seismic Hazards Summit III, 2015.

Kreutzer, S., Dietze, M., Burow, C., Fuchs, M. C., Schmidt, C., Fischer, M., & Friedrich, J. (2017). Luminescence: Comprehensive luminescence dating data analysis.
R package version 0.8.5.

Kreutzer S, Schmidt C, Fuchs MC, Dietze M, Fis- cher M, Fuchs M (2012). Introducing an R package for luminescence dating analysis. Ancient TL, 30(1), 1-8.

Murray, A. S., & Wintle, A. G. (2000). Lumines- cence dating of quartz using an improved single-aliquot regenerative-dose protocol. Radiation measurements, 32(1), 57-73.

Murray, A. S., & Wintle, A. G. (2003). The single aliquot regenerative dose protocol: potential for improvements in reliability. Radiation measurements, 37(4-5), 377-381.

Nelson, M. S., Gray, H. J., Johnson, J. A., Rittenour, T. M., Feathers, J. K., & Mahan, S. A. (2015). User guide for luminescence sampling in archaeolog- ical and geological contexts. Advances in Archaeo- logical Practice, 3(2), 166-177.

Nelson, M. S., & Rittenour, T. M. (2015). Using grain-size characteristics to model soil water content: Application to dose-rate calculation for luminescence dating. Radiation Measurements, 81, 142-149.

Porat, N. (2006). Use of magnetic separation for pu- rifying quartz for luminescence dating. Ancient TL, 24(2), 33-36.

Steffen, D., Preusser, F., & Schlunegger, F. (2009). OSL quartz age underestimation due to unstable sig- nal components. Quaternary Geochronology, 4(5), 353-362.

Singarayer, J. S., & Bailey, R. M. (2004). Component-resolved bleaching spectra of quartz optically stimulated luminescence: preliminary results and implications for dating. Radiation Measurements, 38(1), 111-118.

Van Genuchten, M. T. (1980). A closed-form equa- tion for predicting the hydraulic conductivity of unsaturated soils 1. Soil science society of America journal, 44(5), 892-898.

Vereecken, H., Weynants, M., Javaux, M., Pachep- sky, Y., Schaap, M. G., & Genuchten, M. T. (2010).

Using pedotransfer functions to estimate the van Genucht- enMualem soil hydraulic properties: A review. Vadose Zone Journal, 9(4), 795-820.

4 Supplemental Material

4.1 R code used to calculate ages

```
## USGS R script for Luminescence analysis
# Written by H GRAY 2018-2019

## TO DO:

# fix significant digits formatting

# select water content based on input file

# adjust grain size ranges and dose rates based on prep sheets

# show only accepted aliquots in lum characteristics figure

# draw lines on growth curves in lum characteristics figure

# bibtex citations

# explain rejection criteria in TeX report doc

# Luminescence tests: preheat plateau/dose recovery, fading, Feldspar unbleachable dose,
# during measurement: thermal transfer, recuperation, recycling ratio, error limits, 2D0 test, test dose ~=
    natural


###############################################################################################

## Initialize

rm(list = ls())

library("Luminescence")
library("openxlsx")
library("xtable")
library("filesstrings")
library("ggplot2")
library("gridExtra")


###############################################################################################

## Core inputs

wdir = "C:\\Users\\hgray\\Desktop\\2019 SLV Alluvial Fans Nicovich\\" #don't forget ending \\
setwd(wdir)

# print(cbind(list.files(pattern = "*.binx")),row.names = FALSE)

input_data = read.xlsx("input_table.xlsx", colNames = TRUE, rowNames = FALSE, skipEmptyRows = TRUE)
#input_data = input_data[complete.cases(input_data),]



###############################################################################################

## Basic starting routines, build summary table

num_samples = nrow(input_data)
sample_number_array = input_data$BIN_num

depth_of_samples = input_data$depth # sample depths in meters
field_water_content_of_samples = input_data$water_field
saturation_water_content_of_samples = input_data$water_sat

soil_texture = input_data$soil_texture
soil_moisture_regime = input_data$soil_moisture_regime

mesh_size = input_data$mesh

Th_values = round(input_data$Th,3)
Th_err = round(input_data$Th_err,3)

U_values = round(input_data$U,3)
U_err = round(input_data$U_err,3)

```

```
K_values = round(input_data$K,3)
K_err = round(input_data$K_err,3)

latitude_values = input_data$lat
longitude_values = input_data$long
elevation_values = round(input_data$elevation)

OSL_IRSL_type = input_data$analysis_type
mineral = input_data$mineral
analysis_type = paste(mineral, OSL_IRSL_type,sep=" ")
bin_or_xlsx = input_data$bin_or_xlsx
file_names = input_data$file_name_plus_extension

DR_type = input_data$DR_type

sigma_b_input = input_data$sigma_b
MAM_log = input_data$MAM_log

water_type = input_data$water_type

g_vals = input_data$g_value
g_value_err = input_data$g_value_err
g_vals_days = input_data$g_val_days

sample_list = input_data$Name

notes = input_data$notes

## build grain size arrays and mineral arrays

grain_size_min = rep(NA,num_samples)
grain_size_max = rep(NA,num_samples)

for (grain_iter in c(1:num_samples)){

  if (mesh_size[grain_iter]==80){
    grain_size_min[grain_iter] <- 180
    grain_size_max[grain_iter] <- 250
  }
  if (mesh_size[grain_iter]==100){
    grain_size_min[grain_iter] <- 150
    grain_size_max[grain_iter] <- 180
  }

  if (mesh_size[grain_iter]==120){
    grain_size_min[grain_iter] <- 125
    grain_size_max[grain_iter] <- 150
  }

  if (mesh_size[grain_iter]==170){
    grain_size_min[grain_iter] <- 90
    grain_size_max[grain_iter] <- 125
  }

  if (mesh_size[grain_iter]==230){
    grain_size_min[grain_iter] <- 63
    grain_size_max[grain_iter] <- 90
  }
  if (mesh_size[grain_iter]=="combined"){
    grain_size_min[grain_iter] <- 90
    grain_size_max[grain_iter] <- 250
  }
}

mineral_for_DRAC = rep(NA,num_samples)
conversion_factors  = rep("Guerinetal2011",num_samples)
calc_Rb_external = rep("Y",num_samples) # change to account for ICP-MS data in the future
calc_Rb_internal = rep("N",num_samples) # change to account for ICP-MS data in the future
alpha_attenuation = rep("Bell1980",num_samples)
beta_attenuation = rep(NA,num_samples)
etch_depth_min = rep(NA,num_samples)
etch_depth_max = rep(NA,num_samples)
beta_etch_attenuation_factor = rep("Brennan2003", num_samples)

internal_K_percent = rep("K",num_samples)

for (mineral_iter in c(1:num_samples)){
  if (mineral[mineral_iter]=="Quartz"){
    mineral_for_DRAC[mineral_iter] = "Q"
    beta_attenuation[mineral_iter] = "Guerinetal2012-Q"
```

```
    etch_depth_min[mineral_iter] = 8
    etch_depth_max[mineral_iter] = 10

  }
  if (mineral[mineral_iter]=="Feldspar"){
    mineral_for_DRAC[mineral_iter] = "F"
    beta_attenuation[mineral_iter] = "Guerinetal2012-F"
    etch_depth_min[mineral_iter] = 0
    etch_depth_max[mineral_iter] = 0
    internal_K_percent[mineral_iter] = 10
    calc_Rb_internal[mineral_iter] = "Y"

  }

  if (mineral[mineral_iter]=="Polymineral"){
    mineral_for_DRAC[mineral_iter] = "PM"
    beta_attenuation[mineral_iter] = "Brennan2003"
    etch_depth_min[mineral_iter] = 0
    etch_depth_max[mineral_iter] = 0
  }
}

## Scaling for gamma dose

scale_gamma = rep(NA,num_samples)

for (gamma_iter in c(1:num_samples)){
  if (depth_of_samples[gamma_iter]<=0.3){
    scale_gamma[gamma_iter] = "Y"
  } else {
    scale_gamma[gamma_iter] = "N"
  }
}



num_accepted = rep(NA,num_samples)
num_total = rep(NA,num_samples)

##############################################################################################

## Estimation of the water content based on Nelson and RIttemour 2015

# Import Rosetta data
rosetta_soil_textures = read.xlsx("soil_textures_class_averages.xlsx", colNames = TRUE, rowNames = FALSE,
    skipEmptyRows = TRUE)
rosetta_soil_textures = rosetta_soil_textures[complete.cases(rosetta_soil_textures),]
MAWS_array = read.xlsx("MAWS.xlsx", colNames = TRUE, rowNames = FALSE, skipEmptyRows = TRUE)

#creat dummy arrays
sample_soil_params_array = data.frame()
sample_MAWS_vals = data.frame()

# fill arrays with Rosetta values depending on the sample
for (water_iter in c(1:num_samples)){

 sample_soil_params_array = rbind(sample_soil_params_array,subset(rosetta_soil_textures, Texture_Class==soil_
     texture[water_iter]))
 sample_MAWS_vals = rbind(sample_MAWS_vals, subset(MAWS_array, soil_class==soil_moisture_regime[water_iter]))

}

# add sample names
sample_soil_params_array = cbind(sample_list,sample_soil_params_array)
sample_MAWS_vals = cbind(sample_list, sample_MAWS_vals)

# Break up the Van Genuchten Calc into pieces to limit mistakes
A = (input_data$water_sat+(1.8/1)*(1/100) - sample_soil_params_array$theta_r)
B = (10^sample_soil_params_array$log_alpha) * (abs(sample_MAWS_vals$geo_mean))
C = 1 + B^(10^sample_soil_params_array$log_n)
D = 1 - 1/(10^sample_soil_params_array$log_n)

van_Genuchten_WRC = sample_soil_params_array$theta_r + A/(C^(D))

# add to variables later added to DRAC (Choose between the Nelson and Rittemour method or something else)

modeled_water_content_of_samples = round(100*as.numeric(round(van_Genuchten_WRC*(1/1.8),4)))
modeled_water_err = 0.3*modeled_water_content_of_samples

# modeled_water_content_of_samples = (saturation_water_content_of_samples + field_water_content_of_samples)/2
```

```
# modeled_water_err = (saturation_water_content_of_samples*0.05 + field_water_content_of_samples*0.05)/2

## enter in preferred water content

# preferred_water_content_of_samples = 0.5+saturation_water_content_of_samples #field_water_content_of_samples *
# preferred_water_content_of_samples_err = saturation_water_content_of_samples*0.05 #field_water_content_of_
    samples*0.3

#############################################################################################

# prepare and submit DRAC inputs

DRAC_table = template_DRAC(nrow=num_samples, preset = "quartz_coarse", notification=FALSE)

DRAC_table$'Project ID' <- rep("USGS-Harrison", num_samples)
DRAC_table$'Sample ID' <- sample_list
DRAC_table$Mineral <- mineral_for_DRAC
DRAC_table$'Conversion factors' <- conversion_factors

DRAC_table$'External U (ppm)' = U_values
DRAC_table$'errExternal U (ppm)' <- U_err
DRAC_table$'External Th (ppm)' <- Th_values
DRAC_table$'errExternal Th (ppm)' <- Th_err
DRAC_table$'External K (%)' <- K_values
DRAC_table$'errExternal K (%)' <- K_err
DRAC_table$'Calculate external Rb from K conc?' <- calc_Rb_external
DRAC_table$'Calculate internal Rb from K conc?' <- rep("N",num_samples)

DRAC_table$'Internal K (%)' <- internal_K_percent
DRAC_table$'Calculate internal Rb from K conc?' <- calc_Rb_internal

DRAC_table$'Scale gammadoserate at shallow depths?' <- scale_gamma
DRAC_table$'Grain size min (microns)' <- grain_size_min
DRAC_table$'Grain size max (microns)' <- grain_size_max
DRAC_table$'alpha-Grain size attenuation' <- alpha_attenuation
DRAC_table$'beta-Grain size attenuation ' <- beta_attenuation
DRAC_table$'Etch depth min (microns)' <- etch_depth_min
DRAC_table$'Etch depth max (microns)' <- etch_depth_max
DRAC_table$'beta-Etch depth attenuation factor' <- beta_etch_attenuation_factor

DRAC_table$'Water content ((wet weight - dry weight)/dry weight) %' <- modeled_water_content_of_samples
DRAC_table$'errWater content %' <- modeled_water_err
DRAC_table$'Depth (m)' <- depth_of_samples
DRAC_table$'errDepth (m)' <- depth_of_samples*0.05
DRAC_table$'Overburden density (g cm-3)' <- rep(180, num_samples)
DRAC_table$'errOverburden density (g cm-3)' <- rep(0.1, num_samples)
DRAC_table$'Latitude (decimal degrees)' <- latitude_values
DRAC_table$'Longitude (decimal degrees)' <- longitude_values
DRAC_table$'Altitude (m)' <- elevation_values
DRAC_table$'De (Gy)' <- rep("X", num_samples)
DRAC_table$'errDe (Gy)' <- rep("X", num_samples)


DRAC_output = use_DRAC(DRAC_table, name="USGS_Harrison", print_references = FALSE, verbose=FALSE, citation_style
    ='text')

DRAC_results <- get_RLum(DRAC_output, "DRAC")

write.xlsx(DRAC_results$content, "DRAC_output.xlsx", sheetName="Sheet1")

dose_rates <- DRAC_results$highlights["Environmental Dose Rate (Gy.ka-1)"][1:num_samples,1]
dose_rates_err <- DRAC_results$highlights["errEnvironmental Dose Rate (Gy.ka-1)"][1:num_samples,1]

cosmic_dose_rates <- DRAC_results$highlights["Cosmicdoserate (Gy.ka-1)"][1:num_samples,1]
cosmic_dose_rates_err <- DRAC_results$highlights["errCosmicdoserate (Gy.ka-1)"][1:num_samples,1]

## prep the final data table for later

final_results_table = data.frame(sample_name=sample_list,
                                 latitude = latitude_values,
                                 longitude = longitude_values,
                                 elevation = elevation_values,
                                 depths= depth_of_samples,
                                 water_content = paste(as.character(round(field_water_content_of_samples)),
                                                       " (", as.character(round(saturation_water_content_of_
                                                           samples)),")",
                                                       " [", as.character(round(modeled_water_content_of_samples
                                                           )),"]",sep=""),
                                 k_percent = paste(sprintf("%#.3g",K_values)," $\\pm$ ", sprintf("%.3g", K_err),
                                       sep=""),
```

```
                                uranium_ppm = paste(sprintf("%#.3g",U_values)," $\\pm$ ", sprintf("%.3g",U_err)
                                    , sep=""),
                                thorium_ppm = paste(sprintf("%#.3g",Th_values)," $\\pm$ ", sprintf("%.1g",Th_
                                    err), sep=""),
                                cosmic_dose_rate = paste(sprintf("%#.3g",cosmic_dose_rates)," $\\pm$ ", sprintf
                                    ("%.3g",cosmic_dose_rates_err),sep=""),
                                dose_rate = paste(sprintf("%#.3g",dose_rates)," $\\pm$ ", sprintf("%.1g",dose_
                                    rates_err),sep=""),num_aliquots = rep(NA,num_samples),
                                scatter = rep(NA,num_samples),
                                de_cam = rep(NA,num_samples),
                                de_mam = rep(NA,num_samples),
                                age_cam = rep(NA,num_samples),
                                age_mam = rep(NA,num_samples))

## prep the big data table for excel

final_xlsx_table = data.frame(sample_name=sample_list,
                              latitude = latitude_values,
                              longitude = longitude_values,
                              elevation = elevation_values,
                              sampling_depth= depth_of_samples,
                              field_water_content = field_water_content_of_samples,
                              saturated_water_content = saturation_water_content_of_samples,
                              modeled_water_content = modeled_water_content_of_samples,
                              potassium_percent = K_values,
                              potassium_percent_err = K_err,
                              uranium_ppm = U_values,
                              uranium_ppm_err = U_err,
                              thorium_ppm = Th_values,
                              thorium_ppm_err = Th_err,
                              cosmic_dose_rate = cosmic_dose_rates,
                              cosmic_dose_rate_err = cosmic_dose_rates_err,
                              dose_rate = dose_rates,
                              dose_rate_err = dose_rates_err,
                              analysis_type = analysis_type,
                              grain_size_min = grain_size_min,
                              grain_size_max = grain_size_max,
                              num_aliquots_passed = rep(NA,num_samples),
                              num_aliquots_total = rep(NA,num_samples),
                              scatter = rep(NA,num_samples),
                              de_cam = rep(NA,num_samples),
                              de_cam_err = rep(NA,num_samples),
                              de_mam = rep(NA,num_samples),
                              de_mam_err = rep(NA,num_samples),
                              age_cam = rep(NA,num_samples),
                              age_cam_err = rep(NA,num_samples),
                              age_mam = rep(NA,num_samples),
                              age_mam_err = rep(NA,num_samples))

## prep the miscellaneous parameters tables

final_misc_table_1 = data.frame(sample_name=sample_list,
                              latitude = latitude_values,
                              longitude = longitude_values,
                              analysis = analysis_type,
                              grains = paste(as.character(grain_size_min)," - ", as.character(grain_size_max),
                                  sep=""),
                              water_type = water_type,
                              DR_method = DR_type)

final_misc_table_2 = data.frame(sample_name=sample_list,
                                g_vals = paste(sprintf("%#.3g",g_vals)," $\\pm$ ", sprintf("%.3g", g_value_err),
                                    sep=""),
                                sigma_b_MAM = sigma_b_input,
                                MAM_log = MAM_log,
                                gamma_MAM = rep("NA", num_samples),
                                sigma_MAM = rep("NA", num_samples),
                                p0_MAM = rep("NA", num_samples),
                                mu_MAM = rep("NA", num_samples), stringsAsFactors = FALSE)


final_misc_table_2 = data.frame(lapply(final_misc_table_2, gsub, pattern = "NA $\\pm$ NA", replacement = "-",
    fixed = TRUE), stringsAsFactors = FALSE)


## prep the table for a formatted excel table

final_summary_table = data.frame(sample_name=sample_list,
                                latitude = latitude_values,
                                longitude = longitude_values,
```

```
                                elevation = elevation_values,
                                depths= depth_of_samples,
                                water_content = paste(as.character(field_water_content_of_samples),
                                                      " (", as.character(saturation_water_content_of_samples),"
                                                        )",
                                                      " [", as.character(round(modeled_water_content_of_samples
                                                        *100)),"]",sep=""),
                                k_percent = paste(sprintf("%#.3g",K_values),"   ", sprintf("%.3g", K_err), sep=
                                     ""),
                                uranium_ppm = paste(sprintf("%#.3g",U_values),"   ", sprintf("%.3g",U_err), sep
                                     =""),
                                thorium_ppm = paste(sprintf("%#.3g",Th_values),'   ', sprintf("%.3g",Th_err),
                                     sep=""),
                                cosmic_dose_rate = paste(sprintf("%#.3g",cosmic_dose_rates),"   ", sprintf("%.3
                                     g",cosmic_dose_rates_err),sep=""),
                                dose_rate = paste(sprintf("%#.3g",dose_rates),"   ", sprintf("%.1g",dose_rates_
                                     err),sep=""),
                                num_aliquots = rep(NA,num_samples),
                                de_cam = rep(NA,num_samples),
                                de_mam = rep(NA,num_samples),
                                age_cam = rep(NA,num_samples),
                                age_mam = rep(NA,num_samples))

##############################################################################################

## Build KDE and Radial plots

sample_iter = 0

# sample_name = sample_list[sample_iter]

for (sample_name in sample_list){

print(paste("Running sample: ",sample_name,sep=""))
sample_iter = sample_iter + 1

if (bin_or_xlsx[sample_iter] == 'bin'){

  bin_data = read_BIN2R(file_names[sample_iter])

  dose_rate_matrix = data.frame(aliquot = bin_data@METADATA$POSITION,
                                IRR_DR = bin_data@METADATA$IRR_DOSERATE,
                                IRR_DR_ERR=bin_data@METADATA$IRR_DOSERATEERR)

  dose_rate_temp <- aggregate(dose_rate_matrix[, 2:3], list(dose_rate_matrix$aliquot), mean)

  dose_rate_sort_order = unique(bin_data@METADATA$POSITION)

  Risoe_dose_rate = dose_rate_temp[match(dose_rate_sort_order, dose_rate_temp$Group.1),][c("IRR_DR", "IRR_DR_ERR
      ")]

  results <- analyse_SAR.CWOSL(
    object = invisible(read_BIN2R(file_names[sample_iter],fastForward = TRUE,verbose=FALSE)),
    signal.integral.min = 1,
    signal.integral.max = 5,
    background.integral.min = 200,
    background.integral.max = 250,
    fit.method = "EXP",
    rejection.criteria = list(
      recycling.ratio = 20,
      recuperation.rate = 20,
      testdose.error = 20,
      palaeodose.error = 20,
      exceed.max.regpoint = TRUE),
    plot=FALSE,
    plot.single = FALSE,
    verbose=FALSE
    #  onlyLxTxTable = TRUE
  )

  # Wash the outputs and convert to Grays

  results_subset = subset(results$data, RC.Status == "OK")
  Risoe_dose_rate_subset = Risoe_dose_rate[which(results$data$RC.Status=="OK"),]

  if (nrow(results_subset)<3){
    print(paste("Not enough aliquots passing criteria for sample ", sample_name,sep=""))
    next
  }

```

```
  write.xlsx(results_subset, paste(sample_name,"Equivalent Dose Spreadsheet.xlsx",sep=" "),sheetName=sample_name
      )
  write.xlsx(results$LnLxTnTx.table, paste(sample_name,"LnLxTnTx Spreadsheet.xlsx",sep=" "),sheetName=sample_
      name)

  file.move(paste(wdir,sample_name," Equivalent Dose Spreadsheet.xlsx",sep=""), paste(wdir,"output_tables\\" ,
      sep=""),overwrite=TRUE)
  file.move(paste(wdir,sample_name," LnLxTnTx Spreadsheet.xlsx",sep=""), paste(wdir,"output_tables\\" ,sep=""),
      overwrite=TRUE)

  plot_input = Second2Gray(data.frame(De=results_subset["De"], De_error= results_subset["De.Error"]),
                           Risoe_dose_rate_subset,
                           error.propagation = "gaussian") # Convert to Gray
  # number of accepted aliquots

  num_accepted[sample_iter] = nrow(subset(results$data, RC.Status == "OK"))
  num_total[sample_iter] = nrow(subset(results$data))
}

if (bin_or_xlsx[sample_iter] == 'xlsx'){

  plot_input = read.xlsx(file_names[sample_iter], colNames = TRUE, rowNames = FALSE, skipEmptyRows = TRUE)


}

if (bin_or_xlsx[sample_iter] == 'NA'){
  plot_input = data.frame(De=rep(NA,10),De.Error=rep(NA,10)) # dummy data
}

# Calculate CAM and MAM Equivalent Doses

central_age = calc_CentralDose(plot_input, log = TRUE, plot = FALSE) #sigmab=0.15,
minimum_age = calc_MinDose(plot_input,
                           sigmab=sigma_b_input[sample_iter],
                           log = MAM_log[sample_iter], par = 3, bootstrap = FALSE,
                           level = 0.95, plot = FALSE, multicore = FALSE) #

CA = as.numeric(central_age["summary"]["de"])
CA_err = as.numeric(central_age["summary"]["de_err"])
MA = as.numeric(minimum_age["summary"]["de"])
MA_err = as.numeric(minimum_age["summary"]["de_err"])

CA_age = CA/dose_rates[sample_iter]
MA_age = MA/dose_rates[sample_iter]

# calculate age uncertainty
CA_age_uncert = (CA/dose_rates[sample_iter])*sqrt((CA_err/CA)^2 + (dose_rates_err[sample_iter]/dose_rates[sample
    _iter])^2)
MA_age_uncert = (MA/dose_rates[sample_iter])*sqrt((MA_err/MA)^2 + (dose_rates_err[sample_iter]/dose_rates[sample
    _iter])^2)

if (OSL_IRSL_type[sample_iter]=="IRSL" || OSL_IRSL_type[sample_iter]=="pIRSL"){

  print(paste("Performing fading Correction for sample: ", sample_name,sep=""))

  CA_fadeCorr <- calc_FadingCorr(age.faded=c(CA_age,CA_age_uncert),
                                 g_value = c(g_vals[sample_iter], g_value_err[sample_iter]),
                                 tc=10,
                                 tc.g_value = g_vals_days[sample_iter]*24*60*60,
                                 txtProgressBar = FALSE,
                                 verbose = FALSE)

  CA_age = as.numeric(CA_fadeCorr$age.corr["AGE"][1])
  CA_age_uncert = as.numeric(CA_fadeCorr$age.corr["AGE.ERROR"][1])

  MA_fadeCorr <- calc_FadingCorr(age.faded=c(MA_age,MA_age_uncert),
                                 g_value = c(g_vals[sample_iter], g_value_err[sample_iter]),
                                 tc=10,
                                 tc.g_value = g_vals_days[sample_iter]*24*60*60,
                                 txtProgressBar = FALSE,
                                 verbose = FALSE)

  MA_age = as.numeric(MA_fadeCorr$age.corr["AGE"][1])
  MA_age_uncert = as.numeric(MA_fadeCorr$age.corr["AGE.ERROR"][1])

}

final_results_table["scatter"][sample_iter,1] = paste(round(central_age$summary["OD"],0), "%",sep="")
final_xlsx_table["scatter"][sample_iter,1] = paste(round(central_age$summary["OD"],0), "%",sep="")
```

```
526
527 ## Input results into summary tables ##
528
529
530 final_results_table["num_aliquots"][sample_iter,1] = paste(toString(num_accepted[sample_iter]),
531                                                            " (",
532                                                            toString(num_total[sample_iter]),
533                                                            ")",
534                                                            sep="")
535
536 final_summary_table["num_aliquots"][sample_iter,1] = paste(toString(num_accepted[sample_iter]),
537                                                            " (",
538                                                            toString(num_total[sample_iter]),
539                                                            ")",
540                                                            sep="")
541 # enter in mam and cam De
542 final_results_table["de_mam"][sample_iter,1] = paste(formatC(signif(MA,3), format = "f", digits= 1,dropOtrailing
        = TRUE, flag="#"),
543                                                      " $\\pm$ ",
544                                                      formatC(signif(MA_err,3), format = "f", digits= 1,
                                                           dropOtrailing = TRUE, flag="#"), sep="")
545
546 final_results_table["de_cam"][sample_iter,1] = paste(formatC(signif(CA,3), format = "f", digits= 1,dropOtrailing
        = TRUE, flag="#"),
547                                                      " $\\pm$ ",
548                                                      formatC(signif(CA_err,3), format = "f", digits= 1,
                                                           dropOtrailing = TRUE, flag="#"), sep="")
549
550 final_summary_table["de_mam"][sample_iter,1] = paste(formatC(signif(MA,3), format = "f", digits= 1,dropOtrailing
        = TRUE, flag="#"),
551                                                      "   ",
552                                                      formatC(signif(MA_err,3), format = "f", digits= 1,
                                                           dropOtrailing = TRUE, flag="#"), sep="")
553 final_summary_table["de_cam"][sample_iter,1] = paste(formatC(signif(CA,3), format = "f", digits= 1,dropOtrailing
        = TRUE, flag="#"),
554                                                      "   ",
555                                                      formatC(signif(CA_err,3), format = "f", digits= 1,
                                                           dropOtrailing = TRUE, flag="#"), sep="")
556
557 # enter in ages and uncertainties
558 final_results_table["age_cam"][sample_iter,1] = paste(sprintf("%.3g",CA_age)," $\\pm$ ",
559                                                       formatC(signif(CA_age_uncert,3), format = "f", digits= 1,
                                                            dropOtrailing = TRUE, flag="#"), sep="")
560 final_results_table["age_mam"][sample_iter,1] = paste(sprintf("%.3g",MA_age)," $\\pm$ ",
561                                                       formatC(signif(MA_age_uncert,3), format = "f", digits= 1,
                                                            dropOtrailing = TRUE, flag="#"), sep="")
562
563 final_summary_table["age_cam"][sample_iter,1] = paste(sprintf("%.3g",CA_age),"   ",
564                                                       formatC(signif(CA_age_uncert,3), format = "f", digits= 1,
                                                            dropOtrailing = TRUE, flag="#"), sep="")
565 final_summary_table["age_mam"][sample_iter,1] = paste(sprintf("%.3g",MA_age),"   ",
566                                                       formatC(signif(MA_age_uncert,3), format = "f", digits= 1,
                                                            dropOtrailing = TRUE, flag="#"), sep="")
567
568 # print(formatC(signif(MA_err,digits=3), digits=2,format="fg", flag="#"))
569
570 # add to final excel table
571
572 final_xlsx_table["num_aliquots_passed"][sample_iter,1] <- num_accepted[sample_iter]
573 final_xlsx_table["num_aliquots_total"][sample_iter,1] <- num_total[sample_iter]
574
575 final_xlsx_table["de_cam"][sample_iter,1] <- CA
576 final_xlsx_table["de_cam_err"][sample_iter,1] <- CA_err
577
578 final_xlsx_table["de_mam"][sample_iter,1] <- MA
579 final_xlsx_table["de_mam_err"][sample_iter,1] <- MA_err
580
581 final_xlsx_table["age_cam"][sample_iter,1] <- CA_age
582 final_xlsx_table["age_cam_err"][sample_iter,1] <- CA_age_uncert
583
584 final_xlsx_table["age_mam"][sample_iter,1] <- MA_age
585 final_xlsx_table["age_mam_err"][sample_iter,1] <- MA_age_uncert
586
587
588 # add to misc table
589
590 final_misc_table_2[c("gamma_MAM", "sigma_MAM", "p0_MAM", "mu_MAM")][sample_iter,] =
591   c(round(as.numeric(unlist(minimum_age$mle@coef["gamma"])),3),
592     round(as.numeric(unlist(minimum_age$mle@coef["sigma"])),3),
593     round(as.numeric(unlist(minimum_age$mle@coef["p0"])),3),
```

```
    round(as.numeric(unlist(minimum_age$mle@coef['nu'])),3))

#############################################################################################

## Determine the sensitivity of the water content assumption

water_array = seq(0,1.2*saturation_water_content_of_samples[sample_iter],1)/100

x_alpha = 1.49
x_beta = 1.25
x_gamma = 1.14

water_dose_rates = (DRAC_results$content["TU:FK"][sample_iter,1]/(1 + x_alpha*water_array) + # external alpha dose
                    DRAC_results$content["TU:FM"][sample_iter,1]/(1 + x_beta*water_array) + # external beta dose
                    DRAC_results$content["TU:FO"][sample_iter,1]/(1 + x_gamma*water_array) + # external gamma dose
                    DRAC_results$content["TU:GG"][sample_iter,1] + # cosmic dose
                    DRAC_results$content["TU:FV"][sample_iter,1] + # internal alpha dose
                    DRAC_results$content["TU:FY"][sample_iter,1]) # internal beta dose

water_CAM_array = (CA_age*dose_rates[sample_iter])/water_dose_rates
water_MAM_array = (MA_age*dose_rates[sample_iter])/water_dose_rates

water_CAM_regress = lm(water_array ~ water_CAM_array, data=data.frame(water_array,water_CAM_array))
water_MAM_regress = lm(water_array ~ water_MAM_array, data=data.frame(water_array,water_MAM_array))

water_data_frame = data.frame(water=100*rep(water_array,2),
                              age=c(water_CAM_array,water_MAM_array),
                              age_uncert_pos = c(water_CAM_array + CA_age_uncert, water_MAM_array + MA_age_uncert),
                              age_uncert_neg = c(water_CAM_array - CA_age_uncert, water_MAM_array - MA_age_uncert),
                              age_type=c(rep("CAM Age",length(water_CAM_array)),
                                         rep("MAM Age",length(water_MAM_array))))

## Plot the water chart
png(file = paste(wdir,"output_plots\\", sample_name,"_water_content_plot.png",sep=""),
    width = 6, height = 4, units = "in", res = 300)

p_water <- ggplot(data=water_data_frame,aes(x=water,y=age,group=age_type)) +
  scale_color_manual(values=c("red","blue"), name = "Age Model") +
  scale_fill_manual(values=c('red','blue'), name='95% Conf. Int.') +
  geom_line(aes(color=age_type),size = 1.25) +
  geom_ribbon(aes(ymax = age_uncert_pos,
                  ymin=age_uncert_neg,
                  x=water,
                  fill=age_type),
              alpha = .1) +
  geom_vline(xintercept = c(field_water_content_of_samples[sample_iter],
                            field_water_content_of_samples[sample_iter]*1.05,
                            field_water_content_of_samples[sample_iter]*0.95,
                            saturation_water_content_of_samples[sample_iter],
                            saturation_water_content_of_samples[sample_iter]*1.05,
                            saturation_water_content_of_samples[sample_iter]*0.95,
                            modeled_water_content_of_samples[sample_iter],
                            modeled_water_content_of_samples[sample_iter]+modeled_water_err[sample_iter],
                            modeled_water_content_of_samples[sample_iter]-modeled_water_err[sample_iter]),
             size=0.5,
             linetype=c("solid","dashed","dashed",
                        "solid","dashed","dashed",
                        "solid","dashed","dashed")) +
  geom_text(aes(x=saturation_water_content_of_samples[sample_iter]*1.05,
                y=0.75*max(age_uncert_pos),
                label = "Saturation Moisture",
                angle=90,
                vjust=1.3)) +
  geom_text(aes(x=field_water_content_of_samples[sample_iter]*1.05,
                y=0.75*max(age_uncert_pos),
                label = "Field Moisture",
                angle=90,
                vjust=1.3)) +
  geom_text(aes(x=modeled_water_content_of_samples[sample_iter]*1.05,
                y=0.75*max(age_uncert_pos),
                label = "Modeled Moisture",
                angle=90,
                vjust=1.3)) +
  theme_bw() +
  labs(title =paste("D) Sensitivity of Age to Percent Water Content for ",sample_name,sep=''),
```

```
       x="Percent Water by Weight", y="Age (ka)")
# print(p_water)
#
# dev.off()

#ggsave(paste(wdir,sample_name,"_water_content_plot.png",sep=""),water_plot,width = 7, height = 5, units = "in")

#############################################################################################################

## Plot the results of the aliquots as PDF
pdf(file = paste(wdir,"\\output_plots\\",sample_name,"_plots.pdf",sep=""),
    paper = "letter", height=10)
par(mfrow = c(2, 1))

plot_KDE(plot_input,
         main=paste(sample_name,": ","De Distribution (Kernel Density Estimate)",sep=""),
         summary = c("n","median","kurtosis","skewness"),
         xlab = "Equivalent dose [Gy]")

abline(v=CA, col='red')
abline(v=CA-CA_err, col="red",lty=2)
abline(v=CA+CA_err, col="red",lty=2)

abline(v=MA, col='blue')
abline(v=MA-MA_err, col="blue",lty=2)
abline(v=MA+MA_err, col="blue",lty=2)


plot_RadialPlot(plot_input,
                main=paste(sample_name,": ","De Distribution (Radial Plot)",sep=""),
                centrality = "mean.weighted",
                log.z = TRUE,
                line = c(CA, MA),
                line.col = c("red","blue"),
                summary =  c("n","mean.weighted","sesbs.weighted","in.2s"),
                summary.pos = "topleft",
                # xlab = c("Data error (%)",
                #          "Data precision"),
                # ylab = "Scatter",
                # zlab = "Equivalent dose [Gy]",
                grid.col = "none"
                )
dev.off()

#############################################################################################################

## Plot the results of the aliquots as PNG
png(file = paste(wdir, sample_name,"_plots.png",sep=""),
    width = 1000, height = 500)
par(mfrow = c(1, 2))

p_KDE <- plot_KDE(plot_input,
         main=paste(sample_name,": ","De Distribution (Kernel Density Estimate)",sep=""),
         summary = c("n","median","kurtosis","skewness"),
         xlab = "Equivalent dose [Gy]")

abline(v=CA, col='red')
abline(v=CA-CA_err, col="red",lty=2)
abline(v=CA+CA_err, col="red",lty=2)

abline(v=MA, col='blue')
abline(v=MA-MA_err, col="blue",lty=2)
abline(v=MA+MA_err, col="blue",lty=2)

print(p_KDE)

p_radial <- plot_RadialPlot(plot_input,
                main=paste(sample_name,": ","De Distribution (Radial Plot)",sep=""),
                centrality = "mean.weighted",
                log.z = TRUE,
                line = c(CA, MA),
                line.col = c("red","blue"),
                summary =  c("n","mean.weighted","sesbs.weighted","in.2s"),
                summary.pos = "topleft",
                # xlab = c("Data error (%)",
                #          "Data precision"),
                # ylab = "Scatter",
                # zlab = "Equivalent dose [Gy]",
                grid.col = "none"
                # xlim = c(0,30)
```

```
}
#max(plot_input[,2]/plot_input[,1]*100),min(plot_input[,2]/plot_input[,1]*100)
print(p_radial)
dev.off()


#############################################################################################

## Build a plot of all the naturals and the growth curves all together

if (bin_or_xlsx[sample_iter] == 'bin'){

  ## Decay Curves

  pos_vector = unique(bin_data@METADATA$POSITION)
  decay_curves_data = Risoe.BINfileData2RLum.Analysis(bin_data)
  decay_curves = data.frame(time=numeric(0),lum=numeric(0),position=character(0))

  for (i_curve in 1:length(decay_curves_data)){

    curves_df_temp = data.frame(time=decay_curves_data [[i_curve]]@records[[1]][,1],
                                lum = decay_curves_data [[i_curve]]@records[[1]][,2],
                                position = rep(paste("Position #", as.character(pos_vector[i_curve]), sep=""),
                                               nrow(decay_curves_data [[i_curve]]@records[[1]][,])))

    decay_curves = rbind(curves_df_temp, decay_curves)

  }

  p_decay <- ggplot(data=decay_curves,aes(x=time,y=lum, group=position)) +
    geom_line(aes(color=position),show.legend = FALSE) +
    scale_color_discrete(name = "Aliquot") +
    theme_bw() +
    labs(title = paste("A) Natural Decay Curves: ",
                       sample_name,
                       # " (",
                       # mineral[sample_iter],
                       # " ",
                       # OSL_IRSL_type[sample_iter],
                       # ")",
                       sep=""),
         x="Measurement time (s)", y="Photons")

  # png(file = paste(wdir,"output_plots\\", sample_name,"_decay_curves_compiled.png",sep=""),
  #     width = 6, height = 4, units = "in", res = 300)
  # print(p_decay)
  # dev.off()

  ## Growth Curves

  growth_curves_index =  as.numeric(rownames(subset(results$data, RC.Status == "OK")))

  if (dim(results$LnLxTnTx.table[c("Dose","LxTx","LxTx.Error","Net_TnTx")])[1] != length(rep(as.character(pos_
      vector),each=6))){
    stop(paste("There is a shape mismatch with the bin file for ",sample_name, ".", "File name = ", file_names[
        sample_iter], sep=""))
  }

  growth_curves_data = cbind(results$LnLxTnTx.table[c('Dose","LxTx","LxTx.Error","Net_TnTx")], position = rep(as
      .character(pos_vector),each=6), run=rep(1:6,length(pos_vector)))
  growth_curves_selected = rep(growth_curves_index*6, each=6) - rep(seq(5, 0, -1), length(growth_curves_index))
  growth_curves_data_plot = growth_curves_data[growth_curves_selected,]

  # Risoe_dose_rate_subset[rep(seq_len(nrow(Risoe_dose_rate_subset)), each=6),]
  #
  # growth_curves_data_plot[,1] = growth_curves_data_plot[,1]*Risoe_dose_rate_subset[rep(seq_len(nrow(Risoe_dose
      _rate_subset)), each=6),]["IRR_DR"]

  growth_curves_fitted = data.frame(x_fit=numeric(0),y_fit=numeric(0),position_fit=character(0))

  iter_gc = 0

  for (m in unique(growth_curves_data_plot$position)){

    iter_gc = iter_gc + 1
    subset_gc = subset(growth_curves_data_plot, position==m)
    x = seq(0,max(subset_gc$Dose),length.out=100)
    y_gc = eval(results$Formula[[growth_curves_index[iter_gc]]])
    position_gc = as.character(rep(m,length(x)))

```

```
    temp = data.frame(x_fit=x, y_fit=y_gc, position_fit=position_gc)

    growth_curves_fitted = rbind(growth_curves_fitted, temp)

      }


p_growth <- ggplot(data=growth_curves_data_plot, aes(x=Dose, y=LxTx, group=position, color=position)) +
                    geom_point(show.legend = FALSE) +
                    geom_errorbar(aes(ymin=LxTx-LxTx.Error,ymax=LxTx+LxTx.Error), width = 0.2,show.legend =
                        FALSE) +
                    geom_line(data=growth_curves_fitted, aes(x=x_fit,y=y_fit, group=position_fit, color=
                        position_fit),show.legend = FALSE) +
                    theme_bw() +
                    labs(title = paste('B) Growth Curves: ",
                                       sample_name,
                                       # " (",
                                       # mineral[sample_iter],
                                       # " ",
                                       # OSL_IRSL_type[sample_iter],
                                       # ")",
                                       sep=""),
                         x="Radiation Dose (seconds)", y="Lx/Tx")

p_test_dose <- ggplot(data = growth_curves_data_plot, aes(x=run,y=Net_TnTx, group=position)) +
                      geom_line() +
                      geom_point(shape=21,fill="blue") +
                      theme_bw() +
                      labs(title = "C) Test Dose",
                           x="Run Number", y="Photons")

# png(file = paste(wdir,"output_plots\\", sample_name,"_growth_curves_compiled.png",sep=""),
#     width = 6, height = 4, units = "in", res = 300)
# print(p_growth)
# dev.off()

# png(file = paste(wdir,"output_plots\\", sample_name,"_growth_decay_compiled.png",sep=""),
#     width = 8, height = 6, units = "in", res = 300)
# grid.arrange(p_decay,p_growth,nrow=2)
# dev.off()

png(file = paste(wdir, sample_name,"_compiled_plots.png",sep=""), #"output_plots\\",
    width = 8, height = 6, units = "in", res = 300)

grid.arrange(p_decay,p_growth,p_test_dose,p_water,layout_matrix = rbind(c(1,1,2,2),
                                                                        c(3,4,4,4)))
dev.off()


# eval(eval(parse(text=results$Formula[1])))

##############################################################################################

## Build the decay curves library

pdf(file = paste(wdir,"/output_plots/",sample_name,"_decay_curves.pdf",sep=""),
    paper = "letter",height = 10)
par(mfrow = c(2,2))

iter = 0

position_array = unlist(unique(bin_data@METADATA["POSITION"]), use.names=FALSE)

for (p_iter in position_array){

  temp <- Risoe.BINfileData2RLum.Analysis(bin_data, pos=p_iter)

  plot_RLum.Analysis(
    temp,
    subset = list(recordType = gsub(pattern = "pIRSL",replacement = "IRSL", toString(OSL_IRSL_type[sample_iter
        ]))),
    combine = TRUE,
    norm = FALSE,
    plot.single = TRUE,
    legend = TRUE,
    legend.text = paste(as.character(as.list((bin_data@METADATA["IRR_TIME"][(iter*12 + (1:12)),1]))),"s B",sep
        =""),
    main = paste(sample_name,"position number =",toString(position_array[p_iter]),sep=" ")
  )

```

```
    iter = iter+1
  }

  dev.off()


  ##################################################################################################

  ## Build the growth curves library

  pdf(file = paste(wdir,"/output_plots/",sample_name,"_growth_curves.pdf",sep=""),
      paper = "letter",height = 10)
  par(mfrow = c(3,2))

  for (k in 0:((nrow(results["LnLxTnTx.table"])/6)-1)){

    index = k*6 + 1:6

    x1 = results["LnLxTnTx.table"]["Dose"][index,1]
    x2 = results["LnLxTnTx.table"]["LxTx"][index,1]
    x3 = results["LnLxTnTx.table"]["LxTx.Error"][index,1]
    x4 = results["LnLxTnTx.table"]["TnTx"][index,1]

    plot_GrowthCurve(data.frame(x=x1,y=x2,z=x3), na.rm = TRUE, mode = 'interpolation',
                     fit.method = 'EXP', fit.force_through_origin = TRUE,
                     fit.weights = FALSE, fit.includingRepeatedRegPoints = TRUE,
                     fit.NumberRegPoints = NULL, fit.NumberRegPointsReal = NULL,
                     fit.bounds = TRUE, NumberIterations.MC = 100,legend=FALSE, output.plot = TRUE,
                     xlab="Dose [Gy]",
                     output.plotExtended = FALSE, output.plotExtended.single = TRUE,
                     cex.global = 1, txtProgressBar = TRUE, verbose = FALSE,
                     main = paste("Sample:",sample_name,", Aliquot",toString(k+1),sep=" "))

    plot((1:6),x4/x4[1],
         type="b",
         main='Test Dose Response',
         xlab='Run Number',
         ylab='Normalized Test Dose',
         ylim= c((1 - 2*max(abs(1 - x4/x4[1]))), (1 + 2*max(abs(1 - x4/x4[1])))))

    abline(h=1,col="black")

  }

  dev.off()

} else {

  png(file = paste(wdir, sample_name,"_compiled_plots.png",sep=""), #"output_plots\\",
      width = 8, height = 6, units = "in", res = 300)

  print(p_water)

  dev.off()

  }

}
##################################################################################################

## Output Xlsx file

write.xlsx(final_xlsx_table, 'results_table.xlsx', sheetName="Sheet1")
write.xlsx(final_summary_table, "summary_table.xlsx", sheetName="Summary Table")

## output Tex table on Dose Rates

if (file.exists('DR_table.tex')) {
  file.remove('DR_table.tex')}

sink('DR_table.tex', append=FALSE)
print(xtable(final_results_table[c("sample_name",
                                   # "latitude",
                                   # "longitude",
                                   "elevation",
                                   "depths",
                                   "water_content",
                                   "k_percent",
                                   "uranium_ppm",
                                   "thorium_ppm",
```

```
                                    "dose_rate")],
              auto=TRUE), include.rownames=FALSE)
sink()

current_file <- readLines("DR_table.tex")
current_file <- gsub(pattern = "\\$$\\backslash$pm\\$", replace = "$ \\pm $", x = current_file,fixed=TRUE)
current_file <- head(current_file,-3)
current_file <- current_file[-(1:8)]

writeLines(current_file,"DR_table.tex")


## output tex table on Equivalent Dose

if (file.exists('De_table.tex')) {
  file.remove('De_table.tex')}

sink('De_table.tex', append=FALSE)
print(xtable(final_results_table[-c(2:11)], auto=TRUE),include.rownames=FALSE)
sink()

current_file <- readLines("De_table.tex")
current_file <- gsub(pattern = "\\$$\\backslash$pm\\$", replace = "$ \\pm $", x = current_file,fixed=TRUE)
current_file <- head(current_file,-3)
current_file <- current_file[-(1:8)]

writeLines(current_file,"De_table.tex")


## output tex table on Misc data 1

if (file.exists('misc_table_1.tex')) {
  file.remove('misc_table_1.tex')}

sink('misc_table_1.tex', append=FALSE)
print(xtable(final_misc_table_1, auto=TRUE),include.rownames=FALSE)
sink()

current_file <- readLines('misc_table_1.tex')
current_file <- head(current_file,-3)
current_file <- current_file[-(1:8)]

writeLines(current_file,'misc_table_1.tex')

## output tex table on Misc data 2

if (file.exists('misc_table_2.tex')) {
  file.remove('misc_table_2.tex')}

sink('misc_table_2.tex', append=FALSE)
print(xtable(final_misc_table_2, auto=TRUE),include.rownames=FALSE)
sink()

current_file <- readLines('misc_table_2.tex')
current_file <- gsub(pattern = "\\$$\\backslash$pm\\$", replace = "$ \\pm $", x = current_file,fixed=TRUE)
current_file <- head(current_file,-3)
current_file <- current_file[-(1:8)]

writeLines(current_file,'misc_table_2.tex')




## Generate text for a tex file to describe the samples


if (file.exists("samples.tex")) {
    file.remove("samples.tex")}

TeXinput = file("samples.tex")
#sink("samples.tex", append = TRUE)

sample_iter = 0

for (sample_name in sample_list){

  sample_iter = sample_iter +1

  line1=as.character(paste("\\subsection{",sample_name," Results}",sep=""))
  line2=as.character(paste("\\begin{figure}[h]", sep=""))
```

```
  line3=as.character(paste("\\centering"))
  line4=as.character(paste("\\addtolength{\\leftskip}{-2cm}"))
  line5=as.character(paste("\\addtolength{\\rightskip}{-2cm}"))
  line6=as.character(paste("\\includegraphics[scale=0.5]{", sample_name,"_plots.png}",sep=""))
  line7=as.character(paste("\\caption{",sample_name," $D_E$ KDE and Radial Plot}{Plots of Equivalent Dose for ",
      sample_name,". Red lines shows CAM equivalent dose, blue lines show MAM equivalent dose, solid line shows
       the age, and dashed lines show uncertainty. \\label{fig:",sample_name,"}}", sep=""))
  line8=as.character(paste("\\end{figure}", sep=""))

  write(c(line1,line2,line3,line4,line5,line6,line7,line8),file="samples.tex",append=TRUE)

  line2=as.character(paste("\\begin{figure}[h]", sep=""))
  line3=as.character(paste("\\centering"))
  line4=as.character(paste("\\addtolength{\\leftskip}{-2cm}"))
  line5=as.character(paste("\\addtolength{\\rightskip}{-2cm}"))
  line6=as.character(paste("\\includegraphics[scale=0.7]{", sample_name,"_compiled_plots.png}",sep=""))
  line7=as.character(paste("\\caption{",sample_name," luminescence characteristics}{Plots of luminescence
      characteristics for ",sample_name,
                           ". A) Compilation of the natural luminescence decay curves for each aliquot. B)
                               Compilation of the growth curves for each aliquot generated by the SAR protocol
                               (Table \\ref{tab:RC}). C) Magnitude of test dose response for each SAR cycle. D)
                                Graph of CAM or MAM age as a function of water content. Note that for pre-2015
                               datasets, Plots A through C are not available and only Plot D will be present.
                               \\label{fig:",sample_name,"_compiled}}", sep=""))
  line8=as.character(paste("\\end{figure}", sep=""))

  write(c(line2,line3,line4,line5,line6,line7,line8),file="samples.tex",append=TRUE)


  input_text = paste("We analyzed ",toString(sample_name), " using ", toString(analysis_type[sample_iter]),," on
      ",
                     toString(grain_size_min[sample_iter]),"-",toString(grain_size_max[sample_iter]),
                     " $\\mu m$ size grains. Out of ",toString(num_total[sample_iter])," aliquots, ",
                     toString(num_accepted[sample_iter]),
                     " produced acceptable luminescence characteristics and passed acceptance criteria as listed
                          in Table \\ref{tab:RC}.",
                     " Aliquots that passed acceptance criteria are plotted as a kernal density estimate and as
                         a radial plot in Figure \\ref{fig:",toString(sample_name),").",
                     " Application of the central age model (CAM, Galbraith et al., 1999) produced an equivalent
                          dose of ",
                     toString(final_results_table["de_cam"][sample_iter,1]), " Grays, ",
                     "which leads to a CAM age of ", toString(final_results_table["age_cam"][sample_iter,1])," "
                         ka.",
                     " In contrast, application of the minimum age model (MAM, Galbraith et al., 1999) produces
                         an equivalent dose of ",
                     toString(final_results_table["de_mam"][sample_iter,1]), " Gray, ",
                     "which leads to a MAM age of ", toString(final_results_table["age_mam"][sample_iter,1]), "
                         ka.",
                     sep="")

  input_text = paste(input_text, "\\newline", notes[sample_iter], sep=" ")

  write(input_text,file="samples.tex",append=TRUE)

}

graphics.off()


# system("pdflatex.exe -synctex=1 -interaction=nonstopmode report.tex")

# end of code




#
#
# as
# print(formatC(unname(unlist(final_xlsx_table["age_mam"])), digits=3,format="fg", flag="#"))
```

APPENDIX C

GRAIN SIZE DATA

Grain Size Data from Malvern Mastersizer 3000 (vol.%)

µm	m1	m2a	m2b	m3	m4	m5	m6	m7	m8	m9	m10a	m10b	m11	m12	m13	mHF	
0.871814	0	0	0	0	0	0	0	0	0	0	0	0	0	0	0	0	0
0.990523	0	0	0	0	0.001525	0	0.000348	0	0	0	0	0	0	0.000547	0	0	0
1.125396	0.001243	0.001381	0.000803	0.001138	0.119939	0.000875	0.028745	0	0	0	0	0.001479	0.000563	0.043506	0	0	0
1.278633	0.093636	0.104868	0.066342	0.088538	0.23885	0.067229	0.132125	0	0.00127	0	0.002104	0.114917	0.045191	0.133338	0.000511	0	0
1.452735	0.152296	0.186668	0.133585	0.196504	0.3821	0.160631	0.23211	0	0.094067	0	0.156086	0.253098	0.174173	0.212831	0.03889	0.00042	
1.650544	0.211498	0.270607	0.19713	0.317251	0.531118	0.241999	0.334689	0.000501	0.161781	0	0.274797	0.402719	0.290776	0.292789	0.124455	0.034081	
1.875288	0.266648	0.348058	0.254984	0.434194	0.67339	0.318573	0.429845	0.03799	0.223054	0	0.384965	0.540162	0.399471	0.365891	0.187673	0.090795	
2.130633	0.318525	0.420423	0.307937	0.549393	0.809283	0.392257	0.51983	0.080339	0.279277	0	0.487969	0.667807	0.501942	0.432446	0.256459	0.121685	
2.420746	0.371459	0.495374	0.362136	0.67567	0.94771	0.47082	0.614457	0.106575	0.341105	6.21E-05	0.600491	0.803846	0.61293	0.497972	0.338408	0.155847	
2.750361	0.427875	0.577972	0.421631	0.821266	1.092222	0.55908	0.720165	0.144694	0.417312	0.00504	0.735108	0.961454	0.742814	0.565325	0.436918	0.195244	
3.12486	0.484296	0.664037	0.48321	0.977758	1.231795	0.652542	0.832358	0.194463	0.505878	0.032897	0.885079	1.131805	0.883618	0.629184	0.545596	0.236511	
3.550351	0.533072	0.742582	0.537944	1.122169	1.345455	0.73936	0.938172	0.246894	0.593597	0.074674	1.02408	1.285977	1.010057	0.678616	0.649437	0.271907	
4.033778	0.567814	0.804604	0.578295	1.233128	1.415963	0.809175	1.026662	0.292405	0.667136	0.094444	1.126396	1.396931	1.098094	0.704985	0.734459	0.294253	
4.58303	0.587325	0.849747	0.603814	1.305348	1.439722	0.86018	1.096499	0.32933	0.724346	0.105351	1.187333	1.459955	1.142881	0.707697	0.796923	0.301926	
5.207069	0.59548	0.885785	0.620754	1.348577	1.426665	0.898565	1.155303	0.362602	0.773362	0.113483	1.221577	1.491052	1.157847	0.693937	0.842772	0.29888	
5.91608	0.596822	0.921251	0.636021	1.373626	1.388741	0.931272	1.211399	0.396264	0.822553	0.12494	1.244285	1.50709	1.158085	0.671791	0.879234	0.290197	
6.721632	0.594758	0.962521	0.654794	1.387089	1.335047	0.963131	1.270583	0.431336	0.877004	0.142809	1.264206	1.518346	1.153973	0.647387	0.911229	0.280087	
7.63687	0.591984	1.014353	0.68111	1.393449	1.27312	0.997587	1.336729	0.467393	0.94034	0.169875	1.286929	1.531387	1.154271	0.625476	0.942989	0.272937	
8.67673	0.590618	1.08027	0.718024	1.395849	1.209018	1.037181	1.412441	0.503057	1.014572	0.206708	1.314294	1.549043	1.165694	0.60938	0.97792	0.272646	
9.85818	0.592004	1.162574	0.7675	1.396443	1.146858	1.083552	1.499081	0.536585	1.099781	0.250085	1.344162	1.570471	1.192092	0.600833	1.018158	0.28179	
11.2005	0.596831	1.262723	0.830707	1.398071	1.089012	1.137928	1.597223	0.567474	1.194978	0.292753	1.37182	1.592561	1.235234	0.59998	1.064965	0.301438	
12.7256	0.60537	1.382191	0.908637	1.406324	1.036823	1.201746	1.707406	0.59869	1.299267	0.324348	1.393084	1.613081	1.295715	0.606146	1.118946	0.33069	
14.45835	0.617488	1.522693	1.002372	1.430948	0.990479	1.276839	1.830276	0.638844	1.412832	0.333316	1.406692	1.632685	1.373239	0.617881	1.180146	0.366443	
16.42705	0.633228	1.686965	1.113938	1.487402	0.950122	1.366085	1.967344	0.704099	1.538511	0.310646	1.418166	1.658334	1.467912	0.633832	1.248667	0.404004	
18.6638	0.653202	1.878693	1.24663	1.596027	0.916257	1.473208	2.120795	0.818213	1.682483	0.254322	1.442041	1.704664	1.580502	0.653217	1.324813	0.4384	
21.20512	0.679083	2.102017	1.405083	1.779723	0.889982	1.602358	2.293022	1.010906	1.854288	0.172103	1.502483	1.793768	1.712344	0.676098	1.409271	0.466462	
24.09248	0.714114	2.360462	1.594907	2.059728	0.872992	1.757352	2.485782	1.313858	2.065807	0.056927	1.631465	1.952733	1.864904	0.703428	1.503226	0.489631	
27.37299	0.7636	2.655416	1.821823	2.440794	0.867389	1.940682	2.699167	1.754231	2.32908	0.000747	1.863928	2.20865	2.039141	0.736871	1.608443	0.517144	
31.10018	0.835266	2.984452	2.090334	2.949817	0.875437	2.152599	2.93077	2.346306	2.652985	0	2.229642	2.581246	2.234912	0.778449	1.727347	0.568659	
35.33487	0.93954	3.340152	2.402411	3.541234	0.899767	2.390755	3.175603	3.083804	3.03987	0.000685	2.744311	3.075628	2.451037	0.830345	1.863194	0.675226	
40.14618	1.089284	3.709481	2.75614	4.185146	0.943638	2.650266	3.426528	3.934502	3.482399	0.102428	3.400758	3.675924	2.68558	0.894705	2.019992	0.877123	
45.61261	1.298707	4.073636	3.144464	4.8252	1.010852	2.92384	3.674648	4.839171	3.961326	0.547697	4.162782	4.341662	2.935741	0.973362	2.201772	1.218071	
51.82336	1.58125	4.408646	3.554272	5.391665	1.105164	3.20189	3.909426	5.716333	4.444968	1.562407	4.963843	5.008431	3.196965	1.067452	2.41113	1.735528	
58.87979	1.946895	4.687519	3.966537	5.814047	1.229907	3.473077	4.119169	6.47337	4.891598	3.256253	5.713246	5.594954	3.461899	1.177486	2.647769	2.44853	
66.89705	2.399485	4.884057	4.357893	6.033393	1.388291	3.725491	4.29212	7.022257	5.25512	5.543797	6.31038	6.016563	3.719772	1.304178	2.907662	3.34617	
76.00596	2.934345	4.977219	4.703259	6.014781	1.583822	3.947912	4.417525	7.296326	5.492889	8.126648	6.664139	6.202032	3.956314	1.449667	3.182777	4.380529	
86.35516	3.536395	4.95478	4.978684	5.754956	1.820224	4.130571	4.486154	7.263443	5.573563	10.54481	6.712103	6.10892	4.154336	1.618686	3.461295	5.467122	
98.11355	4.179305	4.815491	5.164034	5.283131	2.100783	4.265454	4.49025	6.932292	5.483196	12.29321	6.434715	5.733535	4.295362	1.819307	3.728462	6.494791	
111.473	4.826138	4.569559	5.245226	4.654924	2.427291	4.346512	4.423371	6.350036	5.228131	12.97002	5.86038	5.112766	4.362583	2.062894	3.96823	7.343976	
126.6515	5.431505	4.236962	5.215312	3.940983	2.798375	4.36948	4.27996	5.592013	4.833649	12.40164	5.059607	4.316896	4.344015	2.36267	4.165024	7.908311	
143.8968	5.945062	3.84372	5.074443	3.21254	3.207206	4.331447	4.054947	4.746048	4.338719	10.70473	4.129857	3.435211	4.23508	2.730449	4.30513	8.115499	
163.4902	6.316414	3.417535	4.829112	2.528651	3.639278	4.230647	3.744562	3.896102	3.788458	8.255928	3.175612	2.558835	4.039991	3.17182	4.377722	7.941287	
185.7515	6.501523	2.984546	4.4916	1.929098	4.071495	4.067164	3.34945	3.109852	3.226869	5.577438	2.289785	1.765742	3.771901	3.681149	4.376102	7.413044	
211.044	6.46967	2.56669	4.079401	1.432746	4.473018	3.843972	2.878718	2.431787	2.690986	3.181942	1.540092	1.111624	3.451009	4.237813	4.298595	6.602535	
239.7804	6.209155	2.179075	3.613453	1.039951	4.807321	3.566766	2.352554	1.881254	2.206376	1.426356	0.961589	0.622618	3.100329	4.804739	4.148231	5.610092	
272.4297	5.730299	1.827443	3.115262	0.737366	5.035448	3.24249	1.802011	1.454513	1.784321	0.390511	0.556037	0.260917	2.740044	5.329932	3.930924	4.544285	
309.5246	5.066179	1.508368	2.605371	0.504075	5.120974	2.87889	1.2694	1.13062	1.422655	0.047358	0.297657	0.104061	2.383901	5.751718	3.654156	3.504607	
351.6704	4.270156	1.214972	2.103961	0.322358	5.03633	2.485903	0.768181	0.882956	1.112246	0.000592	0.147443	0.027883	2.039604	6.008677	3.327507	2.569053	
399.5549	3.40944	0.9424	1.630617	0.17527	4.768413	2.076249	0.3789	0.687886	0.843382	0	0.050841	0.000538	1.710402	6.050852	2.962641	1.787461	
453.9596	2.554598	0.689195	1.201548	0.083672	4.322027	1.663796	0.186806	0.526784	0.608449	0	0.017563	0	1.395624	5.849266	2.571176	1.178651	
515.7721	1.770464	0.45926	0.82799	0.019013	3.721738	1.262849	0.067151	0.386657	0.403966	0	0.007921	0	1.093444	5.403198	2.163992	0.734115	
586.0012	1.107891	0.26216	0.518496	0.000375	3.012831	0.890262	0.024545	0.261716	0.230245	0	0.000158	0	0.805622	4.744096	1.753228	0.42874	
665.793	0.551953	0.09947	0.279536	0	2.258812	0.560787	0.004604	0.153816	0.075139	0	0	0	0.537536	3.933635	1.354531	0.231791	
756.4484	0.202767	0.018611	0.098505	0	1.534289	0.271486	9.15E-05	0.05609	0.014524	0	0	0	0.304025	3.054178	0.986591	0.113737	
859.4499	0.047442	0.000366	0.002029	0	0.874771	0.09615	0	0.007218	0.000288	0	0	0	0.117727	2.19419	0.667446	0.040636	
976.4752	0.008438	0	0	0	0.277601	0.012863	0	0.000105	0	0	0	0	0.021365	1.431246	0.392571	0.006886	
1109.435	0.000169	0	0	0	0.033197	0.00022	0	0	0	0	0	0	0.000418	0.733477	0.182341	0.000127	
1260.499	0	0	0	0	0.000124	0	0	0	0	0	0	0	0	0.19697	0.0689	0	
1432.133	0	0	0	0	0	0	0	0	0	0	0	0	0	0.011796	0.022719	0	
1627.136	0	0	0	0	0	0	0	0	0	0	0	0	0	0.000212	0.012593	0	
1848.692	0	0	0	0	0	0	0	0	0	0	0	0	0	0	0.009991	0	
2100.416	0	0	0	0	0	0	0	0	0	0	0	0	0	0	0.007581	0	
2386.415	0	0	0	0	0	0	0	0	0	0	0	0	0	0	0.000168	0	
2711.357	0	0	0	1.42E-15	0	0	0	0	0	0	0	0	0	0	1.42E-15	0	
3080.544	3.32E-09	4.72E-10	1.04E-10	1.2E-11	4.42E-09	3.79E-09	4.61E-11	1.04E-09	3.56E-10	9.52E-14	6.18E-12	1.12E-13	6.98E-09	2.93E-07	2.09E-07	3.73E-09	

Grain Size Data from Malvern Mastersizer 3000 (vol.%)

ϕ	m1	m2a	m2b	m3	m4	m5	m6	m7	m8	m9	m10a	m10b	m11	m12	m13	mHF	
10.16369	0	0	0	0	0	0	0	0	0	0	0	0	0	0	0	0	0
9.979522	0	0	0	0	0.001525	0	0.000348	0	0	0	0	0	0	0.000547	0	0	0
9.795352	0.001243	0.001381	0.000803	0.001138	0.119939	0.000875	0.028745	0	0	0	0	0	0.001479	0.000563	0.043506	0	0
9.611182	0.093636	0.104868	0.066342	0.088538	0.23885	0.067229	0.132125	0	0.00127	0	0.002104	0.114917	0.045191	0.133338	0.000511	0	
9.427012	0.152296	0.186668	0.133585	0.196504	0.3821	0.160631	0.23211	0	0.094067	0	0.156086	0.253098	0.174173	0.212831	0.03889	0.00042	
9.242842	0.211498	0.270607	0.19713	0.317251	0.531118	0.241999	0.334689	0.000501	0.161781	0	0.274797	0.402719	0.290776	0.292789	0.124455	0.034081	
9.058672	0.266648	0.348058	0.254984	0.434194	0.67339	0.318573	0.429845	0.03799	0.223054	0	0.384965	0.540162	0.399471	0.365891	0.187673	0.090795	
8.874502	0.318525	0.420423	0.307937	0.549393	0.809283	0.392257	0.51983	0.080339	0.279277	0	0.487969	0.667807	0.501942	0.432446	0.256459	0.121685	
8.690332	0.371459	0.495374	0.362136	0.67567	0.94771	0.47082	0.614457	0.106575	0.341105	6.21E-05	0.600491	0.803846	0.61293	0.497972	0.338408	0.155847	
8.506162	0.427875	0.577972	0.421631	0.821266	1.092222	0.55908	0.720165	0.144694	0.417312	0.00504	0.735108	0.961454	0.742814	0.565325	0.436918	0.195244	
8.321993	0.484296	0.664037	0.48321	0.977758	1.231795	0.652542	0.832358	0.194463	0.505878	0.032897	0.885079	1.131805	0.883618	0.629184	0.545596	0.236511	
8.137823	0.533072	0.742582	0.537944	1.122169	1.345455	0.73936	0.938172	0.246894	0.593597	0.074674	1.02408	1.285977	1.010057	0.678616	0.649437	0.271907	
7.953653	0.567814	0.804604	0.578295	1.233128	1.415963	0.809175	1.026662	0.292405	0.667136	0.094444	1.126396	1.396931	1.098094	0.704985	0.734459	0.294253	
7.769483	0.587325	0.849747	0.603814	1.305348	1.439722	0.86018	1.096499	0.32933	0.724346	0.105351	1.187333	1.459955	1.142881	0.707697	0.796923	0.301926	
7.585313	0.59548	0.885785	0.620754	1.348577	1.426665	0.898565	1.155303	0.362602	0.773362	0.113483	1.221577	1.491052	1.157847	0.693937	0.842772	0.29888	
7.401143	0.596822	0.921251	0.636021	1.373626	1.388741	0.931272	1.211399	0.396264	0.822553	0.12494	1.244285	1.50709	1.158085	0.671791	0.879234	0.290197	
7.216973	0.594758	0.962521	0.654794	1.387089	1.335047	0.963131	1.270583	0.431336	0.877004	0.142809	1.264206	1.518346	1.153973	0.647387	0.911229	0.280087	
7.032803	0.591984	1.014353	0.68111	1.393449	1.27312	0.997587	1.336729	0.467393	0.94034	0.169875	1.286929	1.531387	1.154271	0.625476	0.942989	0.272937	
6.848633	0.590618	1.08027	0.718024	1.395849	1.209018	1.037181	1.412441	0.503057	1.014572	0.206708	1.314294	1.549043	1.165694	0.60938	0.97792	0.272646	
6.664463	0.592004	1.162574	0.7675	1.396443	1.146858	1.083552	1.499081	0.536585	1.099781	0.250085	1.344162	1.570471	1.192092	0.600833	1.018158	0.28179	
6.480293	0.596831	1.262723	0.830707	1.398071	1.089012	1.137928	1.597223	0.567474	1.194878	0.292753	1.37182	1.592561	1.235234	0.59998	1.064965	0.301438	
6.296123	0.60537	1.382191	0.908637	1.406324	1.036823	1.201746	1.707406	0.59869	1.299267	0.324348	1.393084	1.613081	1.295715	0.606146	1.118946	0.33069	
6.111953	0.617488	1.522691	1.002372	1.430948	0.990479	1.276819	1.830276	0.638844	1.412832	0.333336	1.406692	1.632685	1.373239	0.617881	1.180146	0.366443	
5.927783	0.633228	1.686965	1.113938	1.487402	0.950122	1.366085	1.967344	0.704099	1.538511	0.310646	1.418166	1.658334	1.467912	0.633832	1.248667	0.404004	
5.743613	0.653202	1.878693	1.24663	1.596027	0.916257	1.473208	2.120795	0.818213	1.682483	0.254322	1.442041	1.704664	1.580502	0.653217	1.324813	0.4384	
5.559443	0.679083	2.102017	1.405083	1.779723	0.889982	1.602358	2.293022	1.010506	1.854288	0.172103	1.502483	1.793768	1.712344	0.676098	1.409271	0.466462	
5.375273	0.714114	2.360462	1.594907	2.059728	0.872992	1.757352	2.485782	1.313858	2.065807	0.056927	1.631465	1.952733	1.864904	0.703428	1.503226	0.489631	
5.191103	0.7636	2.655416	1.821823	2.449794	0.867389	1.940682	2.699167	1.754231	2.32908	0.000747	1.863928	2.20865	2.039141	0.736871	1.608443	0.517144	
5.006933	0.835266	2.984452	2.090334	2.949817	0.875437	2.152599	2.93077	2.346306	2.652985	0	2.229642	2.581246	2.214912	0.778449	1.727347	0.568659	
4.822763	0.93954	3.340152	2.402411	3.541234	0.899767	2.390755	3.175603	3.083804	3.03987	0.000685	2.744311	3.075628	2.451037	0.830345	1.863194	0.675226	
4.638593	1.089284	3.709481	2.75614	4.185346	0.943638	2.650266	3.426528	3.934502	3.482399	0.102428	3.400758	3.675924	2.68558	0.894705	2.019992	0.877123	
4.454424	1.298707	4.073636	3.144464	4.8252	1.010852	2.92384	3.674648	4.839171	3.961326	0.547697	4.162782	4.341662	2.935741	0.973362	2.201772	1.218071	
4.270254	1.58125	4.408646	3.554272	5.391665	1.105164	3.20189	3.909426	5.716333	4.444968	1.562407	4.963843	5.008431	3.196965	1.067452	2.41113	1.735528	
4.086084	1.946895	4.687519	3.966537	5.814047	1.229907	3.473077	4.119169	6.47337	4.891598	3.256253	5.713246	5.594954	3.461899	1.177486	2.647769	2.44853	
3.901914	2.399485	4.884057	4.357893	6.033393	1.388291	3.725491	4.29212	7.022257	5.25512	5.543797	6.31038	6.016563	3.719772	1.304178	2.907662	3.34617	
3.717744	2.934345	4.977219	4.703259	6.014781	1.583822	3.947912	4.417525	7.296326	5.492889	8.126648	6.664139	6.202032	3.956314	1.449667	3.182777	4.380529	
3.533574	3.536195	4.95478	4.978684	5.754956	1.820224	4.130571	4.486154	7.263443	5.573563	10.54481	6.712103	6.10892	4.154336	1.618686	3.461295	5.467122	
3.349404	4.179305	4.815491	5.164034	5.283131	2.100783	4.265454	4.49025	6.932292	5.483196	12.29321	6.434715	5.733535	4.295362	1.819307	3.728462	6.494791	
3.165234	4.826138	4.569559	5.245226	4.654924	2.427291	4.346512	4.423371	6.350036	5.228131	12.97002	5.86038	5.112766	4.362583	2.062894	3.96823	7.343976	
2.981064	5.431505	4.236962	5.215312	3.940983	2.798375	4.36948	4.27996	5.592013	4.833649	12.40164	5.059607	4.316896	4.344015	2.36267	4.165024	7.908311	
2.796894	5.945062	3.84372	5.074443	3.21254	3.207206	4.331447	4.054947	4.746048	4.338719	10.70473	4.129857	3.435211	4.23508	2.730449	4.30513	8.115499	
2.612724	6.316414	3.417535	4.829112	2.528651	3.639278	4.230647	3.744562	3.896102	3.788458	8.255928	3.175612	2.558835	4.039991	3.17182	4.377722	7.941287	
2.428554	6.501523	2.984546	4.4916	1.929098	4.071495	4.067164	3.34945	3.109852	3.226869	5.577438	2.289785	1.765742	3.771901	3.681149	4.376102	7.413044	
2.244384	6.46967	2.56669	4.079401	1.432746	4.473018	3.843972	2.878718	2.431787	2.690986	3.181942	1.540092	1.111624	3.451009	4.237813	4.298595	6.602535	
2.060214	6.209155	2.179075	3.613453	1.039951	4.807321	3.566766	2.352554	1.881254	2.206376	1.426356	0.961589	0.622618	3.100329	4.804739	4.148231	5.610092	
1.876044	5.730299	1.827443	3.115262	0.737366	5.035448	3.24249	1.802011	1.454513	1.784321	0.390511	0.556037	0.260917	2.740044	5.329932	3.930924	4.544285	
1.691874	5.066179	1.508368	2.605371	0.504075	5.120974	2.87889	1.2694	1.13062	1.422655	0.047358	0.297657	0.104061	2.383901	5.751718	3.654156	3.504607	
1.507704	4.270156	1.214872	2.103961	0.322358	5.03633	2.485903	0.768181	0.882956	1.112246	0.000592	0.147443	0.027883	2.039604	6.008677	3.327507	2.569053	
1.323534	3.40944	0.9424	1.630617	0.17527	4.768413	2.076249	0.3789	0.687886	0.843382	0	0.050841	0.000538	1.710402	6.050852	2.962641	1.787461	
1.139364	2.554598	0.689195	1.201548	0.083672	4.322027	1.663796	0.186806	0.526784	0.608449	0	0.017563	0	1.395624	5.849266	2.571176	1.178651	
0.955194	1.770464	0.45926	0.82799	0.019013	3.721738	1.262849	0.067151	0.386657	0.403966	0	0.007921	0	1.093444	5.403198	2.163992	0.734115	
0.771024	1.107891	0.26216	0.518496	0.000875	3.012831	0.890262	0.024545	0.261716	0.230245	0	0.000158	0	0.805622	4.744096	1.753228	0.42874	
0.586854	0.551953	0.09947	0.279536	0	2.258812	0.560787	0.004604	0.153816	0.075139	0	0	0	0.537536	3.933635	1.354531	0.231791	
0.402685	0.202767	0.018611	0.098505	0	1.534289	0.271486	9.15E-05	0.05609	0.014524	0	0	0	0.304025	3.054178	0.986591	0.113737	
0.218515	0.047442	0.000366	0.002029	0	0.874771	0.09615	0	0.007218	0.000288	0	0	0	0.117727	2.19419	0.667446	0.040636	
0.034345	0.008438	0	0	0	0.277601	0.012863	0	0.000105	0	0	0	0	0.021365	1.431246	0.392571	0.006886	
-0.14983	0.000169	0	0	0	0.033197	0.00022	0	0	0	0	0	0	0.000418	0.733477	0.182341	0.000127	
-0.334	0	0	0	0	0.000124	0	0	0	0	0	0	0	0	0.19697	0.0689	0	
-0.51817	0	0	0	0	0	0	0	0	0	0	0	0	0	0.011796	0.022719	0	
-0.70234	0	0	0	0	0	0	0	0	0	0	0	0	0	0.000212	0.012593	0	
-0.88651	0	0	0	0	0	0	0	0	0	0	0	0	0	0	0.009991	0	
-1.07068	0	0	0	0	0	0	0	0	0	0	0	0	0	0	0.007581	0	
-1.25485	0	0	0	0	0	0	0	0	0	0	0	0	0	0	0.000168	0	
-1.43902	0	0	0	1.42E-15	0	0	0	0	0	0	0	0	0	0	1.42E-15	0	
-1.62318	3.32E-09	4.72E-10	1.04E-10	1.2E-11	4.42E-09	3.79E-09	4.61E-11	1.04E-09	3.56E-10	9.52E-14	6.18E-12	1.12E-13	6.98E-09	2.93E-07	2.09E-07	3.73E-09	

Grain Size Data from Malvern Mastersizer 3000 (cumulative vol.%)

ϕ	m1	m2a	m2b	m3	m4	m5	m6	m7	m8	m9	m10a	m10b	m11	m12	m13	mtf
10.16369	100	100	100	100	100	100	100	100	100	100	100	100	100	100	100	100
9.979522	100	100	100	100	100	100	100	100	100	100	100	100	100	100	100	100
9.795352	100	100	100	100	100	99.99847	100	99.99965	100	100	100	100	100	99.99945	100	100
9.611182	99.99876	99.99862	99.9992	99.99886	99.87854	99.99912	99.97091	100	100	100	100	99.99852	99.99944	99.95595	100	100
9.427012	99.90512	99.89375	99.93286	99.91032	99.63969	99.9319	99.83878	100	99.99873	100	99.9979	99.8836	99.95425	99.82261	99.99949	100
9.242842	99.75282	99.70708	99.79927	99.71382	99.25759	99.77126	99.60667	100	99.90466	100	99.84181	99.63051	99.78007	99.60978	99.9606	99.99958
9.058672	99.54133	99.43648	99.60214	99.39657	98.72647	99.52927	99.27198	99.9995	99.74288	100	99.56701	99.22779	99.4893	99.31699	99.83614	99.9655
8.874502	99.27468	99.08842	99.34716	98.96238	98.05308	99.21069	98.84214	99.96151	99.51983	100	99.18205	98.68763	99.08983	98.9511	99.64847	99.8747
8.690332	98.95615	98.668	99.03922	98.41298	97.24379	98.81844	98.32231	99.88117	99.24055	100	98.69408	98.01982	98.58788	98.51865	99.39201	99.75302
8.506162	98.58469	98.17262	98.67708	97.73731	96.29609	98.34761	97.70785	99.77459	98.89944	99.99994	98.09359	97.21597	97.97495	98.02068	99.0536	99.59717
8.321993	98.15682	97.59465	98.25545	96.91605	95.20386	97.78854	96.98768	99.6299	98.48213	99.9949	97.35848	96.25452	97.23214	97.45536	98.61669	99.40193
8.137823	97.67252	96.93061	97.77224	95.93829	93.97207	97.13599	96.15533	99.43544	97.97625	99.962	96.4734	95.12271	96.34852	96.82617	98.07109	99.16542
7.953653	97.13945	96.18803	97.2343	94.81612	92.62661	96.39663	95.21715	99.18854	97.38266	99.88733	95.44932	93.83674	95.33847	96.14755	97.42165	98.89351
7.769483	96.57164	95.38343	96.656	93.58299	91.21065	95.58746	94.19049	98.89614	96.71552	99.79288	94.32293	92.43981	94.24037	95.44257	96.68719	98.59926
7.585313	95.98431	94.53368	96.05219	92.27764	89.77093	94.72728	93.09399	98.56681	95.99118	99.68753	93.13559	90.97985	93.09749	94.73487	95.85027	98.29733
7.401143	95.38883	93.64789	95.43144	90.92906	88.34426	93.82871	91.93869	98.20421	95.21781	99.57405	91.91402	89.4888	91.93964	94.04094	95.0475	97.99845
7.216973	94.79201	92.72664	94.79541	89.55544	86.95552	92.89744	90.72729	97.80794	94.39526	99.44911	90.66973	87.98171	90.78156	93.36914	94.16827	97.70825
7.032803	94.19725	91.76412	94.14062	88.16835	85.62048	91.93431	89.45671	97.37661	93.51826	99.3063	89.40552	86.46336	89.62759	92.72176	93.25704	97.42817
6.848633	93.60527	90.74977	93.45951	86.7749	84.34736	90.93672	88.11998	96.90921	92.57792	99.13642	88.1186	84.93198	88.47331	92.09628	92.31405	97.15523
6.664463	93.01465	89.6695	92.74149	85.37905	83.13834	89.89954	86.70754	96.40616	91.56334	98.92972	86.8043	83.38293	87.30762	91.4869	91.33613	96.88258
6.480293	92.42265	88.50693	91.97399	83.98261	81.99148	88.81599	85.20846	95.86957	90.46356	98.67963	85.46014	81.81246	86.11553	90.88607	90.31797	96.60079
6.296123	91.82582	87.2442	91.14328	82.58454	80.90247	87.67806	83.61124	95.3021	89.26859	98.38688	84.08832	80.2199	84.8803	90.28609	89.253	96.29936
6.111953	91.22045	85.86201	90.23464	81.17821	79.86565	86.47631	81.90383	94.70341	87.96932	98.06253	82.69524	78.60682	83.58458	89.67994	88.13406	95.96867
5.927783	90.60296	84.33932	89.23227	79.74727	78.87517	85.19948	80.07355	94.06456	86.55649	97.7292	81.28854	76.97414	82.21134	89.06206	86.95391	95.60222
5.743613	89.96973	82.65235	88.11833	78.25986	77.92505	83.83339	78.10621	93.36046	85.01798	97.41855	79.87038	75.3158	80.74343	88.42823	85.70524	95.19822
5.559443	89.31653	80.77366	86.8717	76.66384	77.00879	82.36018	75.98541	92.54225	83.33549	97.16423	78.42834	73.61114	79.16293	87.77501	84.38043	94.75982
5.375273	88.63745	78.67164	85.46662	74.88411	76.11881	80.75782	73.69239	91.53135	81.4812	96.99212	76.92585	71.81737	77.45058	87.09891	82.97116	94.29336
5.191103	87.92333	76.31118	83.87171	72.82439	75.24581	79.00047	71.20661	90.21749	79.4154	96.9352	75.29439	69.86464	75.58568	86.39549	81.46793	93.80372
5.006933	87.15973	73.65577	82.04989	70.37459	74.37842	77.05979	68.50744	88.46326	77.08632	96.93445	73.43046	67.65599	73.54654	85.63862	79.85949	93.28658
4.822763	86.32447	70.67131	79.95956	67.42478	73.50299	74.90719	65.57667	86.11695	74.43333	96.93445	71.20082	65.07474	71.31163	84.88017	78.13214	92.71792
4.638593	85.38491	67.33116	77.55714	63.88354	72.60322	72.51643	62.40107	83.03315	71.39346	96.93376	68.45651	61.99911	68.86059	84.04982	76.26895	92.0427
4.454424	84.29564	63.62168	74.801	59.6982	71.65958	69.86617	58.97454	79.09865	67.91106	96.83134	65.05575	58.32319	66.17501	83.15512	74.24896	91.16557
4.270254	82.99694	59.54805	71.65654	54.873	70.64873	66.94233	55.29989	74.25947	63.94974	96.28364	60.89297	53.98153	63.23927	82.18175	72.04719	89.9475
4.086084	81.41569	55.1394	68.10227	49.48133	69.54357	63.74044	51.39047	68.54314	59.50477	94.72123	55.92912	48.9731	60.0423	81.1143	69.63606	88.21197
3.901914	79.46879	50.45188	64.13573	43.66728	68.31366	60.26736	47.2713	62.06977	54.61317	91.46498	50.21588	43.37814	56.5804	79.93682	66.98829	85.76344
3.717744	77.06931	45.56782	59.77784	37.63389	66.92537	56.54187	42.97918	55.04751	49.35805	85.92118	43.9055	37.36158	52.86063	78.63264	64.08063	82.41727
3.533574	74.13496	40.5906	55.07458	31.61911	65.34155	52.59396	38.56165	47.75119	43.86516	77.79453	37.24136	31.15955	48.90432	77.18297	60.89785	78.03674
3.349404	70.59857	35.63582	50.09589	25.86415	63.52132	48.46339	34.0755	40.48774	38.2916	67.24973	30.52926	25.05063	44.74998	75.56429	57.43655	72.56962
3.165234	66.41926	30.82033	44.93186	20.58102	61.42054	44.19793	29.58525	33.55545	32.8084	54.95652	24.09454	19.31709	40.45462	73.74498	53.70809	66.07483
2.981064	61.59312	26.25077	39.68664	15.9261	58.99325	39.85142	25.16188	27.20542	27.58027	41.9865	18.23416	14.20433	36.09204	71.68208	49.73986	58.73086
2.796894	56.16162	22.01381	34.47132	11.98512	56.19487	35.48194	20.88192	21.6134	22.74662	29.58485	13.17455	9.887429	31.74802	69.31941	45.57484	50.82254
2.612724	50.21656	18.17009	29.39688	8.772575	52.98767	31.15049	16.82697	16.86736	18.4079	18.88012	9.044697	6.452218	27.51294	66.58896	41.26971	42.70705
2.428554	43.90014	14.75256	24.56777	6.243924	49.34839	26.91985	13.08241	12.97125	14.61945	10.6242	5.869085	3.893383	23.47295	63.41714	36.89198	34.76576
2.244384	37.39862	11.76801	20.07617	4.314826	45.27689	22.85268	9.732961	9.861402	11.39258	5.046758	3.5793	2.127641	19.70105	59.736	32.51588	27.35271
2.060214	30.92895	9.201321	15.99677	2.88208	40.80388	19.03871	6.854244	7.429615	8.701591	1.864816	2.019208	1.016017	16.25004	55.49818	28.21729	20.75018
1.876044	24.7198	7.022246	12.38331	1.842129	35.99656	15.44195	4.50169	5.548361	6.495215	0.438461	1.07762	0.393399	13.14971	50.69344	24.06906	15.14009
1.691874	18.9895	5.194803	9.268053	1.104763	30.96111	12.19946	2.699679	4.093848	4.710894	0.04795	0.521583	0.132482	10.40967	45.36351	20.13813	10.5958
1.507704	13.92332	3.686434	6.662682	0.600688	25.84013	9.320566	1.430279	2.963228	3.288239	0.000592	0.223926	0.028421	8.025768	39.61179	16.48398	7.091196
1.323534	9.653162	2.471462	4.558721	0.27833	20.8038	6.834662	0.662098	2.080272	2.175993		0.076484	0.000538	5.986164	33.60312	13.15647	4.522143
1.139364	6.243723	1.529062	2.928105	0.10306	16.03539	4.758413	0.283199	1.392386	1.332611		0.025643		4.275762	27.55226	10.19383	2.734682
0.955194	3.689125	0.839867	1.726556	0.019388	11.71336	3.094616	0.096392	0.865602	0.724162		0.00808		2.880138	21.703	7.622652	1.556032
0.771024	1.918661	0.380607	0.898566	0.000375	7.991625	1.831767	0.029241	0.478945	0.320196		0.000158		1.786694	16.2998	5.45866	0.821916
0.586854	0.81077	0.118447	0.38007		4.978793	0.941505	0.004696	0.21723	0.089951				0.981071	11.5557	3.705432	0.393177
0.402685	0.258817	0.018977	0.100534		2.719982	0.380718		0.063413	0.014812				0.443535	7.622069	2.350901	0.161386
0.218515	0.056049	0.000366	0.002029		1.185692	0.109232		0.007323	0.000288				0.13951	4.567891	1.36431	0.047649
0.034345	0.008607				0.310922	0.013082		0.000105					0.021783	2.373701	0.696864	0.007013
-0.14983	0.000169				0.033321	0.00022							0.000418	0.942456	0.304293	0.000127
-0.334					0.000124									0.208979	0.121952	
-0.51817														0.012009	0.053053	
-0.70234														0.000212	0.030333	
-0.88651															0.01774	
-1.07068															0.007749	
-1.25485															0.000168	
-1.43902																
-1.62318																

SAMPLE STATISTICS

	SAMPLE NAME:	m1	m2a	m2b	m3	m4	m5	m6	m7
	FACIES	Gmsc1	Gmsc2	Gmsc2	Sh	Gmscn1	Gms3	Gms2	Sh
	SAMPLE TYPE:	Unimodal, Moderately Sorted	Unimodal, Moderately Sorted	Unimodal, Moderately Sorted	Unimodal, Moderately Sorted	Bimodal, Poorly Sorted	Unimodal, Moderately Sorted	Unimodal, Moderately Sorted	Unimodal, Moderately Well Sorted
	TEXTURAL GROUP:	Muddy Sand	Muddy Sand	Muddy Sand	Sandy Mud	Muddy Sand	Muddy Sand	Sandy Mud	Muddy Sand
	SEDIMENT NAME:	Very Coarse Silty Fine Sand	Very Coarse Silty Very Fine Sand	Very Coarse Silty Very Fine Sand	Very Fine Sandy Very Coarse Silt	Fine Silty Medium Sand	Very Coarse Silty Fine Sand	Very Fine Sandy Very Coarse Silt	Very Coarse Silty Very Fine Sand
FOLK AND WARD METHOD (μm)	MEAN (M_z)	137.0	58.70	86.13	43.48	90.56	77.14	50.33	81.36
	SORTING (σ_I)	1.882	1.803	1.726	1.834	2.685	1.949	1.899	1.439
	SKEWNESS (Sk_I)	-0.389	-0.222	-0.256	-0.364	-0.523	-0.260	-0.263	-0.115
	KURTOSIS (K_G)	1.499	1.135	1.198	1.124	0.862	1.067	0.981	1.296
FOLK AND WARD METHOD (ϕ)	MEAN (M_z)	2.867	4.090	3.537	4.523	3.465	3.696	4.312	3.619
	SORTING (σ_I)	0.750	0.850	0.788	0.875	1.425	0.963	0.925	0.525
	SKEWNESS (Sk_I)	0.389	0.222	0.256	0.364	0.523	0.260	0.263	0.115
	KURTOSIS (K_G)	1.499	1.135	1.198	1.124	0.862	1.067	0.981	1.296
FOLK AND WARD METHOD (Description)	MEAN:	Fine Sand	Very Coarse Silt	Very Fine Sand	Very Coarse Silt	Very Fine Sand	Very Fine Sand	Very Coarse Silt	Very Fine Sand
	SORTING:	Moderately Sorted	Moderately Sorted	Moderately Sorted	Moderately Sorted	Poorly Sorted	Moderately Sorted	Moderately Sorted	Moderately Well Sorted
	SKEWNESS:	Very Fine Skewed	Fine Skewed	Fine Skewed	Very Fine Skewed	Very Fine Skewed	Fine Skewed	Fine Skewed	Fine Skewed
	KURTOSIS:	Leptokurtic	Leptokurtic	Leptokurtic	Leptokurtic	Platykurtic	Mesokurtic	Mesokurtic	Leptokurtic
	MODE 1 (μm):	198.4	81.18	119.1	71.45	330.8	135.3	104.8	81.18
	MODE 2 (μm):					4.895			
	MODE 3 (μm):								
	MODE 1 (ϕ):	2.336	3.626	3.073	3.810	1.600	2.889	3.257	3.626
	MODE 2 (ϕ):					7.677			
	MODE 3 (ϕ):								
	D_{10} (μm):	18.55	9.481	14.90	6.450	5.102	9.737	7.231	27.81
	D_{50} (μm):	184.2	67.69	98.35	58.18	181.6	93.56	61.47	83.02
	D_{90} (μm):	395.4	230.4	300.4	155.7	547.0	341.2	208.9	209.8
	(D_{90} / D_{10}) (μm):	21.32	24.31	20.16	24.14	107.2	35.04	28.89	7.546
	(D_{90} - D_{10}) (μm):	376.9	221.0	285.5	149.3	541.9	331.5	201.7	182.0
	(D_{75} / D_{25}) (μm):	3.257	4.511	4.093	4.193	12.66	5.614	5.681	2.621
	(D_{75} - D_{25}) (μm):	187.7	102.4	138.4	76.29	330.9	162.1	104.9	82.37
	D_{10} (ϕ):	1.338	2.118	1.735	2.883	0.870	1.551	2.259	2.253
	D_{50} (ϕ):	2.606	3.885	3.346	4.104	2.462	3.418	4.024	3.590
	D_{90} (ϕ):	5.752	6.721	6.069	7.277	7.615	6.682	7.112	5.168
	(D_{90} / D_{10}) (ϕ):	4.298	3.174	3.498	2.712	8.748	4.308	3.148	2.294
	(D_{90} - D_{10}) (ϕ):	4.414	4.603	4.334	4.593	6.744	5.131	4.852	2.916
	(D_{75} / D_{25}) (ϕ):	1.904	1.743	1.827	1.623	3.479	2.063	1.843	1.478
	(D_{75} - D_{25}) (ϕ):	1.704	2.173	2.023	2.068	3.662	2.489	2.508	1.390
	% GRAVEL:	0.0%	0.0%	0.0%	0.0%	0.0%	0.0%	0.0%	0.0%
	% SAND:	80.5%	52.9%	66.2%	46.8%	69.0%	62.1%	49.5%	65.5%
	% MUD:	19.5%	47.1%	33.8%	53.2%	31.0%	37.9%	50.5%	34.5%
	% V COARSE GRAVEL:	0.0%	0.0%	0.0%	0.0%	0.0%	0.0%	0.0%	0.0%
	% COARSE GRAVEL:	0.0%	0.0%	0.0%	0.0%	0.0%	0.0%	0.0%	0.0%
	% MEDIUM GRAVEL:	0.0%	0.0%	0.0%	0.0%	0.0%	0.0%	0.0%	0.0%
	% FINE GRAVEL:	0.0%	0.0%	0.0%	0.0%	0.0%	0.0%	0.0%	0.0%
	% V FINE GRAVEL:	0.0%	0.0%	0.0%	0.0%	0.0%	0.0%	0.0%	0.0%
	% V COARSE SAND:	0.0%	0.0%	0.0%	0.0%	0.3%	0.0%	0.0%	0.0%
	% COARSE SAND:	4.3%	1.0%	2.0%	0.0%	12.5%	3.5%	0.1%	1.0%
	% MEDIUM SAND:	24.6%	7.5%	12.8%	2.5%	26.5%	14.3%	5.8%	5.8%
	% FINE SAND:	33.2%	18.2%	25.4%	13.9%	20.0%	22.5%	19.5%	21.0%
	% V FINE SAND:	18.4%	26.2%	26.0%	30.4%	9.7%	21.8%	23.8%	37.7%
	% V COARSE SILT:	6.6%	20.6%	15.7%	23.5%	5.4%	14.9%	18.9%	22.9%
	% COARSE SILT:	3.7%	11.4%	7.7%	10.0%	4.9%	8.7%	12.4%	5.9%
	% MEDIUM SILT:	3.2%	6.6%	4.4%	7.6%	6.1%	6.1%	8.4%	3.0%
	% FINE SILT:	3.2%	4.8%	3.4%	7.2%	7.6%	4.8%	6.2%	2.0%
	% V FINE SILT:	2.2%	3.0%	2.2%	4.2%	5.5%	2.8%	3.7%	0.7%
	% CLAY:	0.5%	0.7%	0.5%	0.7%	1.5%	0.6%	0.9%	0.0%

SAMPLE STATISTICS

	SAMPLE NAME:	m8	m9	m10a	m10b	m11	m12	m13	mHF
	FACIES:	Gmsc3	Sm	Sh	Sh	Gms2	Gmsc1	Gmsc1	Sm
	SAMPLE TYPE:	Unimodal, Moderately Sorted	Unimodal, Very Well Sorted	Unimodal, Moderately Sorted	Unimodal, Moderately Sorted	Bimodal, Moderately Sorted	Unimodal, Moderatley Sorted	Unimodal, Poorly Sorted	Unimodal, Well Sorted
	TEXTURAL GROUP:	Muddy Sand	Sand	Muddy Sand	Sandy Mud	Muddy Sand	Muddy Sand	Muddy Sand	Muddy Sand
	SEDIMENT NAME:	Very Coarse Silty Very Fine Sand	Very Fine Sand	Very Coarse Silty Very Fine Sand	Very Fine Sandy Very Coarse Silt	Very Coarse Silty Very Fine Sand	Very Coarse Silty Medium Sand	Very Coarse Silty Fine Sand	Very Coarse Silty Fine Sand
FOLK AND WARD METHOD (μm)	MEAN (M_z):	64.43	116.2	48.70	40.22	65.44	187.7	99.58	140.7
	SORTING (σ_I):	1.711	1.231	1.803	1.899	1.949	1.932	2.000	1.390
	SKEWNESS (Sk_I):	-0.245	-0.060	-0.427	-0.420	-0.273	-0.501	-0.284	-0.210
	KURTOSIS (K_G):	1.166	1.003	1.148	0.974	1.037	1.360	1.049	1.408
FOLK AND WARD METHOD (ϕ)	MEAN (M_z):	3.956	3.106	4.360	4.636	3.934	2.413	3.328	2.829
	SORTING (σ_I):	0.775	0.300	0.850	0.925	0.963	0.950	1.000	0.475
	SKEWNESS (Sk_I):	0.245	0.060	0.427	0.420	0.273	0.501	0.284	0.210
	KURTOSIS (K_G):	1.166	1.003	1.148	0.974	1.037	1.360	1.049	1.408
FOLK AND WARD METHOD (Description)	MEAN:	Very Fine Sand	Very Fine Sand	Very Coarse Silt	Very Coarse Silt	Very Fine Sand	Fine Sand	Very Fine Sand	Fine Sand
	SORTING:	Moderately Sorted	Very Well Sorted	Moderately Sorted	Moderately Sorted	Moderately Sorted	Moderatley Sorted	Poorly Sorted	Well Sorted
	SKEWNESS:	Fine Skewed	Symmetrical	Very Fine Skewed	Very Fine Skewed	Fine Skewed	Very Fine Skewed	Fine Skewed	Fine Skewed
	KURTOSIS:	Leptokurtic	Mesokurtic	Leptokurtic	Mesokurtic	Mesokurtic	Leptokurtic	Mesokurtic	Leptokurtic
	MODE 1 (μm):	92.23	119.1	92.23	81.18	119.1	426.8	174.6	153.7
	MODE 2 (μm):					6.319			
	MODE 3 (μm):								
	MODE 1 (ϕ):	3.441	3.073	3.441	3.626	3.073	1.231	2.521	2.705
	MODE 2 (ϕ):					7.309			
	MODE 3 (ϕ):								
	D_{10} (μm):	11.77	69.19	7.192	5.663	7.329	13.52	11.64	51.54
	D_{50} (μm):	74.83	117.0	67.19	57.36	83.36	277.0	125.6	145.8
	D_{90} (μm):	225.5	188.4	158.7	143.4	316.4	700.3	458.3	316.3
	(D_{90} / D_{10}) (μm):	19.16	2.723	22.07	25.33	43.17	51.81	39.39	6.137
	(D_{90} - D_{10}) (μm):	213.7	119.2	151.5	137.8	309.1	686.8	446.7	264.8
	(D_{75} / D_{25}) (μm):	3.943	1.701	3.920	5.140	6.233	4.702	6.086	2.383
	(D_{75} - D_{25}) (μm):	101.2	62.66	81.58	79.11	148.6	377.9	221.2	125.2
	D_{10} (ϕ):	2.149	2.408	2.655	2.802	1.660	0.514	1.125	1.661
	D_{50} (ϕ):	3.740	3.095	3.896	4.124	3.585	1.852	2.993	2.778
	D_{90} (ϕ):	6.409	3.853	7.119	7.464	7.092	6.209	6.425	4.278
	(D_{90} / D_{10}) (ϕ):	2.982	1.600	2.681	2.664	4.272	12.08	5.709	2.576
	(D_{90} - D_{10}) (ϕ):	4.260	1.445	4.464	4.663	5.432	5.695	5.300	2.618
	(D_{75} / D_{25}) (ϕ):	1.687	1.282	1.618	1.705	2.057	3.109	2.359	1.575
	(D_{75} - D_{25}) (ϕ):	1.979	0.767	1.971	2.362	2.640	2.233	2.606	1.253
	% GRAVEL:	0.0%	0.0%	0.0%	0.0%	0.0%	0.0%	0.0%	0.0%
	% SAND:	57.2%	93.2%	53.3%	46.4%	58.4%	80.6%	68.4%	87.1%
	% MUD:	42.8%	6.8%	46.7%	53.6%	41.6%	19.4%	31.6%	12.9%
	% V COARSE GRAVEL:	0.0%	0.0%	0.0%	0.0%	0.0%	0.0%	0.0%	0.0%
	% COARSE GRAVEL:	0.0%	0.0%	0.0%	0.0%	0.0%	0.0%	0.0%	0.0%
	% MEDIUM GRAVEL:	0.0%	0.0%	0.0%	0.0%	0.0%	0.0%	0.0%	0.0%
	% FINE GRAVEL:	0.0%	0.0%	0.0%	0.0%	0.0%	0.0%	0.0%	0.0%
	% V FINE GRAVEL:	0.0%	0.0%	0.0%	0.0%	0.0%	0.0%	0.0%	0.0%
	% V COARSE SAND:	0.0%	0.0%	0.0%	0.0%	0.0%	2.1%	0.6%	0.0%
	% COARSE SAND:	0.9%	0.0%	0.0%	0.0%	3.2%	21.0%	7.6%	1.6%
	% MEDIUM SAND:	7.1%	1.4%	1.7%	0.5%	12.0%	30.8%	18.6%	17.1%
	% FINE SAND:	20.1%	41.9%	17.1%	13.9%	21.3%	18.0%	23.3%	40.6%
	% V FINE SAND:	29.1%	49.9%	34.4%	31.6%	21.9%	8.7%	18.3%	27.6%
	% V COARSE SILT:	19.8%	3.7%	20.1%	21.2%	15.0%	5.1%	11.4%	6.2%
	% COARSE SILT:	10.1%	0.9%	8.5%	10.1%	9.3%	3.7%	7.6%	2.5%
	% MEDIUM SILT:	6.2%	1.4%	7.3%	8.6%	6.7%	3.3%	5.7%	1.6%
	% FINE SILT:	4.2%	0.6%	6.5%	8.0%	6.2%	3.7%	4.6%	1.6%
	% V FINE SILT:	2.1%	0.1%	3.7%	4.9%	3.8%	2.8%	2.2%	1.0%
	% CLAY:	0.3%	0.0%	0.6%	0.9%	0.6%	0.8%	0.2%	0.1%

SAMPLE STATISTICS

SAMPLE IDENTITY: **m1**

ANALYST & DATE: Sylvia Nicovich, 5/9/2018

SAMPLE TYPE: Unimodal, Poorly Sorted

TEXTURAL GROUP: Slightly Gravelly Muddy Sand

SEDIMENT NAME: Slightly Very Fine Gravelly Very Coarse Silty Fine Sand

	μm	ϕ
MODE 1:	198.4	2.336
MODE 2:		
MODE 3:		
D_{10}:	18.55	1.338
MEDIAN or D_{50}:	164.2	2.606
D_{90}:	395.4	5.752
(D_{90} / D_{10}):	21.32	4.298
(D_{90} - D_{10}):	376.9	4.414
(D_{75} / D_{25}):	3.257	1.904
(D_{75} - D_{25}):	187.7	1.704

GRAIN SIZE DISTRIBUTION

GRAVEL:	0.0%	COARSE SAND:	4.3%
SAND:	80.5%	MEDIUM SAND:	24.6%
MUD:	19.5%	FINE SAND:	33.2%
		V FINE SAND:	18.4%
V COARSE GRAVEL:	0.0%	V COARSE SILT:	6.6%
COARSE GRAVEL:	0.0%	COARSE SILT:	3.7%
MEDIUM GRAVEL:	0.0%	MEDIUM SILT:	3.2%
FINE GRAVEL:	0.0%	FINE SILT:	3.2%
V FINE GRAVEL:	0.0%	V FINE SILT:	2.2%
V COARSE SAND:	0.0%	CLAY:	0.5%

	METHOD OF MOMENTS			FOLK & WARD METHOD		
	Arithmetic	Geometric	Logarithmic	Geometric	Logarithmic	Description
	μm	μm	ϕ	μm	ϕ	
MEAN ($\bar{x}$):	192.9	120.4	3.054	137.0	2.867	Fine Sand
SORTING (σ):	148.3	3.436	1.781	3.142	1.651	Poorly Sorted
SKEWNESS (Sk):	1.086	-1.443	1.443	-0.389	0.389	Very Fine Skewed
KURTOSIS (K):	4.340	4.832	4.832	1.499	1.499	Leptokurtic

GRAIN SIZE DISTRIBUTION

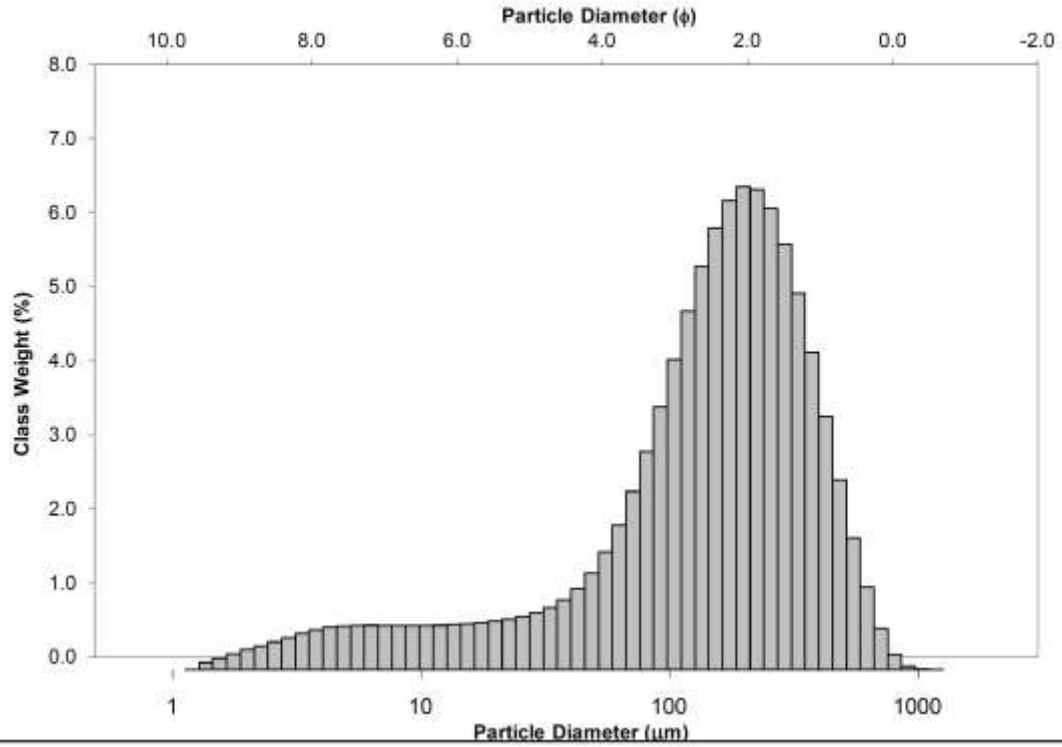

SAMPLE STATISTICS

SAMPLE IDENTITY: **m2a**

ANALYST & DATE: , 5/9/2018

SAMPLE TYPE: Unimodal, Poorly Sorted

TEXTURAL GROUP: Slightly Gravelly Muddy Sand

SEDIMENT NAME: Slightly Very Fine Gravelly Very Coarse Silty Very Fine Sand

	µm	ϕ
MODE 1:	81.18	3.626
MODE 2:		
MODE 3:		
D_{10}:	9.481	2.118
MEDIAN or D_{50}:	67.69	3.885
D_{90}:	230.4	6.721
(D_{90} / D_{10}):	24.31	3.174
(D_{90} - D_{10}):	221.0	4.603
(D_{75} / D_{25}):	4.511	1.743
(D_{75} - D_{25}):	102.4	2.173

GRAIN SIZE DISTRIBUTION

GRAVEL:	0.0%	COARSE SAND:	1.0%
SAND:	52.9%	MEDIUM SAND:	7.5%
MUD:	47.1%	FINE SAND:	18.2%
		V FINE SAND:	26.2%
V COARSE GRAVEL:	0.0%	V COARSE SILT:	20.6%
COARSE GRAVEL:	0.0%	COARSE SILT:	11.4%
MEDIUM GRAVEL:	0.0%	MEDIUM SILT:	6.6%
FINE GRAVEL:	0.0%	FINE SILT:	4.8%
V FINE GRAVEL:	0.0%	V FINE SILT:	3.0%
V COARSE SAND:	0.0%	CLAY:	0.7%

	METHOD OF MOMENTS			FOLK & WARD METHOD		
	Arithmetic	Geometric	Logarithmic	Geometric	Logarithmic	Description
	µm	µm	ϕ	µm	ϕ	
MEAN ($\bar{x}$):	99.73	56.30	4.151	58.70	4.090	Very Coarse Silt
SORTING (σ):	103.9	3.366	1.751	3.388	1.761	Poorly Sorted
SKEWNESS (Sk):	2.113	-0.674	0.674	-0.222	0.222	Fine Skewed
KURTOSIS (K):	8.717	3.147	3.147	1.135	1.135	Leptokurtic

GRAIN SIZE DISTRIBUTION

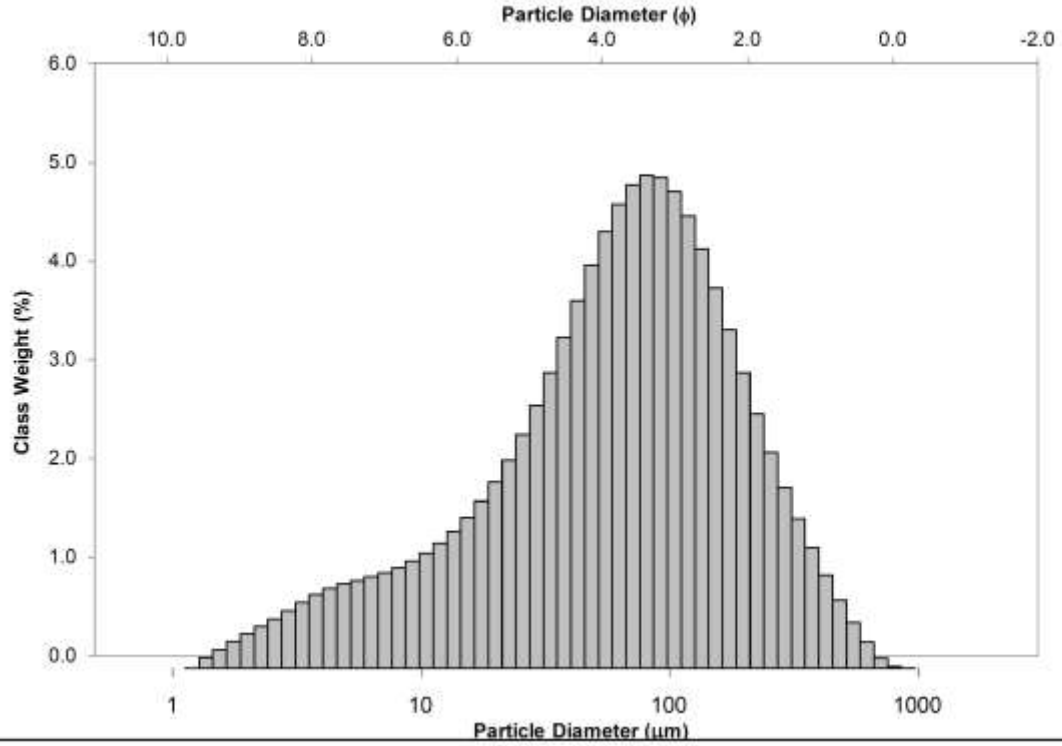

SAMPLE STATISTICS

SAMPLE IDENTITY: **m2b** ANALYST & DATE: , 6/19/2018

SAMPLE TYPE: Unimodal, Poorly Sorted TEXTURAL GROUP: Slightly Gravelly Muddy Sand

SEDIMENT NAME: Slightly Very Fine Gravelly Very Coarse Silty Very Fine Sand

	μm	ϕ
MODE 1:	119.1	3.073
MODE 2:		
MODE 3:		
D_{10}:	14.90	1.735
MEDIAN or D_{50}:	98.35	3.346
D_{90}:	300.4	6.069
(D_{90} / D_{10}):	20.16	3.498
(D_{90} - D_{10}):	285.5	4.334
(D_{75} / D_{25}):	4.063	1.827
(D_{75} - D_{25}):	138.4	2.023

GRAIN SIZE DISTRIBUTION

GRAVEL:	0.0%	COARSE SAND:	2.0%
SAND:	66.2%	MEDIUM SAND:	12.8%
MUD:	33.8%	FINE SAND:	25.4%
		V FINE SAND:	26.0%
V COARSE GRAVEL:	0.0%	V COARSE SILT:	15.7%
COARSE GRAVEL:	0.0%	COARSE SILT:	7.7%
MEDIUM GRAVEL:	0.0%	MEDIUM SILT:	4.4%
FINE GRAVEL:	0.0%	FINE SILT:	3.4%
V FINE GRAVEL:	0.0%	V FINE SILT:	2.2%
V COARSE SAND:	0.0%	CLAY:	0.5%

	METHOD OF MOMENTS			FOLK & WARD METHOD		
	Arithmetic	Geometric	Logarithmic	Geometric	Logarithmic	Description
	μm	μm	ϕ	μm	ϕ	
MEAN ($\bar{x}$):	134.1	80.10	3.642	86.13	3.537	Very Fine Sand
SORTING (σ):	124.4	3.284	1.715	3.210	1.682	Poorly Sorted
SKEWNESS (Sk):	1.695	-0.931	0.931	-0.256	0.256	Fine Skewed
KURTOSIS (K):	6.535	3.733	3.733	1.198	1.198	Leptokurtic

GRAIN SIZE DISTRIBUTION

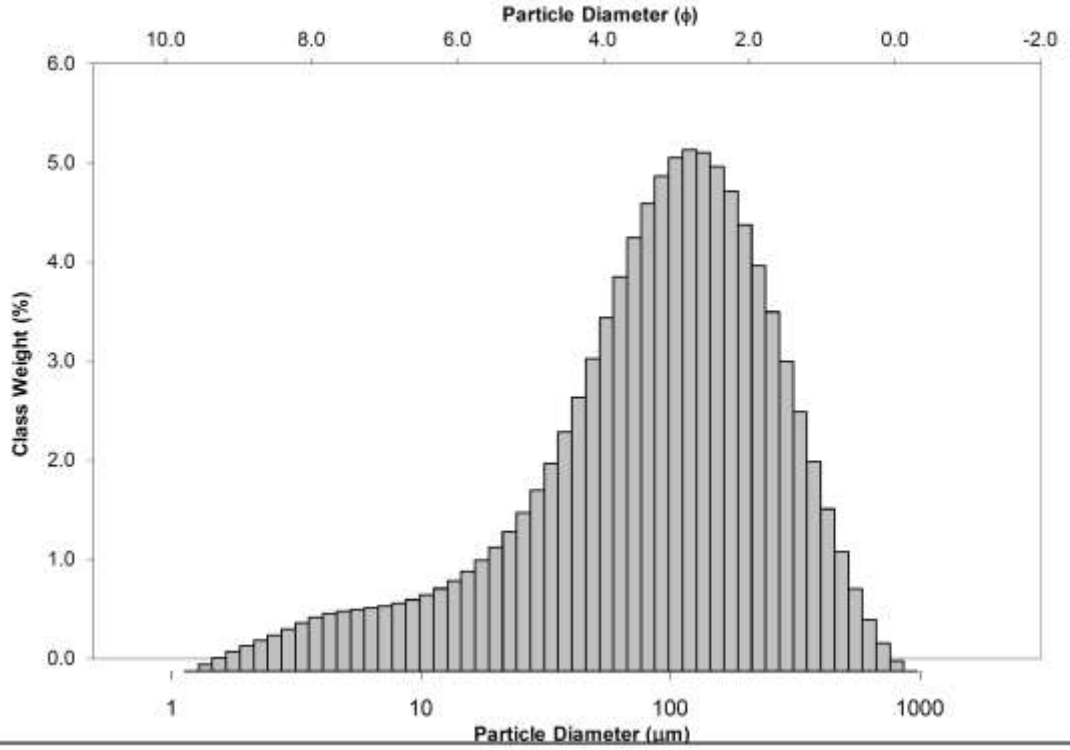

SAMPLE STATISTICS

SAMPLE IDENTITY: **m3**

ANALYST & DATE: , 6/19/2018

SAMPLE TYPE: Unimodal, Poorly Sorted

TEXTURAL GROUP: Slightly Gravelly Sandy Mud

SEDIMENT NAME: Slightly Very Fine Gravelly Very Fine Sandy Very Coarse Silt

	μm	ϕ
MODE 1:	71.45	3.810
MODE 2:		
MODE 3:		
D_{10}:	6.450	2.683
MEDIAN or D_{50}:	58.16	4.104
D_{90}:	155.7	7.277
(D_{90} / D_{10}):	24.14	2.712
(D_{90} - D_{10}):	149.3	4.593
(D_{75} / D_{25}):	4.193	1.623
(D_{75} - D_{25}):	76.29	2.068

GRAIN SIZE DISTRIBUTION

GRAVEL:	0.0%	COARSE SAND:	0.0%
SAND:	46.8%	MEDIUM SAND:	2.5%
MUD:	53.2%	FINE SAND:	13.9%
		V FINE SAND:	30.4%
V COARSE GRAVEL:	0.0%	V COARSE SILT:	23.5%
COARSE GRAVEL:	0.0%	COARSE SILT:	10.0%
MEDIUM GRAVEL:	0.0%	MEDIUM SILT:	7.6%
FINE GRAVEL:	0.0%	FINE SILT:	7.2%
V FINE GRAVEL:	0.0%	V FINE SILT:	4.2%
V COARSE SAND:	0.0%	CLAY:	0.7%

	METHOD OF MOMENTS			FOLK & WARD METHOD		
	Arithmetic	Geometric	Logarithmic	Geometric	Logarithmic	Description
	μm	μm	ϕ	μm	ϕ	
MEAN ($\bar{x}$):	73.10	43.77	4.514	43.48	4.523	Very Coarse Silt
SORTING (σ):	66.75	3.258	1.704	3.327	1.734	Poorly Sorted
SKEWNESS (Sk):	1.834	-0.804	0.804	-0.364	0.364	Very Fine Skewed
KURTOSIS (K):	8.119	2.988	2.988	1.124	1.124	Leptokurtic

GRAIN SIZE DISTRIBUTION

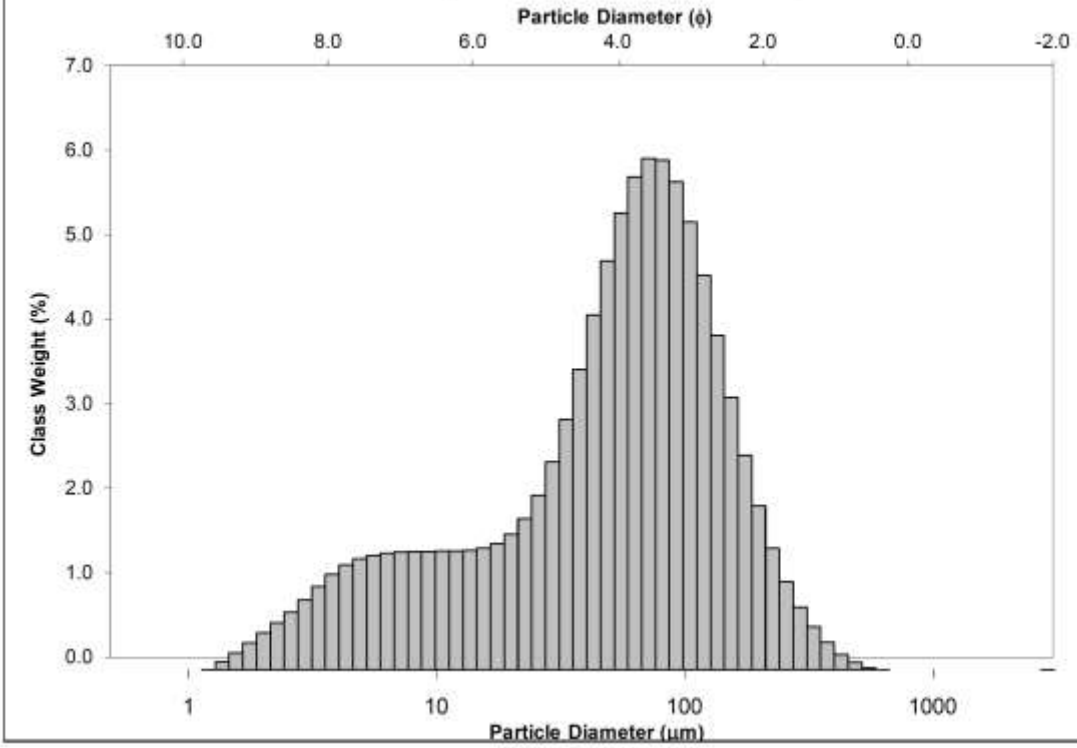

SAMPLE STATISTICS

SAMPLE IDENTITY: **m4** ANALYST & DATE: , 5/9/2018

SAMPLE TYPE: Bimodal, Very Poorly Sorted TEXTURAL GROUP: Slightly Gravelly Muddy Sand

SEDIMENT NAME: Slightly Very Fine Gravelly Fine Silty Medium Sand

	µm	ϕ
MODE 1:	330.6	1.600
MODE 2:	4.895	7.677
MODE 3:		
D_{10}:	5.102	0.870
MEDIAN or D_{50}:	181.6	2.462
D_{90}:	547.0	7.615
(D_{90} / D_{10}):	107.2	8.748
(D_{90} - D_{10}):	541.9	6.744
(D_{75} / D_{25}):	12.66	3.479
(D_{75} - D_{25}):	330.9	3.662

GRAIN SIZE DISTRIBUTION

GRAVEL:	0.0%	COARSE SAND:	12.5%
SAND:	69.0%	MEDIUM SAND:	26.5%
MUD:	31.0%	FINE SAND:	20.0%
		V FINE SAND:	9.7%
V COARSE GRAVEL:	0.0%	V COARSE SILT:	5.4%
COARSE GRAVEL:	0.0%	COARSE SILT:	4.9%
MEDIUM GRAVEL:	0.0%	MEDIUM SILT:	6.1%
FINE GRAVEL:	0.0%	FINE SILT:	7.6%
V FINE GRAVEL:	0.0%	V FINE SILT:	5.5%
V COARSE SAND:	0.3%	CLAY:	1.5%

	METHOD OF MOMENTS			FOLK & WARD METHOD		
	Arithmetic	Geometric	Logarithmic	Geometric	Logarithmic	Description
	µm	µm	ϕ	µm	ϕ	
MEAN ($\bar{x}$):	230.8	95.43	3.389	90.56	3.465	Very Fine Sand
SORTING (σ):	220.0	5.670	2.503	5.986	2.582	Very Poorly Sorted
SKEWNESS (Sk):	1.030	-0.846	0.846	-0.523	0.523	Very Fine Skewed
KURTOSIS (K):	3.612	2.456	2.456	0.862	0.862	Platykurtic

GRAIN SIZE DISTRIBUTION

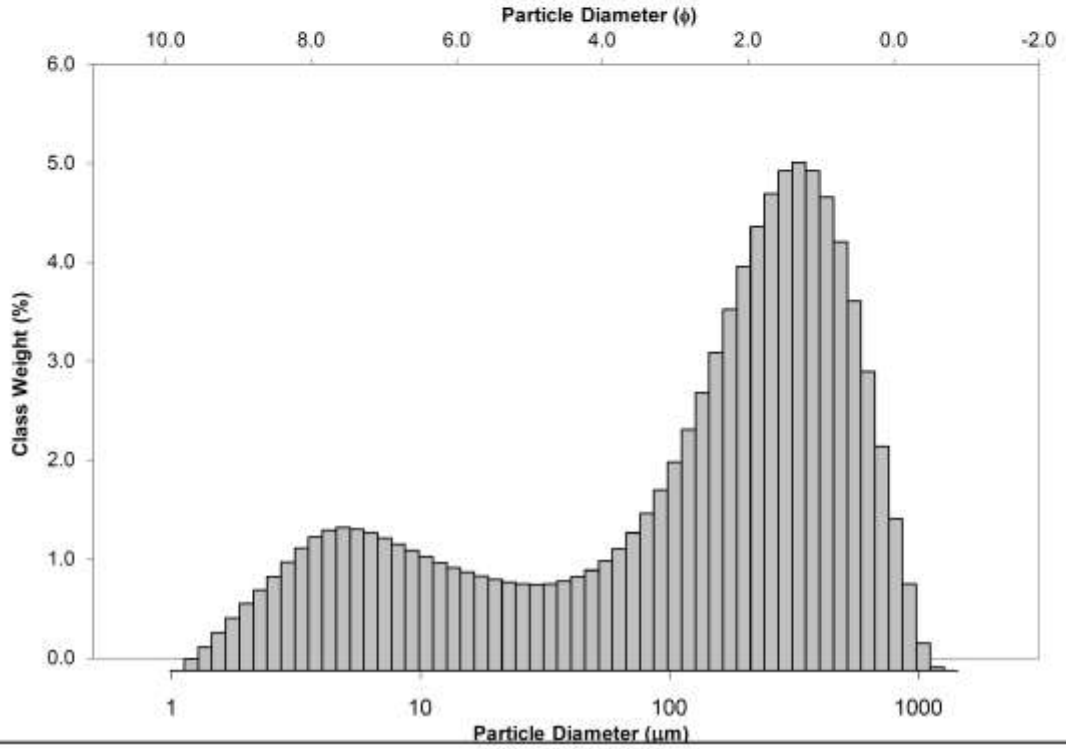

SAMPLE STATISTICS

SAMPLE IDENTITY: **m5**

ANALYST & DATE: , 5/9/2018

SAMPLE TYPE: Unimodal, Poorly Sorted

TEXTURAL GROUP: Slightly Gravelly Muddy Sand

SEDIMENT NAME: Slightly Very Fine Gravelly Very Coarse Silty Fine Sand

	μm	ϕ
MODE 1:	135.3	2.889
MODE 2:		
MODE 3:		
D_{10}:	9.737	1.551
MEDIAN or D_{50}:	93.56	3.418
D_{90}:	341.2	6.682
(D_{90} / D_{10}):	35.04	4.308
(D_{90} - D_{10}):	331.5	5.131
(D_{75} / D_{25}):	5.614	2.063
(D_{75} - D_{25}):	162.1	2.489

GRAIN SIZE DISTRIBUTION

GRAVEL:	0.0%	COARSE SAND:	3.5%
SAND:	62.1%	MEDIUM SAND:	14.3%
MUD:	37.9%	FINE SAND:	22.5%
		V FINE SAND:	21.8%
V COARSE GRAVEL:	0.0%	V COARSE SILT:	14.9%
COARSE GRAVEL:	0.0%	COARSE SILT:	8.7%
MEDIUM GRAVEL:	0.0%	MEDIUM SILT:	6.1%
FINE GRAVEL:	0.0%	FINE SILT:	4.8%
V FINE GRAVEL:	0.0%	V FINE SILT:	2.8%
V COARSE SAND:	0.0%	CLAY:	0.6%

	METHOD OF MOMENTS			FOLK & WARD METHOD		
	Arithmetic	Geometric	Logarithmic	Geometric	Logarithmic	Description
	μm	μm	ϕ	μm	ϕ	
MEAN ($\bar{x}$):	141.3	73.92	3.758	77.14	3.696	Very Fine Sand
SORTING (σ):	146.2	3.786	1.921	3.857	1.948	Poorly Sorted
SKEWNESS (Sk):	1.755	-0.717	0.717	-0.260	0.260	Fine Skewed
KURTOSIS (K):	6.559	2.973	2.973	1.067	1.067	Mesokurtic

GRAIN SIZE DISTRIBUTION

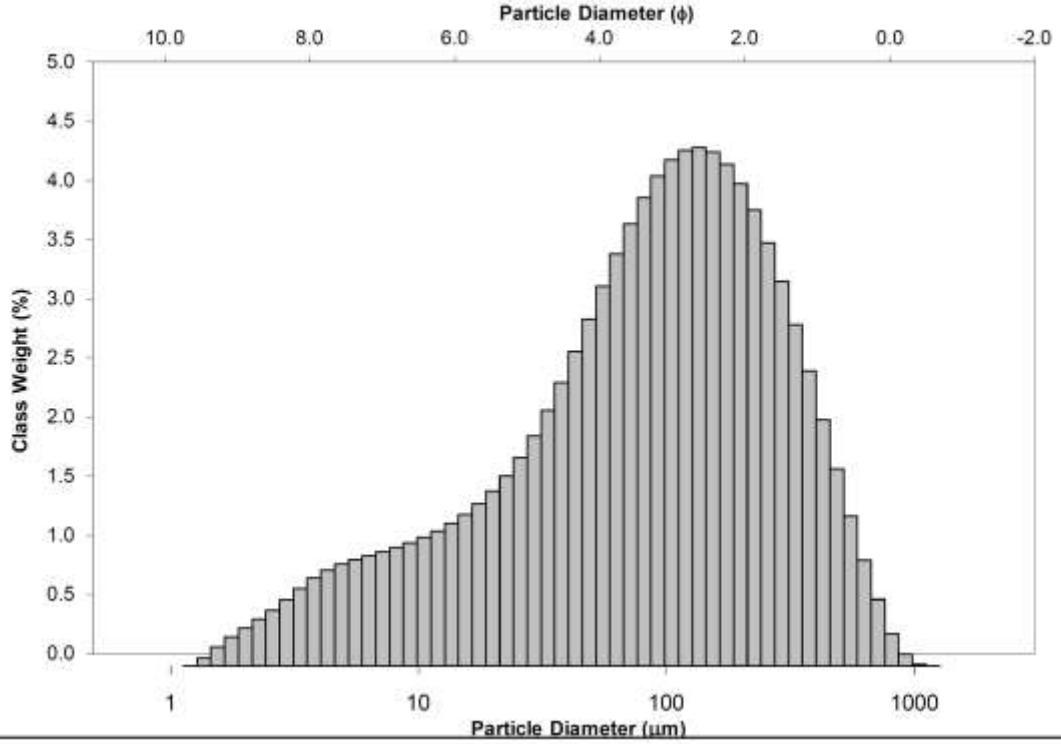

SAMPLE STATISTICS

SAMPLE IDENTITY: **m6**

ANALYST & DATE: , 6/19/2018

SAMPLE TYPE: Unimodal, Poorly Sorted

TEXTURAL GROUP: Slightly Gravelly Sandy Mud

SEDIMENT NAME: Slightly Very Fine Gravelly Very Fine Sandy Very Coarse Silt

	μm	ϕ
MODE 1:	104.8	3.257
MODE 2:		
MODE 3:		
D_{10}:	7.231	2.259
MEDIAN or D_{50}:	61.47	4.024
D_{90}:	208.9	7.112
(D_{90} / D_{10}):	28.89	3.148
(D_{90} - D_{10}):	201.7	4.852
(D_{75} / D_{25}):	5.681	1.843
(D_{75} - D_{25}):	104.9	2.506

GRAIN SIZE DISTRIBUTION

GRAVEL:	0.0%	COARSE SAND:	0.1%
SAND:	49.5%	MEDIUM SAND:	5.9%
MUD:	50.5%	FINE SAND:	19.5%
		V FINE SAND:	23.8%
V COARSE GRAVEL:	0.0%	V COARSE SILT:	18.9%
COARSE GRAVEL:	0.0%	COARSE SILT:	12.4%
MEDIUM GRAVEL:	0.0%	MEDIUM SILT:	8.4%
FINE GRAVEL:	0.0%	FINE SILT:	6.2%
V FINE GRAVEL:	0.0%	V FINE SILT:	3.7%
V COARSE SAND:	0.0%	CLAY:	0.9%

	METHOD OF MOMENTS			FOLK & WARD METHOD		
	Arithmetic	Geometric	Logarithmic	Geometric	Logarithmic	Description
	μm	μm	ϕ	μm	ϕ	
MEAN ($\bar{x}$):	88.36	48.79	4.357	50.33	4.312	Very Coarse Silt
SORTING (σ):	86.34	3.518	1.815	3.608	1.851	Poorly Sorted
SKEWNESS (Sk):	1.568	-0.647	0.647	-0.263	0.263	Fine Skewed
KURTOSIS (K):	5.917	2.746	2.746	0.981	0.981	Mesokurtic

GRAIN SIZE DISTRIBUTION

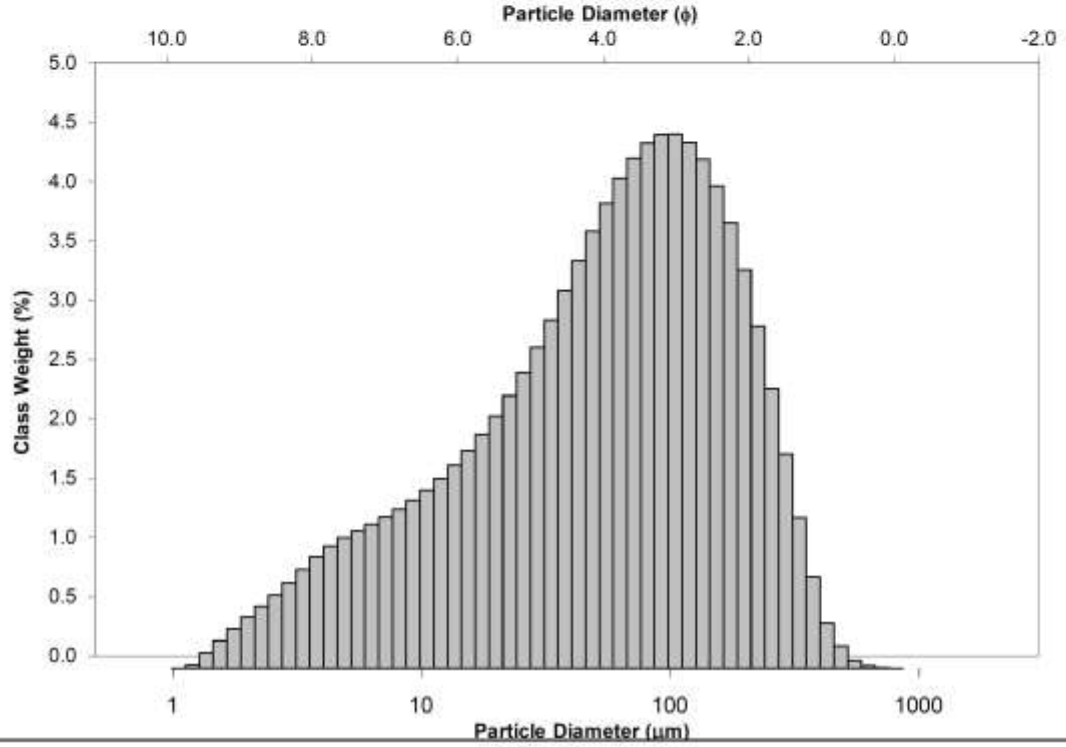

SAMPLE STATISTICS

SAMPLE IDENTITY: **m7**

ANALYST & DATE: , 6/19/2018

SAMPLE TYPE: Unimodal, Poorly Sorted

TEXTURAL GROUP: Slightly Gravelly Muddy Sand

SEDIMENT NAME: Slightly Very Fine Gravelly Very Coarse Silty Very Fine Sand

	μm	ϕ
MODE 1:	81.18	3.626
MODE 2:		
MODE 3:		
D_{10}:	27.81	2.253
MEDIAN or D_{50}:	83.02	3.590
D_{90}:	209.8	5.168
(D_{90} / D_{10}):	7.546	2.294
(D_{90} - D_{10}):	182.0	2.916
(D_{75} / D_{25}):	2.621	1.478
(D_{75} - D_{25}):	82.37	1.390

GRAIN SIZE DISTRIBUTION

GRAVEL: 0.0%	COARSE SAND: 1.0%
SAND: 65.5%	MEDIUM SAND: 5.8%
MUD: 34.5%	FINE SAND: 21.0%
	V FINE SAND: 37.7%
V COARSE GRAVEL: 0.0%	V COARSE SILT: 22.9%
COARSE GRAVEL: 0.0%	COARSE SILT: 5.9%
MEDIUM GRAVEL: 0.0%	MEDIUM SILT: 3.0%
FINE GRAVEL: 0.0%	FINE SILT: 2.0%
V FINE GRAVEL: 0.0%	V FINE SILT: 0.7%
V COARSE SAND: 0.0%	CLAY: 0.0%

	METHOD OF MOMENTS			FOLK & WARD METHOD		
	Arithmetic	Geometric	Logarithmic	Geometric	Logarithmic	Description
	μm	μm	ϕ	μm	ϕ	
MEAN ($\bar{x}$):	107.9	77.15	3.696	81.36	3.619	Very Fine Sand
SORTING (σ):	94.06	2.433	1.283	2.293	1.197	Poorly Sorted
SKEWNESS (Sk):	2.582	-0.832	0.832	-0.115	0.115	Fine Skewed
KURTOSIS (K):	12.83	4.706	4.706	1.296	1.296	Leptokurtic

GRAIN SIZE DISTRIBUTION

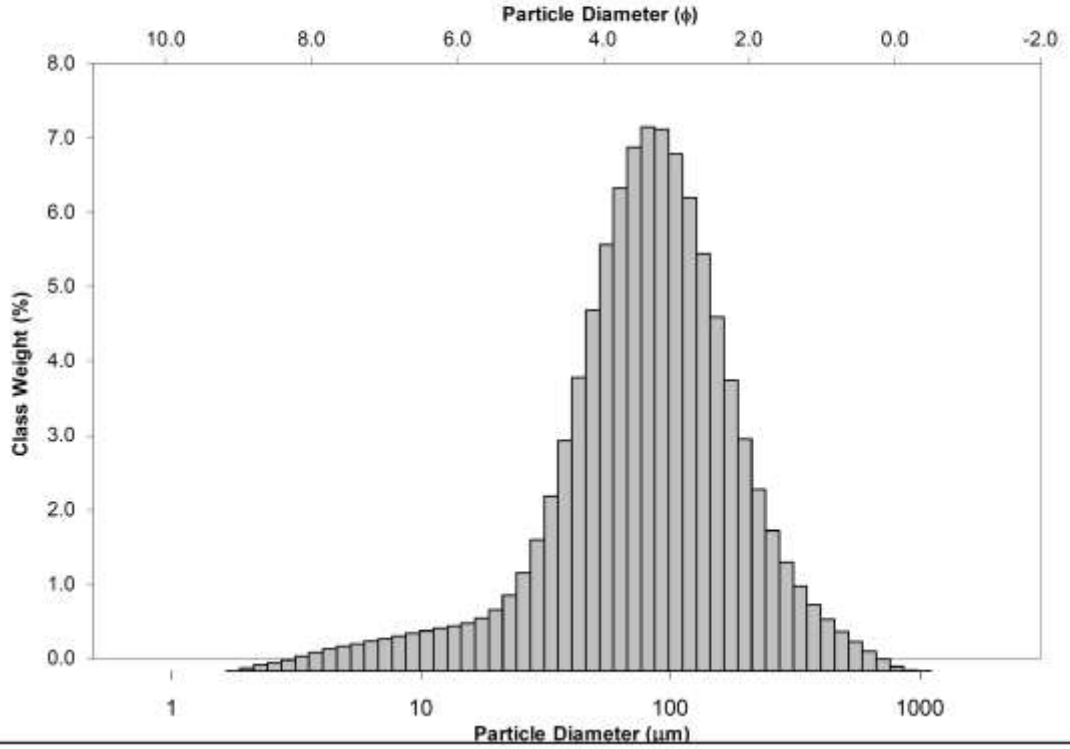

SAMPLE STATISTICS

SAMPLE IDENTITY: **m8** ANALYST & DATE: , 6/19/2018

SAMPLE TYPE: Unimodal, Poorly Sorted TEXTURAL GROUP: Slightly Gravelly Muddy Sand

SEDIMENT NAME: Slightly Very Fine Gravelly Very Coarse Silty Very Fine Sand

	μm	ϕ
MODE 1:	92.23	3.441
MODE 2:		
MODE 3:		
D_{10}:	11.77	2.149
MEDIAN or D_{50}:	74.83	3.740
D_{90}:	225.5	6.409
(D_{90} / D_{10}):	19.16	2.982
(D_{90} - D_{10}):	213.7	4.260
(D_{75} / D_{25}):	3.943	1.687
(D_{75} - D_{25}):	101.2	1.979

GRAIN SIZE DISTRIBUTION

GRAVEL:	0.0%	COARSE SAND:	0.9%
SAND:	57.2%	MEDIUM SAND:	7.1%
MUD:	42.8%	FINE SAND:	20.1%
		V FINE SAND:	29.1%
V COARSE GRAVEL:	0.0%	V COARSE SILT:	19.8%
COARSE GRAVEL:	0.0%	COARSE SILT:	10.1%
MEDIUM GRAVEL:	0.0%	MEDIUM SILT:	6.2%
FINE GRAVEL:	0.0%	FINE SILT:	4.2%
V FINE GRAVEL:	0.0%	V FINE SILT:	2.1%
V COARSE SAND:	0.0%	CLAY:	0.3%

	METHOD OF MOMENTS			FOLK & WARD METHOD		
	Arithmetic	Geometric	Logarithmic	Geometric	Logarithmic	Description
	μm	μm	ϕ	μm	ϕ	
MEAN ($\bar{x}$):	102.6	62.00	4.012	64.43	3.956	Very Fine Sand
SORTING (σ):	99.56	3.124	1.643	3.111	1.637	Poorly Sorted
SKEWNESS (Sk):	2.065	-0.750	0.750	-0.245	0.245	Fine Skewed
KURTOSIS (K):	8.768	3.350	3.350	1.166	1.166	Leptokurtic

GRAIN SIZE DISTRIBUTION

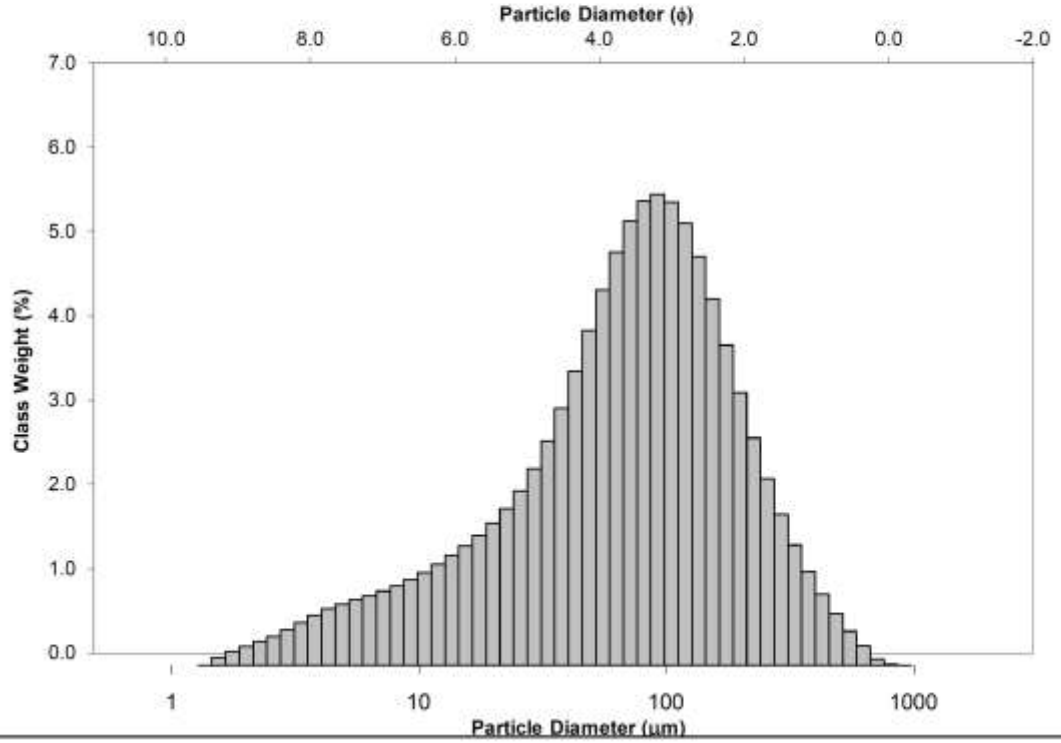

SAMPLE STATISTICS

SAMPLE IDENTITY: **m9** ANALYST & DATE: , 6/19/2018

SAMPLE TYPE: Unimodal, Moderately Well Sorted TEXTURAL GROUP: Slightly Gravelly Sand

SEDIMENT NAME: Slightly Very Fine Gravelly Very Fine Sand

	µm	ϕ
MODE 1:	119.1	3.073
MODE 2:		
MODE 3:		
D_{10}:	69.19	2.408
MEDIAN or D_{50}:	117.0	3.095
D_{90}:	188.4	3.853
(D_{90} / D_{10}):	2.723	1.600
(D_{90} - D_{10}):	119.2	1.445
(D_{75} / D_{25}):	1.701	1.282
(D_{75} - D_{25}):	62.66	0.767

GRAIN SIZE DISTRIBUTION

GRAVEL: 0.0%	COARSE SAND: 0.0%
SAND: 93.2%	MEDIUM SAND: 1.4%
MUD: 6.8%	FINE SAND: 41.9%
	V FINE SAND: 49.9%
V COARSE GRAVEL: 0.0%	V COARSE SILT: 3.7%
COARSE GRAVEL: 0.0%	COARSE SILT: 0.9%
MEDIUM GRAVEL: 0.0%	MEDIUM SILT: 1.4%
FINE GRAVEL: 0.0%	FINE SILT: 0.6%
V FINE GRAVEL: 0.0%	V FINE SILT: 0.1%
V COARSE SAND: 0.0%	CLAY: 0.0%

	METHOD OF MOMENTS			FOLK & WARD METHOD		
	Arithmetic	Geometric	Logarithmic	Geometric	Logarithmic	Description
	µm	µm	ϕ	µm	ϕ	
MEAN ($\bar{x}$):	123.1	110.3	3.181	116.2	3.106	Very Fine Sand
SORTING (σ):	49.06	1.724	0.785	1.480	0.566	Moderately Well Sorted
SKEWNESS (Sk):	0.468	-2.446	2.446	-0.060	0.060	Symmetrical
KURTOSIS (K):	3.591	13.03	13.03	1.003	1.003	Mesokurtic

GRAIN SIZE DISTRIBUTION

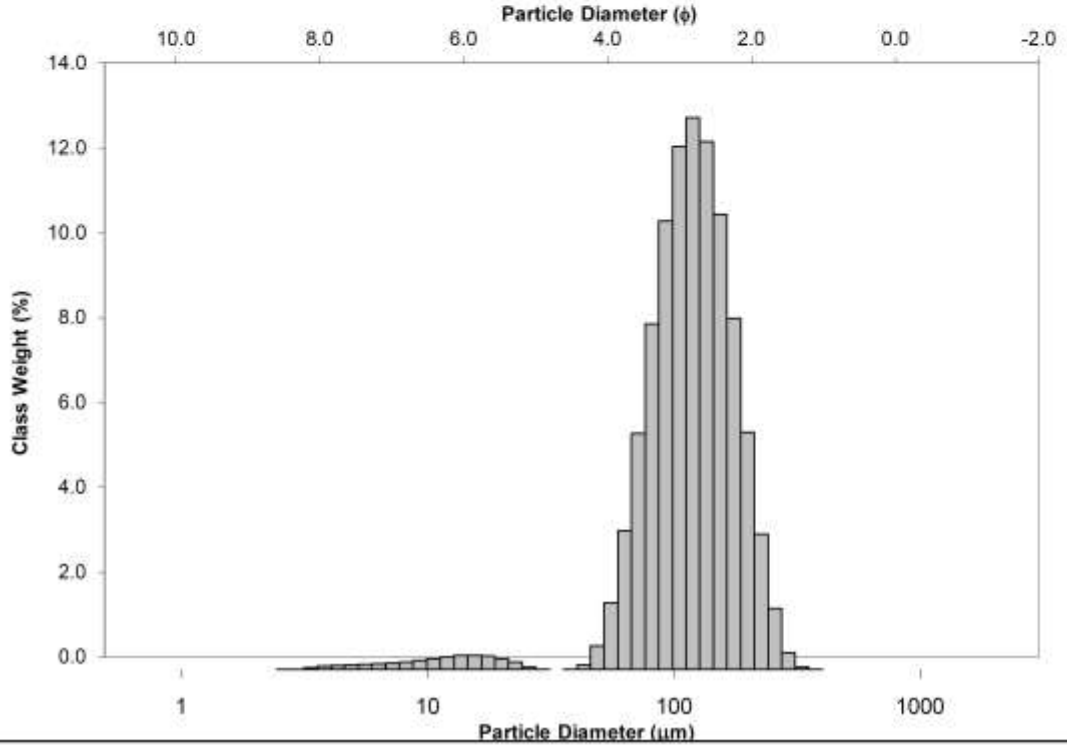

SAMPLE STATISTICS

SAMPLE IDENTITY: **m10a** ANALYST & DATE: , 6/19/2018

SAMPLE TYPE: Unimodal, Poorly Sorted TEXTURAL GROUP: Slightly Gravelly Muddy Sand

SEDIMENT NAME: Slightly Very Fine Gravelly Very Coarse Silty Very Fine Sand

	µm	ϕ
MODE 1:	92.23	3.441
MODE 2:		
MODE 3:		
D_{10}:	7.192	2.655
MEDIAN or D_{50}:	67.19	3.896
D_{90}:	158.7	7.119
(D_{90} / D_{10}):	22.07	2.681
(D_{90} - D_{10}):	151.5	4.464
(D_{75} / D_{25}):	3.920	1.618
(D_{75} - D_{25}):	81.56	1.971

GRAIN SIZE DISTRIBUTION

GRAVEL:	0.0%	COARSE SAND:	0.0%
SAND:	53.3%	MEDIUM SAND:	1.7%
MUD:	46.7%	FINE SAND:	17.1%
		V FINE SAND:	34.4%
V COARSE GRAVEL:	0.0%	V COARSE SILT:	20.1%
COARSE GRAVEL:	0.0%	COARSE SILT:	8.5%
MEDIUM GRAVEL:	0.0%	MEDIUM SILT:	7.3%
FINE GRAVEL:	0.0%	FINE SILT:	6.5%
V FINE GRAVEL:	0.0%	V FINE SILT:	3.7%
V COARSE SAND:	0.0%	CLAY:	0.6%

	METHOD OF MOMENTS			FOLK & WARD METHOD		
	Arithmetic	Geometric	Logarithmic	Geometric	Logarithmic	Description
	µm	µm	ϕ	µm	ϕ	
MEAN ($\bar{x}$):	77.41	48.49	4.366	48.70	4.360	Very Coarse Silt
SORTING (σ):	62.34	3.178	1.668	3.210	1.683	Poorly Sorted
SKEWNESS (Sk):	1.274	-0.964	0.964	-0.427	0.427	Very Fine Skewed
KURTOSIS (K):	5.601	3.176	3.176	1.148	1.148	Leptokurtic

GRAIN SIZE DISTRIBUTION

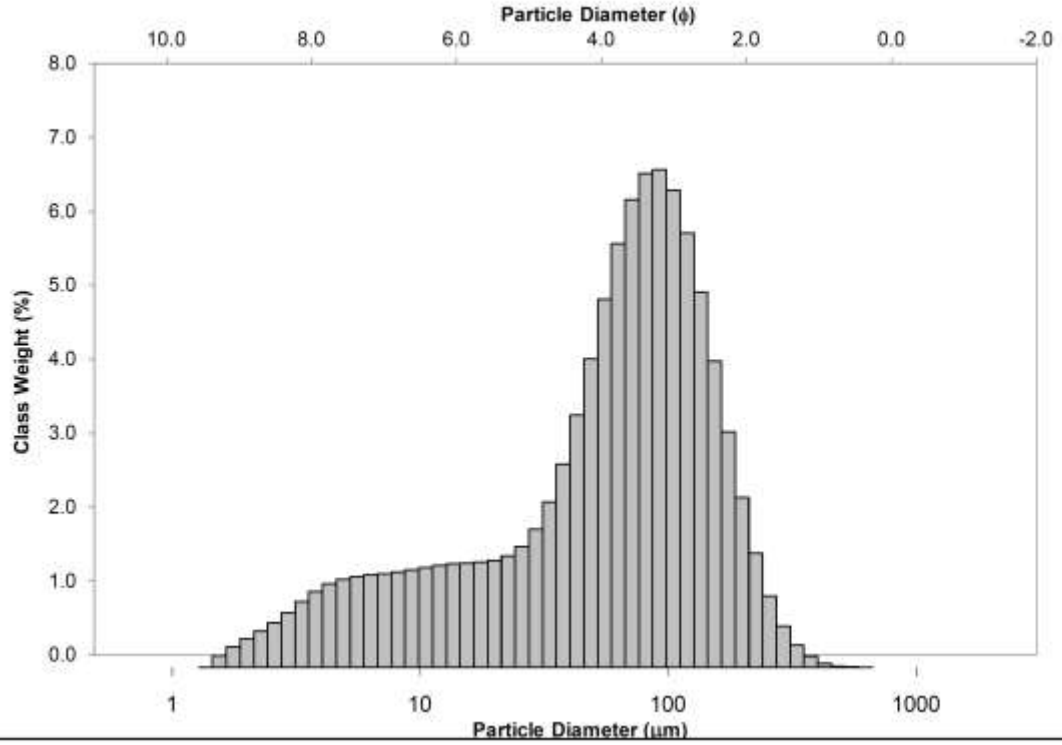

SAMPLE STATISTICS

SAMPLE IDENTITY: **m10b** ANALYST & DATE: , 6/19/2018

SAMPLE TYPE: Unimodal, Poorly Sorted TEXTURAL GROUP: Slightly Gravelly Sandy Mud

SEDIMENT NAME: Slightly Very Fine Gravelly Very Fine Sandy Very Coarse Silt

	μm	ϕ
MODE 1:	81.18	3.626
MODE 2:		
MODE 3:		
D_{10}:	5.663	2.802
MEDIAN or D_{50}:	57.36	4.124
D_{90}:	143.4	7.464
(D_{90} / D_{10}):	25.33	2.664
(D_{90} - D_{10}):	137.8	4.663
(D_{75} / D_{25}):	5.140	1.705
(D_{75} - D_{25}):	79.11	2.362

GRAIN SIZE DISTRIBUTION

GRAVEL:	0.0%	COARSE SAND:	0.0%
SAND:	46.4%	MEDIUM SAND:	0.8%
MUD:	53.6%	FINE SAND:	13.9%
		V FINE SAND:	31.6%
V COARSE GRAVEL:	0.0%	V COARSE SILT:	21.2%
COARSE GRAVEL:	0.0%	COARSE SILT:	10.1%
MEDIUM GRAVEL:	0.0%	MEDIUM SILT:	8.6%
FINE GRAVEL:	0.0%	FINE SILT:	8.0%
V FINE GRAVEL:	0.0%	V FINE SILT:	4.9%
V COARSE SAND:	0.0%	CLAY:	0.9%

	METHOD OF MOMENTS			FOLK & WARD METHOD		
	Arithmetic	Geometric	Logarithmic	Geometric	Logarithmic	Description
	μm	μm	ϕ	μm	ϕ	
MEAN ($\bar{x}$):	67.34	40.26	4.635	40.22	4.636	Very Coarse Silt
SORTING (σ):	56.28	3.336	1.738	3.418	1.773	Poorly Sorted
SKEWNESS (Sk):	1.118	-0.822	0.822	-0.420	0.420	Very Fine Skewed
KURTOSIS (K):	4.429	2.755	2.755	0.974	0.974	Mesokurtic

GRAIN SIZE DISTRIBUTION

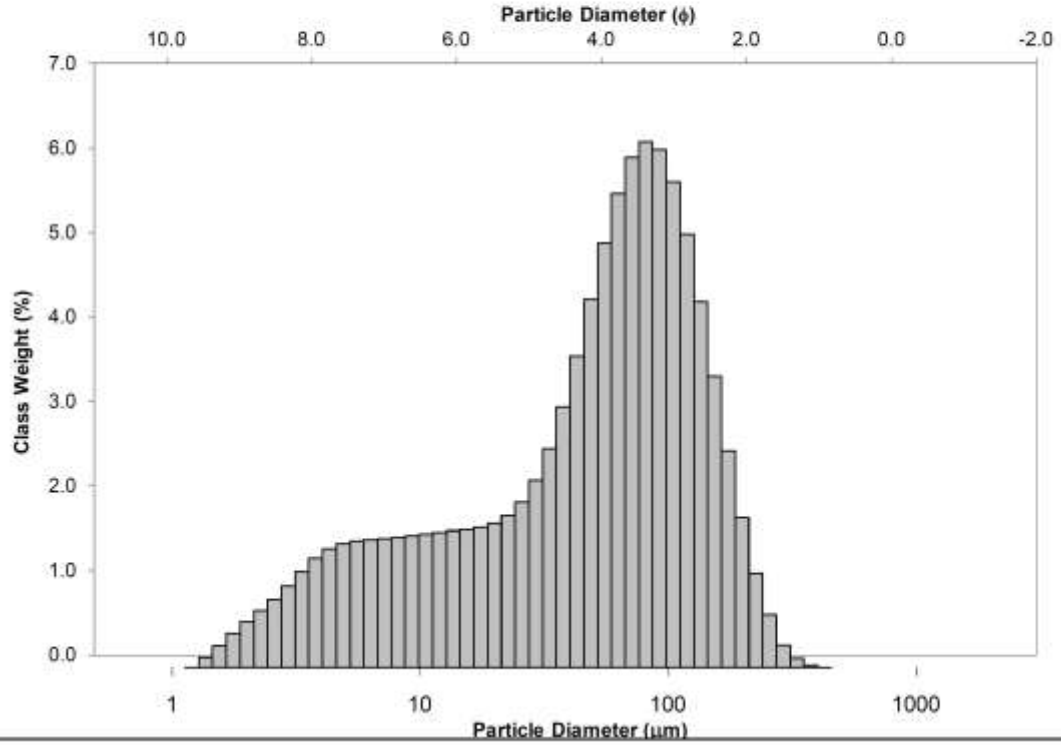

SAMPLE STATISTICS

SAMPLE IDENTITY: **m11** ANALYST & DATE: , 6/19/2018

SAMPLE TYPE: Bimodal, Very Poorly Sorted TEXTURAL GROUP: Slightly Gravelly Muddy Sand

SEDIMENT NAME: Slightly Very Fine Gravelly Very Coarse Silty Very Fine Sand

	µm	ϕ
MODE 1:	119.1	3.073
MODE 2:	6.319	7.309
MODE 3:		
D_{10}:	7.329	1.660
MEDIAN or D_{50}:	83.36	3.585
D_{90}:	316.4	7.092
(D_{90} / D_{10}):	43.17	4.272
(D_{90} - D_{10}):	309.1	5.432
(D_{75} / D_{25}):	6.233	2.057
(D_{75} - D_{25}):	148.6	2.640

GRAIN SIZE DISTRIBUTION

GRAVEL:	0.0%	COARSE SAND:	3.2%
SAND:	58.4%	MEDIUM SAND:	12.0%
MUD:	41.6%	FINE SAND:	21.3%
		V FINE SAND:	21.9%
V COARSE GRAVEL:	0.0%	V COARSE SILT:	15.0%
COARSE GRAVEL:	0.0%	COARSE SILT:	9.3%
MEDIUM GRAVEL:	0.0%	MEDIUM SILT:	6.7%
FINE GRAVEL:	0.0%	FINE SILT:	6.2%
V FINE GRAVEL:	0.0%	V FINE SILT:	3.8%
V COARSE SAND:	0.0%	CLAY:	0.6%

	METHOD OF MOMENTS			FOLK & WARD METHOD		
	Arithmetic	Geometric	Logarithmic	Geometric	Logarithmic	Description
	µm	µm	ϕ	µm	ϕ	
MEAN ($\bar{x}$):	129.8	64.27	3.960	65.44	3.934	Very Fine Sand
SORTING (σ):	142.9	3.976	1.991	4.122	2.043	Very Poorly Sorted
SKEWNESS (Sk):	1.986	-0.630	0.630	-0.273	0.273	Fine Skewed
KURTOSIS (K):	7.805	2.723	2.723	1.037	1.037	Mesokurtic

GRAIN SIZE DISTRIBUTION

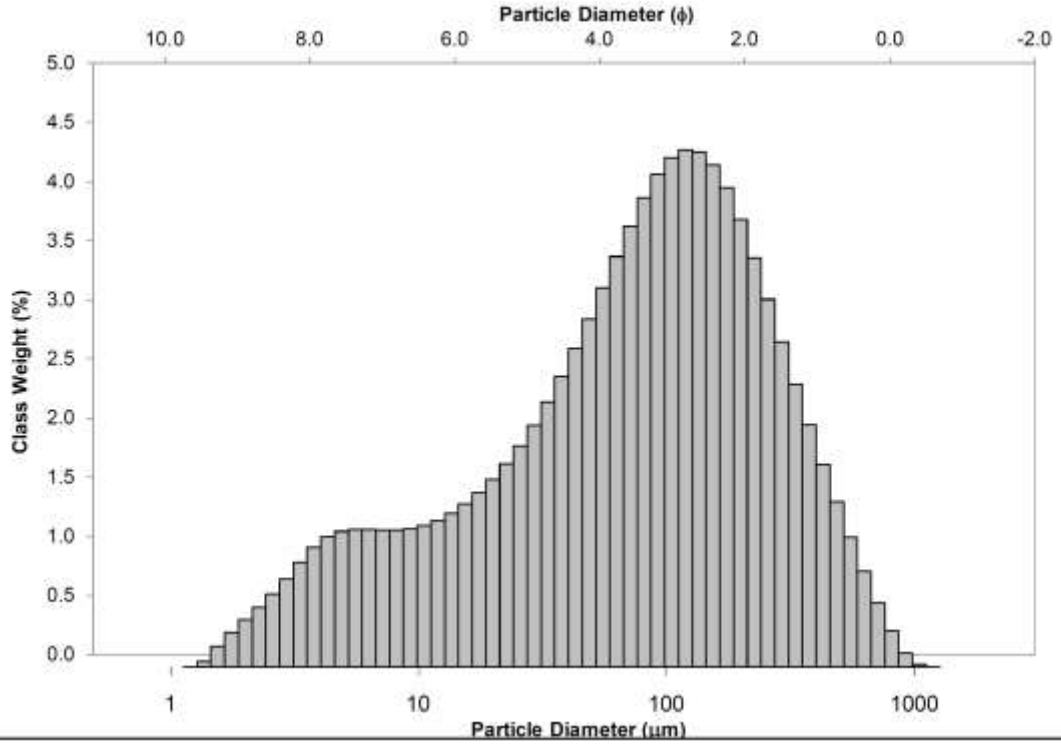

SAMPLE STATISTICS

SAMPLE IDENTITY: **m12** ANALYST & DATE: , 6/19/2018

SAMPLE TYPE: Unimodal, Very Poorly Sorted TEXTURAL GROUP: Slightly Gravelly Muddy Sand

SEDIMENT NAME: Slightly Very Fine Gravelly Very Coarse Silty Medium Sand

	µm	ϕ
MODE 1:	426.8	1.231
MODE 2:		
MODE 3:		
D_{10}:	13.52	0.514
MEDIAN or D_{50}:	277.0	1.852
D_{90}:	700.3	6.209
(D_{90} / D_{10}):	51.81	12.08
(D_{90} - D_{10}):	686.8	5.695
(D_{75} / D_{25}):	4.702	3.109
(D_{75} - D_{25}):	377.9	2.233

GRAIN SIZE DISTRIBUTION

GRAVEL:	0.0%	COARSE SAND:	21.0%
SAND:	80.6%	MEDIUM SAND:	30.8%
MUD:	19.4%	FINE SAND:	18.0%
		V FINE SAND:	8.7%
V COARSE GRAVEL:	0.0%	V COARSE SILT:	5.1%
COARSE GRAVEL:	0.0%	COARSE SILT:	3.7%
MEDIUM GRAVEL:	0.0%	MEDIUM SILT:	3.3%
FINE GRAVEL:	0.0%	FINE SILT:	3.7%
V FINE GRAVEL:	0.0%	V FINE SILT:	2.9%
V COARSE SAND:	2.1%	CLAY:	0.8%

	METHOD OF MOMENTS			FOLK & WARD METHOD		
	Arithmetic	Geometric	Logarithmic	Geometric	Logarithmic	Description
	µm	µm	ϕ	µm	ϕ	
MEAN ($\bar{x}$):	324.3	170.4	2.553	187.7	2.413	Fine Sand
SORTING (σ):	267.7	4.532	2.180	4.257	2.090	Very Poorly Sorted
SKEWNESS (Sk):	0.923	-1.337	1.337	-0.501	0.501	Very Fine Skewed
KURTOSIS (K):	3.536	4.057	4.057	1.360	1.360	Leptokurtic

GRAIN SIZE DISTRIBUTION

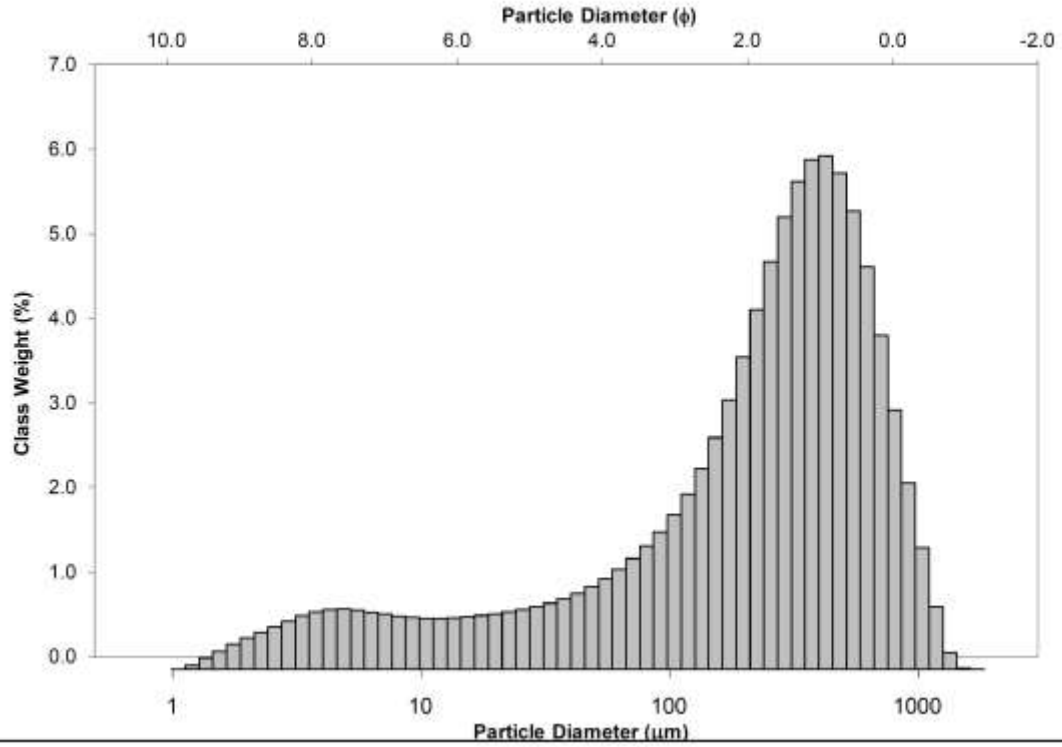

SAMPLE STATISTICS

SAMPLE IDENTITY: **m13** ANALYST & DATE: , 6/19/2018

SAMPLE TYPE: Unimodal, Very Poorly Sorted TEXTURAL GROUP: Slightly Gravelly Muddy Sand

SEDIMENT NAME: Slightly Very Fine Gravelly Very Coarse Silty Fine Sand

	µm	ϕ
MODE 1:	174.6	2.521
MODE 2:		
MODE 3:		
D_{10}:	11.64	1.125
MEDIAN or D_{50}:	125.6	2.993
D_{90}:	458.3	6.425
(D_{90} / D_{10}):	39.39	5.709
(D_{90} - D_{10}):	446.7	5.300
(D_{75} / D_{25}):	6.086	2.359
(D_{75} - D_{25}):	221.2	2.606

GRAIN SIZE DISTRIBUTION

GRAVEL:	0.0%	COARSE SAND:	7.6%
SAND:	68.4%	MEDIUM SAND:	18.6%
MUD:	31.6%	FINE SAND:	23.3%
		V FINE SAND:	18.3%
V COARSE GRAVEL:	0.0%	V COARSE SILT:	11.4%
COARSE GRAVEL:	0.0%	COARSE SILT:	7.6%
MEDIUM GRAVEL:	0.0%	MEDIUM SILT:	5.7%
FINE GRAVEL:	0.0%	FINE SILT:	4.5%
V FINE GRAVEL:	0.0%	V FINE SILT:	2.2%
V COARSE SAND:	0.6%	CLAY:	0.2%

	METHOD OF MOMENTS			FOLK & WARD METHOD		
	Arithmetic	Geometric	Logarithmic	Geometric	Logarithmic	Description
	µm	µm	ϕ	µm	ϕ	
MEAN ($\bar{x}$):	190.2	96.03	3.380	99.59	3.328	Very Fine Sand
SORTING (σ):	202.8	3.960	1.985	4.049	2.018	Very Poorly Sorted
SKEWNESS (Sk):	1.988	-0.716	0.716	-0.284	0.284	Fine Skewed
KURTOSIS (K):	8.790	2.917	2.917	1.049	1.049	Mesokurtic

GRAIN SIZE DISTRIBUTION

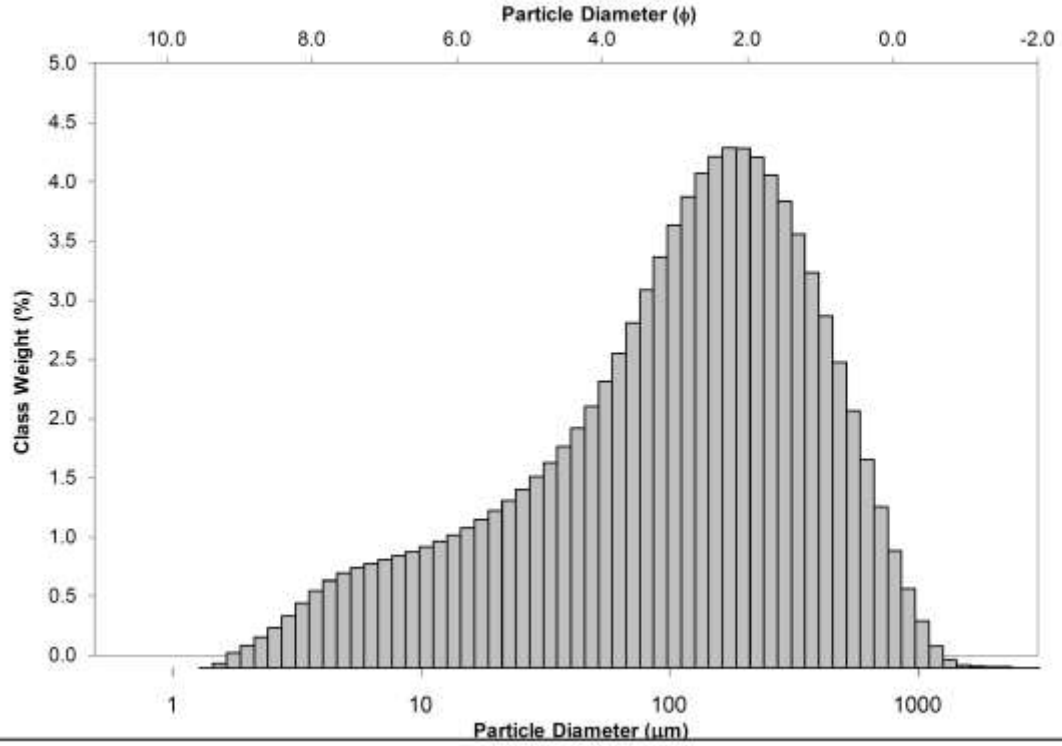

SAMPLE STATISTICS

SAMPLE IDENTITY: **mHF** ANALYST & DATE: , 6/19/2018

SAMPLE TYPE: Unimodal, Poorly Sorted TEXTURAL GROUP: Slightly Gravelly Muddy Sand

SEDIMENT NAME: Slightly Very Fine Gravelly Very Coarse Silty Fine Sand

	μm	ϕ
MODE 1:	153.7	2.705
MODE 2:		
MODE 3:		
D_{10}:	51.54	1.661
MEDIAN or D_{50}:	145.8	2.778
D_{90}:	316.3	4.278
(D_{90} / D_{10}):	6.137	2.576
(D_{90} - D_{10}):	264.8	2.618
(D_{75} / D_{25}):	2.383	1.575
(D_{75} - D_{25}):	128.2	1.253

GRAIN SIZE DISTRIBUTION

GRAVEL:	0.0%	COARSE SAND:	1.8%
SAND:	87.1%	MEDIUM SAND:	17.1%
MUD:	12.9%	FINE SAND:	40.6%
		V FINE SAND:	27.6%
V COARSE GRAVEL:	0.0%	V COARSE SILT:	6.2%
COARSE GRAVEL:	0.0%	COARSE SILT:	2.5%
MEDIUM GRAVEL:	0.0%	MEDIUM SILT:	1.6%
FINE GRAVEL:	0.0%	FINE SILT:	1.6%
V FINE GRAVEL:	0.0%	V FINE SILT:	1.0%
V COARSE SAND:	0.0%	CLAY:	0.1%

	METHOD OF MOMENTS			FOLK & WARD METHOD		
	Arithmetic	Geometric	Logarithmic	Geometric	Logarithmic	Description
	μm	μm	ϕ	μm	ϕ	
MEAN ($\bar{x}$):	169.9	127.2	2.974	140.7	2.829	Fine Sand
SORTING (σ):	115.6	2.482	1.311	2.184	1.127	Poorly Sorted
SKEWNESS (Sk):	1.526	-1.687	1.687	-0.210	0.210	Fine Skewed
KURTOSIS (K):	6.943	7.260	7.260	1.408	1.408	Leptokurtic

GRAIN SIZE DISTRIBUTION